Fermilab

BEAM HALO AND SCRAPING

THE 7TH ICFA MINI-WORKSHOP ON HIGH INTENSITY HIGH BRIGHTNESS HADRON BEAMS

Interlaken Resort on Lake Como, Wisconsin
September 13-15, 1999

EDITORS
Nikolai V. Mokhov and Weiren Chou

Fermi National Accelerator Laboratory
Batavia, Illinois

ORGANIZING COMMITTEE

Jose Alonso (ORNL)
Weiren Chou (FNAL - co-chair)
Pat Colestock (LANL)
Alexandr Drozhdin (FNAL)
Roland Garoby (CERN)
Yoshiro Irie (KEK)
Bernard Jeanneret (CERN)
Hans Ludewig (BNL)
Shinji Machida (KEK)
Phil Martin (FNAL)
Nikolai Mokhov (FNAL - co-chair)
Yoshiharu Mori (KEK)
Thomas Roser (BNL)
Cynthia Sazama (FNAL - secretariat)
Walter Scandale (CERN)
Tom Wangler (LANL)
Chris Warsop (RAL)
Bill Weng (BNL)
Hideaki Yokomizo (JAERI)

Contents

INTRODUCTION

The ICFA Mini-Workshop on Beam Halo and Scraping was held September 13-15, 1999 at the Interlaken Resort on Lake Como, Wisconsin, USA. This was the seventh in a series of mini-workshops on high intensity, high brightness hadron beams. The previous mini-workshops are:

1. May 20-23, 1996 at Fermilab, on Transition Crossing.

2. December 9-11, 1996 at the KEK, on Particle Losses.

3. May 7-9, 1997 at the BNL, on RF.

4. November 5-7, 1997 at CERN, on Transverse Emittance Preservation and Measurement.

5. February 23-25, 1998 at the KEK, on Beam-loading.

6. February 24-26, 1999 at the RAL, on Injection and Extraction.

These mini-workshops are sponsored by the ICFA Beam Dynamics Panel and organized by the ICFA Working Group on High Intensity High Brightness Hadron Beams. (See the web page http://www-bd.fnal.gov/icfa/ for more information.)

This mini-workshop on Beam Halo and Scraping was attended by thirty four people from CERN, KEK, BNL, ORNL, LBNL, IHEP (Protvino), LANL, TRIUMF, ANL, RAL, JAERI and Fermilab. The list of participants can be found at the end of this proceeding.

The first 1-1/2 days were plenary sessions with 21 presentations. On the afternoon of the second day, three working groups (WG) were formed:

WG-I on beam halo, led by A. Fedotov (BNL) and J. Holmes (ORNL);

WG-II on beam loss, led by T. Wangler (LANL), J. Wei (BNL) and J. Alonso (LBNL);

WG-III on beam collimation, led by D. Kaltchev (TRIUMF) and Y. Mori (KEK).

The charges to the working groups are:

WG-I Beam Halo: What is beam halo? What is the source of it? Beam halo in a linac *vs* in a ring. Beam halo in an accumulator *vs* in a synchrotron. Beam halo simulations *vs* measurements. Suggestion for future experiments. Design issues for beam halo minimization.

WG-II Beam Loss: What are the main origins of beam loss? How to measure it? What are the criteria of tolerable beam loss? Benchmark comparison of different Monte Carlo codes. Code simulations *vs* measurements.

WG-III Beam Collimation: Comparison of different collimation methods. How to do momentum collimation? Where to locate collimators?

There were a lot of interesting and stimulating discussions on these and other related issues. One important outcome of this workshop is the agreement that an average beam loss of 1 W/m in the uncontrolled area should be a reasonable limit for hands-on maintenance.

Each group gave a summary report at the final plenary session. The summaries and presentations at the plenary sessions are published in this proceeding. A contributed paper by S. Koscielniak is also included. After the workshop, there was a guided tour to Fermilab's accelerator complex and detectors.

We are indebted to the working group leaders and all the participants for their great efforts to make this workshop a success. We are also thankful to C. Sazama and P. Poole for their administrative support. Dmitri Mokhov helped at some stages of the proceedings preparation.

I. MACHINE PARAMETERS

Proton Driver

W. Chou[1]

Fermi National Accelerator Laboratory
P.O. Box 500, Batavia, Illinois 60510

1 INTRODUCTION

The proton driver under design at Fermilab is a high intensity rapid cycling proton synchrotron. Its function is to deliver intense short proton bunches to the target for muon production. These muons will be captured, phase rotated, bunched, cooled, accelerated and finally, injected into a storage ring for neutrino experiments. In this sense, the proton driver is *the front end* of a neutrino factory. The first serious effort for designing a proton driver at Fermilab was during the summer of 1997 led by S. Holmes. The results were summarized in Ref. [1]. The present design study is a continuation of that effort. In particular, this design is tailored to meet the specific needs of a neutrino factory.

In addition to serve a neutrino factory, the proton driver may have other applications. For example, it would replace the present Fermilab Booster as a high intensity new booster. As such it could provide 6 times as high proton flux and 12 times as high beam power to the MiniBooNE experiment. It could also increase the beam intensity in the Main Injector by a factor of 4. The anti-proton production rate and Tevatron luminosity would be enhanced accordingly.

There are two primary requirements of the proton driver:

1. High beam power: $P_{\text{beam}} = 1.2$ MW.
   This requirement is similar to other high intensity proton machines that are presently under design or construction, *e.g.*, the SNS at the ORNL, the ESS in Europe and the Joint Project (formerly known as the JHF) in Japan. This similarity makes it possible to establish a world-wide collaboration for tackling various technical design issues in a coherent manner.

2. Short bunch length at exit: $\sigma_b = 3$ ns.
   This requirement is *unique* for the proton driver. It brings up a number of interesting and challenging design issues that we must address in the study. The bunch length is related to the longitudinal emittance ε_L and momentum spread Δp by:

$$\sigma_b \propto \frac{\varepsilon_L}{\Delta p}$$

In order to get short bunch length, it is essential to have:

- small longitudinal emittance (emittance preservation during the cycle);

- large momentum acceptance (in the rf and as well as in the lattice);

- bunch compression at the end of the cycle.

---

[1]e–mail: chou@fnal.gov

It is interesting to compare the proton driver with the LHC or the former SSC. The LHC and SSC require proton beams very bright in the transverse plane. Transverse emittance (ε_T) preservation is of crucial importance in order to reach the design luminosity. In the longitudinal plane, however, ε_L would be blown up by two orders of magnitude in the injector chain in order to avoid instability and intrabeam scattering problem. The proton driver, on the contrary, requires high brightness in the longitudinal plane because of short bunch length, whereas ε_T would be diluted by painting during the injection from the linac to the ring in order to reduce the space charge effect.

2 CHOICE OF MAJOR DESIGN PARAMETERS

The design goal of the neutrino factory at Fermilab is 2×10^{20} useful muons per year to the neutrino experiments. Assuming one third of the muons in the storage ring is useful, it requires 6×10^{20} muons per year in the ring. Further assumptions are: one needs 15 protons (at 16 GeV) for every muon, and there are 2×10^7 seconds for experiments each year. These give 4.5×10^{14} protons per second. At a repetition rate (rep rate) of 15 Hz, 3×10^{13} protons per cycle is required. Therefore, the average beam current is 72 μA. At 16 GeV, this gives a beam power of about 1.2 MW.

The beam power is the product of three parameters – proton energy E_p, number of protons per cycle N_p and rep rate f_{rep}:

$$P_{\text{beam}} = f_{\text{rep}} \times E_p \times N_p$$

The rep rate is chosen to be 15 Hz for three reasons: (1) Fermilab has a 15 Hz linac that can be used for the proton driver. Any rep rate higher than 15 Hz would require a major change in the present linac. (2) A rep rate lower than 15 Hz would mean more protons per cycle, which will be difficult in the present linac. (3) This proton driver is designed with an upgrade capability for a future multi-TeV muon collider. The life time of a 2 TeV muon is about 40 ms. The 15 Hz rep rate is comparable to the muon decay rate.

The proton energy of 16 GeV is chosen due to the following considerations: (1) Lower energy is not preferred. Because it would give higher longitudinal phase space density N_b/ε_L (in which N_b is the number of protons per bunch), higher space charge tune shift ΔQ at top energy (which would make bunch compression more difficult) and larger momentum spread $\frac{\Delta p}{p}$. (2) The present Fermilab linac can deliver 3×10^{13} particles at 15 Hz. If the proton energy is lower than 16 GeV, it would require more particles from the linac, which will be difficult. (3) The present linac is 400 MeV. For a 16 GeV ring, the dynamic range is about 18, which should be fine. If further raising the energy, the dynamic range would become too large and cause trouble to the magnets.

It is clear that the parameter choice made above are based on the proton driver design itself. However, when considering the downstream subsystems that the proton driver would serve, there are two issues that should be pointed out:

1. A recent MARS simulation of the muon yield *vs.* proton energy for a graphite target shows a peak around $E_p = 6$ GeV. If this result is confirmed by target experiments (*e.g.,* HARP at CERN and E951 at BNL) and by other simulations (*e.g.,* FLUKA at CERN), it will play a role in the choice of E_p in the final design.

   From the cost point of view, however, a lower energy ring does not necessarily translate into lower cost. For the same beam power, the cost of a 16 GeV ring using the existing 400 MeV linac could be comparable to that of a lower energy ring plus an upgraded linac. (A detailed cost comparison is yet to be done.)

2. A rough estimate of the power consumption of the downstream subsystems, which are mostly in burst mode operation, shows that it would be prohibitively expensive for high rep rates. Thus, a lower rep rate is preferred. However, the target would obviously prefer a higher rep rate. Therefore, a trade-off investigation is needed for rep rate optimization. But this is out of the scope of the current study.

In addition to P_{beam}, f_{rep}, E_p and N_p, there are two more important parameters to choose, namely, the bunch length σ_b and number of bunches in the ring.

- Bunch length: A shorter bunch is preferred by the muon decay channel (to capture more muons per proton) and by muon polarization. However, several quantitative calculations of muon yield *vs.* bunch length indicate that, when σ_b is increased from 1 ns to 3 ns, the decrease in muon yield is small ($< 10\%$). The polarization, on the other hand, has a stronger dependence on σ_b. But it is not required by the current study. For the proton driver, a 3 ns bunch is much easier to produce than a 1 ns bunch, because a longer bunch would give smaller space charge tune shift ΔQ, smaller momentum spread $\frac{\Delta p}{p}$, and smaller bunch compression ratio. Therefore, it is decided to choose $\sigma_b = 3$ ns.

- Number of bunches: For given total number of protons in the ring and the length of each bunch, it is preferred to have more bunches. However, the downstream induction linac, which is for muon phase rotation, can only deliver 4 pulses per cycle. This limits the bunch number to 4 in the present design. It should be pointed out that, there is a new US-Japan initiative (between Fermilab and the KEK) for developing low frequency (several MHz) high gradient (0.5-1 MV/m) rf system. This would open up the possibility of using rf phase rotation replacing the induction linac. In this case, the bunch number could be increased to 18 or higher.

The proton driver for the neutrino factory is called Phase I. Details of Phase I design will be described in the following sections. A possible future upgrade of the proton driver to serve a muon collider is called Phase II. Table 1 lists the main parameters of the two phases. However, Phase II design will not be discussed in this report. As a comparison, the present proton source parameters are also listed in Table 1.

3 TECHNICAL SYSTEMS

The proton driver consists of a new 16 GeV synchrotron that would be installed in a new tunnel, a moderate Linac upgrade and two new transport lines (400 MeV and 16 GeV). The design of each technical system has been worked out to some detail and will be briefly described below.

3.1 New linac front end

In order to use much of the present linac as an injector for Phase I of the proton driver, the linac must provide H^- ions in excess of 5400 mA-μs (60 mA and 90 μs). Although both the beam current and pulse length are within the capability of the system, the beam loss and induced radiation in the structure at high intensity operation would become a problem so hands-on maintenance may suffer. Therefore, it is planned to change the front end for increasing the transverse brightness of the beam. The new front end consists of a brighter source (either a modified magnetron or a DESY rf type volume source), a short electrostatic focusing structure (LEBT), a 201 MHz RFQ from 30 keV to 1 MeV, an isochronous transport line made of two 270° bending magnets (the α-magnets) and five quads, a second 201 MHz RFQ from 1 MeV to 2.235 MeV, and a modified Tank 1 (DTL), in which the first 18 drift tubes will be eliminated. The rest of the linac (*i.e.,* Tank 2 to 5 and the CCL) will remain as it is now. With these modifications, it is expected that the transverse beam emittance ε_T at 400 MeV would be decreased from 8 π mm-mrad (present value) to 3 π mm-mrad. This would greatly reduce beam losses in the linac, which is believed to be mainly due to the aperture limit in the system.

3.2 Chopper

A new type of chopper has been designed and built in collaboration with the KEK. [2] This is a pulsed beam transformer made of three 1"-thick Finemet cores. It is driven by two HTS 81-09 transistors for a bipolar operation. It is placed in front of the RFQ and modulates the injection beam energy by $\pm 10\%$. The rise- and fall-time of the chopper is about 30 ns. A prototype has been installed on the linac of the HIMAC, a medical accelerator center in Japan. The beam test was successful [3].

3.3 400 MeV line

The 400 MeV line connects the linac to the 16 GeV ring. It will be made of permanent magnets, similar to the present 8 GeV line.

3.4 16 GeV line

In the present layout, the 16 GeV transport line is about 2 km long and connects the driver to the target station. A ma-

Table 1: Proton Driver Parameters of Present, Phase I and Phase II

	Present	Phase I (ν-factory)	Phase II (μμ-collider)
Linac (operating at 15 Hz)			
Kinetic energy (MeV)	400	400	1000
Peak current (mA)	40	60	80
Pulse length (μs)	25	90	200
H^- per pulse	6.3×10^{12}	3.4×10^{13}	1×10^{14}
Average beam current (μA)	15	81	240
Beam power (kW)	6	32	240
Pre-booster (operating at 15 Hz)			
Extraction kinetic energy (GeV)			3
Protons per bunch			2.5×10^{13}
Number of bunches			4
Total number of protons			1×10^{14}
Normalized transverse emittance (mm-mrad)			200π
Longitudinal emittance (eV-s)			2
RF frequency (MHz)			7.5
Average beam current (μA)			240
Beam power (kW)			720
Booster (operating at 15 Hz)			
Extraction kinetic energy (GeV)	8	16	16
Protons per bunch	6×10^{10}	7.5×10^{12}	2.5×10^{13}
Number of bunches	84	4	4
Total number of protons	5×10^{12}	3×10^{13}	1×10^{14}
Normalized transverse emittance (mm-mrad)	15π	60π	200π
Longitudinal emittance (eV-s)	0.1	2	2
RF frequency (MHz)	53	1.7	7.5
Extracted bunch length σ_t (ns)	0.2	3	1
Average beam current (μA)	12	72	240
Target beam power (kW)	100	1200	4000

jor portion of it would be in the Tevatron tunnel. A preliminary design using FODO lattice has been worked out. One concern about transporting intense ($N_b = 7.5 \times 10^{12}$) short ($\sigma_b = 3$ ns) bunches in this long line is possible bunch lengthening due to space charge and lack of longitudinal focusing. However, PARMILA simulation shows that the beam longitudinal emittance growth is negligible in this line.

3.5 16 GeV ring lattice

In order to minimize longitudinal emittance dilution, a principal requirement in the lattice design is that it should be transition free. This excludes the traditional FODO lattice for a 16 GeV ring. One must consider the flexible momentum compaction (FMC) type lattice. Other requirements include: $B_{max} \leq 1.5$ T, large dynamic aperture ($> 100\pi$ mm-mrad), large momentum acceptance ($\frac{\Delta p}{p} = \pm 2.5\%$), and dispersion free straight sections for rf. Due to the importance of a collimation system in this high intensity machine, the collimator design must be coupled to the lattice design.

There are presently two FMC lattices under study. One

is triangular shape. The circumference is 711.3 m, which is 1.5 times the size of the present booster. Another lattice is racetrack shape. Both give large or imaginary γ_t and use sextupoles to increase the momentum acceptance. The choice will be made after a careful comparison between the two lattices.

3.6 Injection and extraction

In order to reduce space charge effects, the injected beam will be painted in both transverse and longitudinal phase space. The horizontal injection system consists of 4 orbit bumpers and 2 fast kickers. The latter are used for painting and are located 90° apart (in phase) from the foil on each side of the foil. The foil temperature rise and beam emittance dilution during multiple passes through the foil have been calculated and should not be a problem.

Because this machine uses a resonant power supply, only 1-turn fast extraction is considered. At this moment, only one extraction point has been designed. A second extraction point is possible if one could demonstrate that it would be safe to place rf in dispersive region (*i.e.,* in the arcs).

3.7 RF system

The required total rf voltage is about 1.2 MV. Due to the compact size of this machine, the cavity must have high gradient (30 kV/m). Study shows that Finemet cores (which is a new type of magnetic alloy) can withstand higher rf B-field than regular ferrite and, thus, provide higher gradient. The problem about Finemet is that it has low Q and is lossy. But this can be partially solved by cutting the core to two halves. In order to reduce eddy current heating, the sharp edges of the cut core should be shaped such that the radial B-field is minimized. A prototype 14 kV, 7.5 MHz Finemet cavity has been built at Fermilab in collaboration with the KEK. It will be tested in the Main Injector for 132 ns bunch spacing coalescing experiment.

In addition to this acceleration rf system, another rf system for bunch compression is also under investigation. [4] The main difference between the two systems is the duty factor. The one for acceleration will be used for 50% of the cycle, whereas that for bunch compression is put to use for just hundreds μs in a cycle. Therefore, the latter could work at mush higher gradient (0.5-1 MV/m).

3.8 Magnets

The main requirements are large aperture (dipole: 12.7×31.8 cm^2, quad: 8.56 cm pole tip radius) and large good field region (dipole: $\frac{\Delta B}{B} < 10^{-3}$ within ± 10 cm). The lamination uses 0.014" silicon steel M17. The quadrupole design is basically the same as the large quad in Fermilab Accumulator, except that it will use 4-piece laminations instead of 2-piece.

3.9 Power supplies

Four proposals have been considered: (1) programmable IGBT (as the MI sextupole power supply), (2) single 15 Hz resonance circuit (as in the present booster), (3) dual-resonance (15 Hz plus 12.5% 30 Hz component), and (4) dual-frequency (up-ramp 10 Hz, down-ramp 30 Hz). After a careful comparison, (3) is chosen. The reasons are the following. It is cheaper (by a factor of 2) than (1); it can save 25% rf power compared with (2); and it has no ripple problem at injection, which is a main concern of (4).

In addition to the main power supply, a second power supply for correcting the tracking error between dipole and quad has also been designed. It drives the trim coils in the quads and uses bucking choke for cancelling the transformer effect between the main and trim coils.

3.10 Vacuum system

In a rapid cycling machine, the eddy current in the beam pipe is a major problem. The ISIS solution, which uses ceramic pipe equipped with a metallic cage inside, works well. However, it requires additional vertical aperture of the magnet. The alternative is to use thin metallic pipe. Three designs are being pursued: a 0.05" Inconel pipe with cooling tubes, a 0.005" Inconel pipe with ribs, and a composite material pipe with a thin Inconel (or Ti-Al) sheet inside. The pipe size is 5" × 9".

The vacuum system design would give a vacuum of 10^{-8} torr or lower. Such a vacuum would eliminate the concern about possible *e-p* instability as observed in the PSR at LANL.

3.11 Collimators

A 2-stage collimator system has been designed. Calculation shows that it can capture more than 99% of the lost particles. With such a high efficiency, even for 10% loss at injection or 1% loss at ejection, the beam loss level in most of the tunnel would be below 1 W/m. Therefore, hands-on maintenance would be possible. The area near the collimators would be radioactively hot and require special local shielding.

4 TECHNICAL DESIGN ISSUES

4.1 High longitudinal brightness

One of the most demanding issues in the proton driver design is how to achieve the required longitudinal brightness. Table 2 is a comparison of the longitudinal brightness N_b/ε_L in existing as well as planned proton machines.

The proton driver Phase I requires 3.8×10^{12} particles per eV-s, which is higher than most of the existing machines, with the exception of the PSR and ISIS. (The PSR is an 800 MeV accumulator ring. The ISIS, although an 800 MeV synchrotron, uses low field magnets, a small rf system, and has no sextupoles.)

In order to achieve high longitudinal brightness, one has to preserve ε_L, which is in contrast to the controlled blow-up of ε_L in many high intensity machines for keeping beam stable. The following measures are taken for ε_L preservation:

- Avoid transition crossing in the lattice design. This eliminates a major source of emittance dilution.

- Avoid longitudinal microwave instability by keeping the beam below transition (The capacitive space charge impedance helps stabilize the beam when below transition) and keeping the resistive impedance small (using a uniform metallic beam pipe).

- Avoid coupled bunch instability by using low Q rf cavity.

- Apply inductive inserts for space charge compensation.

- Apply active longitudinal feedback system.

4.2 Bunch compression

A bunch compression is needed at the end of the cycle in order to shorten the bunch to 3 ns. There are at least three possible ways to do this gymnastics: (1) RF amplitude jump, (2) RF phase jump and, (3) γ_t manipulation. The achieved compression ratio of either method is in the range of 3-5.

Table 2: Longitudinal Brightness of Proton Machines

Machine	E_{max} (GeV)	N_{tot} (10^{12})	N_b (10^{12})	ε_L (eV-s)	N_b/ε_L (10^{12}/eV-s)
Existing:					
CERN SPS	450	46	0.012	0.5	0.024
FNAL MR	150	20	0.03	0.2	0.15
FNAL Booster	8	4	0.05	0.1	0.5
PETRA II	40	5	0.08	0.12	0.7
KEK PS	12	3.6	0.4	0.4	1
DESY III	7.5	1.2	0.11	0.09	1.2
FNAL Main Inj	150	60	0.12	0.1	1.2
CERN PS	14	25	1.25	0.7	1.8
BNL AGS	24	63	8	4	2
LANL PSR	0.797	23	23	1.25	18
RAL ISIS	0.8	25	12.5	0.6	21
Planned:					
Proton Driver Phase I	16	30	7.5	2	3.8
Proton Driver Phase II	16	100	25	2	12.5
Japan JHF	50	200	12.5	5	2.5
AGS for RHIC	25	0.4	0.4	0.3	1.3
PS for LHC	26	14	0.9	1.0	0.9
SPS for LHC	450	24	0.1	0.5	0.2

Method (1) is most common among the labs. Although Fermilab has many years of experience with this operation, the high bunch intensity poses new problems:

1. During debunching, the beam momentum spread will decrease. This may give rise to microwave instability.

2. Also during debunching, the rf voltage will decrease. This may cause severe beamloading effects.

3. In a regular bunch rotation simulation, the momentum compaction is assumed to be a constant α_0. However, the proton driver lattice is nearly isochronous ($\alpha_0 \approx 0$). The higher order terms α_1 become important. Thus, particles with different $\frac{\Delta p}{p}$ have different path length ΔL. This complicates the bunch rotation process.

4. Due to short bunch length, the tune shift ΔQ from direct space charge and image charge remains large even at 16 GeV. This ΔQ also gives different path length ΔL. In other words, the path length of each particle depends not only on its longitudinal position but also on its transverse amplitude. This effect couples the longitudinal and transverse motion and is a new challenge to beam dynamics study.

Items 3 and 4 causes the so-called "η-spread" (η is the slip factor), which must be taken into account in theoretical modelling as well as in numerical simulations.

These problems have got the attention of beam physicists. Several labs (Fermilab, BNL, KEK, CERN, GSI and Indiana Univ.) have decided to carry out experimental studies in a "contest" — to see who can get the highest peak current, longitudinal brightness and compression ratio.

4.3 Transient beamloading

This problem is crucial to the intense short bunch operation. The single bunch intensity (7.5×10^{12}) gives a charge $q = 1.2\ \mu C$. For a 14 kV cavity and a gap capacitance $C = 300$ pF, the single pass beamloading voltage q/C would reach 3 kV, which has to be compensated. However, because the bunch is very short ($\sigma_b = 3$ ns), how to inject a short current pulse to do the compensation is challenging. This is a high priority item in the proton driver study. The plan is to use an rf feedforward system for global compensation and an rf feedback system for reducing bunch-to-bunch and turn-by-turn variations for a total reduction of 20-30 dB.

4.4 Space charge and instabilities

Space charge is a main limitation to achieve high intensity proton beams, in particular at injection. In order to reduce the Laslett tune shift, a large transverse emittance (60π mm-mrad, normalized, 95%) is used. Both transverse and longitudinal phase spaces will be painted for a uniform particle distribution. It is also planned to use inductive inserts to reduce the potential well distortion from the space charge. An experiment is going on at the PSR/LANL using inductive modules provided by Fermilab. The results are encouraging. For given rf voltage, the achievable beam intensity is increased when the inserts are applied. More measurements will be done to study the effects of the inserts to the beam.

There are two categories of instability problems in the proton driver. One is the "conventional" type, for instance, impedance budget, resistive wall, slow head-tail, Robinson, coupled bunch, etc.. These are by no means trivial. How-

ever, one knows how to deal with them. Another type is "non-conventional," which is not well understood but is important to the proton driver. For example:

- Longitudinal microwave instability below transition. In theory, the capacitive space charge impedance helps to make beam stable when it is below transition. However, a recent SPS experiment showed that, even below transition, a coasting beam can be unstable. It is not clear if the same would be true for a bunched beam. More experiments are needed.

- Fast head-tail (transverse mode-coupling) in the presence of strong space charge. This type of instability is clearly observed in electron machines. However, it has never been observed in any proton machine. There are two possible explanations:

  1. If the betatron tune spread ΔQ_β in a proton machine is many times larger than the synchrotron tune Q_s, then the mode lines ($m = 0, \pm 1, ...$) would get smeared and there won't be any coupling.
  2. In low- and medium-energy proton machines, the space charge force is significant. It would shift $m = -1$ mode downward as the beam intensity increases. Meanwhile, the inductive broadband wall impedance would shift this mode upward. Thus, they intend to cancel each other. This makes the coupling between the mode $m = 0$ and $m = -1$ more difficult.

  These claims need support from more careful analytical and numerical study.

- Synchro-betatron resonance due to dispersion in rf section. Due to the compact size of the proton driver, some rf cavities may have to be installed in the dispersion region. The concern is about the synchro-betatron resonance $kQ_\beta \pm mQ_s = n$. In previous studies, the case $k = 1$ has been fully analyzed [5]. However, the cases of $k = 2, 3, ...$ remain open.

4.5 Particle loss, collimation and shielding

Here the main concern is the hands-on maintenance, which requires the residual dose below certain level before one may proceed to do any repair work. Monte Carlo simulations using the code MARS show that, at an average particle loss rate of 1 W/m, the residual dose after 30 days irradiation and 4 hours cool down would be below 100 mrem/hr. This result agrees with that obtained at LANL and ORNL. To meet this requirement, a collimation system has been designed. It has a capture efficiency better than 99% and would allow 10% particle loss at injection and 1% loss at extraction during normal operation.

The MARS code was also used for radiation shielding calculation. The needed dirt thickness for shielding 1-hour accidental full beam loss is 29 feet. It is close to the result obtained from the simplified scaling formula (the Dugan criterion), which gives 32 feet.

4.6 Other issues

A number of other design issues are also under investigation, including FMC lattice design for large momentum and dynamic aperture, beam injection when magnet current has a second harmonic (*i.e.*, $\dot{B}$ has a large non-zero value), injection painting, tracking error correction, cooling and induced field error correction of thin metallic pipes, high intensity high brightness H^- source design, fringe field correction of large aperture dipoles and quads, etc.

5 SUMMARY

Over the past year a team in the Beams Division has been working on the proton driver for Fermilab. Significant progresses have been made to reach the Phase I design goals. A Phase I proton driver consists of a modest improvement of the linac front end, a new 16 GeV synchrotron in a new tunnel and two new beam lines (400 MeV and 16 GeV). It meets the needs of a neutrino factory and can provide a 1.2 MW proton beam with 3 ns bunch length. It also allows an upgrade path to a beam power of 4 MW and bunch length of 1 ns, which will be required by a future muon collider. In addition to serve a neutrino factory and/or a muon collider, the system would also serve as a complete functional replacement for the Fermilab Booster, providing upgraded capabilities in the future for the programs that the Booster would otherwise have served. New physics programs based on the stand-alone capabilities of the proton driver as an intense source of proton beams would also be enabled.

The Fermilab management has scheduled an internal technical review of the proton driver design study on April 17-19, 2000. A complete design report will be due early 2001.

6 REFERENCES

[1] S. Holmes, editor, "A Development Plan for the Fermilab Proton Source," FERMILAB-TM-2021 (1997).

[2] W. Chou *et al.*, KEK Report 98-10 (September 1998); also see FERMILAB-Conf-99/102, which is published in PAC'99 proceedings.

[3] Y. Mori et al, "Fast Beam Chopper with MA Cores", presented at EPAC'00, June 2000, Vienna, Austria.

[4] W. Chou and A. Van Ginneken, "Phase Rotation Using Low Frequency (Few MHz) RF," Fermilab MuCool Note 90 (February, 2000).

[5] T. Suzuki, Part. Acc., **18**, p. 115 (1985).

STATUS OF THE PROPOSAL FOR A SUPERCONDUCTING PROTON LINAC AT CERN

R. Garoby, M. Vretenar

PS Division, CERN, CH-1211 Geneva 23, Switzerland

Abstract

A superconducting proton linac delivering a mean beam power of 4 MW is being considered at CERN as a potential front end for the proton driver of a neutrino factory. Built mostly with the rf equipment to be recuperated from LEP after its decommissioning, it would provide H- ions at a kinetic energy of 2 GeV, which is adequate for the production of pions and muons. The requirements specific to a neutrino factory are summarized, and the basic design of such a linac-based proton driver is given. Subjects of further studies are outlined.

1 INTRODUCTION

Superconducting proton linacs are efficient at providing a high beam intensity up to slightly more than 1 GeV kinetic energy and they are exploited in most projects aiming at high beam power [1, 2, 3, 4]. A previous study [5] has shown that a 2 GeV superconducting linac can be built at CERN using the large inventory of 352 MHz rf and superconducting cavities available after the decommissioning of LEP-2. The existing complex of high energy accelerators as well as the radio-active ion facility (ISOLDE) would benefit from the higher beam performance and repetition rate, while the renewal of the low energy part of the accelerator chain would positively improve the long term reliability. Moreover, the proposal was recently made [6] to design that linac for a higher mean beam power and use it as the front-end of a proton driver for a neutrino factory [6].

However the time structure of the beam required by the complex of muon accelerators behind the target is not directly feasible out of a linac, and special techniques must be implemented making use of an accumulator ring. These requirements were highlighted at a recent workshop [7] and possible solutions have since been envisaged.

2 REQUIREMENTS OF A NEUTRINO FACTORY

Existing studies for muon colliders and neutrino factories have concluded that 4 MW of proton beam power is adequate for achieving their physics goal [8]. During the first workshop on neutrino factories [7] the working group on targets quickly established that:
- this is the maximum power any conceivable target could reasonably handle,
- pion and consequently muon production in the low energy range depends mainly on beam power for $T \geq 2$ GeV.

Consequently the 4 MW figure has been used as a common specification for all proton driver scenarios.

The time structure of the pions/muons beam after the target must comply with the needs of the muon acceleration complex. Table 1 summarizes the requirements for the proton beam hitting the target, assuming that the muon beam is treated as foreseen in reference 7. This corresponds to a peak power during the beam pulse exceeding 10 GW (assuming the fastest tolerable repetition rate of 100 Hz, and a beam pulse of 4 μs) which is far outside the capability of an rf linac. An accumulator ring is therefore absolutely necessary.

Table 1: Requirements imposed on the proton beam time structure

Parameter	Value	Source of constraint
Bunch duration (rms)	~ 1 ns	Uncertainty in pion decay time
Time interval between bunches	> 100 ns	First bunch rotation after target
	> 300 ns	Second bunch rotation
Total duration of beam pulse	a few μs	Revolution time in the muon storage ring (single turn injection)
Beam pulse repetition rate	≤ 100 Hz	Background rejection in the distant experiments
		Power consumption in the muon accelerator complex

Since the longitudinal emittance of the bunches must be small, the accumulation process has to be able to provide the ultimate density tolerable in the ring. Charge exchange accumulation is the only possible solution and hence the linac must deliver H⁻ ions. Moreover, gaps are necessary in the bunch train received by the accumulator to minimise loss and optimise longitudinal emittance of the accumulated beam. A fast beam chopper is therefore needed for precise control of the bunch train.

3 PROTON DRIVER BASED ON A SUPERCONDUCTING PROTON LINAC (SPL)

3.1 SPL design

Based on the design work published in 1998 [5], the proposed linac has the characteristics listed in Table 2. The beam power during the pulse is 20 MW (10 mA at 2 GeV) so that a 20 % duty factor is used to deliver the specified mean beam power of 4 MW (for example 2 ms pulses at 100 Hz repetition rate, or 4 ms at 50 Hz). The schematic layout of the Linac is shown in Figure 1. Superconducting rf structures are used in the range of kinetic energies between 100 MeV and 2 GeV, while the lowest energy part operates at room temperature.

Table 2: Superconducting linac characteristics

Energy	2	GeV
Mean current	10	mA
Duty cycle	20	%
Beam power	4	MW
Maximum bunch current (maximum number of charges per bunch)	40 (7×10^8)	mA
Transverse emittance (rms, norm.)	0.6	μm
Longitudinal emittance (total)	80	μeVs
Rms bunch length at output	6	ps

The H⁻ beam from the source is bunched and accelerated up to 2 MeV by a first Radio Frequency Quadrupole (RFQ) at 352 MHz. At that energy, a fast travelling wave electrostatic chopper (rise and fall times < 2 ns) eliminates the unwanted bunches and provides the optimum bunch train for filling the accumulator with a minimum of uncontrolled beam loss and induced activation. A promising design with the required rise time is being developed at Los Alamos for the SNS project [9]. For a given mean current of 10 mA during the pulse, the required source current as well as the bunch current depend upon the chopping factor.

The value of 40 mA assumed in Table 2 is possible with existing H⁻ sources and space charge effects are tolerable. A second RFQ brings the energy up to 7 MeV. Dedicated sections inside both RFQs provide matching to the chopper and to the second RFQ.

Between 7 MeV and 20 MeV, the beam is accelerated in a standard room temperature Drift Tube Linac (DTL) section. Above 20 MeV less conventional DTL sections are used with the focusing quadrupoles either in only a fraction of the drift tubes (Quasi-DTL) or outside of the DTL tanks (Separated-DTL).

The superconducting (SC) structure starts at 100 MeV. It is sub-divided into 4 sections made of cavities optimised for beta 0.48, 0.66, 0.8 and 1 respectively. The 4-cell cavities at beta 0.48 will be fabricated in bulk niobium, while the others use the standard CERN technology of niobium sputtering on copper [10]. The 4-cell cavities at beta 0.66 exploit some components recuperated from the LEP-2 cavities like the input coupler, while the 5-cell beta 0.8 cavities are housed in LEP-2 cryostats. Existing LEP-2 cavities are directly employed along the 320 m long beta 1 section. The existing input rf coupler is perfectly compatible with the SPL current of 10 mA.

The effective accelerating gradients in the four sections are shown in Figure 2. In spite of the fact that the present LEP run has demonstrated that LEP-II cavities can operate above their design value of 6 MV/m and that a further improvement could be expected in pulsed mode, the SPL design is based on a conservative value of 7 MV/m for the beta 1 section. The reason is that the existing LEP waveguide distribution system, based on 8 cavities per klystron, can be re-used without modification. In case gradients higher than 10 MV/m could be reached in pulsed mode by at least part of the LEP cavities, a layout with 4 cavities per klystron and a much shorter linac would become the natural choice. For the 5-cell beta 0.8 cavities, instead, a gradient of 9 MV/m can be reasonably assumed, extrapolating from the CW measurements done on a test cavity. This gradient would need 4 cavities per klystron. The section made of beta 0.66 cavities has a much lower gradient, based on the tests
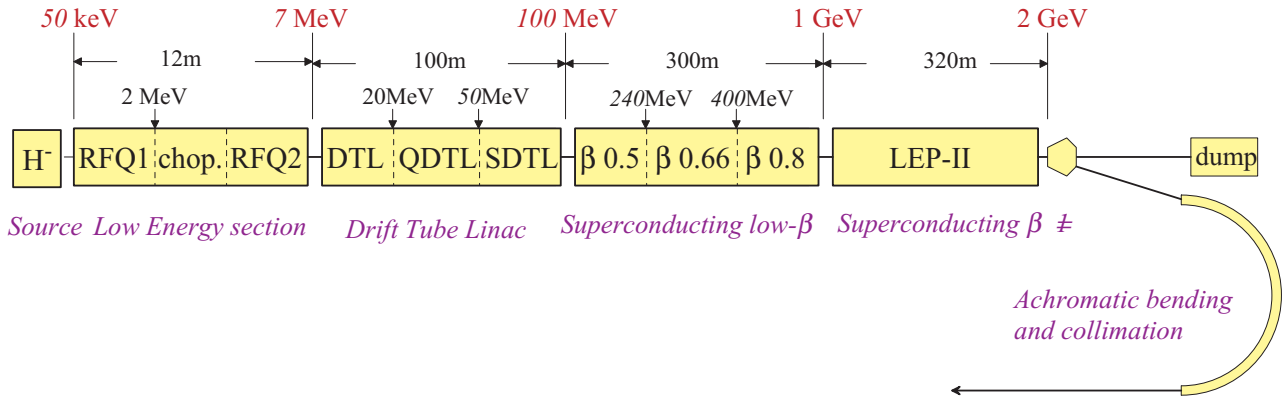

Figure 1: Schematic layout of the SPL

done on a niobium-sputtered cavity, and again 8 cavities per klystron would be appropriate. To overcome the problem related to sputtering at low angles, a new beta 0.7 test cavity is in production, with a geometry optimised for the sputtering process. This type of cavity is expected to be able to run at higher gradients, and finally to replace the entire beta 0.66 section in the SPL design.

modules with their cryostats are re-used, i.e. only 36% of the 72 presently installed in LEP. Moreover, 12 cryostats are recuperated for the beta 0.8 modules, giving a total of 38 cryostats that can be re-used (53%). Most of the LEP-2 klystrons (36 plus some spares), the high voltage distribution boxes, the high voltage high power converters and a large fraction of the waveguide distribution system
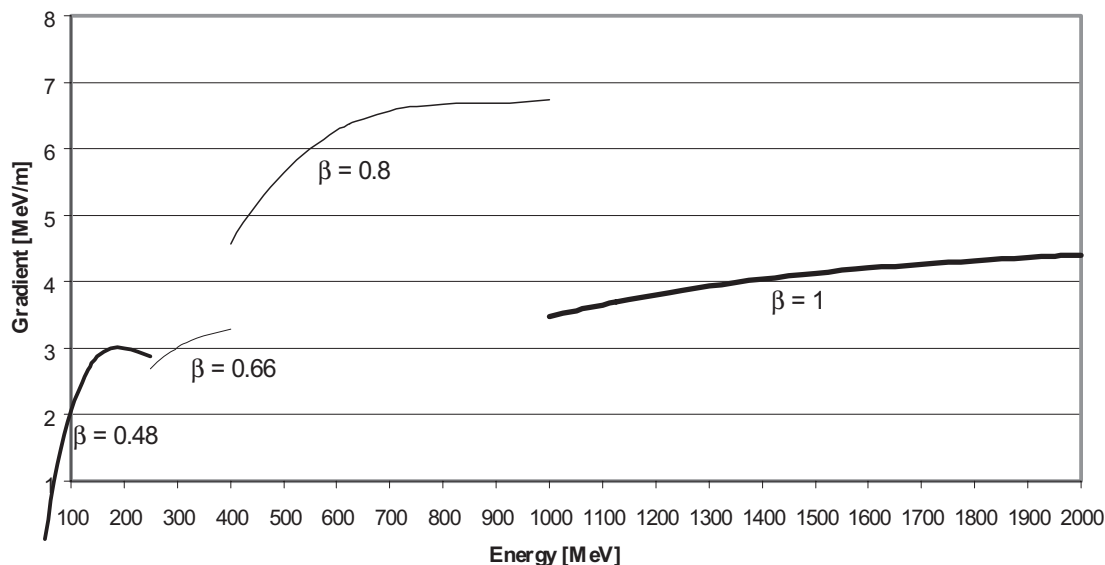

Figure 2: Effective gradients in the 4 sections of the superconducting linac

Pulsing superconducting rf structures presents some difficulties due to microphonic vibrations which randomly detune the resonators and perturb the phase and amplitude of the accelerating field. However simulations show that adequate servo-systems can in principle reduce these effects to acceptable levels, especially in the case of the stiff Nb-sputtered copper cavities [5]. On the other hand, pulsed operation should allow for higher gradients than in CW (tests are foreseen in the near future), and it should also help operate at lower Q-values, the static cryogenic losses being dominant.

The hardware components of the linac and some of their characteristics are listed in Table 3. Each of the 33 klystrons used in the superconducting part operates at a maximum power of 800 kW, with a comfortable safety margin for phase and amplitude control with respect to their maximum power of 1.3 MW.

Each klystron feeds 8 cavities in the beta 0.48, 0.66 and 1 sections, and 4 cavities in the beta 0.8 section which works at a higher gradient. The power per klystron in the two lower beta sections is deliberately kept low (200-400 kW) to limit to 8 the number of cavities each one of them feeds and ease the regulation problem and the complexity of the distribution network. A total of 26 LEP-2 4-cavity

are recuperated, making up about 90% of the linac rf system.

The management of beam losses is a major concern for the design of such a high intensity linac. The general agreement among accelerators experts is that in order to allow hands-on maintenance of the machine, distributed losses have to be kept below 1 W/m. For the SPL, this means a relative loss of only 2.5×10^{-7} per meter at 2 GeV. Particular care has therefore to be put into the design in order to avoid the migration of particles into diffused halos that would lead to uncontrolled losses along the machine. This can be achieved by preventing mismatches between sections, making use of proper matching units and by avoiding abrupt changes in the focusing parameters. The important role played by space charge in halo formation favors in this respect the lower bunch currents. For example, in the SC section the beam dynamics is space charge dominated for bunch currents exceeding 40 mA. An important feature of the superconducting cavities used in the SPL is the large aperture (between 200 and 240 mm), that allows most of the halo particles to be transported up to the end of the linac in the transport line, where they can be properly removed by special collimators.

Table 3: SPL hardware

Section	Output energy [MeV]	Frequency [MHz]	No. Cavities	RF Power [MW]	No. Klystrons	Length [m]
RFQ1	2	352.2	1	0.5	1	2.5
RFQ2	7	352.2	1	0.5	1	4
DTL	100	352.2	29	5.8	6	99
SC β=0.48	235	352.2	40	1.4	5	89
SC β=0.66	360	352.2	24	1.2	3	60
SC β=0.8	1010	352.2	48	6.5	12	148
SC LEP-2	2000	352.2	104	9.9	13	320
TOTAL			303	25.8	41	~723

3.2 Accumulation / compression scheme

The capabilities of the accumulation and compression set-up will probably dictate a number of characteristics of the proton driver, like the minimum number of bunches, the maximum number of protons per pulse and consequently the minimum repetition rate. Work is progressing in that direction but no conclusion can be drawn yet concerning feasibility. Although different designs are under investigation, they share the basic principles illustrated in Figure 3.

In the case represented, the linac is pulsed every 10 ms (100 Hz) and provides a beam pulse of 2 ms duration. This beam pulse is accumulated in a first ring, using charge exchange injection. Assuming a ring which fits inside the existing ISR tunnel at CERN, the revolution time is 3.4 μs so that 590 turns are injected in 2 ms. The pulse is made up of bursts of 30 consecutive 1 ns long bunches of 6×10^8 protons, spaced by one wavelength at 352.2 MHz (2.84 ns) with a periodicity of 284 ns (100 wavelength at 352.2 MHz). These bursts build up the intensity in 12 macro-bunches (~ 85 ns long) circulating
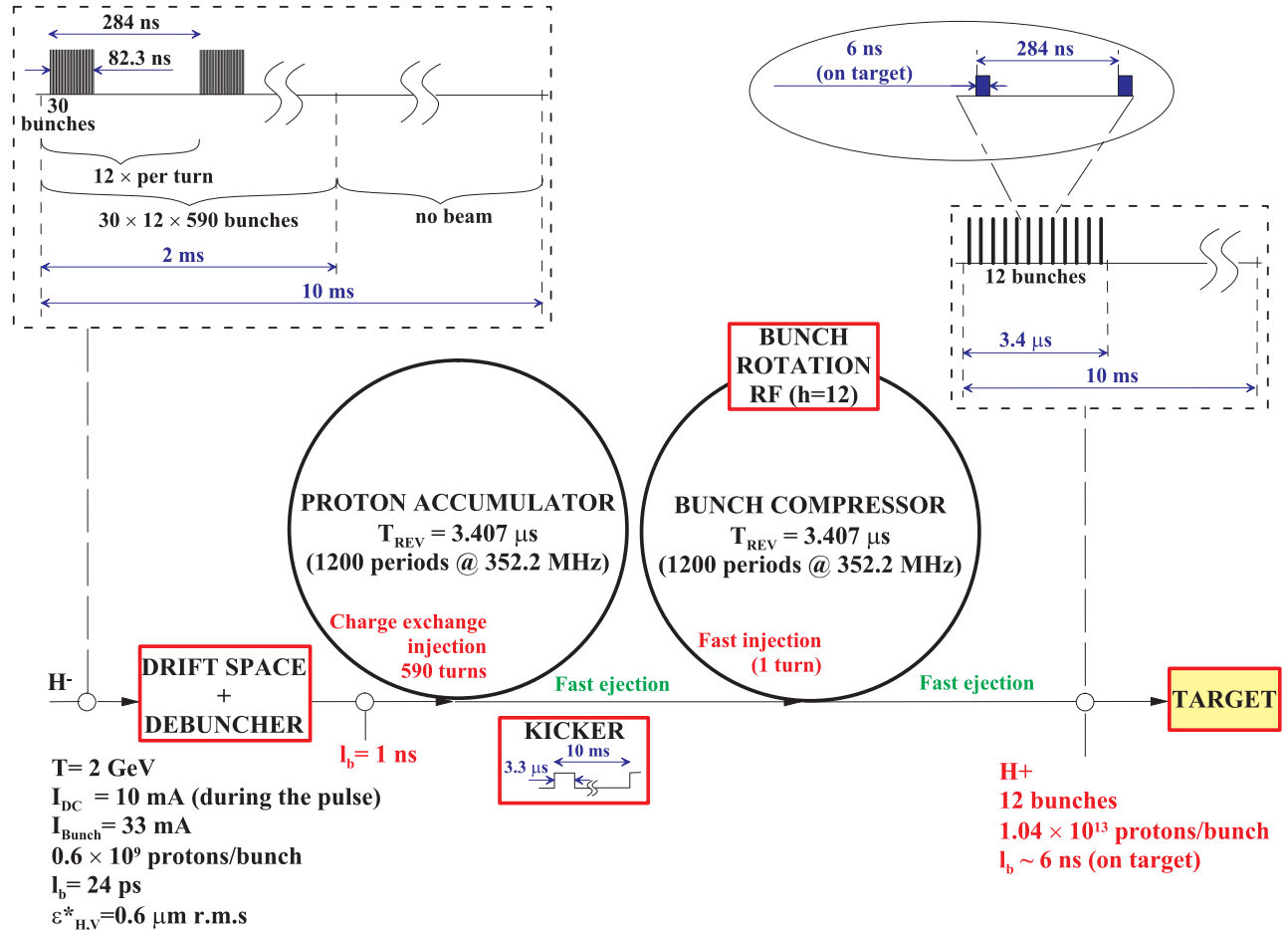

Figure 3: Beam accumulation and bunch compression scheme

16

in the accumulator. After the linac pulse each bunch is made up of 1.04×10^{13} protons, and the accumulator contains a total of 1.25×10^{14} protons.

A promising idea for achieving a high enough longitudinal density of protons is for the accumulator to be isochronous. Bunches can be progressively populated without spreading in azimuth and in principle without the need for an rf system.

Sketches of a macro-bunch in the longitudinal phase plane during accumulation (a) and after bunch compression (b) are shown in Figure 4.

Moreover, experimental results are necessary to precisely quantify the relative efficiency of pion collection from protons of various energies and help decide upon the optimum proton beam energy.

Finally, since research and development concerning devices and concepts used for the muon accelerator complex have only recently begun, new ideas are likely to appear and modify the requirements on the proton beam characteristics. In this respect, the flexibility of a linac-based facility makes it superior to a facility built with rapid cycling synchrotrons.
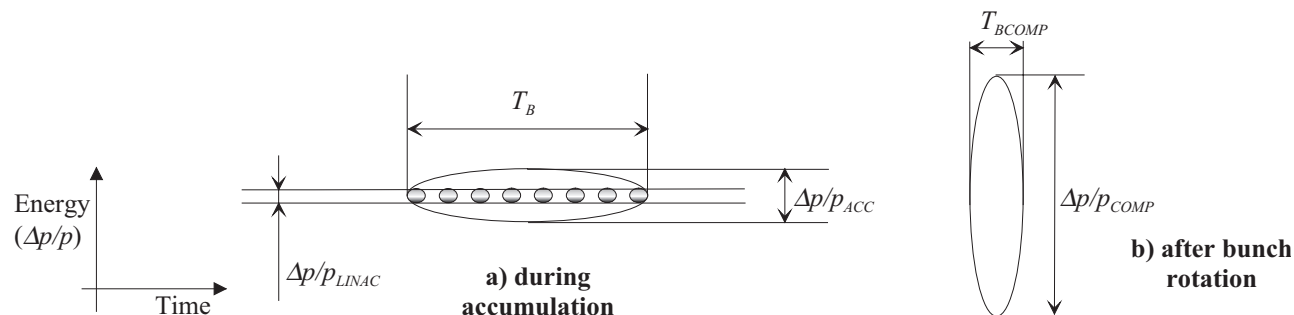

Figure 4: Macro-bunch in the longitudinal phase plane

At the end of the 2ms injection process, macro-bunches are long and have a small energy spread (estimated parameters: T_B=85 ns, $\Delta p/p_{ACC}$=2.8$\times10^{-3}$). Conservation of longitudinal emittance imposes that:

$$T_B \times \Delta p / p_{ACC} = T_{BCOMP} \times \Delta p / p_{COMP}$$

so that, for given bunch lengths during accumulation and on the target, the final momentum spread is directly proportional to the momentum spread at the end of accumulation.

Since the bunch sent to the target must be short it has to have a large $\Delta p/p$ (estimated parameters: T_{BCOMP}=6 ns, $\Delta p/p_{COMP}$=4$\times10^{-2}$). Such a large $\Delta p/p$ is difficult to handle in the accumulator ring which would need a very large physical aperture because of its large momentum compaction factor and large size. The proposal is therefore to transfer the 12 bunches immediately after the end of accumulation into a compression ring, with a much smaller momentum compaction factor and adequate rf for bunch rotation.

Acceptances of such an isochronous ring, beam stability in all planes, design of a realisable charge exchange injection scheme are among the numerous issues being addressed to evaluate the feasibility of such an accumulation/compression set-up.

4 CONCLUSION

A superconducting 2 GeV linac is capable of efficiently delivering the 4 MW of beam power required on the target of a neutrino factory. But adequate beam characteristics also depend upon the design of the accumulator and compressor rings which is still in progress.

REFERENCES

[1] G. Lawrence, High power proton linac for APT: status of design and development, Proceedings of the 1998 Linac Conference, Chicago, p.26
[2] J.M. Lagniel, High intensity linac studies in France, Proceedings of the 1998 Linac Conference, Chicago, p.706
[3] C. Pagani et al., Status of the INFN high current SC proton linac for nuclear waste transmutation, Proceedings of the 1998 Linac Conference, Chicago, p.1013
[4] K. Bongardt, M. Pabst, A. Letchford, High intensity injectors linacs for spallation sources, Proceedings of the 1998 Linac Conference, Chicago, p.339
[5] A. Lombardi & M. Vretenar (editors), Report of the study group on a superconducting proton linac as a PS injector, CERN/PS 98-063 (RF/HP)
[6] B. Autin, A. Blondel, J. Ellis (editors), Prospective study of muon storage rings at CERN, CERN 99-02
[7] "ν - Fact'99", Lyon, 5-9 July 1999, (http://lyoinfo.in2p3.fr/nufact99/)
[8] C.M. Ankenbrandt et al., Status of Muon Collider research and development and future plans, BNL-65623, Fermilab-PUB-98/179, LBNL-41935
[9] S.S. Kurennoy, J.F. Power, Meander-Line current structure for SNS fast beam chopper, Proc. of the 1999 Particle Acc. Conf., New York, p.1399
[10] O., Aberle, D. Boussard, S. Calatroni, E. Chiaveri, E. Haebel, R. Hanni, R. Losito, S. Marque, J. Tuckmantel, Technical developments on reduced-β superconducting cavities at CERN, Proc. of the 1999 Particle Acc. Conf., New York, p.949

II. BEAM HALO

Beam Halo Working Group Summary

A. V. Fedotov[1], C. Ankenbrandt,
R. L. Gluckstern, J. Holmes, S. Kurennoy,
S. Machida, K. Y. Ng, J. Qiang, R. Ryne

1 CHARGE TO WORKING GROUP

1. Definition of beam halo.
2. Difference of halo formation between linacs and rings.
3. Difference between accumulator rings and synchrotrons.
4. Comparison between simulations and measurements.
5. Future experiments.
6. Minimization of halo.
7. Ratio of β_{max}/β_{min}.
8. Other issues.

2 DEFINITION OF BEAM HALO

In general, one refers to "halo" as long as there are tails outside the beam core. Regardless of their extent, these tails are referred to as halo. The definition of halo as particles only outside several sigmas of the beam distribution is arbitrary and may be misleading.

• The definition of halo is not important. What really matters is the source of halo. For example, "Parametric Halo" (P.H.) is caused by the parametric $(2:1)$ resonance between individual particles and collective modes of the bunch.

• P.H. is believed to be the main source of halo in Linacs.

• P.H. may also exist in circular machines. Its existence will be strongly machine dependent. Depending on machine specifics, P.H. will not necessarily be an important source of halo. For typical circular machines other sources of halo may be more important.

3 DIFFERENCE OF HALO FORMATION BETWEEN LINACS AND RINGS

• Linacs - main effect: P.H.

• Rings - 1. P.H. is possible, and should be studied for each individual machine. 2. Machine resonances.

• P.H. (Linacs) - strong tune depressions govern rapid halo development.

• P.H. (Rings) - small tune depressions result in very slow halo development. The most important question regarding P.H. in Rings is the rate of halo development.

4 DIFFERENCE BETWEEN ACCUMULATOR RINGS AND SYNCHROTRONS

At low energy (where space-charge is important) this difference is irrelevant to P.H. development. This question is important primarily for halo formation due to resonance crossing: 1. Resonance crossing in the direction of space-charge tune shift increase is accompanied by total beam loss. 2. Resonance crossing in the direction of space-charge tune

---

shift decrease (for example, due to acceleration) results only in a finite beam size increase.

5 COMPARISON BETWEEN SIMULATIONS AND MEASUREMENTS

There are no good measurements of P.H. in real machines. Some measurements were attempted, with unclear results, at LANL in 70's. Experimental observation of P.H. was also reported at University of Maryland in the early 90's. Currently, all predictions rely on computer simulations.

6 FUTURE EXPERIMENTS

Some proposed experiments are: LANL (LEDA experiment) - year 2000; BNL (AGS booster experiment) - year 2000; Japan (HIMAC experiment) - in progress. It is planned to measure and study beam profiles and beam loss. Unfortunetly, standard diagnostic techniques allow only one percent accuracy instead of required 10^{-4} or even 10^{-3}. However, special diagnostic techniques will be employed for these purposes at the LEDA experiment.

7 MINIMIZATION OF HALO

• Linacs: Use strongly focused well-matched beam, and apertures much larger than rms beam size.

• Rings: Split bare tunes to stay away from coupling resonances; stay away from machine and structure resonances. Also, keep in mind that different beam distributions and beam shapes lead to different maximum tune shifts.

8 RATIO OF β_{MAX}/β_{MIN}

• This question is not related to natural coherent oscillations and thus is irrelevant to P.H. development.

• Small ratios are desired to minimize effect of non-linearities; stay away from envelope instabilities.

9 OTHER ISSUES

• Longitudinal halo - 1. Longitudinal P.H. is an important issue for Linacs. 2. It is expected that longitudinal P.H. will not develop in Rings.

• Dispersion - Effect of dispersion on halo formation should be studied for Rings with low tune depression.

• Analytic predictions are relatively limited, therefore, reliable 2D and 3D computer simulations are needed for halo studies in Rings.

---

[1]e–mail: fedotov@sun2.BNL.gov

Halo Formation in High Intensity Linacs [1]

R. L. Gluckstern[2]

Physics Department, University of Maryland, College Park, Maryland 20742

A. V. Fedotov

Brookhaven National Laboratory, Upton, New York 11973

Abstract

The latest designs for high current ion linacs (Accelerator for the Transmutation of Waste, Accelerator for the Production of Tritium, Heavy Ion Drivers, Spallation Neutron Source Injector) require minimal radioactivation by the beam striking the beam pipe. As a result, efforts are being made to understand and control the growth of beam halo. There is general agreement that the main mechanism for halo development in linacs is the parametric resonance between the ion oscillations in the beam bunch and collective oscillations of the bunch itself induced by mismatch in the linac. Analytic studies for a 2-D KV beam were found to give excellent agreement with corresponding computer simulations, which were then extended to other 2-D beams. Recently, analytic and numerical studies were performed for 3-D beam bunches (6-D phase space distributions), focusing attention on the formation of longitudinal halos and the possibility of bunch growth or loss of longitudinal bunch stability, as well as coupling between the longitudinal and transverse halos.

1 INTRODUCTION

In this paper we will review the current understanding of halo formation in linear focusing channels. Analytic models have been developed to study halo development in both 2-D beams and 3-D beam bunches in a linac. These models suggest that the most likely explanation for the halos which have been observed and which are likely to be seen in future high current linacs involves the parametric resonance between the collective modes and the motion of individual ions. When these models are used in conjunction with multiparticle simulations involving millions of particles, which are now practical with supercomputers and parallel processing, one can have great confidence in the predictions for halo formation and emittance growth which are so crucial for the designs of high current acceleration of short beam bunches.

2 2-D MODEL

Early attention was devoted to the analytic study of 2-D round beams in a continuous focusing channel. In particular, the KV distribution [1], a hyperspherical shell in the

4-D phase space with the self-consistent [2] distribution

$$f(H) = N\delta(H_0 - H), \qquad (2.1)$$

where

$$H = \frac{mv^2}{2} + \frac{kr^2}{2} + e\Phi_{sc}(r), \qquad (2.2)$$

had the useful features of a uniform charge density within the beam, and uniform density in the x and y phase space projections. Here H_0 and N are constants, k is the constant external focusing gradient, and $e\Phi_{sc}(r)$ is the potential energy at r due to space charge.

Use of the equation for the beam envelope [3] permitted the analytic description of a "breathing" beam, in which the charge density oscillated between too tight and too loose a match to the external focusing force. These oscillations provided a periodic force to the ion motion, which was simple harmonic as long as the ions remained inside the beam. But for ions which traveled beyond the beam boundary, the oscillations were non-linear. In this case the ion's non-linear motion in the presence of a periodic force allowed it to be trapped in the parametric resonance, where the breathing frequency was twice the ion oscillation frequency. The analytic model thus predicted the formation of a "halo" [4] for certain combinations of mismatch and tune depression.

Specifically, for an azimuthally symmetric 2-D KV beam, the equation of motion for a particle moving radially in a smoothed external focusing field is

$$r'' + k^2 r = \kappa \left\{ \begin{array}{ll} r/a^2 & , \quad r \le a \\ 1/r & , \quad r \ge a \end{array} \right\}, \qquad (2.3)$$

where $\kappa = eI/2\pi\varepsilon_0 mv^3$ is the perveance of the beam. Equation (3) describes linear motion with constant wave number $q = (k^2 - \kappa/a^2)^{1/2}$ within the core whose radius is a, but it also provides a wave number which increases with amplitude, once the particle travels outside the core.

If the beam is mismatched by some sudden change in the focusing system, the core radius a will oscillate with symmetric wave number $p = (4q^2 + 2\kappa/a^2)^{1/2}$ when these oscillations have small amplitude (mismatch correction is necessary for large mismatches [5]). The driving wave number p is therfore greater than twice the incoherent wave number within the core. Particles for which the amplitude increases have an effective increase in q. These particles then populate a halo surrounding the core when $p = 2q_{eff}$ condition is satisfied. A similar analysis can be performed for the antisymmetric transverse mode.

Analytically, one proceeds from Eq. (3) to a constant of motion by averaging over all wave numbers except $p - 2q$ [4]. The resulting phase-space trajectories produce a peanut-shaped structure with an inner separatrix and an outer separatrix. Halo formation takes place when particles cross the inner separatrix and then quickly move along the outer separatrix. While the model accurately predicts the radial extent of the halo as a function of the size of the mismatch and the tune depression, it does not address the question of the rate of halo development or the chaotic motion.

[2] e–mail: rlg@physics.umd.edu

Numerical simulations using the "particle-core" model confirmed the validity of the models, and pointed as well to the existence of chaotic motion as the tune depression became more severe [6]-[11].

Subsequent work focused on the possible mechanism for particles escaping from the beam into the region of non-linear oscillation [12]. In addition, numerical simulations were run for other, more physical, self-consistent stationary distributions of the form

$$f(r,v) = N(H_0 - H)^n, \qquad (2.4)$$

with $n = 0, 1$ [13]. These simulations exhibited the same halo structure and phase space patterns seen for the KV distribution, but with somewhat different quantitative dependence on mismatch and tune depression. The localization of the halo radius to approximately the same value predicted by the KV distribution gave linac designers confidence that a beam pipe wall could be placed far enough from the beam to avoid intercepting the halo particles.

3   3-D MODEL

Attention then shifted to short 3-D beam bunches of ellipsoidal shape with $c/a = $ length/width ratio in the range 2-4 [14, 15]. We continued our effort to study the self-consistent phase space stationary distributions of the form

$$f(r,v) = N(H_0 - H)^n, \qquad (3.5)$$

but this time, for $n = -1/2$, the differential equation for the charge density was linear and could be solved analytically [15]. In addition, for $c/a > 2$, the "breathing" modes could be approximately separated into transverse and longitudinal modes, each of which was capable of generating a halo. Thus the picture was of a beam bunch which, when mismatched accordingly, generated either a transverse or a longitudinal halo, or both. The signature of the longitudinal halo was the same as that of the transverse halo (a "peanut diagram" in the phase space projection). The transverse and longitudinal mismatch and tune depression parameter space was extensively explored with numerical simulations [15]. But a new concern surfaced: Would the longitudinal halo permit the loss of ions from the rf bucket? Unfortunately, the bucket "walls" cannot be moved far away without increasing the length and cost of the linac. Details about effects of non-linear RF fields can be found in [16].

Other issues involving halo formation were looked at, including equipartitioned distributions which were rms matched but not self-consistent [17]. These involved a rapid initial phase space redistribution, leading to a relatively small change in the parameters and extent of the halo formation due to the mismatch. In addition, they also point to the presence of a transverse-longitudinal coupling which allows either kind of halo to develop from either a transverse or longitudinal mismatch [17].

4   STATIONARY 6-D PHASE SPACE DISTRIBUTION

4.1   Analytic approximation to a spheroidal bunch

We take for the azimuthally symmetric 6-D phase space distribution

$$f(x,p) = N(H_0 - H)^{-1/2}, \qquad (4.6)$$

where

$$H = k_x r^2/2 + k_z z^2/2 + e\Phi_{sc}(x) + mv^2/2. \qquad (4.7)$$

Here $p = mv$, $r^2 = x^2 + y^2$, and k_x, k_z are the smoothed transverse and longitudinal restoring force gradients. The quantity $\Phi_{sc}(x)$ is the electrostatic potential due to the space charge of the bunch. The distribution is normalized such that

$$\int dx \int dp f(x,p) = 1. \qquad (4.8)$$

The charge distribution corresponding to Eq. (6) is

$$\begin{aligned} \rho(x) &= Q \int dp f(x,p) \\ &= NQm^3 \int dv \left[G(x) - \frac{mv^2}{2} \right]^{-1/2}, \quad (4.9) \end{aligned}$$

where

$$G(x) \equiv H_0 - \frac{k_x r^2}{2} - \frac{k_z z^2}{2} - e\Phi_{sc}(x). \qquad (4.10)$$

Performing the integral over $dv \equiv v^2 dv d\Omega_v$ in Eq. (9) leads to

$$\rho(x) = QG(x) / \int dx G(x), \qquad (4.11)$$

where the normalization constant satisfies

$$2\sqrt{2}\pi^2 Nm^{3/2} \int dx G(x) = 1. \qquad (4.12)$$

From Eq. (10) and Poisson's equation, we write

$$\nabla^2 G(x) = -k_s - e\nabla^2\Phi_{sc} = -k_s + (e/\varepsilon_0)\rho(x), \qquad (4.13)$$

where

$$k_s = 2k_x + k_z. \qquad (4.14)$$

Using Eq. (11), we obtain the partial differential equation for $G(x)$

$$\nabla^2 G(x) = -k_s + \kappa^2 G(x), \qquad (4.15)$$

where

$$\kappa^2 = (eQ/\varepsilon_0) / \int dx G(x). \qquad (4.16)$$

The solution of Eq. (15) for an axisymmetric, spheroidal shaped bunch can most easily be written in the spherical coordinates R, θ for which

$$z = R\cos\theta , \; r = R\sin\theta, \qquad (4.17)$$

as

$$G(x) = (k_s/\kappa^2)g(x), \qquad (4.18)$$

where

$$g(x) = 1 + \sum_{\ell=0}^{\infty} \alpha_\ell P_{2\ell}(\cos\theta) i_{2\ell}(\kappa R). \qquad (4.19)$$

Here $P_{2\ell}(\cos\theta)$ are the even (fore-aft symmetric) Legendre polynomials and $i_{2\ell}(\kappa R)$ are the spherical Bessel functions (regular at $\kappa R = 0$) of imaginary argument.

Since $g(x)$ is proportional to the charge density, the edge of the bunch is defined as the border $g(x) = 0$, closest to the origin. We therefore choose the α_ℓ's so that the surface of the bunch reproduces, as closely as possible, the ellipsoidal surface.

We also note that $m\langle \dot{x}^2 \rangle = m\langle \dot{y}^2 \rangle = m\langle \dot{z}^2 \rangle = m\langle v^2 \rangle/3$ because H depends only on v^2 and x. Thus our choice of a stationary distribution of the form $f(H)$ *automatically* corresponds to equipartition (equal average kinetic energy in the three spatial directions).

4.2 Numerical implementation

We have developed a 3-D particle-in-cell (PIC) code HALO3D to test the analytic model described above, and to explore halo formation [15]. The single-particle equations of motion are integrated using a symplectic, split-operator technique [18]. The space charge calculation uses area weighting ("Cloud-in-Cell") and implements open boundary conditions with the Hockney convolution algorithm [19]. The code runs on parallel computers, and in particular, the space charge calculation has been optimized for parallel platforms using the Ferrell-Bertschinger method [20]. Some details about the code can be found in [21].

We initially populate the 6-D phase space according to Eq. (6), and then mismatch the x, y, z coordinates by factors $\mu_x = \mu_y = 1 + \delta a/a$, $\mu_z = 1 + \delta c/c$ and the corresponding momenta by $1/\mu_x = 1/\mu_y$, $1/\mu_z$, with a, c being the minor and major semiaxes of our spheroidal bunch, respectively.

4.3 Longitudinal halo

We performed a systematic study for different c/a and mismatch factors in the range of interest [22], by looking at the halo extent at the time when the beam comes to a roughly saturated state after the development of a halo. Our new result is the dependence of the halo extent on tune depression. One sees a significant increase in halo extent for severe tune depressions. In addition the halo extent clearly depends on the mismatch parameter. The approximately linear dependence of the halo extent on the mismatch factor μ indicates that a serious effort should be made to match the beam to the channel as accurately as possible.

Simulation results [15] show that the halo intensity (roughly defined as the fraction of particles outside the core in phase space) depends primarily on the mismatch. Severe mismatches lead to several percent of the particles in the halo, which is clearly outside acceptable limits. No significant dependence of halo intensity on the tune depression is seen. Also, for tune depression $\eta_z \leq 0.4$ the clear peanut

diagram in the longitudinal phase space now has a chaotic behavior.

One more important feature is how fast the halo develops. We first make the observation that for comparable mismatches the longitudinal halo develops much faster than the transverse halo when the mismatches and/or tune depressions are not severe. Such behavior simply occurs because for fixed charge we have $\eta_z < \eta_x$ for elongated equipartitioned bunches. For severe mismatches and/or tune depressions both the longitudinal and transverse halos develop very quickly. Of particular interest is the clear dependence of halo onset on tune depression. Specifically, for more severe tune depression the halo starts to develop earlier. More details can be found in [15].

4.4 Transverse halo

The transverse halo closely duplicates all the features observed for non-linear stationary distributions in 2-D simulations [13]. The agreement between 2-D and 3-D simulations is very good. The only two differences seen are related to the onset/rate of halo development. In the recent 3-D simulations there is a clear dependence on the tune depression which was not the case in the corresponding 2-D simulations [13]. The second difference is that the transverse halo in the 3-D simulations develops significantly faster than in 2-D for comparable mismatches and tune depressions. More details can be found in [15].

4.5 Coupling effects

In performing 3-D simulations we encounter halo formation in a beam bunch, where we clearly see coupling between the longitudinal and transverse motion. It was already noted [15] that due to the coupling between r and z, a transverse or longitudinal halo is observed even for a very small mismatch (less than 10%) as long as there is a significant mismatch in the other plane. Further numerical investigation [17] of this question showed that the effect of coupling becomes extremely important for nearly spherical bunches ($c/a \leq 2$) which is typical of the parameter range of interest for the APT design [22]. For example, for the short bunch with $c/a = 2$, with only a longitudinal initial mismatch ($\mu_z = 1.5$, $\mu_x = \mu_y = 1.0$), one finds particles at large amplitude in both the longitudinal and transverse directions [17].

5 NON-STATIONARY 6-D PHASE SPACE DISTRIBUTION

After we established the parameters which lead to halo formation in 3-D beam bunches for the self-consistent 6-D phase space stationary distribution [15], we explored rms matched distributions which are *not* self-consistent, to determine the extent to which the relatively rapid redistribution of the 6-D phase space contributes to the formation of halos [17].

5.1 Stability of the matched distribution

We have shown that an rms matched 3-D beam can produce transverse and/or longitudinal halos for a wide range of space charge intensity even when it is initially perfectly matched. Of course, from a practical point of view such halos are not important because the halo extent is very small for the mismatch factor $\mu = 1.0$ (the detailed study of the halo extent on a mismatch factor was presented in [15, 17]).

The redistribution process in a non-stationary beam with initial zero mismatch causes the core to perform an oscillation about its initial distribution which is equivalent to introducing a relatively small mismatch for the stationary distributions. The important consequence is that the redistribution process by itself (zero initial rms mismatch) does not lead to significant emittance growth [17].

5.2 Initially mismatched beam

Numerical 3-D simulations with the initially mismatched non-stationary distributions [17] confirmed all the characteristics of halos observed for the stationary distribution [15]. The main difference is that for a non-stationary distribution the halo extent is larger (especially for the Gaussian) than the halo extent of the stationary distribution with the same initial mismatch parameters.

6 HALO FORMATION IN A PERIODIC FOCUSING CHANNEL

The halo properties in periodically focused cases have been also extensively studied [23]-[29]. Apart from the instabilities due to the structure-driven resonances, these studies showed a close resemblance to the continuous focusing channel results.

7 OTHER ISSUES INVOLVING HALO FORMATION

7.1 Coulomb scattering

Various mechanisms can potentially cause beam halo. Some recent studies suggested that Coulomb collisions in the beam bunch can contribute significantly to beam bunch growth and halo development in linear accelerators. Despite the general belief that collisions are not important it is clear that a rigorous treatment of this question is needed. In an effort to explore this issue in detail we have undertaken an analysis of the effects of Coulomb scattering between ions in a self-consistent spherical bunch [30].

We have calculated the effect of single Coulomb scattering of a self-consistent 6-D distribution for a spherical beam bunch. In this calculation we found that single collisions are capable of populating a thin spherical shell around the beam bunch. This result is for the stationary phase space distribution with $n = -1/2$, but it is probably quantitatively similar for other higher values of n. When the beam is non-equipartitioned or the beam with the stationary distribution

is rms mismatched, the thickness of the shell can be significantly larger, depending on the equipartitioning factor. However, the rate of this process is very small. For the relatively singular distribution with $n = -1/2$, a proton bunch with a normalized emittance $\varepsilon_N \sim 10^{-6}$ [m rad] and a radius of 1 cm will populate the shell with a probability of 10^{-11} per kilometer of linac. For distributions with $n > 0$, this rate of population is further reduced by a factor 10^{-4}.

Our conclusion is that the effect of single Coulomb collisions on halo development in high current ion linear accelerators is not important. A similar analysis for non-stationary distributions was performed by N. Pichoff [31], who arrived at the same conclusions.

We then related our analysis to diffusion caused by many small angle Coulomb collisions, with the conclusion that the effect of multiple Coulomb collisions in halo development in high current ion accelerators is also expected not to be important [30].

7.2 Halo formation in circular accelerators

Space-charge can also lead to emittance growth and halo generation in circular accelerators. In undertaking a study of the space-charge dynamics in high intensity rings one needs to consider two different effects.

The first one is associated with the intrinsic halo formation due to the core mismatch, corresponding to a parametric resonance of the coherent frequency with twice the incoherent depressed tune of individual ions. Although the tune depression in the ring is very small compared with high intensity linacs this effect may still generate a halo of significant size around the beam core.

The second effect is associated with the machine resonances due to magnet imperfections, and is governed by the resonant effect of different coherent mode frequencies [32]-[33].

These and other issues of halo formation in circular accelerators are summarized in [34].

8 SUMMARY

Analytic models have been developed to study halo development in both 2-D beams and 3-D beam bunches in a linac. The detailed study requires both an analytical model which explains available observations as well as computer simulations to verify both the assumptions of the model and its predictions.

Our recent contributions to these efforts have been the construction of a model which identifies a major mechanism for transverse halo formation in linac [4], followed by the construction of a self-consistent 6-D phase space distribution for studies of halo formation in spheroidal bunches in a linear external confining field [15]. What we found [4] is that halo formation appears to arise from a parametric resonant coupling of individual particle oscillations with collective oscillation of the charged bunch. We explored the dependence of the halo properties (extent, rate of growth, intensity, etc.) on the longitudinal and transverse rms tune

depressions and mismatches [15]. These studies automatically assumed equipartition of kinetic energy between the longitudinal and two transverse directions. We then performed numerical studies with an rms matched, but otherwise non-self-consistent 6-D distribution [17]. In these studies we found that starting with a non-self-consistent distribution altered the parameters for halo formation obtained for the self-consistent distribution only slightly.

It may be possible to avoid halo formation due to the parametric resonance by careful matching in the 6-D phase space, but, at present, it seems prudent to accomodate the halo in linac disign. Fortunately, the rate of diffusion is sufficiently slow so that the halo extent does not appear to grow significantly once it is formed.

9   REFERENCES

[1] I.M. Kapchinsky, Theory of Resonance Linear Accelerators, Harwood Academic Publishers, New York, 1985.

[2] Any distribution which is only a function of the Hamiltonian will be self-consistent.

[3] M. Reiser, Theory and Design of Charged Particle Beams, Wiley, New York (1994).

[4] R.L. Gluckstern, Phys. Rev. Letters 73, 1247 (1994).

[5] A.V. Fedotov and R.L. Gluckstern, Mismatch corrections to the envelope modes, these Proceedings.

[6] B.I. Bondarev and A.P. Durkin, Zh.Techn.Phys., USSR, vol. 56, No 11, pp. 2132-2138, 1986.

[7] J.S. O'Connell, T.P. Wangler, R.S. Mills, and K.R. Crandall, in Proceedings of the 1993 Particle Accelerator Conference (IEEE, Washington, DC, 1993), p. 3657.

[8] R.A. Jameson, in 'Frontiers of Accelerator Technology' (Proceed. of the Joint US-CERN-Japan Intern'l School, 1994), World Scient., Singapore (1996).

[9] J.M. Lagniel, Nucl. Inst. Meth. A345 (1994) 46; A345 (1994) 405.

[10] A. Riabko, M. Ellison, X. Kang, S.Y. Lee, D. Li, J.Y. Liu, X. Pei, and L. Wang, Phys. Rev. E 51, 3529 (1995).

[11] H. Okamoto and M. Ikegami, Phys. Rev. E 55, 4694 (1997).

[12] R.L. Gluckstern, W-H. Cheng, and H. Ye, Phys. Rev. Letters 75, 2835 (1995); R.L. Gluckstern, W-H. Cheng, S.S. Kurennoy and H. Ye, Phys Rev. E 54, 6788 (1996).

[13] R.L. Gluckstern and S.S. Kurennoy, in Proceedings of the 1997 Particle Accelerator Conference, Vancouver, Canada (IEEE, Piscataway, NJ, 1998), p. 1950.

[14] J.J. Barnard and S.M. Lund, in Proceedings of the 1997 Particle Accelerator Conference, Vancouver, Canada (IEEE, Piscataway, NJ, 1998), p. 1929; S.M. Lund and J.J. Barnard, ibid., p. 1932.

[15] R.L. Gluckstern, A.V. Fedotov, S. Kurennoy and R. Ryne, Phys. Rev. E 58, 4977 (1998).

[16] J.J. Barnard, S.M. Lund and R.D. Ryne, in Proceedings of the 1998 Linear Accelerator Conference, Chicago, IL (1998).

[17] A.V. Fedotov, R.L. Gluckstern, S.S. Kurennoy and R.D. Ryne, Phys. Rev. ST Accel. Beams, 2, 014201 (1999).

[18] E. Forest, J. Bengtsson, and M.F. Reusch, Phys. Lett. A 158, 99 (1991).

[19] R.W. Hockney and J.W. Eastwood, Computer Simulation Using Particles, Adam Hilger, NY (1988).

[20] R. Ferrell and E. Bertschinger, Int. J. Mod. Phys. C 5, 933 (1994).

[21] R. Ryne, S. Habib, J. Qiang, K. Ko, Z. Li, B. McCandless, W. Mi, C. Ng, M. Saparov, V. Strinivas, Y. Sun, X. Zhan, V. Decyk, G. Golub, in Proceedings of the 1998 Linear Accelerator Conference, Chicago, IL (1998).

[22] APT Conceptual Design Report, Los Alamos Report No. LA-UR-97-1329, 1997.

[23] C. Chen and R.C. Davidson, Phys. Rev. E 49, 5679 (1994).

[24] C. Chen and R.C. Davidson, Phys. Rev. Lett. 72, 2195 (1994).

[25] Q. Qian, R.C. Davidson and C. Chen, Phys. Plasmas 1, 3104 (1994).

[26] S.Y. Lee and A. Riabko, Phys. Rev. E 51, 1609 (1995).

[27] Q. Qian and R.C. Davidson, Phys. Rev. E 53, 5349 (1996).

[28] M. Ikegami and H. Okamoto, Jpn. J. Appl. Phys. 36, 7028 (1997).

[29] M. Pabst, K. Bongardt and A. Letchford, in Proceedings of the 1998 EPAC (Stockholm, Sweden, 1998), p. 146.

[30] R.L Gluckstern and A.V. Fedotov, Phys. Rev. ST Accel. Beams, 2, 054201 (1999).

[31] N. Pichoff, DAPNIA/SEA Report 98-46, France (1998).

[32] R.L. Gluckstern, in Proceedings of the 1970 Linear Accelerator Conference, edited by M.R. Tracy (Fermilab, Batavia, IL), p. 811.

[33] R. Baartman, AIP Conference Proceeding 448, edited by A.U. Luccio and W.T. Weng (AIP, N.Y., 1998), p. 56; and references therein.

[34] A.V. Fedotov, R.L. Gluckstern and M. Venturini, Halo formation issues in circular accelerators, these Proceedings.

Halo Formation Issues in Circular Accelerators

A. V. Fedotov[1]

Brookhaven National Laboratory, Upton, New York 11973

R. L. Gluckstern and M. Venturini

Physics Department, University of Maryland, College Park, Maryland 20742

1 INTRODUCTION

Space-charge can lead to emittance growth and halo generation in circular accelerators. In undertaking a study of the space-charge dynamics in high-intensity rings (Example: Spallation National Source-SNS) one needs to consider two different effects:

1. Machine resonances due to magnet imperfections. This effect is governed by coherent mode frequencies (See, for example: F. Sacherer [1], S. Machida [2], R. Baartman [3]).

2. Intrinsic halo mechanism due to the core mismatch. This effect is similar to the parametric-resonance halo formation in high-current linacs (Example: Accelerator for Production of Tritium-APT). (See extensive literature on halo formation in linacs [4])

2 COHERENT TUNES AND MACHINE RESONANCES

We start our discussion with the half-integer resonance.

• Half-integer resonances are introduced by gradient errors in quadrupoles. As will be shortly shown these resonances occur at the coherent frequencies of beam oscillations.

• Intrinsic halo formation is associated with the parametric resonance of incoherent frequencies and collective modes of beam oscillations.

The immediate question arises: Why in one case are incoherent frequencies important while in the other case - coherent?

Specifically, the intrinsic parametric halo mechanism is governed by the following equation of motion:

$$x'' + q^2 x = \mu \frac{2\kappa}{a_0^2} x \cos ps, \qquad (2.1)$$

where κ is the space charge perveance and $q^2 = k^2 - \kappa/a_0^2$ is the depressed incoherent frequency, using the typical linac notation. The mechanism of halo formation is therefore the parametric resonance between p and q, with $q = p/2$ being the dominant one. For simplicity, we will refer to the halo formed by such a mechanism as PH (Parametric Halo).

Half-integer resonances are governed by the following equation:

$$x'' + \nu^2 x = \alpha_n \nu_0^2 x \cos n\theta, \qquad (2.2)$$

[1]e–mail: fedotov@sun2.BNL.gov

where $\nu^2 = \nu_0^2 - \kappa/a_0^2$ is the depressed incoherent tune in circular accelerator notation. Here n denotes the harmonic component in the magnet errors and α_n stands for its amplitude. One typically assumes from Eq. (2) that the resonance occurs at $\nu = n/2$ (parametric resonance between n and ν). In fact, Eq. (2) seems similar to Eq. (1). However, in Eq. (2), contrary to Eq. (1), the fact that the beam radius performs oscillations is not yet taken into account, while in Eq. (1) this is exactly the source of the driving term.

2.1 Cancelation of resonance with incoherent tune

Assuming a round beam in the presence of both space-charge and gradient errors, we have the following envelope equation:

$$a'' = \frac{\varepsilon^2}{a^3} - \nu_0^2 a + \frac{\kappa}{a} + \alpha_n \nu_0^2 a \cos n\theta. \qquad (2.3)$$

We now assume small oscillations of the beam radius $a = a_0(1 + u)$ and obtain

$$u'' + p^2 u \approx \alpha_n \nu_0^2 \cos n\theta, \qquad (2.4)$$

with p being a symmetric frequency of envelope oscillations. Using the particular solution for u, we get

$$a = a_0 \left[1 + \frac{\alpha_n \nu_0^2 \cos n\theta}{p^2 - n^2} \right]. \qquad (2.5)$$

Taking the variation of beam radius into account, Eq. (2) becomes

$$x'' + \nu^2 x = \left(-\frac{2\kappa}{a_0^2} \alpha_n \frac{\nu_0^2}{p^2 - n^2} + \alpha_n \nu_0^2 \right) x \cos n\theta, \qquad (2.6)$$

which gives, after applying the phase-amplitude analysis, the following resonance condition:

$$2\nu(2\nu - n) = \alpha_n \nu_0^2 \left(1 - \frac{2\kappa}{a_0^2(p^2 - n^2)} \right). \qquad (2.7)$$

Using $p^2 = 4\nu^2 + 2\kappa/a_0^2$, the resonance condition becomes

$$2\nu(2\nu - n) = \alpha_n \nu_0^2 \frac{(4\nu^2 - n^2)}{p^2 - n^2}. \qquad (2.8)$$

Thus we have exact cancelation for the $\nu = n/2$ resonance. There is no "quadrupole" resonance at the incoherent tune. A similar analysis applies for an antisymmetric envelope mode.

2.2 Discussion

The typical ("incoherent tune shift") procedure for predicting the space-charge limits is based on the assumption of constant beam size, which is incorrect. The envelope modulation produces an electric field that exactly cancels the gradient perturbation for this intensity. In general one can show that incoherent tune is irrelevant for machine resonances:

for integer resonance $->$ using the equation of motion of first moments;

for half-integer resonance $->$ using second moments (envelope equation);

for high-order resonance $->$ using the corresponding equation of high order moments or the Vlasov equation.

The simplest way to explore high-order resonances is to use the Vlasov equation. For 1-D planar beam the general theory was developed by F. Sacherer [1]. It was then extended to a 2-D round beam by R.L. Gluckstern [5], and recently for a non-round beam by I. Hofmann [6]. Following the Sacherer-Gluckstern formalism, it is possible to confirm that for a 2-D beam the high-order resonances also occur at coherent frequencies as was recently shown by M.Venturini [7]. The main question is to what extent these findings are of practical importance.

We shall use Baartman's notation for the resonance condition:

$$\nu_0 - C\Delta\nu = \frac{n}{m}. \tag{2.9}$$

With $C = 1$, the resonance would occur at the incoherent tune. Here n corresponds to the excited harmonic in the magnet and m corresponds to the order of the resonance. For the first few resonances the coefficients are the following:

$m = 2 -> C_{symm} = 1/2, C_{asymm} = 3/4$,

$m = 3 -> C = 3/4, 11/12$,

$m = 4 -> C = 7/8, 13/16, 31/32$.

These coefficients can easily be obtained from the results given in [6], and are summarized in [3]. They can be also obtained from [5]. From these coefficients it is clear that the difference between the coherent and incoherent resonances is important only for low-order resonances. In addition, one can easily check that the symmetric mode allows the largest space-charge increase, as first found by L. Smith [8] for the $m = 2$ resonance.

For the half-integer resonance with $m = 2$, the symmetric coefficient is $C = 1/2$ which gives $\Delta\nu_{sc} = 2\Delta\nu_{incoh}$ For this specific mode, if the largest possible tune shift can be 0.5, assuming the absence of higher resonances, this would indicate that the actual maximum tune shift can be as much as one unit: $\Delta\nu_{sc,max} = 1$. This would be the case for "solenoidal" type gradient errors with the potential $(x^2 + y^2)$. However, errors in individual magnets: quadrupole, sextupole, etc. are of "antisymmetric" type. For $m = 2$, the coefficient of the antisymmetric mode is $C = 3/4$ which gives only $\Delta\nu_{sc} = \frac{4}{3}\Delta\nu_{incoh}$. For this mode, if the largest incoherent tune shift is 0.5 this would indicate that the actual maximum tune shift can be $\Delta\nu_{sc,max} = 2/3$. Thus, this effect for the more typical errors generated by the antisymmetric potential $(x^2 - y^2)$ is not as big as in the case of a symmetric mode.

Similarly, for sextupole type errors and $m = 3$, the coefficient $C = 11/12$ which gives $\Delta\nu_{sc,max} = \frac{12}{11}\Delta\nu_{incoh}$. Thus it becomes clear that for higher orders the difference between the coherent and incoherent frequencies not of practical importance. Also, the resonant growth becomes neg-ligible due to the increasing non-linearity of driving terms.

Having in mind that errors will be most likely produced by the individual magnets and that antisymmetric modes are most likely to be excited in the typical accelerator lattice, we should also note that combination of magnets (for example symmetric triplet) can generate "symmetric" errors and thus excite the symmetric modes.

From space-charge limit considerations the fact that resonance occurs at coherent frequencies is mainly important for the $m = 2$ resonance. We should note that the previosly presented coefficient $C = 3/4$ which gave $\Delta\nu_{sc} = \frac{4}{3}\Delta\nu_{incoh}$ was obtained for closely spaced vertical and horizontal tunes ($|\nu_{0x} - \nu_{0y}| \ll \Delta\nu/4$). It turns out that introducing tune split can lead to smaller coefficient and increase the space-charge limit.

• With the tune split ($|\nu_{0x} - \nu_{0y}| > \Delta\nu/4$), we have $C = 5/8$ which gives $\Delta\nu_{sc,max} = \frac{8}{5}\Delta\nu_{incoh}$. We now have only one mode because the envelope modulations in x and y do not stay in phase and we have decoupled motion.

In the case of the tune split we therefore obtain the largest space-charge limit assuming antisymmetric type of errors.

We now remind the reader that the coefficients and discussion presented above were based on the assumption of a round beam. Clearly, for a non-round beam, even in the split tune case one gets different modes (and coefficients) in the x and y planes. Once again, the coefficients for such modes can be easily obtained for the $m = 2$ resonance from the envelope equation [3], and for high-order resonances from the Vlasov equation [6].

3 INTRINSIC HALO MECHANSIM

As we saw in the previous section, in circular accelerators, machine resonances can easily lead to emittance growth. In this section we try to understand whether the PH, which is believed to be the main source of halo in linac, should be expected in circular machines.

Investigation of PH in circular machines requires addressing two very important issues:

1. Rate of halo development for low space-charge.

Based on a phase-amplitude analysis [9], there is the possibility of 2 : 1 parametric resonance for any space-charge not equal to zero. For strong tune depressions of the order of $\eta \sim 0.5$ we have a large halo extent. But even for tune depression of only a few percent ($\eta \sim 0.98$) we still have a large halo extent.

• The width of the separatrix is mainly governed by the rms mismatch (small space-charge dependence does exist, and it is distribution dependent [10]).

• But for $\eta -> 1$ (zero space-charge) there is no force, and thus there is no mechanism for a PH.

The question thus arises whether we should expect the PH for very low space charge. To answer this question, we note that particles can be trapped into a parametric resonance only after some time, during which they approach the unstable fixed points via chaos or instabilities. For strong tune depression the motion of particles near the core

is highly irregular. In phase space, one typically sees numerous islands corresponding to higher order resonances. The time during which particles can move across these islands and approach the unstable fixed points of the 2 : 1 parametric resonance is relatively fast. In the limit of zero space-charge the motion near the core is very regular and the rate of the development of instabilities becomes very small. Also, the unstable fixed points of the 2 : 1 resonance move away from the origin. Therefore, for space-charge typical for high-intensity rings ($\eta \sim 0.98$), it would take much more time for particles to be trapped into 2 : 1 resonance than for typical linac tune depressions.

• Rate of halo development thus becomes an extremely important question for high-intensity rings.

Clearly, to estimate the rate of PH development in the limit of low space charge, realistic PIC code simulations are required.

2. Phase mixing of natural beam oscillations.

In a linac (and in typical simplified computer simulations) we first introduce an initial mismatch, then look at the time evolution of such an rms mismatched beam. The excited mismatched mode leads to halo formation after some time. In proposed rings with multi-turn injection schemes, the excited successive mode can be destroyed because the mismatches come in different phases.

Studies using simplified models (which assume that the mismatched mode always exists undisturbed for a long time) can be misleading.

It is thus important to investigate all sources of beam mismatch, and understand whether natural coherent oscillation can exist in the system under consideration.

4   OTHER ISSUES

4.1   Combined effect of PH and machine resonance

If the working point is such that we do not hit a half-integer resonance after the tune shift is applied, can we hit it when and if a PH is developed?

Since the frequency of individual particles inside the beam increases with amplitude we will move further away from the half-integer resonance below the depressed tune (here we neglect higher-order resonances). Also, there is no problem with the integer resonance above the bare tune since, even though the frequency increases with amplitude, it can never pass the bare tune. Of course, taking into account the existence of higher order resonances (for example the sextupole resonance) one should expect some increase in the beam dimensions due to resonance crossing in the direction of decreasing space-charge tune shift.

4.2   Longitudinal halo

Due to the almost spherical beam in some linacs (Example: Accelerator for the Production of Tritium) there is strong coupling between the horizontal and longitudinal motion. A longitudinal halo can be easily generated and can lead to particle loss from the RF bucket. The question of longitudinal PH is therefore an important issue for linacs.

In circular high-intensity machines (such as SNS) beams are very long, and motion is decoupled. The effect of non-linear RF is expected to be much stronger than the longitudinal space-charge effect $->$ no parametric-resonance longitudinal halo is expected

4.3   Dispersion

• Dispersion matching seems to be an important issue in space-charge dominated beams (see for example: [11]).
• To what extent dispersion matching is important for emittance dominated beams with only a few percent of tune depression ($\eta \sim 0.98$) should be studied.

5   REFERENCES

[1] F. Sacherer, Lawrence Rad. Lab Report UCRL-18454 (Ph.D. thesis, University of California at Berkeley), 1968.

[2] S. Machida, Nucl. Inst. Meth. **A309**, p. 43, 1991.

[3] R. Baartman, AIP Conference Proceeding 448, edited by A.U. Luccio and W.T. Weng (AIP, N.Y. 1998), p. 56.

[4] R.L. Gluckstern and A.V. Fedotov, these Proceedings.

[5] R.L. Gluckstern, in Proceedings of the 1970 Linear Accelerator Conference, edited by M.R. Tracy (Fermilab, Batavia, IL), p. 811, 1970.

[6] I. Hofmann, Phys. Rev. E **57**, p. 4713, 1998.

[7] M. Venturini, Response of a KV beam in the presence of multipole errors, unpublished, 1999.

[8] L. Smith, Proc. Int. Conf. on High Energy Accelerators (Dubna, Russia), p. 1232, 1963.

[9] R.L. Gluckstern, Phys. Rev. Letters, **73**, p. 1247, 1994.

[10] A.V. Fedotov, Dependence of halo extent on tune depression, unpublished, 1998.

[11] M. Venturini, M. Reiser and R. Kishek, p. 278; S.Y. Lee, p. 38; J. Barnard et al, p. 221; AIP Conference Proceeding 448, edited by A.U. Luccio and W.T. Weng (AIP, N.Y. 1998).

Analysis of Beam Profile Broadening at High Intensity in the PSR Accumulator Ring

J. A. Holmes, J. D. Galambos, D. K. Olsen

SNS Project, Oak Ridge National Laboratory, Oak Ridge, TN 37831-8218

F. Merrill, and R. J. Macek

Los Alamos National Laboratory, Los Alamos, NM 87545

Abstract

Profile measurements of proton beams taken after extraction from the Proton Storage Ring (PSR) at Los Alamos National Laboratory show significant broadening in the vertical direction at high intensities. Careful beam dynamics simulations of the injection, accumulation, and extraction processes yield good agreement with the measured beam profiles. Analysis of the simulations suggests that the vertical broadening at high intensities is a result of the space charge tune shifted beam exciting the $\nu_y = 2$ integer betatron resonance. Both experiment and simulations show that raising the bare tunes slightly reduces the profile broadening. For the PSR injection scheme with single harmonic RF longitudinal focusing, the longitudinal beam distribution becomes quite peaked after several hundred turns of accumulation. This peaking causes the space charge density and tune shift to be strongest at the bunch center, so that the transverse beam broadening is most pronounced in this region. For simulations in which second harmonic RF focusing is included, the peaking of the longitudinal beam distribution and the transverse beam broadening are reduced. When second harmonic RF focusing is combined with raised bare tunes in the simulations, the beam profile broadening is negligible. These results suggest that high-intensity beams can be well contained in accumulator rings through a proper choice of operating tunes, injection scheme, and RF focusing.

1 INTRODUCTION

Beam dynamics in high intensity rings has become important due to a number of new machines under consideration, including the Spallation Neutron Source (SNS), European Spallation Source (ESS), Japan Hadron Facility (JHF), μ-Collider Driver, and others. These machines are characterized by large beam currents and by stringent uncontrolled beam loss requirements. For example, the accelerator system of the Spallation Neutron Source (SNS) [1] will deliver a 1 GeV pulsed proton beam to a liquid Hg target at 60 Hz. The accumulator ring is being designed to support 2 MW of beam, which implies that it must be capable of holding more than 2×10^{14} protons in each pulse. In order to expedite hands-on maintenance, the requirement for uncontrolled losses is set to about one part in 10^6 per meter. Because of the

necessity of high beam intensity and low uncontrolled beam loss, space charge contributions to beam loss are an essential concern in high intensity rings.

In order to study beam dynamics in high-intensity rings, a number of computer codes have been developed [2-4]. These codes perform particle-tracking calculations through the periodic ring lattice in the presence of space charge forces. They differ from tracking codes without space charge in the necessity to accurately model the collective space charge forces in a self-consistent manner. This places stringent numerical requirements on the computational representation with respect to integration step size, number of tracked particles, and spatial description of the beam [5]. In addition to testing the convergence requirements of individual codes, there has been some success in benchmarking different computer codes for high-intensity ring beam dynamics with respect to each other [6]. However, direct detailed comparisons of computer codes for high-intensity ring beam dynamics with experimental data and the use of such codes to then analyze and explain the data are still lacking. This work contains such a comparison and presents an explanation of the observed transverse beam broadening at high beam intensity in the Proton Storage Ring (PSR) [7] at Los Alamos National Laboratory (LANL).

The PSR affords an ideal site to study the space charge dynamics of high-intensity rings. H⁻ particles are injected into this 90 meter ring, consisting of 10 field periods of one FODO cell each, at 800 MeV from the LANSCE linac through a stripper foil in a multi-turn process to accumulate beams of up to 4×10^{13} particles. The resulting space charge tune shifts of up to 0.2 are quite comparable to those of the proposed SNS accumulator ring. Because the bare tunes in PSR are roughly $\nu_x \approx 3$ and $\nu_y \approx 2$, compared to $\nu_{x,y} \approx 6$ in SNS, the space charge tune depression ratio is actually larger in PSR than in SNS. In order to study the PSR beam dynamics computationally, transverse profile measurements were taken of the full-intensity beam in the extraction line using a wire scanner diagnostic. The entire injection, accumulation, and extraction scenarios were then carefully simulated using the ORBIT computer code [4], and the resulting transverse profiles were calculated at the wire scanner and compared with the experimental results. The computational results were found to be in

good agreement with experiment, particularly regarding systematic behavior with respect to beam intensity and tune changes. Careful analysis of the computational results was carried out to explain the observed systematics.

Section II of this paper presents an overview of the experimental and computational PSR studies carried out here. In Section III, the experimental and calculated results compared. Section IV presents an analysis of the compuational results to describe the physics determining the observed beam behavior, and by extending the calculations to include second harmonic longitudinal RF focusing, suggests a solution to avoid the observed broadening of the vertical beam profile at high intensity. Finally, Section V presents our conclusions and describes future enhancements of our analysis.

2 THE EXPERIMENT AND THE SIMULATION

In the present experiments, injection was carried out for $1025\,\mu s$, which corresponds to 2864 turns of accumulation. The number of injected particles/turn was 1.45×10^{10}, yielding a maximum of 4.14×10^{13} particles at full intensity. By injecting from the linac every second, fourth, or eighth turn, one-half, one-fourth, and one-eigth intensity profiles were obtained, respectively. In PSR, the linac emittance is much smaller than the final ring emittance. By moving the closed orbit during injection, it is possible to "paint" a particle distribution. Injection for these studies was carried out with fixed horizontal displacement and angle of the closed orbit relative to the injected beam. The vertical displacement and angle of the closed orbit relative to the injected beam were varied during the first $825\,\mu s$ of injection to paint the vertical phase space distribution. Although the horizontal injection parameters are constant, the ring dispersion function is nonzero at the foil, and the beam energy spread combines with dispersion to provide horizontal spreading of the beam distribution.

Immediately following injection, the beam was extracted in a single turn and transported to a wire scanner beam profile diagnostic in the extraction line. The purpose of this study was to measure the transverse beam profile shape for various beam intensities and bare tune settings. A series of measurements was completed in which the bare tunes of the ring were set to $\nu_x = 3.17$, $\nu_y = 2.14$ and all parameters were maintained precisely except for varying the injected particle intensity. This was varied as described above by injecting from the linac every second, fourth , or eighth turn, to obtain one-half, one-fourth, and one-eigth intensity profiles, respectively. Following this series of measurements, the bare tunes of the ring were raised slightly to $\nu_x = 3.19$, $\nu_y = 2.17$, and the full-intensity measurement repeated. All other linac,

injection, and PSR parameters, such as ion source strength, closed orbit bumps, etc., were held fixed.

Corresponding to each beam profile measurement, a complete simulation of the injection, accumulation, and extraction process was carried out using the ORBIT particle-tracking computer code [4]. ORBIT features a detailed injection model, including linac beam distribution and time-dependent closed orbit bump. The longitudinal particle transport model contains RF focusing and longitudinal space charge forces, and the transverse transport model includes linear and nonlinear external magnet forces and a particle-in-cell (PIC) model for evaluation of the tranverse space charge forces. In the present calculations, the nonlinear magnet forces were neglected, so that the only nonlinear transverse forces were due to space charge. However, the linear lattice elements of PSR, including drift spaces, bending magnets, and quadrupoles, were represented in detail.

The numerical representation in the calculations included an injection of 50 particles/turn, resulting in a final total of 143200 injected particles, 128×128 grid points for the fast Fourier transform (FFT) algorithm in the space charge evaluation, and 197 integration steps/turn (corresponding to about 20 steps/FODO cell). Full details on the physics model and numerical considerations in the ORBIT code are given in reference [5]. We now turn our attention to the comparison of the experimental and computational results.

3 MEASURED AND CALCULATED RESULTS

We now present and compare the measured and the calculated beam profiles at the wire scanner in the extraction line. For this purpose, adjustments were made to the calculated data. Because the absolute transverse location of the wire scanner was not precisely known, the centers of the calculated and experimental distributions were matched. Also the vertical scale of the calculated distributions was adjusted so that the areas under the calculated distribution curves matched those from the wire scanner data. The widths and shapes of the calculated distributions were not adjusted.

A scan was carried out to vary the injected beam intensity. Four cases, corresponding to 4.14×10^{13}, 2.07×10^{13}, 1.00×10^{13}, 0.50×10^{13} protons at bare tunes of $\nu_x = 3.17$ and $\nu_y = 2.14$, were included. Figure 1 plots the measured and calculated horizontal and vertical beam profiles. The shape of the horizontal profiles, both for the measured and calculated cases, is rather independent of the beam intensity. The profiles are peaked and of fixed width, consistent with the painting scheme in which the horizontal injection location is less than 4 mm from that of the closed orbit.
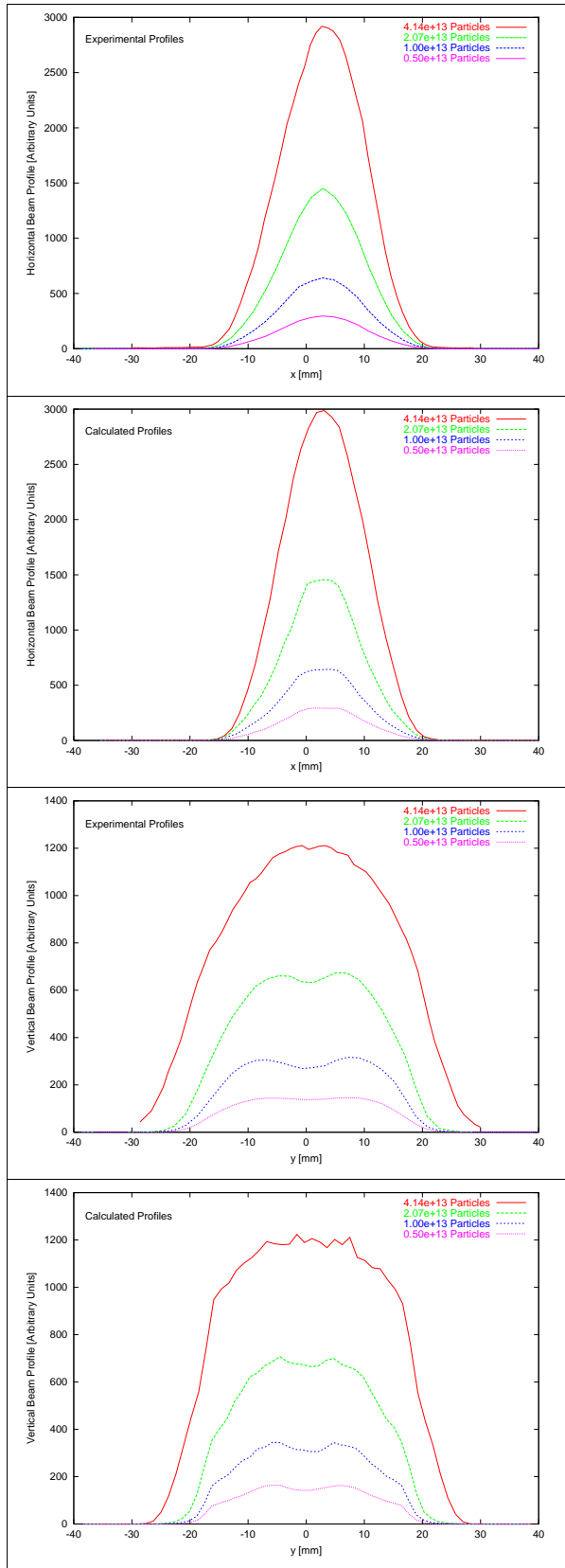
Figure 1. Horizontal and vertical experimental and calculated beam profiles at the wire scanner for different beam intensities.

The vertical profiles, on the other hand, are much broader than the horizontal profiles, also consistent with the painting scheme in which the vertical injection is nearly 17 mm from the closed orbit after 825 μs. However, unlike the horizontal profiles, which are insensitive to the beam intensity, the vertical beam profiles broaden considerably at the highest-intensity case. For the three lower intensities, the width of the vertical beam profiles remains constant. This intensity-dependent effect occurs both in the experimental and the calculated results. Our strategy will be to understand the cause of this high-intensity vertical profile broadening by studying the calculations.

Figure 2 presents, for the highest-intensity case, a comparison of the measured and calculated beam profiles. As stated earlier, the calculated profiles are centered on the experimental profiles and normalized to give the same integrated areas, but no other adjustments are made. Because space charge forces provide the only nonlinearities in the calculations and because the vertical profile broadening must be a nonlinear effect, we also plot the results of the calculations with the space charge forces set to zero. For the horizontal beam profiles, the results give good agreement between calculated and experimental beam profiles. This is true independent of intensity. Even the profiles obtained without space charge are only slightly narrower, and hence taller, than the experimental and calculated profiles. Hence, in the horizontal direction space charge forces broaden the beam profiles slightly and there are no strong intensity-dependent effects. For the vertical beam profiles, the detailed agreement between experiment and calculation is not as good as for the horizontal profiles. This is especially true at low beam intensity. This could be due to the neglect of other nonlinearities and magnet errors in the calculations. Further studies are underway to elucidate this. However, the calculated results with space charge, particularly at high intensity, agree much better with the measured profiles than do the calculations without space charge. The hollowness of the profiles calculated without space charge is the result of the off-axis injection scheme in the vertical plane. Furthermore, space charge provides the correct systematics, with the profiles broadening considerably at the highest beam intensity. This is not observed in the absence of space charge and there is no other mechanism in the calculations to provide such an effect. We next consider, for the high beam intensity, the effect of raising the tunes slightly.

Figure 3 shows the experimental and calculated vertical beam profiles at the wire scanner for the high-intensity case, 4.14×10^{13} protons, for both the default tunes $\nu_x = 3.17$, $\nu_y = 2.14$ and the increased tunes $\nu_x = 3.19$, $\nu_y = 2.17$. For both the experimental and calculated horizontal profiles there is very little difference caused by increasing the bare tunes. However, raising the tunes leads to a noticeable narrowing of the vertical beam profiles, as can be seen in both the experimental and the calculated results. When the calculated and experimental

profiles are superposed for the case with raised tunes, the comparison of results is similar to that observed in Figure 2.
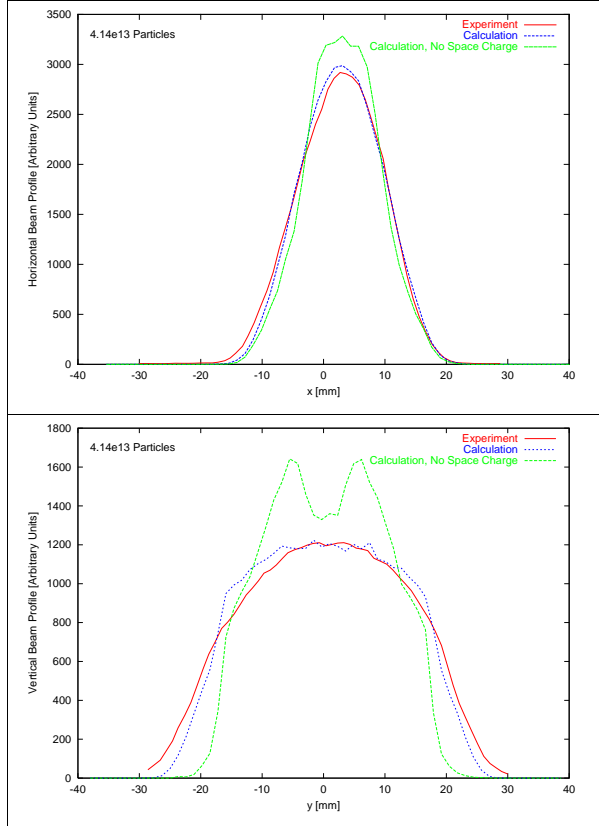

Figure 2. Horizontal and vertical experimental and calculated beam profiles at the wire scanner at the highest beam intensity.
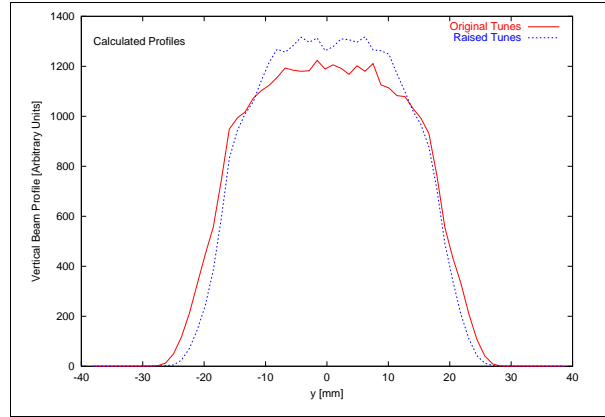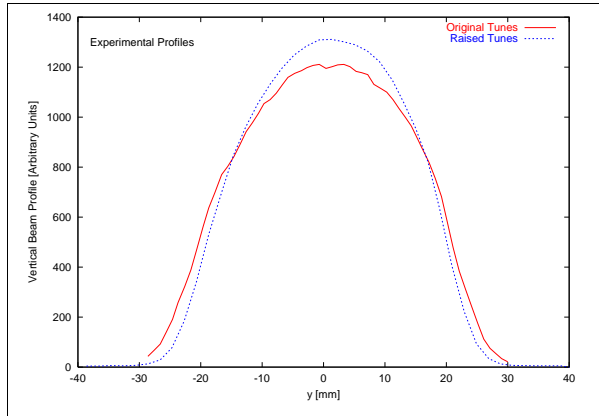

Figure 3. Vertical experimental and calculated beam profiles at the wire scanner for default and raised tunes.

To summarize the basic results, a broadening of the vertical beam distribution is observed at high intensity, both for experimental and calculated beam profiles. Calculations performed without the space charge force fail to show this broadening. Increasing the bare tunes decreases the high intensity vertical profile broadening. In the horizontal direction the results show lttle sensitivity to either the beam intensity or to the tunes. Although the agreement between the calculated and experimental results is not perfect, they reveal the same systematic behavior with beam intensity and tune; and the calculations with space charge agree substantially better with experiment than do those not including space charge. Future calculations will incorporate magnet errors and higher order terms in order to seek to improve the detailed agreement.

The broadeneing of the vertical beam profile at high beam intensity and the reduction of this broadening when the bare tunes are increased suggests that the observed broadening could be associated with the integer betatron resonance $\nu_x = 2$. This possibility will be studied in detail in the next section.

4 ANALYSIS OF THE BEAM BROADENING

The phenomena we wish to understand is embodied in the difference between the two highest-intensity cases in the intensity scan, namely 2.07×10^{13} and 4.14×10^{13} protons, as it is the latter case that displays significant profile broadening. Figure 4 plots the time histories of the rms vertical emittances of the calculated beams for these cases, together with the values obtained when space charge is excluded. The emittances and moments for the case having 2.07×10^{13} protons closely track those obtained when space charge effects are not included in the calculations. Thus, for cases below the highest intensity, the effect of space charge is primarily to smooth out the hollow profile in the vertical plane that results from the off-axis painting scheme (see Figure 1). There is no net broadening effect. For the highest intensity case, the profile begins to broaden noticeably after about 700 turns,

as can be seen in the emittances. Although not shown here, there is a lack of large oscillations in the second moments of the beam that suggests that the injected beam is not extremely rms mismatched. Hence, the contribution of quadrupole oscillations to the broadening through the parametric resonance [8] and halo generation is small.
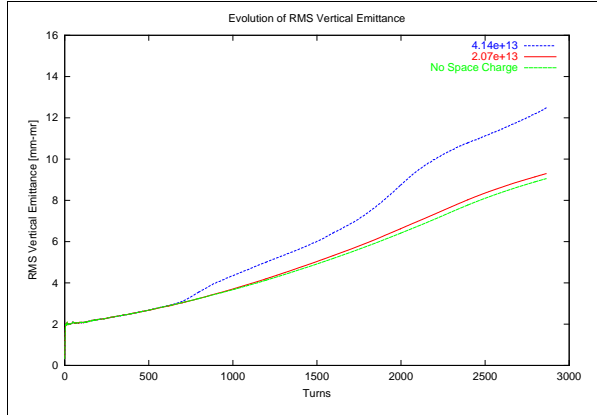

Figure 4. Vertical rms emittance evolution for the two highest-intensity cases and when space charge is neglected.

A calculation of the incoherent tunes of all the beam particles at 1000, 2000, and 2864 turns shows significant numbers of the particles in the highest intensity case, 4.14×10^{13} protons, with incoherent vertical tunes of 2.0 or less. However, for the case with 2.07×10^{13} protons, the tunes remain above 2. This suggests that the integer resonance could be related to the observed beam broadeneing at high intensities. Also, for 2000 turns and greater, the incoherent horizontal tunes of many beam particles cross the integer resonance at 3.0. There is not, however, associated with this a significant horizontal beam broadening. It has been pointed out by Baartman [9] that the coherent tunes determine resonant behavior in intense beams, and a greater fraction of the particles are found to have vertical tunes < 2.0 than horizontal tunes < 3.0. Furthermore, given that the PSR lattice structure has 10 superperiods, the $\nu_y = 2.0$ resonance is a fifth order structure resonance while the $\nu_x = 3.0$ is tenth order. It is therefore more likely that the coherent vertical tune falls within the $\nu_y = 2.0$ resonance than that the coherent horizontal tune excites the $\nu_x = 3.0$ resonance.

Figure 5 plots the time histories of the rms vertical emittances for the high-intensity default tune and increased tune cases, together with the no space charge results. The rms emittance evolution shows that the high-intensity case with raised tunes undergoes some vertical profile broadening due to space charge forces, but that this occurs to a lesser extent than for the default tune case. Calculation of the incoherent tunes also shows that fewer beam particles lie at tunes below 2.0 for the raised tune case than for the default tune case.
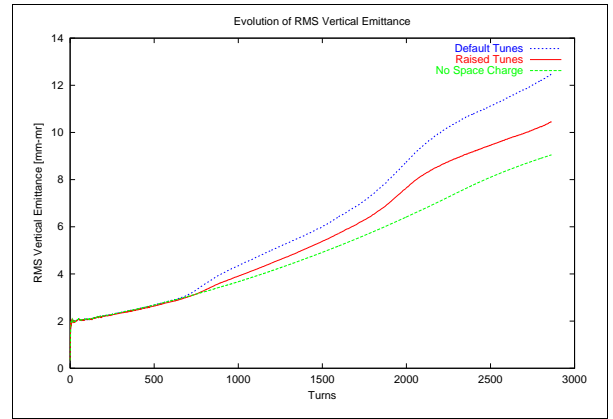

Figure 5. Vertical rms emittance evolution for the default- and raised-tune cases and when space charge is neglected.

These results are consistent with the picture that the $\nu_y = 2.0$ resonance is involved in the observed beam broadening, but stronger support can be gained by an analysis of the longitudinal evolution of the beam. Not only does this analysis demonstrate the role of the $\nu_y = 2.0$ resonance in the beam broadening, but it also suggests a way to avoid the beam broadening.

Figure 6 plots the longitudinal beam density profiles during injection at 500, 1000, 2000, and 2864 turns for the high-intensity case with the default bare tunes $\nu_x = 3.17$, $\nu_y = 2.14$. It is seen that the injection scheme and longitudinal motion combine to produce longitudinal beam profiles that are very peaked about the longitudinal beam center. Because of this, beam densities will be very high in this region and space charge effects will be strong.
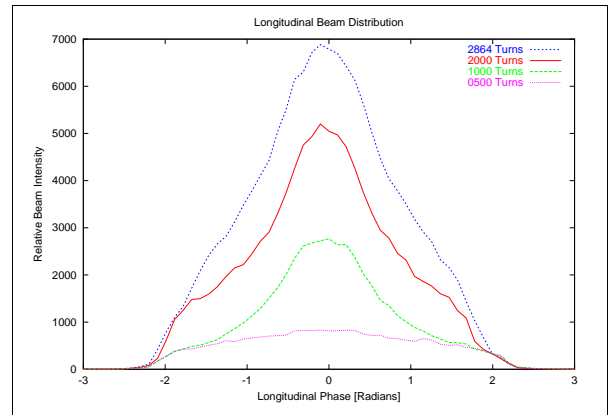

Figure 6. Longitudinal beam density profiles for the high-intensity case with the default tunes.

This is illustrated in Figure 7, which shows the incoherent vertical tunes as a function of the longitudinal coordinate at 2864 turns for the default tunes case at beam intensities of 2.07×10^{13} and 4.14×10^{13} protons and for the high-intensity default and raised tune cases. The figure shows that the incoherent tunes are very dependent on the longitudinal position and that, for the default tune

high-intensity case, the tunes of the particles in the center of the bunch fall squarely about the value 2.0. For the lower-intensity case, 2.07×10^{13} protons, the incoherent tunes are also dependent upon the longitudinal position, but they remain above 2.0 throughout the distribution. Figures 1 and 4 showed that there was almost no vertical beam broadening in this case. For the case of raised bare tunes, $\nu_x = 3.19$, $\nu_y = 2.17$, the distribution of incoherent tunes does cross 2.0 in the bunch center, but not as strongly as in the default case.
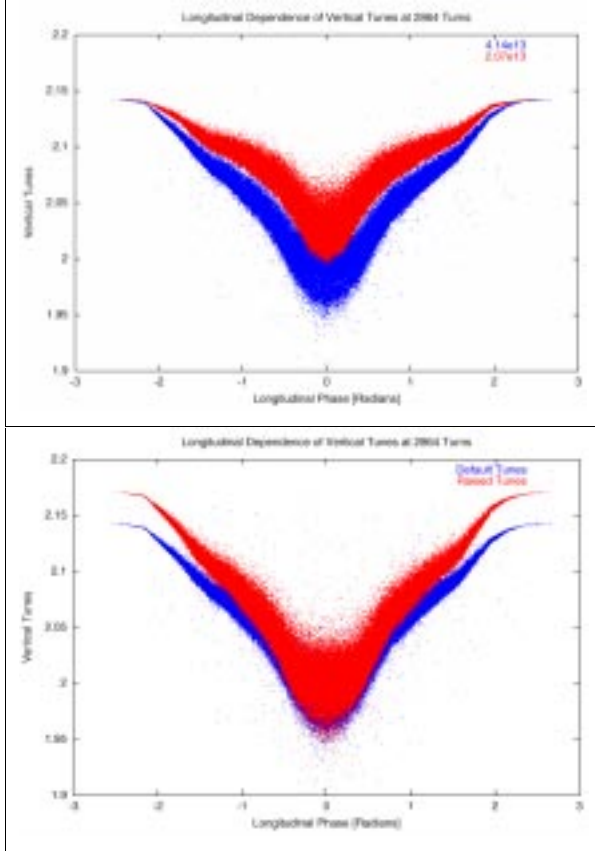
Figure 7. Incoherent vertical tunes versus longitudinal phase space angle at 2864 turns for the default tune cases with 2.07×10^{13} and 4.14×10^{13} protons, and for the high-intensity cases with default and raised tunes.

Figure 8 plots the vertical positions of the beam particles as functions of the longitudinal coordinate for the low- and high-intensity cases considered in Figure 7. Although all three cases in Figure 7 show some tendancy for the beam to spread vertically in the center of the bunch, this tendancy is most pronounced in the high-intensity default tunes case and least pronounced in the lower-intensity case. These results are totally consistent with the $\nu_y = 2.0$ betatron resonance as the cause of the beam broadening.
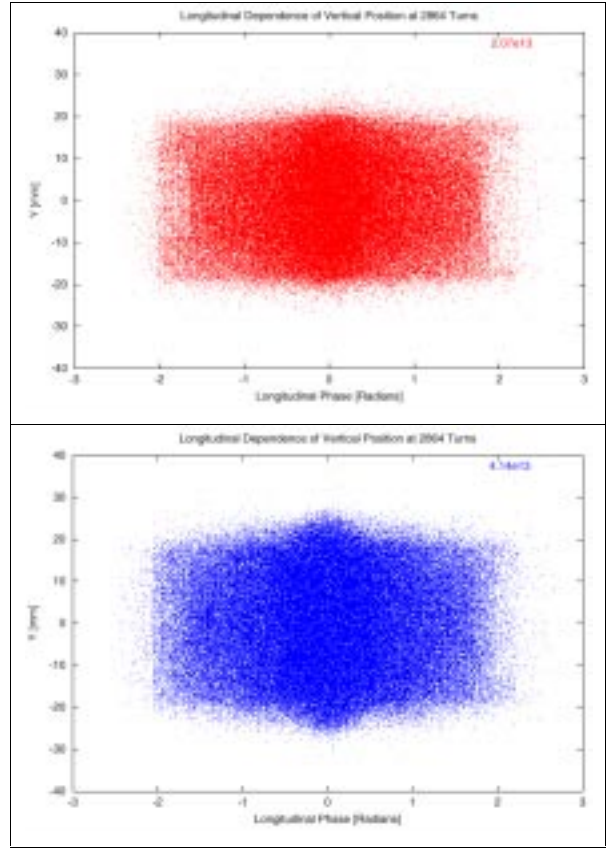
Figure 8. Vertical positions versus longitudinal phase space angle at 2864 turns for the default tune cases with 2.07×10^{13} and 4.14×10^{13} protons.

The present discussion suggests that the observed beam broadening in the vertical direction is the result of encountering the $\nu_y = 2.0$ betatron resonance, primarily at the center of the bunch where the beam density is large. This density buildup is a direct result of the injection and RF focusing scheme. One possible scenario to reduce the peaking of the longitudinal particle density is to include a second harmonic in the RF focusing. Figure 9 shows the result of adding second harmonic RF focusing to the high-intensity default tunes case at –0.5 times the amplitude of the ramped first harmonic. The longitudinal density profile is becomes less peaked due to the modified RF scheme, and the evolution of the vertical rms emittance shows that there is less beam broadening than for the default first harmonic scheme.
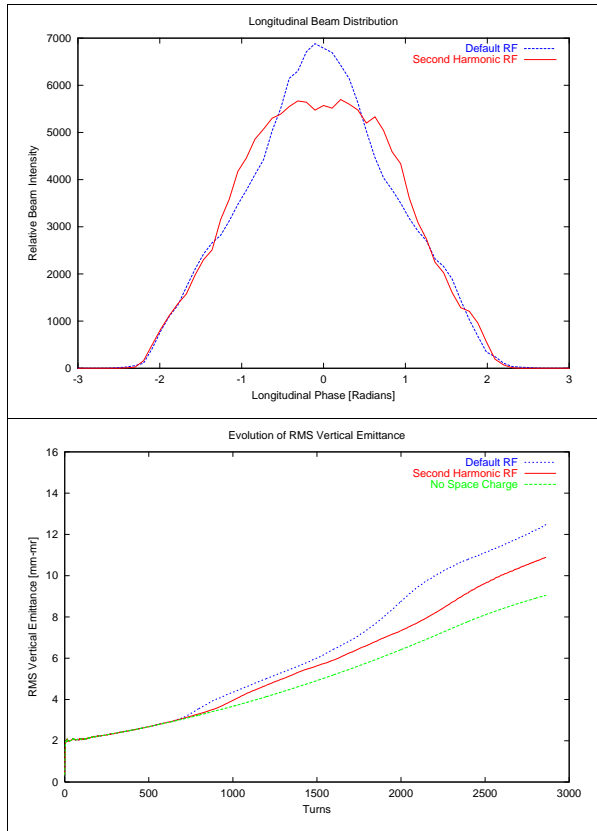
Figure 9. Longitudinal density profiles at 2864 turns and rms vertical emittance evolution for the high intensity default RF case and for second harmonic RF case.

As Figures 3 and 5 show that increasing the bare tunes to move above the $\nu_y = 2.0$ resonance diminishes beam broadening and Figure 9 shows that reducing the longitudinal peaking of the beam through second harmonic RF focusing also diminishes beam broadening, it is interesting to combine these approaches by applying second harmonic RF focusing to the case with raised bare tunes. The results of this calculation are shown in Figure 10. The vertical rms emittance shows almost no growth beyond that of the case without space charge, indicating very little beam spreading. The incoherent vertical tunes are mostly above 2.0 at 2864 turns, even in the bunch center, and as late as 2000 turns into the injection cycle virtually all incoherent tunes are above 2.0. The longitudinal distribution of vertical particle positions at the end of injection shows almost no spreading due to space charge. Thus, by decreasing the maximum beam density and by raising the bare tunes further above 2.0, calculations indicate that it is possible to prevent the spreading of the high-intensity beam that is caused by the $\nu_y = 2.0$ betatron resonance.
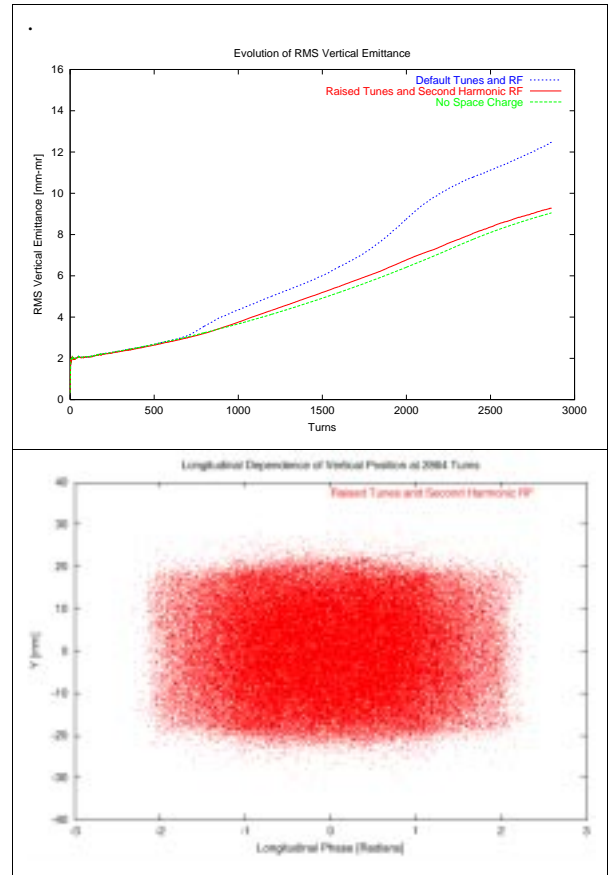
Figure 10. Vertical rms emittance evolution and vertical positions versus longitudinal position at 2864 turns for the raised tunes and second harmonic RF case.

5 CONCLUSIONS AND FUTURE WORK

We have compared experimenal profile measurements with calculated numerical simulations of high-intensity proton beams taken after extraction from the Proton Storage Ring (PSR) at Los Alamos National Laboratory. The simulations include a careful rendering of the PSR injection, accumulation, and extraction scenarios, lattice, and RF focusing scheme. Self-consistent space charge forces constitute the only nonlinearities included in the present calculations. Agreement between the measured and calculated results is reasonably good, but when space charge forces are omitted the vertical profiles differ significantly. Although the detailed shapes of the vertical distributions are somewhat different, both experimental and calculated results show the same systematics, namely significant broadening in the vertical direction at high intensities. Because this occurs with no other changes in the injection scenario, the broadening is a nonlinear process. Analysis of the simulations suggests that the vertical broadening at high intensities is a result of the space charge tune shifted beam encountering the $\nu_y = 2$ integer betatron resonance.

Both experiment and simulations show that raising the bare tunes slightly reduces the profile broadening. For the

PSR injection scheme with single harmonic RF longitudinal focusing, the longitudinal beam distribution becomes quite peaked after several hundred turns of accumulation. This peaking causes the space charge density and tune shift to be strongest at the bunch center, so that the transverse beam broadening is most pronounced in this region. For simulations in which second harmonic RF focusing is included, the peaking of the longitudinal beam distribution and the transverse beam broadening are reduced. When second harmonic RF focusing is combined with raised bare tunes in the simulations, the beam profile broadening is negligible. These results suggest that high-intensity beams can be well contained in accumulator rings through a proper choice of operating tunes, injection scheme, and RF focusing. Future work will involve the inclusion of magnet errors and higher order effects in the calculations in order to resolve the remaining detailed differences between the experimental and calculated beam profile shapes.

6 ACKNOWLEDGEMENTS

REFERENCES

[1] *National Spallation Neutron Source Conceptual Design Report, Volumes 1 and 2*, NSNS/CDR-2/V1, 2, (May, 1997); On the World Wide Web at http://www.ornl.gov/~nsns/CDRDocuments/CDR.html.

[2] S. Machida, *The Simpsons Program*, AIP Conference Proceedings 297, (1993) 459.

[3] F. Jones, *Users' Guide to ACCSIM*, TRIUMF Design Note TRI-DN-90-17, (1990).

[4] J. Galambos, J. Holmes, D. Olsen, A. Luccio, and J. Beebe-Wang, *ORBIT Users Manual*, http://www.ornl.gov/sns/APGroup/Codes/ORBITUserMan1_10.html.

[5] J. Holmes, J. Galambos, D. Jeon, D. Olsen, J. Cobb, "Dynamic Space Charge Calculations for High Intensity Beams in Rings" in *Proceedings of the ICAP,* 1998; J. A. Holmes, V. V. Danilov, J. D. Galambos, D. Jeon, and D. K. Olsen, accepted for publication in *Phys. Rev. Special Topics – AB,* (1999).

[6] A. Fedotov, J. Beebe-Wang, S. Machida, and J. Galambos, *private communication* (1999).

[7] D. H. Fitzgerald, A. Ahn, B. Blind, M. Borden, R. Macek, F. Neri, M. Plum, C, Rose, H. Thiessen, C. Wilkinson, and M. Zumbro, in *Proceedings of the 1997 Particle Accelerator Conference,* (IEEE, Piscataway, NJ, 1998) 1012; C. Wilkinson, F. Neri, D. Fitzgerald, B. Blind, R. Macek, O. Sanderson, and H. Thiessen, in *Proceedings of the 1997 Particle Accelerator Conference,* (IEEE, Piscataway, NJ, 1998) 1015.

[8] R. L. Gluckstern, *Phys. Rev. Lett.* **73,** (1994) 1247; R. A. Jameson, in *Proceedings of the 1993 Particle Accelerator Conference*, (IEEE, Piscataway, NJ, 1993) 3926; J. S. O'Connell, T. P. Wangler, R. S. Mills, and K. R. Crandall, in *Proceedings of the 1993 Particle Accelerator Conference*, (IEEE, Piscataway, NJ, 1993) 3657; J. M. Lagniel, *Nucl. Instr. Meth. A* **345**, (1994) 46; J. M. Lagniel, *Nucl. Instr. Meth. A* **345**, (1994) 405; I. Hofmann, L. J. Laslett, L. Smith, and I. Haber, *Part. Accel.* **13**, (1983) 145; J. Struckmeier and M. Reiser, *Part. Accel.* **14**, (1983) 227.

[9] R. Baartman, Proceedings of Workshop on Space Charge Physics in High Intensity Hadron Rings (Shelter Island, NY, 1998), p.56.

Mismatch Correction for the Envelope Modes

A. V. Fedotov[1]

Brookhaven National Laboratory, Upton, New York 11973

R. L. Gluckstern

Physics Department, University of Maryland, College Park, Maryland 20742

1 INTRODUCTION

As a result of systematic studies of halo formation in high-current ion linacs, there is general agreement that halos in such machines develop as a result of the parametric resonance between the ion oscillations in the beam bunch and collective oscillations of the bunch itself. In order to understand the effect of large mismatches, it is useful to derive mismatch corrections for the coherent envelope modes of the bunch. It turns out that expressions recently presented in the literature [1] are too approximate, and a more accurate calculation is needed. We therefore present a more accurate derivation based on the perturbation and phase-amplitude methods.

2 SYMMETRIC ENVELOPE MODE

We start with the normalized envelope equations in 2-D:

$$X'' + X - \frac{2\Gamma}{X+Y} - \frac{1}{X^3} = 0, \qquad (2.1)$$

$$Y'' + Y - \frac{2\Gamma}{X+Y} - \frac{1}{Y^3} = 0, \qquad (2.2)$$

where we use the notation $\Gamma = (1 - \eta^2)/\eta$ for the space-charge perveance, presented in [1]. Here η is tune depression. We now assume small oscillations around the matched beam dimensions and write $X \to X_0 + u$, $Y \to Y_0 + v$. For a round beam with $X_0 = Y_0$ and $u = v = \delta$, we obtain

$$\delta'' + \delta\left(1 + \frac{\Gamma}{X_0^2} + \frac{3}{X_0^4}\right) + \delta^2\left(-\frac{\Gamma}{X_0^3} - \frac{6}{X_0^5}\right)$$
$$+ \delta^3\left(\frac{\Gamma}{X_0^4} + \frac{10}{X_0^6}\right) = 0, \qquad (2.3)$$

which is identical to the 1-D radial problem with X_0 replaced by R_0. From the matched condition $R'' = 0$ we have $R_0^2 = 1/\eta$. Thus we can rewrite Eq. (2.3) as

$$x'' + x(1 + 3\eta^2 + 1 - \eta^2) - x^2\eta^{3/2}(6\eta + 1/\eta - \eta)$$
$$+ x^3\eta^2(10\eta + 1/\eta - \eta) = 0, \qquad (2.4)$$

where we used x instead of δ. We now rewrite Eq. (2.4) in the following form:

$$x'' + q^2 x = \alpha x^2 - \beta x^3, \qquad (2.5)$$

where $q^2 = 2 + 2\eta^2$ is the usual frequency of the symmetric ("breathing") mode, $\alpha = \sqrt{\eta}(5\eta^2 + 1)$ and $\beta = \eta(9\eta^2 + 1)$. In order to obtain an accurate amplitude correction to the frequency q we now use the phase-amplitude method [2].

We first consider only the quadratic non-linear term αx^2 in Eq. (2.5), and search for a solution in the form

$$x = A\sin(qs + \phi), \qquad (2.6)$$

$$x' = Aq\cos(qs + \phi), \qquad (2.7)$$

implying

$$A'\sin\psi + A\phi'\cos\psi = 0. \qquad (2.8)$$

Here $\psi = qs + \phi$, and A and ϕ are taken to be slowly varying amplitude and phase parameters. Our equation then becomes

$$A'\cos\psi - A\phi'\sin\psi = \frac{\alpha A^2 \sin^2(qs+\phi)}{q}. \qquad (2.9)$$

From Eqs. (2.8) and (2.9) we thus obtain

$$A' = \frac{\alpha A^2}{q}\sin^2\psi\cos\psi, \qquad (2.10)$$

$$A\phi' = -\frac{\alpha A^2}{q}\sin^3\psi, \qquad (2.11)$$

which we rewrite as

$$A' = \frac{\alpha A^2}{4q}(\cos\psi - \cos 3\psi), \qquad (2.12)$$

$$\phi' = -\frac{\alpha A}{4q}(3\sin\psi - \sin 3\psi). \qquad (2.13)$$

We now expand A and ϕ in powers of α: $A = A_0 + \alpha A_1 + \alpha^2 A_2 + \ldots$ and $\phi = \phi_0 + \alpha\phi_1 + \alpha^2\phi_2 + \ldots$. Matching terms with α to the first power, we have

$$A_1' = \frac{A_0^2}{4q}(\cos\psi_0 - \cos 3\psi_0), \qquad (2.14)$$

$$\phi_1' = -\frac{A_0}{4q}(3\sin\psi_0 - \sin 3\psi_0). \qquad (2.15)$$

Integrating Eqs. (2.14)-(2.15), we obtain

$$A_1 = \frac{A_0^2}{4q^2}(\sin\psi_0 - \frac{\sin 3\psi_0}{3}), \qquad (2.16)$$

$$\phi_1 = \frac{A_0}{4q^2}(3\cos\psi_0 - \frac{\cos 3\psi_0}{3}), \qquad (2.17)$$

which shows that the average of ϕ in first order goes to zero, that is $<\phi_1> = 0$. We thus need to go to second order in α in the phase ϕ in order to obtain the non-vanishing contribution from the term αx^2 in Eq. (2.5) as was done in [1]. Therefore, matching powers of α^2, we have

$$\phi_2' = -\frac{A_1}{4q}(3\sin\psi_0 - \sin 3\psi_0)$$
$$- \frac{A_0\phi_1}{4q}(3\cos\psi_0 - 3\cos 3\psi_0). \qquad (2.18)$$

[1]e–mail: fedotov@sun2.BNL.gov

Substituting A_1, ϕ_1 from Eqs. (2.16), (2.17), and performing averaging, we finally obtain

$$< \phi_2' >= -\frac{5}{12}\frac{A_0^2}{q^3}. \qquad (2.19)$$

We now repeat a similar analysis for the cubic term in Eq. (2.5) to obtain

$$A\phi_1' = \frac{\beta A^3}{q}\sin^4\psi, \qquad (2.20)$$

$$< \phi_1' >= \frac{3}{8}\frac{\beta A_0^2}{q}. \qquad (2.21)$$

Note that this factor $3/8$ is more accurate than the factor $1/2$ obtained by a simplified averaging procedure used in [1]. For the frequency $\nu = q + \phi'$ we thus have

$$\nu = q - \frac{5}{12}\frac{\alpha^2 A_0^2}{q^3} + \frac{3}{8}\frac{\beta A_0^2}{q}. \qquad (2.22)$$

For small A_0, we then obtain

$$\nu^2 = q^2 + 2A_0^2(\frac{3\beta}{8} - \frac{5\alpha^2}{12q^2}). \qquad (2.23)$$

This amplitude correction for the frequency agrees with the one given in [3]. With the definition of the mismatch parameter $M = A_0/R_0$, we thus have

$$\nu^2 = 2(1+\eta^2) + M^2\left[\frac{3}{4}(1+9\eta^2) - \frac{5}{12}\frac{(1+5\eta^2)^2}{(1+\eta^2)}\right], \qquad (2.24)$$

which can be rewritten as

$$\nu^2 = 2(1+\eta^2) + M^2\left[\frac{(1+11\eta^2)(1-\eta^2)}{3(1+\eta^2)}\right]. \qquad (2.25)$$

This expression is different from the one presented in [1]. It gives completely different dependence on the tune depression η. While the expression presented in [1] gives a quadratic dependence on η with the maximum contribution when $\eta = 1$ (zero space-charge), Eq. (2.25) indicates that the mismatch correction term goes to zero in the limit of zero space-charge. This seems correctly to describe the fact that non-linear detuning for the symmetric mode comes from the space-charge. Application of our formula in Eq. (2.24) to a circular machines with relatively small space-charge shows that the mismatch correction for the symmetric mode is negligible. Also, a similar correction term can be obtained by a different method [4]. One can rewrite Eq. (2.24) in the form presented in [4] using the following forms for α and β:

$$\alpha = \frac{6}{R_0^5} + \frac{1}{R_0^3}\frac{1-\eta^2}{\eta}, \quad \beta = \frac{10}{R_0^6} + \frac{1}{R_0^4}\frac{1-\eta^2}{\eta}. \qquad (2.26)$$

3 ANTISYMMETRIC ENVELOPE MODE

From Eqs. (2.1) and (2.2) we now have

$$(u-v)'' \quad + \quad (u-v) + \frac{3(u-v)}{X_0^4} - \frac{6(u^2-v^2)}{X_0^5}$$
$$+ \quad \frac{10(u^3-v^3)}{X_0^6} = 0. \qquad (3.27)$$

We cannot now simply replace $(u-v)$ by δ as it was done in [1]. We thus rewrite Eq. (3.27) as

$$p'' + q_-^2 p = \frac{6}{X_0^5}pn - \frac{10}{X_0^6}p\left(\frac{3n^2+p^2}{4}\right), \qquad (3.28)$$

where $p = u-v$, $n = u+v$ and $q_-^2 = 1+3\eta^2$ is the frequency of the antisymmetric ("quadrupole") mode without the mismatch correction. Exciting a pure antisymmetric mode then means setting $n = 0$, leading to

$$p'' + q_-^2 p = -\frac{10}{X_0^6}\frac{p^3}{4}. \qquad (3.29)$$

Thus there is only a cubic non-linearity term in the equation. We then again apply a phase-amplitude analysis similar to the one presented for the symmetric mode to obtain

$$\nu_-^2 = q_-^2 + M^2\frac{15}{8}\eta^2. \qquad (3.30)$$

This result for the antisymmetric mode is different from the one presented in [1] due to the additional factor $1/4$ in the cubic-nonlinearity term in Eq. (3.29), and due to a more accurate averaging technique.

4 SUMMARY

In these notes we obtained the mismatch corrections for the envelope modes in a 2-D beam. We showed that the phase-amplitude method leads to more accurate results than those presented in [1]. Of specific interest is the result for the symmetric mode which shows that in the limit of zero space-charge the mismatch correction goes to zero. As a result, when applied to circular machines with low space-charge, the mismatch correction for the symmetric mode is negligible and we can use the usual "breathing" frequency (without the mismatch correction) with a very good accuracy.

5 REFERENCES

[1] M. Ikegami, Phys. Rev. E **59**, 2330 (1999).

[2] N.N. Bogoliubov and Y.A. Mitropolsky, Asymptotic Methods in the Theory of Nonlinear Oscillations, Gordon and Breach, New York (1961).

[3] L.D. Landau and E. M. Lifschitz, Mechanics, Pergamon Press (1976).

[4] A. Riabko et al., Phys. Rev. E **51**, 3529 (1995).

Collective Instabilities and Halo Formation of Space-Charge Dominated Beams in a Particle-Beam Nonlinear-Dynamics Approach [1]

K. Y. Ng[2]
Fermilab, P.O. Box 500, Batavia, IL 60510

Abstract

Nonlinear dynamics deals with parametric resonances and diffusion, which are usually beam-intensity independent and rely on a particle Hamiltonian. Collective instabilities deal with beam coherent motion, where the Vlasov equation is frequently used in conjunction with a beam-intensity dependent Hamiltonian. We address the questions: Are the two descriptions the same? Are collective instabilities the results of encountering parametric resonances whose driving force is intensity dependent? The space-charge dominated beam governed by the Kapchinskij-Vladimirskij (K-V) envelope equation [1] is used as an example.

1 INTRODUCTION

Traditionally, the thresholds of collective instabilities are obtained by solving the Vlasov equation, the dynamics of which comes from the single-particle wakefield-dependent Hamiltonian. The Vlasov equation is often linearized so that the modes of collective motion can be described by a set of orthonormal eigenfunctions and their corresponding complex eigenvalues give the initial growth rates. The perturbation Hamiltonian ΔH_1 may have a time-independent component, for example, the space-charge self-field that determines the potential-well distortion of the unperturbed particle distribution, and the part involving the nonlinear magnetic fields, that gives rise to the dynamical aperture limitation. It may also have a time-dependent component, which includes the time-dependent effects of wakefields and produces coherent motion of beam particles. The harmonic content of the wakefields depends on the structure of accelerator components. If one of the resonant frequencies of the wakefields is equal to a fractional multiple of the unperturbed tune of unperturbed Hamiltonian H_0, a resonance is encountered. Depending on the stochasticity of the phase space, particles may be trapped into the resonant islands or diffuse towards resonant structures far away forming beam halos or getting lost. This may result in a runaway situation such that collective instability is induced.

Experimental measurements indicate that a small time dependent perturbation can create resonance islands in the longitudinal or transverse phase space and profoundly change the bunch structure [2]. For example, a modulating transverse dipole field close to the synchrotron frequency can split up a bunch into beamlets. Although these phenomena are driven by beam-intensity independent sources,

they can also be driven by the space-charge force and/or the wakefields of the beam which are intensity dependent. Once perturbed, the new bunch structure can further enhance the wakefields inducing even more perturbation to the circulating beam. Experimental observation of hysteresis in collective beam instabilities seems to indicate that resonance islands have been generated by the wakefields.

For example, the Keil-Schnell criterion [3] of longitudinal microwave instability can be derived from the concept of bunching buckets, or islands, created by the perturbing wakefields. Particles in the beam will execute *synchrotron* motion inside these buckets leading to growth in the momentum spread of the beam. In fact, the collective growth rate is exactly equal to the angular synchrotron frequency inside these buckets. If the momentum spread of the beam is much larger than the bucket height, only a small fraction of the particles in the beam will be affected and collective instabilities will not occur. This mechanism has been called Landau damping.

As a result, we believe that the collective instabilities of a beam may also be tackled from a particle-beam nonlinear-dynamics approach, with collective instabilities occurring when the beam particles are either trapped in resonance islands or diffuse away from the beam core because of the existence of a sea of chaos. The advantage of the particle-beam nonlinear-dynamics approach is its ability to understand the hysteresis effects and to calculate the beam distribution beyond the threshold condition. Such a procedure may be able to unify our understanding of collective instabilities and nonlinear beam dynamics. Here, the stability issues of a space-charge dominated beam in a uniformly focusing channel are considered as an example [4].

2 ENVELOPE HAMILTONIAN

First, the envelope Hamiltonian is normalized to unit emittance and unit period. In terms of the normalized and dimensionless envelope radius R, together with its conjugate momentum P, the Hamiltonian for the beam envelope in a uniformly focusing channel can be written as [5, 6]

$$H_e = \frac{1}{4\pi}P^2 + V(R) , \qquad (2.1)$$

$$V(R) = \frac{\mu^2}{4\pi}R^2 - \frac{\mu\kappa}{\pi}\ln\frac{R}{R_0} + \frac{1}{4\pi R^2} , \qquad (2.2)$$

where $\mu/(2\pi)$ is the *unperturbed* particle tune, $\kappa = Nr_{\rm cl}/(\mu\beta^2\gamma^3)$ the *normalized* space-charge perveance, N the number of particles per unit length having classical radius $r_{\rm cl}$, and β and γ the relativistic factors of the beam. The normalized K-V equation then reads

$$\frac{d^2R}{d\theta^2} + \left(\frac{\mu}{2\pi}\right)^2 R = \frac{2\mu\kappa}{4\pi^2 R} + \frac{1}{4\pi^2 R^3} . \qquad (2.3)$$

The radius R_0 of the matched beam envelope or core occurs at the lowest point of the potential; i.e., $V'(R_0) = 0$, or

$$\mu R_0^2 = \sqrt{\kappa^2 + 1} + \kappa = \frac{1}{\sqrt{\kappa^2 + 1} - \kappa} . \qquad (2.4)$$

From the second derivative of the potential, the small amplitude tune for envelope oscillations is therefore
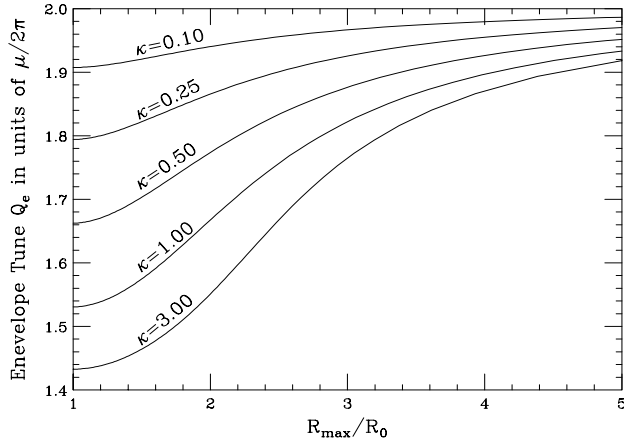
Figure 1: Envelope tune Q_e versus envelope mismatch R_{max}/R_0 for various space-charge perveance κ. Notice that Q_e is represented by ν_e at $R_{max}/R_0 = 1$ when the beam envelope is matched.

$$\nu_e = \frac{2\mu}{2\pi}\left[1 - \kappa\left(\sqrt{\kappa^2+1} - \kappa\right)\right]^{1/2} \qquad (2.5)$$

which approaches μ/π and $\sqrt{2}\mu/(2\pi)$ as κ approaches 0 and ∞, respectively.

For a mismatched beam, R varies between R_{min} and R_{max}. To derive the tune of the mismatched envelope, it is best to go to the action-angle variables (J_e, ψ_e). The envelope tune and action are then

$$Q_e = \frac{dE_e}{dJ_e} = \nu_e + \alpha_e J_e + \cdots, \qquad J_e = \frac{1}{2\pi}\oint P\,dR. \qquad (2.6)$$

where E_e is the Hamiltonian value of the beam envelope, and the detuning α_e, defined by $H_e = \nu_e J_e + \frac{1}{2}\alpha_e J_e^2 + \cdots$, is computed to be

$$\alpha_e = \frac{3}{16\pi^3 R_0^4 \nu_e^2}\left[\mu\kappa + \frac{5}{R_0^2}\right] - \frac{5}{48\pi^5 R_0^6 \nu_e^4}\left[\mu\kappa + \frac{3}{R_0^2}\right]^2 + \cdots.$$

To obtain the envelope tune for large mismatch, one must compute numerically the action integral to obtain

$$Q_e = \frac{dE_e}{dJ_e} = 2\pi\left[\oint \frac{\partial P}{\partial E_e}dR\right]^{-1}, \qquad (2.7)$$

The envelope tune is plotted in Fig. 1 as a function of the maximum envelope radius R_{max}, which, for small mismatch, is related to the envelope action J_e by

$$R = R_0 + \left(\frac{J_e}{\pi\nu_e}\right)^{1/2}\cos Q_e\theta. \qquad (2.8)$$

3   COLLECTIVE-MOTION APPROACH

Gluckstern, Cheng, Kurennoy, and Ye [7] have studied the collective beam stabilities of a space-charge dominated K-V beam in a uniformly focusing channel. The particle distribution f is separated into the unperturbed distribution f_0 and the perturbation f_1:

$$f(u,v,\dot{u},\dot{v};\theta) = f_0(u^2+v^2+\dot{u}^2+\dot{v}^2) + f_1(u,v,\dot{u},\dot{v};\theta),$$

where u and v are the normalized transverse coordinates which are functions of the 'time' variable θ. Their derivatives with respect to time are denoted by $\dot{u}$ and $\dot{v}$. The unperturbed distribution,

$$f_0(u^2+v^2+\dot{u}^2+\dot{v}^2) = \frac{I_0}{v_0\pi^2}\delta(u^2+v^2+\dot{u}^2+\dot{v}^2 - 1),$$

is the steady-state solution of the K-V equation (2.3) and is therefore time-independent. In the notation of Gluckstern, Cheng, Kurennoy, and Ye, I_0 is the average beam current and v_0 the longitudinal velocity of the beam particles. The perturbed distribution generates an electric potential G, which is given by the Poisson's equation

$$\nabla^2 G(u,v,\theta) = -\frac{1}{\varepsilon_0}\int d\dot{u}\int d\dot{v}f_1(u,v,\dot{u},\dot{v};\theta), \qquad (3.1)$$

so that the Hill's equations in the two transverse planes become

$$\ddot{u}+u = -\frac{e\beta}{m_0 v_0^2 \varepsilon}\frac{\partial G}{\partial u}, \qquad \ddot{v}+v = -\frac{e\beta}{m_0 v_0^2 \varepsilon}\frac{\partial G}{\partial v}, \qquad (3.2)$$

where ε stands for the transverse emittance of the beam and m_0 the rest mass of the beam particle.

For small perturbation, the perturbation distribution is proportional to the derivative of the unperturbed distribution. This enables us to write

$$f_1(u,v,\dot{u},\dot{v};\theta) = g(u,v,\dot{u},\dot{v};\theta)f_0'(u^2+v^2+\dot{u}^2+\dot{v}^2). \quad (3.3)$$

Substituting into the linearized Vlasov equation, we obtain

$$\frac{\partial g}{\partial\theta} + \dot{u}\frac{\partial g}{\partial u} + \dot{v}\frac{\partial g}{\partial v} - u\frac{\partial g}{\partial\dot{u}} - v\frac{\partial g}{\partial\dot{v}} = \frac{2e\beta}{m_0 v_0^2 \varepsilon}\left[\dot{u}\frac{\partial G}{\partial u} + \dot{v}\frac{\partial G}{\partial v}\right].$$
$$(3.4)$$

Noting that the potential G is a polynomial, Gluckstern, et. al. are able to solve for g and G consistently in terms of hypergeometric functions. Thus a series of orthonormal eigenmodes are obtained for the perturbed distribution with their corresponding eigenfrequencies. These modes are characterized by (j,m), where j is the radial eigennumber and m the azimuthal eigennumber.

For the azimuthally symmetric $m=0$ modes, $(1,0)$ is the breathing mode of uniform density at a particular time while the $(2,0)$ mode oscillates with a radial node between $R=0$ and $R=R_0$ so that the density becomes nonuniform. The higher modes are similar, with mode $(j,0)$ having $j-1$ radial nodes. When the eigenfrequency of a mode is complex, the mode becomes unstable with a collective growth rate. Stability is studied in terms of tune depression $\eta = \sqrt{\kappa^2+1} - \kappa$ and the amount of envelope mismatch. The former is defined as the ratio of the particle tune with space charge to the particle tune without space charge for a *matched* beam. Thus η ranges from 0 to 1; $\eta = 1$ implies zero space charge while $\eta = 0$ implies infinite space charge.

Gluckstern, et. al. showed that mode $(1,0)$ is stable for any mismatch and tune depression. Mode $(2,0)$ becomes unstable at zero mismatch when the tune depression $\eta < 1/\sqrt{17} = 0.2435$. It is also unstable when the mismatch is large. This is plotted in Fig. 2 with the stable regions of modes $(2,0)$, $(3,0)$, and $(4,0)$ enclosed, respectively, by the solid, dashed, and dot-dashed curves, a reproduction of Ref. 4. These latter two modes become unstable at zero mismatch when the tune depressions are less than 0.3859 and 0.3985, respectively. They found that the modes become more unstable as the number of radial nodes increases. Among all the azimuthals, they noticed that the azimuthally symmetric modes $(m=0)$ are the most unstable.
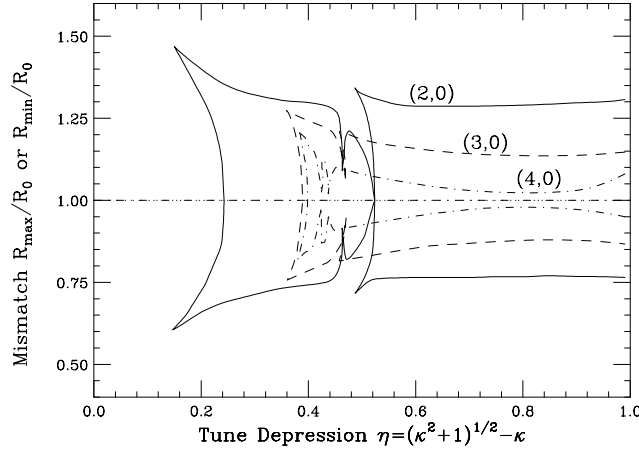
Figure 2: Beam stability plot versus particle tune depression η and beam envelope mismatch. The stability regions for modes (2,0), (3,0) and (4,0) are enclosed, respectively, by the solid, dashed, and dot-dashed curves. (Reproduced from Ref. 4).

4 PARTICLE-BEAM APPROACH

4.1 Particle Hamiltonian

We want to investigate whether the instability regions in the plane of tune depression and mismatch can be explained by nonlinear parametric resonances. First, let us study the transverse motion of a particle having zero angular momentum. The situation of finite momentum will be discussed later in Sec. 6. We choose y as the particle's transverse coordinate with canonical angular momentum p_y. Its motion is perturbed by an azimuthally symmetric oscillating beam core of radius R. The particle Hamiltonian is [6]

$$H_p = \frac{1}{4\pi}p_y^2 + \frac{\mu^2}{4\pi}y^2 - \frac{2\mu\kappa}{4\pi R^2}y^2\,\Theta(R-|y|)$$
$$-\frac{2\mu\kappa}{4\pi}\left(1+2\ln\frac{|y|}{R}\right)\Theta(|y|-R)\,, \quad (4.1)$$

giving the equation of motion for y,

$$\frac{d^2y}{d\theta^2} + \left(\frac{\mu}{2\pi}\right)^2 y = \frac{\mu\kappa}{2\pi^2 R^2}y\,\Theta(R-|y|) + \frac{\mu\kappa}{2\pi^2|y|}\,\Theta(|y|-R)\,.$$
$$(4.2)$$

For a weakly mismatched beam, the envelope radius is $R = R_0 + \Delta R\cos Q_e\theta$. The particle Hamiltonian can also be expanded in terms of the equilibrium envelope radius R_0, resulting $H_p = H_{p0} + \Delta H_p$. The unperturbed Hamiltonian is

$$H_{p0} = \frac{1}{4\pi}p_y^2 + \frac{\mu^2}{4\pi}y^2 - \frac{2\mu\kappa}{4\pi R_0^2}y^2\,\Theta(R_0-|y|)$$
$$-\frac{2\mu\kappa}{4\pi}\left(1+2\ln\frac{|y|}{R_0}\right)\Theta(|y|-R_0)\,, \quad (4.3)$$

and the perturbation

$$\Delta H_p \approx -\frac{\mu\kappa}{\pi R_0^2}\left[\frac{\Delta R}{R_0}(y^2-R_0^2)\right.$$
$$\left.+\frac{3\Delta R^2}{2R_0^2}\left(y^2-\tfrac{1}{3}R_0^2\right)+\cdots\right]\Theta(R_0-|y|)\,. \quad (4.4)$$

Note that many non-contributing terms, like the ones involving the δ-function and δ'-function, have been dropped.

Additionally, envelope oscillations do not perturb particle motion outside the envelope radius; thus the perturbing potential in Eq. (4.4) exists only inside the envelope.

For a matched beam, $\Delta H_p = 0$. Inside the core of uniform distribution, the particle motion is linear and its tune can be readily obtained:

$$\nu_p = \frac{\mu}{2\pi}\left(1-\frac{2\kappa}{\mu R_0^2}\right)^{1/2} = \frac{\mu}{2\pi}\left(\sqrt{\kappa^2+1}-\kappa\right)\,.$$

Thus, $\eta = \sqrt{\kappa^2+1}-\kappa$ is the tune depression.

When the particle spends time oscillating outside the beam envelope, its tune has to be computed numerically. First, the particle action is defined as

$$J_p = \frac{1}{2\pi}\oint p_y dy\,. \quad (4.5)$$

The particle tune Q_p is then given by

$$Q_p = \frac{dE_p}{dJ_p} = 2\pi\left[\oint\frac{\partial p_y}{\partial E_p}dy\right]^{-1}\,, \quad (4.6)$$

where E_p is the Hamiltonian value of the beam particle. The result is shown in Fig. 3 for various space-charge perveance κ. We see that when the particle motion is completely inside the beam envelope ($J_p < \frac{1}{2}$), the particle tune is a constant and is given by ν_p depending on κ only. As the particle spends more and more time outside the beam envelope, its tune increases because the space-charge force decreases as y^{-1} outside the envelope.

4.2 Particle Tune Inside a Mismatched Beam

To simplify the algebra, it is advisable to scale away the unperturbed particle tune $\mu/(2\pi)$ through the transformation: $\mu R^2 \to R^2$, $\mu y^2 \to y^2$, and $\mu\theta/(2\pi) \to \theta$. The envelope and particle equations become

$$\frac{d^2R}{d\theta^2} + R = \frac{2\kappa}{R} + \frac{1}{R^3}\,, \quad (4.7)$$

$$\frac{d^2y}{d\theta^2} + y - \frac{2\kappa}{R^2}y\,\Theta(R-|y|) - \frac{2\kappa}{y}\Theta(|y|-R) = 0\,. \quad (4.8)$$

For one envelope oscillation period, the envelope radius R is periodic and Eq. (4.8) *inside* the envelope core becomes a Hill's equation with effective *field gradient* $K(\theta) = 1-$
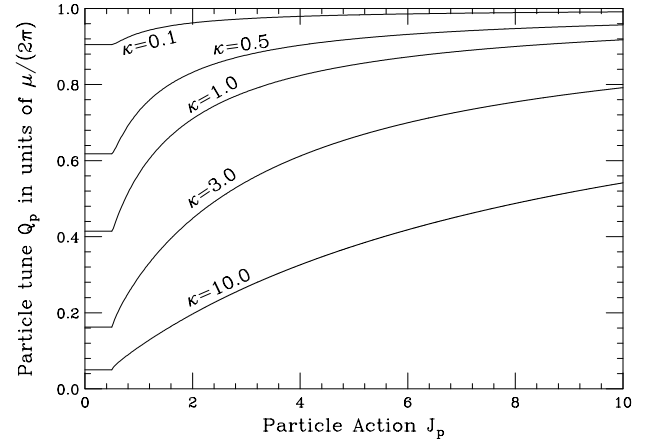

Figure 3: Particle tune Q_p as function of particle action J_p and space-charge perveance κ for a matched beam.

$2\kappa/R^2(\theta)$. The solution is then exactly the same as the Floquet transformation by choosing $y = aw(\theta)\cos[\psi(\theta) + \delta]$. It is easy to show that the differential equation for w is exactly the envelope equation of Eq. (4.7). Thus we can replace w by R, and R^2 becomes the effective *betatron function*. Since the particle makes Q_p/Q_e betatron oscillations during one envelope fluctuation period, where Q_p is the particle tune, we have

$$\frac{Q_p}{Q_e} = \frac{\Delta\psi}{2\pi} = \frac{1}{2\pi}\oint \frac{d\theta}{R^2(\theta)} \ . \tag{4.9}$$

In Floquet's notation, with $\hat{y} = y/R$, Eq. (4.2) describing the motion of a particle modulated by a beam envelope becomes

$$\frac{d^2\hat{y}}{d\psi^2} + \hat{y} + 2\kappa R^2\left[\frac{\hat{y}^2 - 1}{\hat{y}}\right]\Theta(|\hat{y}| - 1) = 0 \ . \tag{4.10}$$

Thus, all particles inside the beam envelope have a fixed tune depending on the amount of space charge and envelope mismatch. Particles spending part of the time outside the beam envelope will have larger tunes. The Floquet transformation can also be accomplished by a canonical transformation employing the generating function

$$F_2(y, \hat{p}_y; \theta) = \frac{y\hat{p}_y}{R(\theta)} + \frac{yR'(\theta)}{2R(\theta)} \ , \tag{4.11}$$

where the prime denotes derivative with respect to θ. The new Hamiltonian in the Floquet coordinates becomes

$$\hat{H}_p(\hat{y}, \hat{p}_y; \theta) = \frac{1}{R^2(\theta)}(\hat{y}^2 + \hat{p}_y^2) + \kappa(\hat{y}^2 - \ln\hat{y}^2)\Theta(|\hat{y}| - 1) \ . \tag{4.12}$$

For a small mismatch core fluctuation, we can write $R = R_0(1 - M\cos Q_e\theta)$, where M can be interpreted as the mismatch parameter. The integral in Eq. (4.9) can be performed analytically to give

$$Q_p = \frac{\nu_p}{(1 - M^2)^{3/2}} \ , \tag{4.13}$$

where $\nu_p = R_0^{-2} = \sqrt{\kappa^2 + 1} - \kappa$ is the particle tune when the envelope is matched. The analytic formula of Eq. (4.13), however, is only valid when the mismatch parameter $M \lesssim 0.2$. The reason is that the envelope equation is nonlinear in the presence of space charge. In other words, while minimum envelope radius is given by $R_{\min} = (1 - M)R_0$, the maximum envelope radius is always $R_{\max} > (1 + M)R_0$. In fact, when $M \to 1$, $R_{\min} \to 0$, but $R_{\max} \to \infty$. This can be seen in top plot of Fig. 4 with $(R_{\max} - R_0)/R_0$ versus $M = (R_0 - R_{\max})/R_0$. If the envelope oscillations were symmetric about R_0, the plot would follow the $45°$ dashed line instead. We see that the deviation is large when the mismatch and tune depression are large. When the approximation $R = R_0(1 - M\cos Q_e\theta)$ breaks down, the particle tune can still be easily evaluated by performing the integral in Eq. (4.9) numerically. The lower plot of Fig. 4 shows the deviation of the actual particle tune Q_p from its analytic formula of Eq. (4.13).

5 PARAMETRIC RESONANCES

Particle motion is modulated by the oscillating beam envelope. Therefore, to study the resonance effect, we need to
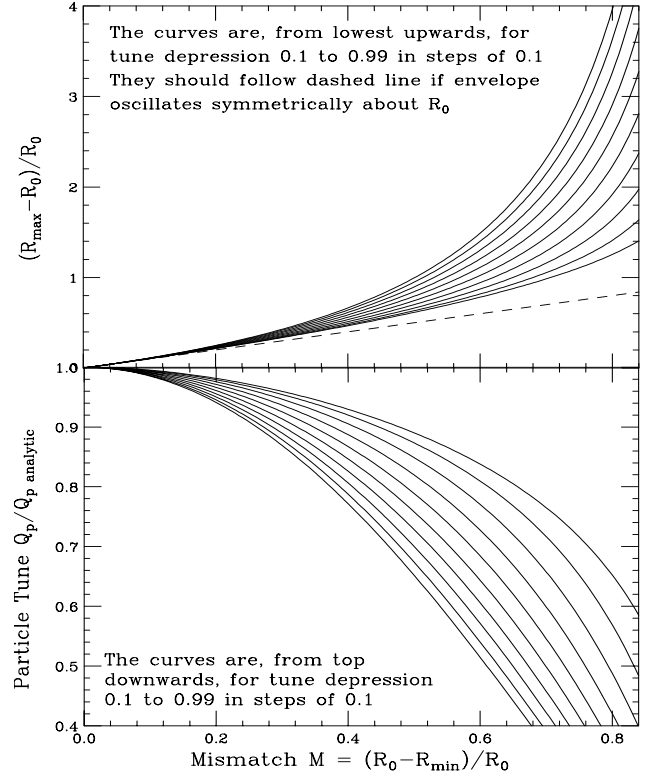

Figure 4: Top: $(R_{\max} - R_0)/R_0$ vs $M = (R_0 - R_{\max})/R_0$ showing the large asymmetric envelope oscillation about the equilibrium radius R_0 when both the mismatch and tune depression are large. Bottom: Deviation of the actual particle tune Q_p from the value given Eq. (4.13) in the presence of mismatch.

include the perturbation part ΔH_p of the particle Hamiltonian. We expand it as a Fourier series in the angle variable ψ_p yielding, for example,

$$(y^2 - R_0^2)\Theta(R_0 - |y|) = \sum_{n=-\infty}^{\infty} G_n(J_p)e^{in\psi_p} \ . \tag{5.1}$$

Since ΔH_p is even in y, only even n harmonics survive. The particle Hamiltonian then becomes

$$H_p = H_{p0} + \frac{\mu\kappa}{2\pi R_0^2}\sum_{m=1}^{\infty}\sum_{\substack{n>0\\ \text{even}}}(m+1)M^m|G_{nm}| \times$$
$$\times \sum_{i=\pm1}\cos(n\psi_p + imQ_e\theta + \gamma_n) + \cdots, \tag{5.2}$$

where γ_n are some phases and use has been made of $R = R_0(1 - M\cos Q_e\theta)$, the approximation for small mismatch.

Focusing on the $n{:}m$ resonance, a canonical transformation to the resonance rotating frame (I_p, ϕ_p) gives

$$\langle H_p \rangle = E_p(I_p) - \frac{m}{n}Q_eI_p + h_{nm}(I_p)\cos n\phi_p \ , \tag{5.3}$$

with the effective κ-dependent resonance strength

$$h_{nm} = \frac{(m+1)M^m\mu\kappa}{2\pi R_0^2}|G_{nm}(I_p)| \ . \tag{5.4}$$

As usual, there are n stable and n unstable fixed points which can be found easily. Since ΔH_p is a polynomial up to y^2 only and $y \propto \sin\psi_p$, we have, inside the envelope,
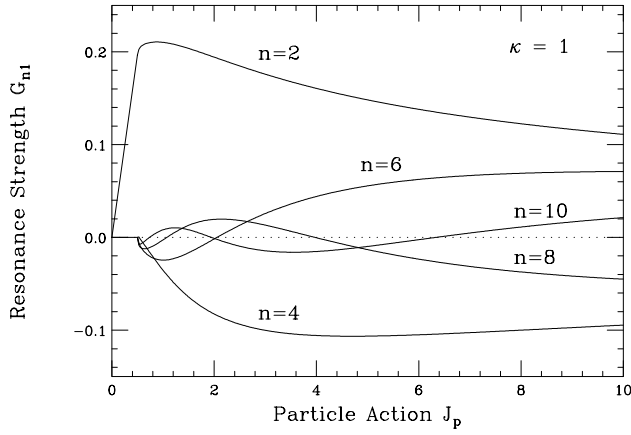
Figure 5: Plot of driving strengths of first-order resonances G_{n1} versus particle action J_p. Inside the envelope ($J_p < \frac{1}{2}$), only G_{21} is nonzero. Once outside the envelope, however, $|G_{n1}|$ for $n \geq 2$ increases rapidly from zero.

$$G_{nm} = \frac{1}{4\pi Q_e} J_p \delta_{n2} , \qquad (5.5)$$

implying that only 2:m resonances are possible. Outside the envelope the resonance driving strengths can also be computed, and are plotted in Fig. 5. We see that although the driving strengths G_{n1} for $n > 2$ vanish inside the envelope ($J_p < \frac{1}{2}$), they increase rapidly once outside. Including noises of all types, particles inside the K-V beam envelope can leak out. This situation is particularly true when the particle tune is equal to a fractional multiple of the envelope tune. A small perturbation may drive particles outside the beam envelope. Once outside, because of the nonvanishing driving strengths, these particles may be trapped into resonance islands or diffuse into resonances farther away. Once trapped or diffused, they cannot wander back into the envelope core. As more and more envelope particles leak out, the core stabilization is lost and an instability occurs.

Our job is, therefore, to map out the location of parametric resonances in the plane of mismatch and tune depression. Because particles are affected only by resonances when they are just outside the envelope core, their tunes are essentially the tune inside the beam envelope. At zero mismatch, the threshold for the n:m resonance can therefore be derived by equating ν_p/ν_e to m/n. Thus

$$\frac{\nu_p}{\nu_e} = \frac{\sqrt{\kappa^2+1}-\kappa}{2\left[1-\kappa\left(\sqrt{\kappa^2+1}-\kappa\right)\right]^{1/2}} \leq \frac{m}{n} , \qquad (5.6)$$

or

$$\kappa \geq \frac{\left(\frac{n}{m}\right)^2 - 4}{\sqrt{8\left[\left(\frac{n}{m}\right)^2 - 2\right]}} . \qquad (5.7)$$

In particular, for the 6:1 resonance, $\kappa \geq 8/\sqrt{17} = 1.9403$, or the tune depression is $\eta \leq 1/\sqrt{17} = 0.2425$, which agrees with Gluckstern's instability threshold for mode (2,0).

For a mismatched beam, the threshold for the n:m resonance is obtained by equating Q_p/Q_e at that mismatch to m/n. These resonances are labeled in Fig. 6 in the plane of
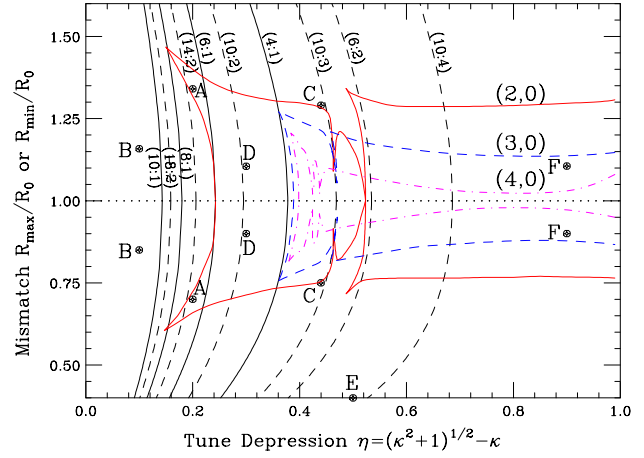

Figure 6: Plot of parametric resonance locations in the plane of tune-depression and beam envelope mismatch. First-order resonances are shown as solid while second- and higher-order resonances as dashes. Overlaid on top are the instability boundaries of modes (2,0), (3,0), and (4,0) derived by Gluckstern, *et. al.*

tune depression and mismatch. The locus of the 2:1 resonance is the vertical line $\eta = 1$. This is obvious, because at zero space charge the particle tune is exactly two times the envelope tune regardless of mismatch. Also, it is clear from Eq. (4.10) that there will not be any Mathieu instability or half-integer stop-band [8]. Thus it appears that the 2:1 resonance would not influence the stability of a space-charge dominated beam. This is, in fact, not true. The stable fixed points of the 2:1 resonance are usually far away from the beam envelope. Thus particles can diffuse towards the 2:1 resonance to form beam halo. As more and more particles continue to diffuse from the beam core into the 2:1 resonance, the beam becomes unstable.

Trackings have been performed for particles outside the envelope core using the fourth-order symplectic integration developed by Forest and Berz [9]. The Poincaré surface of section is shown in Fig. 7A for the situation $\eta = 0.20$ ($\kappa = 2.4$) and $M = 0.3$, corresponding to Points A in Fig. 6. The innermost torus is the beam envelope. The sections are taken every envelope oscillation period when the envelope radius is at a minimum. For each envelope oscillation period, 500 to more than 1000 time steps have been used. We see that as soon as particles diffuse outside the beam envelope, they will encounter the 6:1 resonance, which is bounded by tori. This explains the front stability boundary of Gluckstern's mode (2,0). Since the 4:1 resonance is a strong one, its locus explains the front stability boundaries of Gluckstern's (3,0) and (4,0) modes also.

The Poincaré surface of section corresponding to Points B of Fig. 6 with $\eta = 0.10$ ($\kappa = 4.95$) $M = 0.15$ is shown in Fig. 7B. This is a close-up view showing only the region near the beam envelope; the 2:1 resonance and its separatrices are not shown because they look similar to those depicted in Fig. 7A. We see resonances like 14:2, 8:1, 16:2, 9:1, 10:1, etc, which are so closely spaced that they overlap to form a chaotic region. Particles that
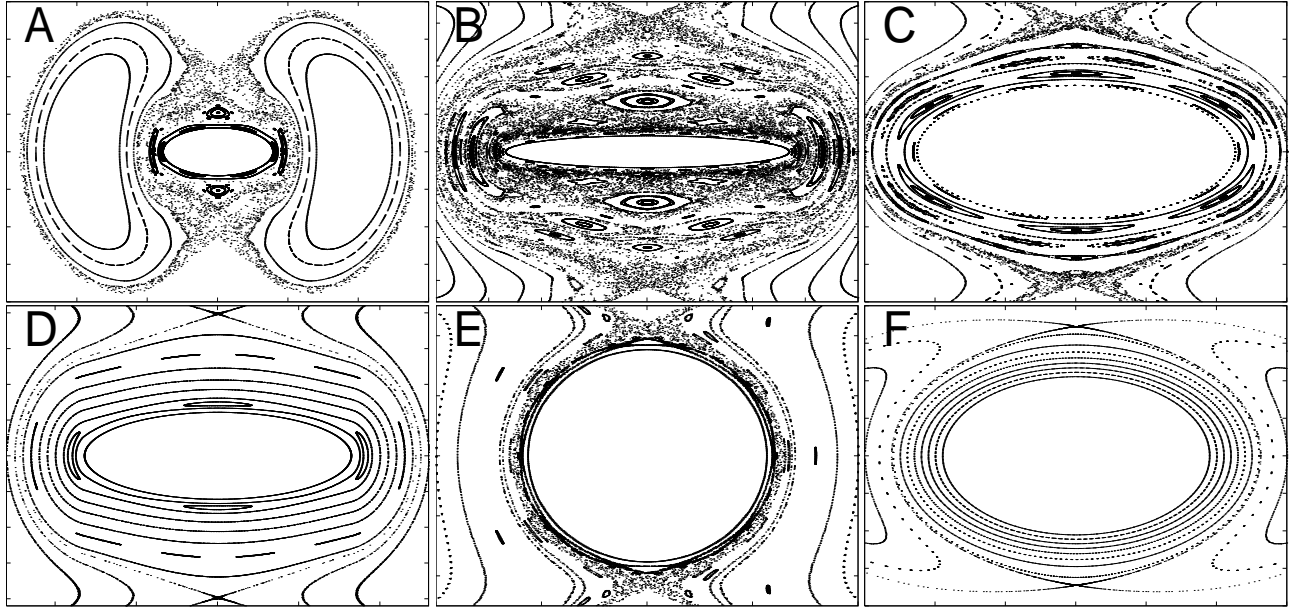
44

Figure 7: Poincaré surface of section in particle phase space (y, p). Plot A is with $(\eta, M) = (0.20, 0.30)$, Plot B (0.10, 0.15), Plot C (0.44, 0.25), Plot D (0.30, 0.10), Plot E (0.50, 0.60), Plot F (0.90, 0.10), corresponding, respectively, to Points A, B, C, D, E, F in Fig. 6. The last 5 are close-up plots, showing only up to the unstable fixed points and internal separatrices of the 2:1 resonance.

diffuse outward from the beam envelope will wander easily towards the 2:1 resonance along its separatrix. This region, where $\eta \lesssim 0.2$, is therefore very unstable.

Figure 7C shows the close-up Poincaré surface of section of Points C in Fig. 6 with $\eta = 0.44$ ($\kappa = 0.916$) and $M = 0.25$. Here the particles see many parametric resonances when they are outside the beam envelope; first the 10:3, followed by the 6:2, 8:3, 10:4, and then a chaotic layer going towards the 2:1 resonance. The resonances are separated by good tori and the instability growth rate should be small. Thus, this is the region on the edge of instability.

On the other hand, the Poincaré surface of section in Fig. 7D corresponding to Points D of Fig. 6 with $\eta = 0.30$ ($\kappa = 1.517$) and $M = 0.10$ shows the 6:2 resonance well separated from the 10:4 resonance with a wide area of good tori. Also the width of the 10:4 resonance is extremely narrow so that particles can hardly be trapped there. Unlike the situation in Figs. 7B and 7C, there is no chaotic region at the unstable fixed points and inner separatrices of the 2:1 resonance, making diffusion towards this resonance impossible. This region will be relatively stable.

Next consider the region with very large beam envelope mismatch like Points E of Fig. 6 with $\eta = 0.50$ ($\kappa = 0.75$) and $M = 0.60$. (The other Point E is at $R_{max}/R_0 = 2.067$ and is therefore not visible in Fig. 6). The close-up Poincaré surface of section in Fig. 7E shows the beam envelope radius at $y = 0.566$ when $p_y = 0$. We can see that the unstable fixed points and the inner separatrices of the 2:1 resonance are very close by and are very chaotic. As soon as a particle diffuses out to $y = 0.62$, it reaches the chaotic sea and wanders towards the 2:1 resonance. Because the chaotic region is so close to the beam envelope, this region of large mismatch is also unstable, which is Gluckstern's region of

instability at large mismatch.

Finally, we look at Points F of Fig. 6, which have small space charge $\kappa = 0.0106$ or $\eta = 0.90$ and small mismatch $M = 0.10$. The Poincaré surface of section is shown in Fig. 7F. The beam envelope is surrounded by good tori far away from the separatrices of the 2:1 resonance and no parametric resonances are seen. This is evident also from Fig. 6 that this region is not only free from primary resonances but also many higher-order resonances. The unstable fixed points and the separatrices of the 2:1 resonance are well-behaved and not chaotic. Thus, these points are very stable. If we keep the same space-charge perveance and increase the amount of envelope mismatch, we also do not see in the Poincaré surface of section any parametric resonances between the beam envelope and the separatrices for the 2:1 resonance. However, although the separatrices of the 2:1 resonance are not chaotic, they become closer and closer to the beam envelope. When the separatrices are too close, particles that are driven by a small perturbation away from the beam envelope will have a chance of traveling along the separatrices of the 2:1 resonance to form beam halo. From our discussions, it is clear that to avoid instability and halo formation, the beam should have small mismatch and be in a region that is far away from parametric resonances in the plane of mismatch and tune depression. The best solution for stability is certainly when the beam has small mismatch and small space-charge perveance.

The deep fissures of the (2,0) mode near $\eta = 4.7$ and 5.3 in Fig. 2 or 6 are probably the result of encountering the 10:3 and 6:2 parametric resonances. The width of the fissures should be related to the width of the resonance islands, which can be computed in the standard way. In general, a lower-order resonance island, like the 4:1, is much wider

than a higher-order resonance island, like the 6:1.

We tried very hard to examine the region between the 4:1 and 10:3 resonances with a moderate amount of mismatch. We found this region very stable unless it is close to the 10:3 resonance. We could not, however, reproduce the slits that appear in Gluckstern's (4,0) mode.

6 ANGULAR MOMENTUM

Most K-V particles have nonzero angular momentum. When angular momentum is included in the discussion, we first extend the particle Hamiltonian of Eq. (4.12) in Floquet notations to both the x and y transverse planes:

$$\hat{H}_p = \frac{1}{2R^2}(\hat{x}^2 + \hat{y}^2 + \hat{p}_x^2 + \hat{p}_y^2)$$
$$+ \kappa[\hat{x}^2 + \hat{y}^2 - \ln(\hat{x}^2 + \hat{y}^2)]\,\Theta(\hat{x}^2 + \hat{y}^2 - 1)\,. \quad (6.1)$$

It is preferable to use the circular coordinates $(\hat{r}, \varphi)$ as independent variables; their canonical momenta are, respectively, $\hat{p}_r$ and $\hat{p}_\varphi$. The particle Hamiltonian becomes

$$\hat{H}_p = \frac{1}{2R^2}\left(\hat{r}^2 + \hat{p}_r^2 + \frac{\hat{p}_\varphi^2}{\hat{r}^2}\right) + \kappa(\hat{r}^2 - \ln\hat{r}^2)\,\Theta(\hat{r} - 1)\,, \quad (6.2)$$

where $\hat{r}^2 = \hat{x}^2 + \hat{y}^2$ and

$$\begin{pmatrix} \hat{p}_r \\ \hat{p}_\varphi/\hat{r} \end{pmatrix} = \begin{pmatrix} \cos\varphi & \sin\varphi \\ -\sin\varphi & \cos\varphi \end{pmatrix} \begin{pmatrix} \hat{p}_x \\ \hat{p}_y \end{pmatrix}\,. \quad (6.3)$$

Extending the generating function in Eq. (4.11) to include the x coordinates, it is straightforward to show

$$r = R\hat{r} \quad \text{and} \quad \hat{p}_\varphi = \hat{x}\hat{p}_y - \hat{y}\hat{p}_x = xp_y - yp_x\,. \quad (6.4)$$

Thus $\hat{p}_\varphi$ is the angular momentum of the particle, which is a constant of motion. Since it has the same functional form in both coordinate systems, its overhead accent $\hat{}$ will no longer be necessary. Particles belonging to the unperturbed K-V distribution are therefore subjected to the restriction

$$\hat{r}^2 + \hat{p}_r^2 + \frac{p_\varphi^2}{\hat{r}^2} = 1\,, \quad (6.5)$$

from which we obtain

$$\hat{r}^2 = \frac{1 - \hat{p}_r^2}{2} + \left[\left(\frac{1 - \hat{p}_r^2}{2}\right)^2 - p_\varphi^2\right]^{1/2}\,. \quad (6.6)$$

Thus a K-V particle has an angular momentum restricted by

$$|p_\varphi| \leq \frac{|1 - \hat{p}_r^2|}{2} \leq \frac{1}{2}\,, \quad (6.7)$$

which agrees with the result of Riabko [6] that $2J_r + |p_\varphi| = \frac{1}{2}$, where J_r is the radial action. The equation of motion for the particle radial position inside the beam core is

$$\frac{d^2\hat{r}}{d\psi^2} + \hat{r} - \frac{p_\varphi^2}{\hat{r}^3} = 0\,, \quad (6.8)$$

where the Floquet phase advance $d\psi = d\theta/R^2$ has been used. Notice that this is exactly the same as the envelope equation in Eq (4.7) with $\kappa = 0$. We proved in Sec. 2 that the envelope tune is exactly twice the particle tune when $\kappa \to 0$. Hence, comparing with the equation of motion of a zero-angular-momentum particle in the presence of a mismatched space-charge dominated beam, i.e., Eq. (4.10), we can conclude that the particle radial tune inside the beam
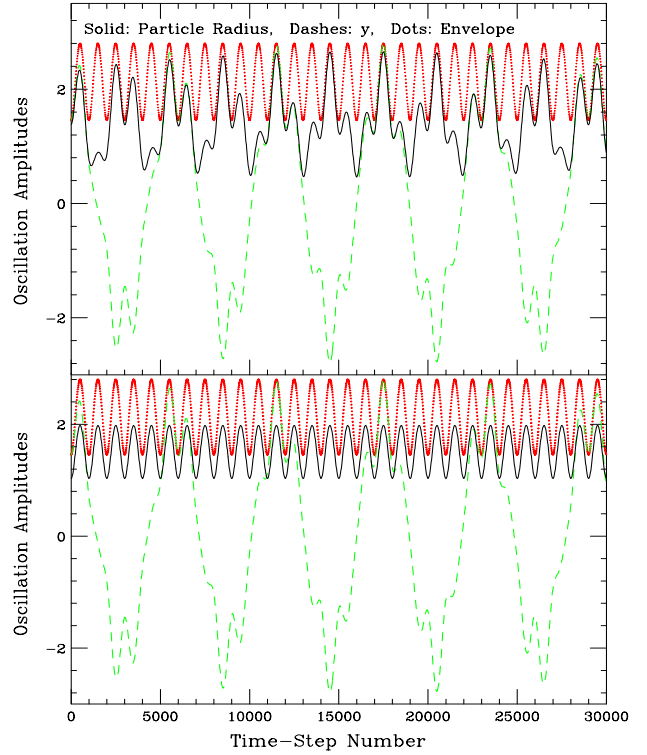

Figure 8: Plots showing the time evolution of the radial position r of a K-V particle in solid inside a beam envelope with nonzero p_φ, mismatch $M = 0.30$ and $\kappa = 2.059$ ($\eta = 0.23$). The evolution y of a $p_\varphi = 0$ particle is shown in dashes. The simulation is at the 6:1 resonance for the $p_\varphi = 0$ particle. Top plot shows the radial motion with $p_\varphi = 0.30$ which is twice as fast as the oscillating motion of a $p_\varphi = 0$ particle. Lower plot is for $p_\varphi = 0.50$. Now the particle radius r is related to the envelope radius R by $r = \sqrt{|p_\varphi|}R = R/\sqrt{2}$, giving a false impression that the radial tune becomes equal to the envelope tune.

core is exactly twice the zero-angular-momentum particle tune for any space charge and mismatch.

Simulations have been performed for the time evolution of the radial motion of a beam particle and then compared with the time evolution of the transverse motion of a particle with zero momentum. One of the simulations is shown in the upper plot of Fig. 8. The particle is a K-V particle with angular momentum $p_\varphi = 0.3$ satisfying the K-V restriction of Eq. (6.6) in a mismatched beam envelope with $M = 0.30$ having a tune depression of $\eta = 0.23$. We see that the shape of oscillations of r shown as solid is very similar to that of y with zero angular momentum shown as dashes. Since r does not go negative, its tune appears to be twice the tune of a zero-angular-momentum particle. This plot was performed near a 6:1 resonance for a zero-angular-momentum particle and it therefore translates into a 3:1 resonance for a nonzero-angular-momentum particle.

It is interesting to point out that as $|p_\varphi| \to \frac{1}{2}$, the humps that exhibit in the time evolution of the radial motion become more pronounced and the time evolution eventually becomes proportional to the envelope oscillation, as is

46

demonstrated in lower plot of Fig. 8. Now the radial tune appears to change suddenly to the envelope tune instead. In fact, this is easy to understand. The equation of motion for the particle radial position is

$$r'' + r = \frac{2\kappa}{R^2}r + \frac{p_\varphi}{r^3} \ . \qquad (6.9)$$

Compared with the envelope equation (4.7), it is evident that $r = \sqrt{|p_\varphi|}R$ is a solution. In the Floquet representation, Eq. (6.8) also reflects such a solution. Thus, it is apparent that the radial tune can assume two different values. This ambiguity can be resolved by investigating the Poincaré surface of section of the radial motion. In the Floquet coordinates, the trajectory is represented by one point, $\hat{r} = \sqrt{|p_\varphi|}$ and $\hat{p}_r = 0$. In the (r, p_r) coordinates, the Poincaré surface of section is also a single point since the phase-space position of the particle is plotted only every envelope period. In fact, from Eq. (6.2), the Hamiltonian in the Floquet representation, it is clear that the solution $\hat{r} = \sqrt{|p_\varphi|}$ is the lowest point of the radial potential. This is the equilibrium solution which, in the case of a Hill's equation, is equivalent to a particle traveling along an orbit passing through the centers of all elements. Therefore, even in this solution, the radial tune is *not* equal to the envelope tune, but remains twice the tune in the Cartesian coordinates.

Because of the above discussion, all the n:m parametric resonances that we studied in Sec. 5 just translate into the $\frac{n}{2}$:m resonances in a r-p_r Poincaré surface of section. As a result, the stability investigation in the previous section should hold even when particles with finite angular momentum are included.

7 CONCLUSIONS

We have now an interpretation of the collective instabilities in the plane of envelope mismatch and tune depression through the particle-beam nonlinear-dynamics approach. Because of the existence of noises of all types in the accelerators and the K-V equation is far from realistic, some particles will diffuse away from the K-V distribution. Although these particles may encounter parametric resonances once outside the beam core, an equilibrium will be reached if these resonances are bounded by invariant tori. It may happen that the island chains outside the beam envelope are so close together that they overlap to form a chaotic sea. When the last invariant torus breaks up, particles leaking out from the core diffuse towards the 2:1 resonance, which is usually much farther away from the beam envelope, to form beam halos. As particles escape from the beam envelope, the beam intensity inside the envelope becomes smaller and the equilibrium radius of the beam core shrinks. Thus more particles will find themselves outside the envelope. As this process continues because no equilibrium can be reached, the beam eventually becomes unstable.

It is possible that many collective instabilities can be explained by the particle-beam nonlinear-dynamics approach. The wakefields of the beam interacting with the particle distribution produce parametric resonances and chaotic regions. Instabilities will be the result of particles trapped inside these resonance islands. The perturbed bunch structure further enhances the wakefields to induce these collective instabilities of the whole beam.

So far, we have been able to explain the results of Gluckstern, *et. al* qualitatively. However, there are differences quantitatively. To the lowest order, the Vlasov equation studied by Gluckstern, *et. al.* does involve the perturbation force induced by the *perturbation* distribution via the Poisson's equation. In our nonlinear-dynamics approach, the particle that escapes from the beam envelope core, always sees the Coulomb force of the *entire unperturbed beam core*, independent of any variation of the core distribution due to the leakage of particles. This is due to the fact that the envelope Hamiltonian and the particle Hamiltonian have been treated separately. This leads to a dependency of the particle equation of motion on the envelope radius, but not the dependency of the equation of motion of the envelope radius on the particle motion. We believe that this is the reason why we have not been able to compute the growth rates of the instabilities. However, an improvement of the present model is nontrivial. This is not the problem of one particle interacting with a beam core in such a way that the perturbation of the beam core can be neglected, because a beam core that is not modified cannot lead to instability of any form. To treat the problem properly, the Hamiltonian will have to include undoubtedly all the beam particles interacting with each other, from which the time evolution of the beam core is to be determined. This appears to be a very complex problem, and this is exactly why the Vlasov equation is introduced. The Vlasov equation is a time-dependent differential equation of the beam core or beam distribution and requires only the single-particle Hamiltonian. Thus, it appears that the Vlasov equation will be unnecessary only when the beam particle distribution does not play an essential role, for example, in the issues of Robinson instability, the two-particle strong head-tail instability, the two-particle chromaticity-driven head-tail instability, etc.

8 REFERENCES

[1] I.M. Kapchinskij and V.V. Vladimirskij, Proc. Int. Conf. on High Energy Accelerators, CERN, Geneva, 1959, p.274.

[2] D.D. Caussyn, *et. al.*, Phys. Rev. **A46**, 7942 (1992); M. Ellison, *et. al.*, Phys. Rev. Lett. **70**, 591 (1993); M. Syphers, *et. al.*, Phys. Rev. Lett. **71**, 720 (1993); D. Li, *et. al.*, Phys. Rev. **E48**, R1638 (1993); DD. Li, *et. al.*, Phys. Rev. **E48**, 3 (1993); H. Huang, *et. al.*, Phys. Rev. **E48**, 4678 (1993); Y. Wang, *et. al.*, Phys. Rev. **E49**, 1610 (1994); Y. Wang, *et. al.*, Phys. Rev. **E49**, 5697 (1994); S.Y. Lee, *et. al.*, Phys. Rev. **E49**, 5717 (1994); M. Ellison, *et. al.*, Phys. Rev. **E50**, 4051 (1994); L.Y. Liu, *et. al.*, Phys. Rev. **E50**, R3344 (1994); D. Li, *et. al.*, Nucl Inst. Meth. **A364**, 205 (1995).

[3] E. Keil and W. Schnell, CERN Report SI/BR/72-5, 1972; D. Boussard, CERN Report Lab II/RF/Int./75-2, 1975.

[4] K.Y. Ng and S.Y. Lee, "Particle-Beam Approach to Collective Instabilities—Application to Space-Charge Dominated Beams," Proc. 16th Advanced ICFA Beam Dynamics Workshop on Nonlinear and Collective Phenomena in Beam Physics, Arcidosso, Sep. 1-5, 1998.

[5] S.Y. Lee and A. Riabko, Phys. Rev. **E51**, 1609 (1995).

[6] Riabko, A., Ellison, M., Kang, X., Lee, S.Y., Li, D., Liu, J.Y., Pei, X., and Wang, L., *Phys. Rev.* **E51**, 3529 (1995).

[7] R.L. Gluckstern, W-H. Cheng, and H. Ye, Phys. Rev. Lett. **75**, 2835 (1995); R.L. Gluckstern, W-H. Cheng, S.S. Kurennoy, and H. Ye, Phys. Rev. **E54**, 6788 (1996).

[8] In Ref. 6, the section on Mathieu instability and stop-band is incorrect.

[9] Forest, E. and Berz, M., LBL Report LBL-25609, ESG-46, 1989.

III. BEAM LOSS

BEAM LOSS WORKING GROUP REPORT

J. Alonso, LBNL, Berkeley CA 94720

Abstract

This Working Group explored the relationship between beam loss and production of radiation in accelerator environments. The radiation protection policies in the US, Japan and at CERN were discussed, as were practical limits on residual radioactivity to allow for hands-on maintenance of accelerator components. Codes and measurements on operating facilities indicate acceptable dose levels if beam loss can be kept to 1 W/m or less. Intercomparison between the three codes presented indicate consistency at the 20-50% level. However, current experimental data are inadequate to provide accurate benchmarking. Fractional beam losses on existing linacs and medium-energy (< 10 GeV) rings are very high, typically > 10%. To maintain the 1 W/m limit, SNS and other new very-high-current machines must impose "uncontrolled" loss budgets around 1 in 10^4, or a factor of 10^3 less. Design considerations are presented that are expected to achieve this level of efficiency.

1 INTRODUCTION

The Beam Loss Working Group was co-chaired by Tom Wangler (LANL), Jie Wei (BNL) and Jose Alonso (LBNL). Participating in the discussion were Weiren Chou, Nikolai Mokhov, Charles Ankenbrandt, Alexandr Drozdhin, Oleg Krivosheev, Craig Moore, and Robert Webber (FNAL); Roland Garoby (CERN); Takeichiro Yokoi, Shinji Machida, and Yoshiharu Mori (KEK); and Hideaki Yokomizo (JAERI). Subsequent contributions were provided by Robert Hardekopf (LANL), Ken Barat and Henry Tran (LBNL), and Marco Silari (CERN).

The format of this report follows pretty much the sequence of discussions and presentations:

a) tolerable beam losses, including both regulatory requirements for radiation exposure, and conditions affecting hands-on maintenance of accelerator components;
b) calculations of radiation levels from given beam losses;
c) measurements and experiments at existing accelerators;
d) operational experience with beam losses at existing facilities; and
e) specific design considerations for controlling beam losses in new high-current accelerators.

Several important conclusions were drawn from these discussions:

a) The complex processes for determining residual radiation levels in accelerator tunnels from beam loss are reasonably well understood, and several good codes have been developed that provide results that are quite consistent. Different accelerator component configurations, and the amount of material close to the beam can result in a surprisingly wide variation in radiation levels, e.g. self shielding from compact lattices with large dipole magnets quite significantly reduces ambient gamma background.
b) Though quite consistent, there is need for benchmarking these codes against real physical measurements. This would significantly enhance, and increase one's confidence in the predictive power of these codes.
c) Existing measurements of radiation levels, while useful, are not complete enough to serve as the above-mentioned benchmarks. In most cases, while radiation levels are well measured, spatial distribution and quantities of particles lost are not established to the same level of accuracy.
d) To allow hands-on maintenance of accelerator components without unreasonable constraints, dose levels should be below 1 mSv/h (measured 30 cm from component surface). This corresponds to beam loss of about 1 W/m along the beam enclosure; this figure is roughly independent of beam energy, for energies above 100 MeV. Thus a greater number of particles can be lost at lower energies, as activation is less efficient. Note: the beam loss goal for the APT linac design was lower, 0.1 W/m above 100 MeV, to provide adequate margin for meeting the high availability requirement.
e) Existing "medium-energy" high-current synchrotrons experience very significant beam losses. Under the best of circumstances, losses well in excess of 10% are observed, in some cases bringing activation levels uncomfortably close to hands-on-maintenance limits. Such loss levels could not be tolerated for new high-current projects such as SNS and muon-production systems; typical specifications for "uncontrolled" beam loss are less than 0.01% for entire accelerator above energies of around 100 MeV, to stay below the 1 W/m level.
f) Such low losses are probably achievable, with careful attention to lattice design, large acceptance/emittance ratios, low tune shifts, proper injection and stacking, efficient collimation, and understanding of halo formation mechanisms.

2 TOLERABLE BEAM LOSS

Beam loss produces radiation. If beam energy is above the Coulomb barrier, prompt radiation will be primarily gamma or neutron, while residual radiation, owing to activation of material close to the accelerator, will be primarily beta and/or gamma. Radiation from activated material will be mainly stationary (non-transportable), however mobility of activated groundwater, as well as air or airborne effluent, can lead to release of radioactivity into the environment.

Tolerable beam loss relates to two criteria:

a) regulatory requirements for radiation levels and release of material to the environment, and
b) allowable levels of residual radioactivity for not impeding maintenance of technical components.

2.1 Regulations and applications in the United States

Requirements for radiation levels in the environment are inferred from 40 CFR 61 (Subpart H—National Emission Standards for Emissions of Radionuclides other than Radon from Department of Energy Facilities), while specific exposure limits within a DOE site are set in 10 CFR 835 (Occupational Radiation Protection).

2.1.1 Regulations – beyond site boundary

The general criteria for both regulations relate to doses accumulated in humans. Thus, for instance, there is no direct specific requirement for a radiation limit beyond the site-boundary, only an indirect one: that a member of the general public must not receive a dose equivalent greater than **100 μSv/yr** (10 mrem/yr) from any release to the environment. Note, this number of 10 mrem/yr derives from 40 CFR 61.92 which relates specifically to dose from emission of radionuclides to the ambient air. In the absence of other specific requirements, designers of a radiation-producing facility should assume that this guideline applies to water-borne activity, as well as to prompt radiation (i.e. fast neutron and gamma) observed at any place beyond the boundary of the site.

For implementing this guideline, one must fold in the probability of an individual being exposed to the radiation produced by the facility. Thus one must determine, for instance, occupancy factors for general public in areas subject to prompt radiation; air-flow patterns for any airborne releases as related to populated zones that might be affected; and potential for ground-water migration into drinking-water supplies.

Tritium release represents a special case. The table below, compiled by Henry Tran from LBNL represents a collection of applicable limits relating to tritium release goals, and provides a very concise set of guidelines that can be used by facility designers.

Standards and Guidance for Tritium
As of 04/30/1999
(Compiled by Henry H. Tran, C.H.P.)

Regulated Media or Type	Regulatory Agency	Referenced Standards, Limits, or Guidances	Comments
Drinking Water	• Nuclear Regulatory Commission (40 CFR Part 141) • Department of Energy (DOE Order 5400.5)	740 Bq/L (20, 000 pCi/L)	This concentration is based on the dose of 40 μSv/yr. It is only applicable to public or private water systems with at least 15 service connections or serving at least 25 persons.
Off-site Liquid Effluents (Ground Water, Creek Water, Surface Water)	• Nuclear Regulatory Commission (40 CFR Part 141) • Nuclear Regulatory Commission (10 CFR Part 20, 1991) • Department of Energy (DOE Order 5400.5)	• Potable Water: 740 Bq/L • Non-potable Water: 37,000 Bq/L	• The 740 Bq/L limit is applied only if off-site liquid effluent is potable and it meets the drinking water definition (see comments in Drinking Water section above). • The 37,000 Bq/L limit is applied to all non-potable off-site liquid effluent. Please note that this is the annual average liquid effluent concentration at <u>the boundary of unrestricted area</u> (fence line).

Sanitary Sewer Water Annual Quantity	Nuclear Regulatory Commission (10 CFR Part 20, 1991)	1.85×10^{11} Bq/yr (5 curies/year)	State of California and East Bay Municipal Utility District (EBMUD) also adopted this federal standard.
Sanitary Sewer Water Concentration	Nuclear Regulatory Commission (10 CFR Part 20, 1991)	3.7×10^5 Bq/L	Monthly average concentration
Annual Air Emission	Environmental Protection Agency (40 CFR Part 61)	100 µSv/yr	This dose limit could be converted to the annual Curie activity using CAP88 computer code. To reach this 100 µSv/yr limit for a Maximally Exposed Individual (MEI) at the Lawrence Hall of Science (LHS), Berkeley Lab must release approximately 10^{14} Bq(3000 Ci)/year.
Ambient Air Concentration at Maximally Exposed Individual Location	Environmental Protection Agency (40 CFR Part 61)	55 Bq/m^3	This is the annual average ambient air concentration at the <u>Maximally Exposed Individual location</u> (for LBNL, this location is the Lawrence Hall of Science). This is not a limit, but a threshold value that initiates stack monitoring & dose modeling requirements.
Ambient Air Concentration at Site Boundary	Nuclear Regulatory Commission (10 CFR Part 20)	3,700 Bq/m^3	Annual average gaseous effluent concentration <u>at the boundary of unrestricted area</u> (fence line).
Vegetation	• Nuclear Regulatory Commission (10 CFR Part 20, 1991) • Department of Energy (DOE Order 5400.5)	1 mSv/yr	There is no specific concentration limit for tritium in vegetation. Limits on residual concentration should be derived from dose limits stated in public radiation protection requirement. (this pathway is bound by the 1 mSv/yr limit).
Soil & Sediment	Environmental Protection Agency (Publication 9285.7-018)	370 Bq/g	This concentration guidance is the risk-based Preliminary Remediation Goal (PRG) used in EPA Superfund site's remedial investigation and feasibility study.
Surface Contamination of Property (all Media) for Unrestricted Release	Department of Energy (DOE Order 5400.5)	1.7 Bq/cm^2	This limit applies to the release of contaminated property for unrestricted use by the public.
Liquid Scintillation & Animal Carcasses	Nuclear Regulatory Commission (10 CFR Part 20, 1991)	1,850 Bq/g	Exempt concentration for disposal of animal carcasses and materials used for liquid scintillation counting.

Packaging and Transportation Exempt Quantities	• Department of Transportation (49 CFR) • Nuclear Regulatory Commission (10 CFR Part 71)	< 75 Bq/g	Exemption from all DOT requirements for any materials containing less than this amount.
Threshold Quantity for Considering Need for an Emergency Plan	Nuclear Regulatory Commission (10 CFR Part 30.72)	7.4×10^{14} Bq (20,000 curies)	Quantities of tritium requiring consideration of the need for an emergency plan for responding to a release.
Radiation from all pathways or media	• Nuclear Regulatory Commission (10 CFR Part 20, 1991) • Department of Energy (DOE Order 5400.5) • International Commission on Radiological Protection (ICRP Publications 26 and 45) • National Council on Radiation Protection and Measurements (NCRP Report No. 91)	1 mSv/yr	This dose limit includes both external and internal exposures.

Reference: Bernard Shleien, The Health Physics and Radiological Health Handbook, Scinta Inc, Silver Spring, MD, 1992.

Note: 1 curie (Ci) = 3.7×10^{10} becquerels (Bq)

1 becquerel = 1 disintegration/second

1 sievert (Sv) = 100 rem

2.1.2 Regulations – within site boundary

10 CFR 835 provides the basic guidelines for exposure limits. Fully-trained and qualified radiation workers shall not receive a total effective dose greater than **50 mSv** (5 rem) **per year** (835.202 (a) (1)). Total occupational exposure to a fetus shall be less than **5 mSv** (835.206 (a)), and minors shall receive less than **1 mSv/yr** (835.207). A member of the general public (anybody not fully trained or qualified as a radiation worker) entering a controlled area is limited to less than **1 mSv/yr** (835.208).

Within these limits, all DOE facilities are required to establish an ALARA (As Low As Reasonably Achievable) policy, that generally calls for lower exposure levels than those mandated by 10 CFR 835. In most laboratories, for instance, the 50 mSv limit has been reduced to 20 or even 10 mSv. In addition, DOE Order 420.2 (Safety of Accelerator Facilities) states that "The contractor must approve and implement a written statement of the shielding policy for … radiation." (DOE O 420.2 Att 1 (h)). Design guidelines are typically set in these documents so that expected radiation exposure levels for on-site staff are considerably below mandated levels.

Again, translating these exposure doses to ambient radiation levels produced by the accelerator require folding in occupancy factors. However, this is easier to do in the case of a well-defined work environment where working hours at specific occupied areas can be well estimated, and relationship between radiation sources, shielding and geometry can be determined. For instance, shielding and work area locations can be specified so that a technician working 2000 hours per year should not have his primary work area in a background greater than a few µSv/h.

2.1.3 Application – shielding

Initial facility designs usually implement shielding thickness sufficient for completely passive protection of personnel and environment. The DOE Accelerator Safety Order (420.2) requires definition of an "Accelerator Safety Envelope" (ASE) defining the maximum operating conditions expected, thus providing for the maximum levels that shielding must be designed to.

For cost-savings reasons, there is usually little margin between the shielding design and the maximum operating conditions defined in the ASE, so it is not unusual following a number of years of operation and improvements that significantly higher performance levels are achieved for the facility. As a consequence, it is not unusual for the installed shielding to be inadequate to meet the requirements imposed by the improved performance. Establishing a new ASE, and getting

approval for operation through the normal Readiness Review process requires mitigation of any shielding shortfalls. This can be achieved either through increasing shielding thickness or adding heavier material (e.g. steel); by implementation of active limits (dose limiting monitors in critical areas that can regulate accelerator output); or by improving beam performance in the accelerator so that beam loss (hence radiation) is reduced.

Needless to say, hindsight usually shows that the investment in more shielding at the initial construction of a new facility pays handsome dividends.

However, as is the theme of this Workshop, the reduction of beam loss is the route to be preferred for important reasons: in addition to reducing the amount of radiation that must be shielded, the residual background level is reduced (making for easier hands-on maintenance) and there will be less radiation damage to components increasing overall system lifetimes.

2.1.4 Application – hands-on maintenance

Hands-on maintenance of accelerator equipment is obviously highly desirable: to allow for most effective trouble-shooting, to ensure quickest repair and thus minimizing down-time and maximizing overall system availability. Criteria need to be defined for radiation limits where such maintenance is, or is no longer possible.

Again, the overall limits are set by 10 CFR 835, but these relate to exposures to an individual, not to actual radiation levels in an accelerator tunnel. Thus, it is up to each facility to define its own guidelines for such operation.

As an example, one can take the guidelines established for LANSCE at Los Alamos National Laboratory (provided by T. Wangler) and summarized in the table below.

Maintenance Restrictions in Radiation Fields

Level of Activation	Type of Maintenance
< 100 µSv/h	Unconstrained "hands-on" maintenance. Note: No more than 200 hours/year for any one worker (to stay below 20 mSv/yr)
100 µSv/h – 1 mSv/h	Hands-on maintenance; limited access time
1 mSv/h – 100 mSv/h	Hands-on maintenance, strictly controlled; very limited access time
> 100 mSv/h	Remote maintenance required.

Exposure levels can be mitigated by several techniques: by use of local, movable shielding emplaced to block radiation from areas not being directly worked on; by waiting the maximum amount of time possible for cooling of short-lived isotopes; and by design of equipment for maximum ease of access and maintenance, and appropriate tools to allow for quick work at a reasonable distance (long-handles).

Some forethought during initial design and construction can again yield handsome dividends in this area: providing tunnels large enough to allow uncluttered, easy access and suitable space for portable shielding and long-reach tools; and good crane access to allow for rapid movement of equipment and portable shielding.

2.2 Regulations and applications in Japan

Statutory requirements in Japan are approximately equivalent to those in the US. However, the design criteria imposed on projects, and performance standards for operating facilities require margins for radiation levels substantially lower than encountered in the US.

Yokomizo provided the following information:

- Soil and groundwater must see doses at the outside surface of the concrete surrounding the accelerator tunnel of less than 1.1 µSv/h (if distributed along the length of the accelerator, or 11 µSv/h if concentrated at a point). For the projected losses of 1 W/m along the length of the accelerating structure, this implies a concrete wall thickness of 1.7 to 2.2 meters of concrete to keep the radiation levels on the outside surface of the concrete at or below the legal requirements.
- Radiation measured at the ground surface must be less than 0.2 µSv/h. For typical accelerator tunnels, this can translate into roof thickness of as much as 4 meters of concrete.
- Contribution to site-boundary radiation from the accelerator must be less than 30 µSv/yr (3 mrem/yr).
- Maximum field for which unrestricted access is allowed for trained radiation workers is 6 µSv/h (0.6 mrem/h).
- Guidelines for radiation exposure to workers who must work in radiation environments are that total dose accumulated in one week must be less than 0.3 mSv (<30 mrem/wk).

2.3 Regulations and applications at CERN

M Silari contributed the following section relating to radiation protection at CERN.

CERN radiation protection policy stipulates that exposure to ionizing radiation to people, and the radiological effects on the environment shall be as low as reasonably achievable (ALARA). This policy is in line with the radiation protection regulations in force in the two Host States (France and Switzerland) and with the recommendations of established international bodies such as the International Commission on Radiological Protection (ICRP). The general principles of CERN policy, personnel protection, classification of working areas, the rules to handle radioactive material and sources,

and the protection of the environment are addressed in the CERN Radiation Safety Manual (CERN, Safety Code F, 1996.)

2.3.1 Classification of areas and dose-rate limits

Certain parts of the fenced land belonging to CERN are considered to be Designated Areas. Outside these areas, the dose must be kept below the limit of public exposure (1 mSv/yr). Thus persons who spend their entire working time outside Designated Areas cannot be regarded as being occupationally exposed.

Designated Areas are either considered as Supervised or Controlled areas. The former are areas in which working conditions are constantly kept under review but no special procedures are required. Those employed there are unlikely to receive effective doses above 1 mSv/yr (again, the annual exposure limit to a member of the general public) in the course of their normal work, taking account of their working hours. In Controlled Areas normal working conditions will require persons to follow well-established procedures and to have been given specific information and training concerning radiation exposures, and so to have been designated as "radiation workers." In the normal course of their work, such persons are liable to receive an effective dose greater than 1 mSv/yr, i.e. an effective dose greater than the limit for persons who are not individually monitored.

In order of increasing severity of control, Controlled Radiation Areas are classified as:

- **Simple controlled areas**, where persons working in the area must carry personal monitors (film-badges), but where all necessary precautions are taken to ensure that normal work over a year will not give rise to an effective dose greater than the limit for persons being exposed to radiation in the course of their work (20 mSv over 12 months).
- **Limited-stay areas**, where persons working in the area must carry personal monitors (film-badges) and where permanent residence (i.e. office or work bench) in the area is not permitted. An Operational Dosimetry System (e.g, quartz fibre dosimeters, electronic dosimeters, etc. carried by each worker) is necessary to control the rate of accumulation of dose during work in such areas.
- **High radiation areas**, where dose rates may reach levels (2 mSv/h) such that doses up to the annual limit could be received in less than ten hours work in localised zones inside the area. No visitors can be allowed and strict access control must be maintained.
- **Prohibited areas**, where dose rates may reach levels (100 mSv/h) such that the annual dose limit could be reached in less than ten minutes' work in localised zones inside the area. Access can only be authorised under very special circumstances.

The classification of the preceding areas is a function of the dose rate and the envisaged occupancy times. There is one other type of area classification, that of an Exclusion Area where, because of the risk of high levels of radiation during circumstances such as beam operation, access is excluded by an integral perimeter fence and an interlock system.

One Design Constraint for all accelerator installations is that the dose rate in an accessible area from a continuous loss under the worst credible circumstances should never exceed 100 mSv/h. Above this limit, access must not be possible because the area becomes a Prohibited Radiation Area.

Experience has shown that annual doses remain well below the annual dose limits if one takes as a Design Constraint that the dose rate in a Simple Controlled Area, averaged over 24 hours for normal, expected loss situations, is kept lower than 10 µSv/h. The Design Constraints for other classes of areas where people are likely to work permanently, are summarized in the table below. It should be noted that these dose-rate constraints are supplemented by installing radiation monitoring systems set to warn operators if levels exceed three times the design level during actual operation. If levels exceed ten times the design constraints the offending operation must be stopped. This allows the shielding to be improved or the area classification hardened.

Design dose-rates outside shielding

Area classification	Dose rate
Normal loss	
Simple Controlled	< 10 µSv/h
Supervised	< 1 µSv/h
Non-designated	< 100 nSv/h
Maximum loss rate Any area	< 100 mSv/h

One then has to reach a balance between these different constraints. For example, if in a Simple Controlled Area the shielding attenuation provided meets the constraint for a full-loss, it will automatically meet the normal dose-rate constraint of 10 µSv/h if the loss is less than 0.01 % of the full beam. For expected losses above this level, extra shielding is needed. Even at that level of expected loss, interlocked monitors must be provided.

2.3.2 Protection of the environment

CERN pays a lot of attention to protect persons living in the vicinity of the Organisation site against ionizing radiation. In all circumstances the regulations and standards decreed by the Host States must be guaranteed by CERN on the site and outside its boundaries. Protective measures are taken against the various sources

of radiation hazards, namely direct exposure from radiation escaping from the site, radioactive releases (gaseous and liquid) connected with the operation of the accelerators, the disposal of radioactive waste (liquid and solid), the transport and dispatch of radioactive materials, and the radioactive emissions in the event of incidents or accidents.

The value of ambient dose equivalent caused by ionizing radiation or radioactivity emitted by CERN beyond the boundaries of its site must not exceed 1.5 mSv per year. The effective dose resulting from CERN activities and received by any person living or working outside the Organization's boundaries must not exceed 0.3 mSv per year. This limit includes both external and internal exposure, the latter resulting from the intake of radioactive releases. These emissions must be limited in such a way that the annual effective dose from these releases for persons living outside the Organization's boundaries does not exceed 0.2 mSv.

3 BEAM LOSS – ACTIVATION CALCULATIONS

Radiation associated with accelerators can be divided into two distinct categories: prompt and residual. Both are clearly dependent on beam loss, but the former drives shielding requirements mainly for fast neutrons, while the latter relates to radioactivity levels in accelerator tunnels after the accelerator has been turned off that affect personnel access and maintenance procedures.

The primary emphasis in this Working Group was the evaluation of residual radiation levels in accelerator tunnels. Three different code suites were presented for converting beam loss into activation levels, these being based on: LAHET, developed at Los Alamos; HETC/MCNP/ORIHET at Oak Ridge and MARS at FNAL. Note, these three approaches are also used for assessing overall shielding requirements, and prompt radiation fields.

The basic result from all three calculational approaches is that if beam loss can be kept to below 1 watt per meter along the accelerator length, radiation levels will be adequately low to allow for hands-on maintenance. The constant "power" level roughly folds in the energy-dependence of radioactive product yield, and hence the tolerance to higher number of particles lost at lower energies. Note, however, that for accelerators producing megawatt beams, "allowed" beam losses are parts in a million or less per meter of length.

In comparing results from each calculational method, difficulty in performing direct intercomparisons was noted because of the lack of a "standard" parameter set. In order to facilitate such intercomparisons, such a standard set was proposed for adoption:

Dose rate determination:

- Following 100 days of steady-state operation
- Measured 30 cm from machine component surface
- After a 4-hour cool-down time

Several rules of thumb were presented to facilitate intercomparisons, and to use as practical guides for assessing radiation environments:

- Sullivan formula for time-dependence of dose at a given location:

$$D = D_O * \ln (1 + T_i/T_c)$$

Where D is dose, D_o is the benchmark dose, T_i is the irradiation time, and T_c the cooldown time. Formula is valid for copper and iron, and where T_i is greater than 30 days and T_c greater than 1 hour. This formula provides a guideline for the amount of time required to allow structures to cool down to levels appropriate for maintenance.

- The decrease over time of radiation fields is roughly independent of beam energy, so cooldown time for boosters or higher-energy accelerators will be about the same.
- Dose rates scale roughly as 1/r, the radial distance from the beam center.

3.1 Calculation results (for "standard conditions" and 1 W/m beam loss)

3.1.1 Oak Ridge: 0.8 mSv/h

Per Santoro et al (R. Santoro, J. Johnson J. Drishler, "Dose Rate Inside the SNS Linac Tunnel from Activation of the Magnet Copper Conductor and the Concrete Wall", SNS Technical Note SNS/TSR-0130, 3/99), radiation levels following 100 days of irradiation and 4 hours cooldown, at a distance of 50 cm from the edge of a copper block in which 1 nA of 1 GeV proton beam is stopped, are calculated to be 0.5 mSv/h. This scales to 0.8 mSv/h at 30 cm, using the above 1/r guideline. Again, HETC and MCNP were used to calculate neutron fluxes and overall nuclide production; ORIHET produced the gamma spectra and ANSIN the radiation fields resulting from the assumed geometry. This geometry had a 7.5 cm radius, 1 meter long copper cylinder stopping the beam, sitting at the center of a 2.3 meter radius concrete tunnel. Although activation of the concrete is calculated, radiation fields are dominated by the copper.

3.1.2 Los Alamos: 0.9 mSv/h

Per Fikani (M. Fikani, "Activation Dose Rates in the Accelerator Tunnel -2", APT memo PPO-TPO-mem-01551, 11/98), radiation levels are calculated via LAHET code suite in a periodic structure consisting of quadrupoles between superconducting cavities. The

quadrupoles are assumed to be primary sources of beam loss, and the 0.9 mSv/h value is calculated in proximity to these magnets. As such it is then an overestimate of average radiation field, by about a factor of two.

3.1.3 Fermilab:

> 0.9 to 2 mSv/h, areas with little self-shielding
> 0.005 to 0.01 mSv/h close to ring magnets

Krivosheev and Mokhov (reported this conference) presented calculations using the MARS suite of codes for the FNAL 8 GeV Booster, and for the proposed 3 GeV preBooster and 16 GeV Booster for the Proton Driver project. Remarkable is the wide variation in the calculated radiation levels, dependent on the particular accelerator configuration. In areas close to large bending magnets, the steel provides a great deal of self-shielding, dropping radiation levels by a large factor. Note, the numbers given are scaled according to the above guidelines, calculations were performed for dose rates at magnet surfaces. This scaling (by 1/r) is probably inaccurate as radiation field will be determined by line-of-sight from more highly activated components as one moves away from the magnet surface.

Note, the Oak Ridge and Los Alamos cases were calculated for basic linac configurations, without large bulks of steel that contribute so substantially to self-shielding. On the whole, the consistent agreement, for similar arrangements of material, between the three different methods is quite remarkable, and it is clear that any differences are far outweighed by specific differences in configuration of accelerator components in the tunnel.

3.2 Benchmarking

Agreement between different calculations is of course quite encouraging, however it is important to verify that these calculations are consistent with real measurements. As will be seen in the next section, accurate experimental measurements that could be used for such benchmarking are not available. Nonetheless, measurements that have been made are not inconsistent with the above calculations.

4 BEAM LOSS – ACTIVATION MEASUREMENTS

Surveys of radiation levels in accelerator tunnels are routinely performed after a shutdown and prior to allowing personnel access. These measurements are performed for personnel safety and cannot as such be used as controlled experiments with data readily suitable for the above-stated benchmarking purposes. The uncertainty lies in the lack of a clear quantitative determination of the source term, namely the spatial and temporal profile of beam loss along the accelerator or transport structure.

Work was reported at this Workshop from Los Alamos and Fermilab of attempts to correlate activity measurements with quantitative beam-loss determinations, but these efforts have not yet yielded the level of data needed for a fully quantitative comparison with code calculations.

An instrumented experimental setup is being developed on the FNAL Booster, with extracted beam running into a steel cylinder stopper, in which controlled gamma measurements can be performed following known particle fluences stopped in the steel. Measurements with this system could provide the required benchmarking data. The main issue with this experiment will be to accumulate sufficient running time to properly simulate actual conditions in a normally-operating accelerator schedule.

Note, a number of "shielding experiments" have been performed at various sites over the years, for the purpose of benchmarking codes and assessing shielding needs for new facilities. These efforts have mainly concentrated on containment of prompt radiation. The work described in this section refers mainly to measurements related to residual radioactivity in the tunnels that affect maintenance procedures.

4.1 LANSCE Linac

Activation profiles along the length of the linac have been made, which clearly identify the areas of beam loss. A figure is shown in Hardekopf's contribution to this Workshop's proceedings. These measurements have proven very valuable in assessing beam-dynamics design issues, and the importance of matching beam parameters with transport lattice optics. As could be anticipated, losses occur primarily in the vicinity of quadrupole magnets, where beam envelopes are large, and in areas where mismatched beam conditions occur.

A model for the beam loss profile was developed by G. Lawrence, in which he folded onto the measured activation levels the energy dependence of neutron-production for protons striking steel and copper, and used the total measured beam loss in the accelerator (approx. 400 nA for full-power – 1.2 mA 800 MeV operation) as normalization to obtain a quantitative beam-loss profile along the accelerator. Results, as reported by Hardekopf, are between 0.25 (at high energies) and 0.6 (at the highest loss points around 100-200 MeV) mSv/h per W/m of beam loss. Note, the activation measurements were made in accordance with the "standard" conditions described in the previous section.

While qualitative agreement is good, the disparity along the length of the linac, and the probable uncertainty in measured beam loss (less than a part in 10^3) make the authors state that, "these measurements… do not lead to an accurate experimental calibration… of the Monte-Carlo calculations." [Hardekopf, these proceedings].

4.2 LANSCE – PSR

Thorough radiation surveys around the PSR have been taken, with measured levels ranging over a factor of 100 (1 to 100 mSv/h) at different points in the ring. Known points of very high loss are the injection and extraction regions.

Evaluations by Fitzgerald [again reported by Hardekopf] point out the uncertainty of ascribing the distribution of beam loss around the ring, and depending on the model employed return values of activity levels between 1 and 2 mSv/h per W/m, for again the "standard" conditions. While qualitatively close to the calculations, the factor of two uncertainty renders these measurements again not suitable for detailed quantitative comparisons.

4.3 FNAL Linac

Activity plots along the linac length were reported by Webber showing hot spots at several points, corresponding to DTL-CCL matching areas and places where possible misalignments cause higher beam loss. However, except for stating that typical efficiency of beam transport from 10 MeV to 400 MeV is around 95% (implying approx. 25 nA lost along the linac length), no report was given of a quantitative comparison between beam loss and activation level. Because of the overall low duty factor of this linac, the activity levels have not been considered as a serious problem to hands-on maintenance that would require mitigation beyond normal precautions.

4.4 FNAL Booster

Webber also reported measurements around the 8 GeV Booster. Considerable work has been done in this area, however the primary concerns have been with the adequacy of shielding against prompt radiation as currents have increased in the Booster.

Tunnel activity surveys have been taken as well, but again have not been correlated with beam losses to determine benchmark data.

In principle, however, it might be possible to obtain a reasonably good data set from the Booster. An extensive survey of prompt radiation levels above the shielding have been taken, which can provide the loss patterns around the ring, after extrapolation back through the shielding material at each location. As reasonably good measurements have been made of beam loss, from normal beam diagnostics (and as losses are large enough to be measurable within the accuracy of these instruments), a good normalization factor could be developed for the prompt loss pattern. It is clear, however, that developing a good data set via this technique would involve considerable effort.

Still the best approach for benchmarking would be a dedicated experiment. Such a prospect was presented at the Workshop: a block of steel placed at an auxiliary extraction point, in an area where suitable monitoring instrumentation can be located. Under controlled conditions, residual radiation fields around the stopping point can be measured, with a very well-defined source term. The issue, however, will be to be able to accumulate a sufficient amount of running time to simulate actual accelerator operating conditions. Best would be to be able to continuously accumulate beam on this target in a parasitic mode during the normal operating schedule. Meaningful benchmarking would require at least three months of continuous operation in a consistent, reproducible mode.

5 BEAM LOSSES AT OPERATING HIGH-CURRENT RINGS

Accelerator technology is pushing in the direction of higher and higher intensity beams. Beam loss becomes an increasingly important element in the operation of these machines, due to activation or downright destruction of components, with the associated problems of limited access for maintenance, and operational delays.

The table below lists currently-operating high-current rings, highlighting principal parameters and in particular, beam loss experience. Most rings are rapid-cycling synchrotrons, they are used as boosters or short-pulse neutron sources. All have single-turn extraction which tends to be very efficient except that kicker magnets and septa can become aperture restrictions and sources of beam loss during capture. All employ multi-turn injection, all but one using foil stripping of H⁻. All are pushing against space-charge limit and have relatively high tune shifts. Losses almost all occur during the injection and capture process; for rings injected at low energies this beam loss is much less of a problem than it is for higher energy injection scenarios.

The losses given are what should be called "uncontrolled" losses, that is beam that contributes to activation of the machine and its components. Foil stripping is not a completely efficient process, for instance a fraction of the beam can emerge as neutral hydrogen. However, it is possible to design the injection system to channel any unstripped beam into a dump. So although beam loss is inevitable, one can make a distinction between "controlled" and "uncontrolled" loss. The sum of the two is the difference between beam presented to the injection system and the beam emerging into the extraction channel, while only the "uncontrolled" loss actually contributes to radioactivity levels that affect maintainability.

Currently-Operating High Current Rings

Machine	Type	E(inj)	E(extr)	ΔQs	Inj type	#turns	Typ ppp	Loss
ISIS	RCS	70	800	0.4	foil	300	1.6 e 13	10%
PSR	Accum	800	800	0.2	foil	2300	3.1 e 13	0.3%
KEK-PSB	RCS	40	500	0.23	foil	50	2 e 12	10%
FNAL-B	RCS	400	8000	0.4	foil	15	2 e 12	30%
AGS-B	RCS	200	1900	0.5	foil	200	1.5 e 13	28%
IPNS	RCS	50	450	0.25	foil	140	3 e 12	17%
CERN-PSB	RCS	50	1400	0.4	septum	15/ring	1e 13/ring	50%

In machines with a relatively low repetition rate (hence lower average output power), substantial losses can be tolerated without affecting maintainability. Synchrotrons with lower energy injection can also support higher losses as the activation efficiency is not as high. However, in machines such as the PSR, with high injection energy and high rep rate (20Hz), beam loss has a substantially greater impact. For this reason, even for the very low uncontrolled loss percentage, radiation levels are very high in several parts of the machine, and a cooldown period must be planned prior to personnel access for maintenance. Even though losses are substantially higher at other machines listed in the table, none have serious maintainability problems.

In coming generations of machines: SNS, ESS, various muon and neutrino factories; average currents must exceed present-day performances by substantial factors. Control of beam losses rises to an extremely high level of importance. The following section describes strategies that are being employed in design of these next-generation facilities to mitigate this problem.

6 DESIGN CONSIDERATIONS FOR MINIMIZING BEAM LOSS

Addressing accelerator physics and design issues associated with high intensity beams has been a dominant theme in recent years. In fact, designing accelerators to minimize beam loss has emerged as perhaps the leading paradigm in the field today. That this is now possible has been facilitated by development of significantly better understanding of the dynamics of high-intensity beams, including halo formation, as well as more realistic simulation codes capable of accurate predictions of component and overall system behavior.

The following section details specific design considerations to minimize beam loss.

6.1 Beam-loss driven design considerations: rings

J. Wei presented guidelines being employed in the design of the SNS ring to control beam loss. Note, the design goal for the SNS ring is for uncontrolled beam loss at a level less than a part in ten thousand, or 0.01%.

a) Acceptance to emittance ratio as large as possible (3 or larger). A very large dynamic aperture allows for some degree of misalignment or beam missteering, but also provides room to contain beam tails that might develop. Halo formation in rings is still under active study, the best mitigation is to provide sufficient space to accommodate whatever growth that might occur.

b) Minimize tune spread. Keeping tune shifts low, by providing large apertures and lower beam densities, and a high bunching factor, minimizes chance of beam growth and resonances.

c) Large momentum acceptance. Provides adequate phase space for capture and subsequent longitudinal motion of the beam. Adequate RF voltage, with dual-harmonic capabilities must be provided.

d) Injection scheme optimization. The physics of H⁻ injection is very complex. Optimizing the foil thickness, for instance, requires balancing incomplete stripping (leaving a not-inconsequential portion of the beam in an excited neutral state that could be subsequently Lorentz-stripped, leading to unacceptable halo and loss), and excess heating and nuclear reactions if the foil is too thick. Painting schemes also must minimize the number of times the circulating proton beam encounters the foil on subsequent turns. A key element of this optimization is to ensure that as much as possible of the incident beam not successfully injected into the ring, is efficiently transported into a dump well separated from the ring.

e) Careful attention to instability control. This involves impedance control, tapering beampipes, and controlling electron production in the ring via, for instance, surface coatings. The full-intensity beam has a potential well several kilovolts deep, capable of capturing any electron free inside the vacuum system. The PSR has experienced severe instabilities, now attributed to the two-stream instability mechanism.

f) Efficient collimation. Maintainability is affected by activation from "uncontrolled" beam loss around the ring. If aperture restrictions are introduced in the form of well-designed collimators, capable of absorbing the beam power and of containing neutrons produced by stopping particles and hence preventing activation in areas where personnel access is desired, then beam loss has less serious consequences. Beam lost in such collimators can be considered as "controlled."

g) Maintaining a clean rf gap. Particles injected outside of the rf bucket, or that leak out of it, can be lost through large-amplitude excursions. In addition, even a very low (<1%) charge density between beam bunches is sufficient to maintain enough of a potential well to prevent dissipation of electrons accumulated during the passage of the bunches. It is the buildup of this population of electrons that is thought to lead to the two-stream instability. Mechanisms for ensuring a clean gap include: high-quality chopping of injected beam; adequate rf voltage to prevent leakage; an active gap-cleaning system involving, for instance, repetitive kicks applied during passage of gap region that drive any particles in the gap into the collimation system.

6.2 Beam-loss considerations: linacs

Experience at LANSCE has led to development of several considerations for optimizing high-current linac design.

a) Good matching. Linacs typically consist of different types of structures, each optimized for a particular beam velocity range. Care must be taken to ensure proper optical matching of beam in the transition regions between the different types of structures.

b) Halo mitigation: adequate aperture. Good understanding is emerging now on the dynamics of halo generation and growth in linacs. As these lead to formation of tails on the beam distribution extending substantially out from the main beam core, best mitigation is to ensure sufficient aperture in the linac structure to accommodate these tails. In addition, it is necessary to control as best as possible any emittance growth that might occur in the linac, thus preserving available aperture.

c) Good vacuum. H$^-$ stripping is a significant source of beam loss if vacuum is not kept below the 10^{-6} pascal ($\approx 10^{-8}$ torr) range (10^{-7} torr if hydrogen is the only constituent).

6.3 Practical considerations

Most all of the above guidelines add cost to the system. Large apertures, high vacuum, extensive and expensive collimation, all come at a not inconsiderable price. Very careful optimization must be performed to determine where to place scarce resources. However, designers and managers must realize the impact of cutting corners in the areas of beam-loss control, as operational availability, and component reliability and lifetime can be very directly affected. It should always be remembered that the cost of retrofitting is almost always very substantially higher than the cost of implementing suitably conservative designs from the start.

BEAM LOSS AND ACTIVATION AT LANSCE AND SNS

Robert A. Hardekopf, Los Alamos National Laboratory, Los Alamos, NM

Abstract

This paper reviews the sources of beam loss in the Los Alamos Neutron Science Center (LANSCE) 800-MeV linac and Proton Storage Ring (PSR) and the activation caused by this loss. The losses and resulting activation at LANSCE are compared with the design of the Spallation Neutron Source (SNS) linac to develop an understanding of SNS activation limits. Theoretical activation calculations using Monte-Carlo codes for the SNS linac and the Accelerator Production of Tritium (APT) linac are compared with experimental values at LANSCE to develop confidence in the calculations. Limits for personnel exposure during maintenance periods that are used at LANSCE are reviewed and applied to machine availability requirements.

1 INTRODUCTION

High-intensity accelerators are often limited by beam losses that cause radiation to exceed limits outside the accelerator vault or that cause activation of the accelerating structures. In the former case, proper shielding combined with radiation monitoring and protection systems are important. In the latter case, it is often the requirement for maintenance on accelerator systems in the tunnel or vault that limits beam loss. High activation levels might require either remote-handling equipment that adds to the facility cost, or long cool-down periods before maintenance that reduce availability. The designers of high-intensity accelerators try to avoid both of these situations by a detailed understanding of beam loss mechanisms and by incorporating design features that avoid beam losses. Since such features often add to the accelerator cost, it is important to have a clear understanding of the trade-offs between cost and availability. The purpose of this paper is to review operating experience at the LANSCE proton accelerator and PSR accumulator ring to gain confidence in activation calculations for new high-intensity accelerators, particularly the Spallation Neutron Source (SNS) linac, which is currently in design [1,2]. For reference, Fig. 1 shows the overall layout of the LANSCE 800-Mev linac, which accelerates both protons and H$^-$ ions.
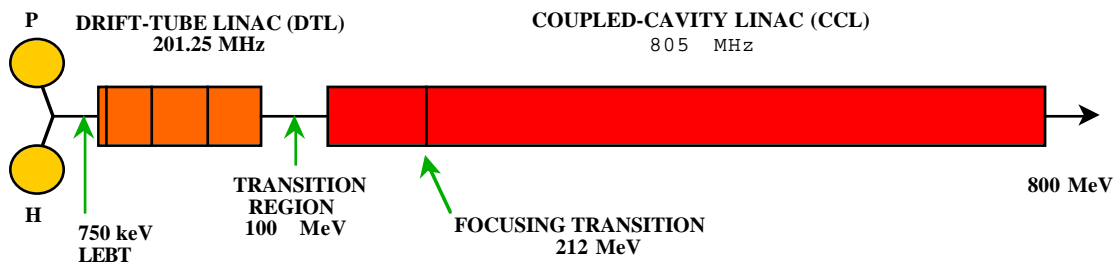
Fig. 1. Schematic of the LANSCE 800-MeV Linac

2 LANSCE AND SNS PARAMETERS

The relevant factors comparing the two linear accelerators are presented in Table 1. It is important to note that LANSCE primarily operates with protons in its high-intensity (1 MW) mode, while SNS will operate only with H$^-$ and at a factor of two higher power (2 MW). Since one of the major potential causes of beam loss is the stripping of H$^-$ ions, this difference, as well as beam emittance differences and other design parameters, must be taken into account in any comparison. One way to make the comparison is to understand and predict the sources of beam loss at LANSCE and then apply the same codes and activation calibrations to SNS. This is the approach we take in this paper as follows:

a) Predict beam loss from models.
b) Relate beam loss to activation.
c) Compare calculations with experiment.
d) Set limits based on maintenance requirements.

3 BEAM LOSS MECHANISMS

A thorough discussion of beam loss mechanisms is beyond the scope of this paper. There are discussions in the linac section of the SNS Conceptual Design Review (CDR) document [3] and in references contained therein. A discussion of losses from beam halo in linacs is found in Chap. 9.14 of Wangler's book [4]. The major beam loss mechanisms that must be considered for the SNS linac are discussed below

Table 1. LANSCE & SNS Linac Parameters

PARAMETER	LANSCE	SNS
Energy (MeV)	800	1000
Average current (mA)	1	2
Peak current (mA)	17	56
Pulse repetition rate (Hz)	120	60
Pulse length (ms)	~1	~1
Chopping transmission (%)	100 for H^+	65
Micropulse frequency (MHz)	201	402
Particles per micropulse	5×10^8	8×10^8
Frequency transition (MHz)	201-805	402-805
H^+ trans. emit. (π-mm-mr)	0.4	-
H^- trans. emit. (π-mm-mr)	1.6	0.4
CCL lattice period ($\beta\lambda$)	17 - 34	12
CCL bore radius (cm)	1.9	2.0
Aperture to beam rms ratio	4 – 7	9 – 14
Average gradient (MeV/m)	~1	~2

a) *Transverse losses*: These occur on limiting apertures (usually at the quadrupole focusing magnets). Even assuming a good lattice design, losses can still occur because of mismatches at transitions, misalignments, missteering, poor input emittance, and halo formation from space charge or other non-linear effects.

b) *Longitudinal losses:* These occur when beam escapes from the RF-accelerating bucket. Losses can occur because of tails in the longitudinal phase space, unmatched frequency transitions, phase and amplitude errors of the RF cavities, and beam turn-on transients.

c) *Gas stripping:* This can occur with H^- beams if there is inadequate vacuum in the beamline.

d) *Magnetic stripping:* This can occur with H^- beams in high-field bending magnets or in the high-field regions of focusing magnets.

Other sources of potential beam loss, such as Coulomb scattering from residual gas molecules or intra-beam scattering have also been evaluated [3], but they are negligible compared with the major sources listed above.

3.1 Linac Aperture Considerations

Multi-particle simulations are used to estimate beam losses that may occur from scraping on a limiting aperture in the linac. A typical plot is shown in Fig. 2, where the rms beam size is compared with the maximum beam extent when several sources of quadrupole-alignment errors and RF-field errors are simulated [5]. These simulations usually include first-order space charge effects that can also lead to halo growth. Conclusions from such error studies can be used to set the linac aperture to provide a reasonable safety margin, as listed in Table 1. However,

operational factors such as larger-than-expected beam emittance, accuracy of beam diagnostics, number and effectiveness of steerers, turn-on transients, and operator
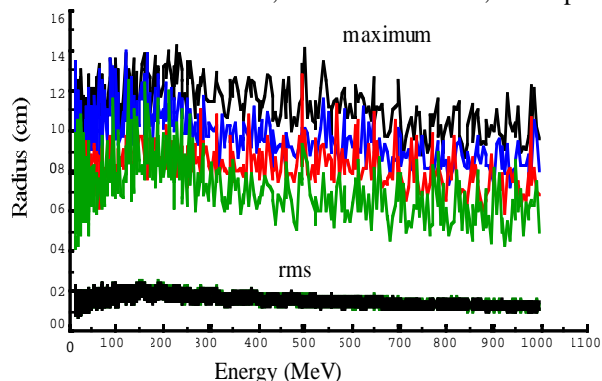
Fig. 2. Simulations of SNS linac beam with sets of random errors and no mismatch [5].

skill must also be considered. If mismatches in either transverse or longitudinal focusing occur, as in the case of LANSCE, aperture losses may occur. Fig. 3 shows activation measured at LANSCE following a 3-month run period. Garnett et al. [6] and Merrill and Rybarcyk. [7] have compared these activations with particle simulations that include the known mismatches at LANSCE and find good qualitative agreement with the simulations as shown in Fig. 3. However, no losses are predicted at the high-energy end of the linac where activation levels are still about 4 mrem/hr.
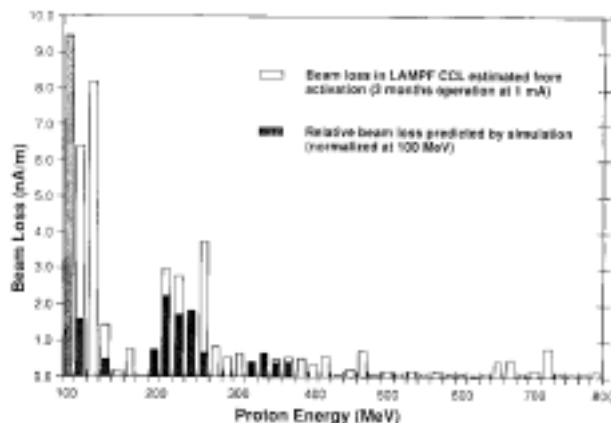
Fig. 3. Beam loss along the LANSCE linac as a function of proton energy. Inference from measured activation is compared to simulation.

3.2 Gas Stripping of H- Beam

Stripping of H^- from interaction with residual gas molecules can be calculated from known atomic cross sections as a function of energy. The curves for hydrogen and nitrogen are shown in Fig. 4 [8].

Figure 5 shows the allowed pressure in the beam path for hydrogen and nitrogen for a beam loss of 1 watt/m for a 2-

mA H⁻ beam. It is convenient to use watts/m instead of nA/m for beam loss, since activation varies less strongly with beam power than with current.
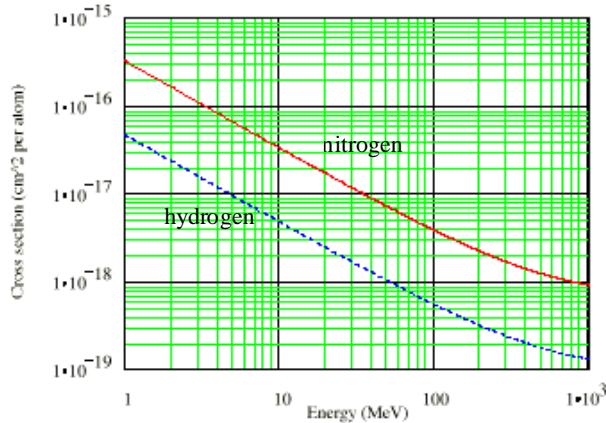

Fig. 4   Atomic cross-sections for stripping of H⁻ ions in nitrogen (solid line) and hydrogen (dotted line).
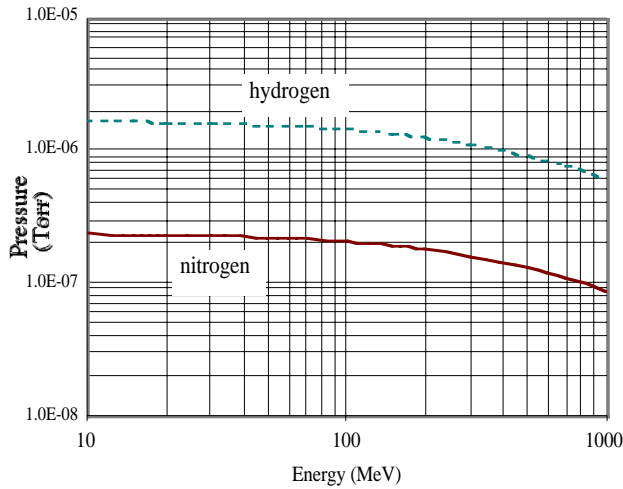

Fig. 5. Pressure corresponding to 1 watt/m beam loss for a 2-mA H⁻ beam.

Using the neutron yield per proton as a function of energy and assuming a direct proportionality between neutrons produced and activation, Shafer [8] was able to chart the vacuum requirement as a function of energy for a given activation level as shown in Fig. 6. For this calculation, he used the calibration of activation from beam loss calculated by Monte-Carlo codes as discussed later. It can readily be seen from these curves that a very good vacuum (< 10^{-7} Torr) is required to minimize beam loss from stripping of H⁻ ions, especially at higher energies. Since vacuum in this range can readily be achieved with good practices, such losses can be reduced to levels that permit unrestricted hands-on maintenance, as discussed later.
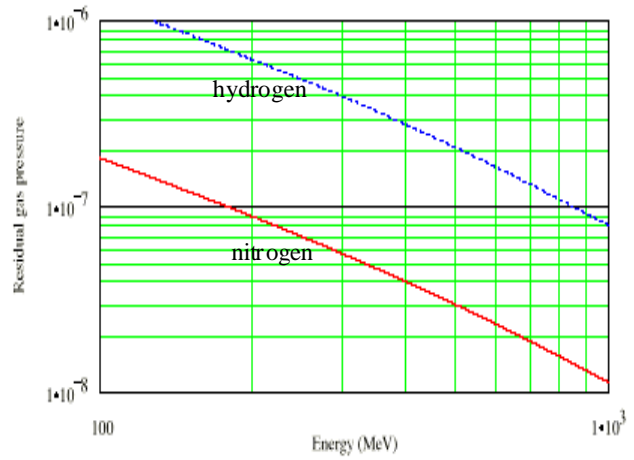
Fig. 6.   Allowed residual pressure of nitrogen (solid line) and hydrogen (dotted line) for 2-mA H⁻ beam to achieve 0.13 watts/meter, corresponding to activation of 10 mrem/hr at 30 cm, four hours after shutdown [8].

3.3 Magnetic Stripping of H⁻ Beam

Similar to the above, one can calculate H⁻ stripping in a magnetic field as a function of energy for different field strengths. In a linac, the highest field strengths are near the pole tips of the quadrupole focusing magnets. This corresponds to beam at the largest possible radius from the centerline. For the SNS linac, which has fairly strong focusing to confine the beam, the fractional magnetic stripping loss was calculated by Jason [9] and is shown in Fig. 7. For this linac, the full aperture is 2 cm over most of the length, and there would only be a small fraction of beam near this radius. For beam at a radius of 1 cm the magnetic stripping loss is less than 10^{-10} up to the maximum SNS energy of 1 GeV.
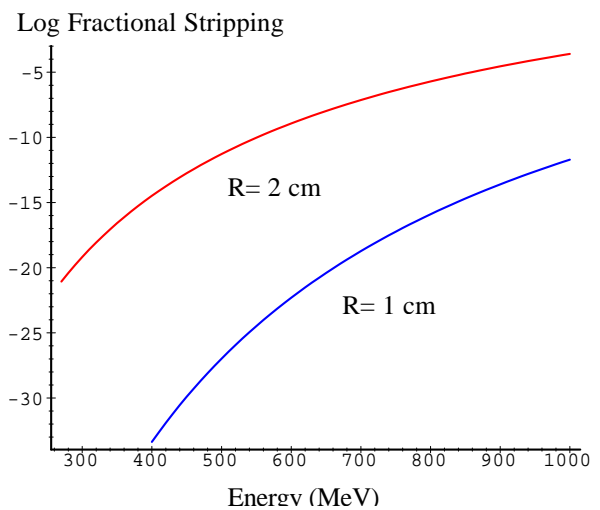
Fig. 7. Calculation of H⁻ stripping in quadrupole magnet field for the SNS linac as a function of energy for two beam radii [9].

4 DOSE RATE CALCULATIONS

Several groups have calculated activation resulting from proton beam loss by applying Monte-Carlo codes for radionuclide production and neutron transport. Two calculations of particular relevance to SNS were done by Santoro et al. [10] for SNS and by Fikani [11] for APT.

4.1 SNS Simulations by Santoro, Johnson, and Drishler

The activation of a simulated magnet and the concrete in the linac tunnel walls due to proton beam losses was calculated for proton beam energies of 333, 667 and 1000 MeV by Santaro et al. at ORNL [10]. Line losses were assumed to be 1 nA/m for all proton energies. In their model, the proton beam was incident on a 1-m-long copper cylinder (radius = 7.5 cm) placed in the center of a 30-m-long concrete-lined tunnel. The copper cylinder yields an overestimate of the radionuclide production in the magnet and the neutron leakage into the surrounding concrete, so the results are conservative. The interior dimensions of the tunnel were taken to be 4.64 m x 4.64 m with a concrete wall thickness of 0.457 m. The concrete was surrounded by 9 m of soil. The production of radionuclides in the copper and concrete were calculated using the High Energy Transport Code HETC in combination with the MCNP code to transport low energy ($\leq$ 20 MeV) neutrons. The radionuclide production was used in the ORIHET code to generate the decay gamma-ray spectra. The exposure time was taken to be 30 years corresponding to the total operating lifetime of the SNS. The spectra correspond to those at four hours after accelerator shutdown.

These spectra were used as the source terms to estimate the dose rate inside the accelerator tunnel as a function of incident proton energy. Calculations were performed using the one-dimensional transport code ANSIN with a cylindrical geometry model of the copper and tunnel walls. The results are shown in Fig. 8.
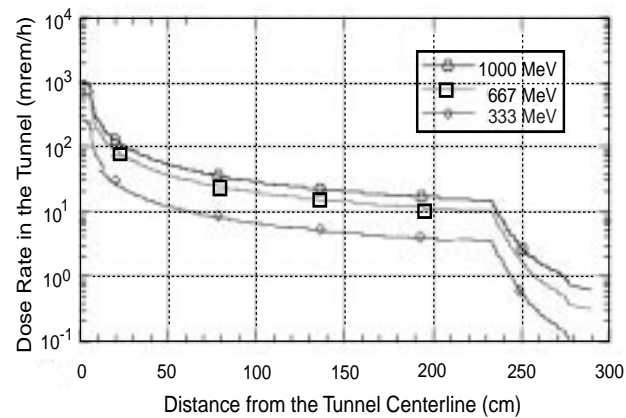
Fig.8 Dose rate in the SNS tunnel as a function of distance from the beam for 100-day irradiation, 4 hours after shutdown [10].

The contribution to the dose rate in the tunnel from the activated concrete is less than two percent of the copper dose rate at all energies. At 57.5 cm from the centerline (50 cm from the edge of the copper cylinder), the dose-rates due to the activated copper are 15, 45, and 65 mrem/hr, respectively, for incident proton energies of 333, 667, and 1000 MeV. The 1000-MeV data can be interpolated to 30 cm (1 foot) to get 80 mrem/hr per watt/m at 1000 MeV, the calibration used by Shafer [8]. At distances $\geq$1 m, the dose rates drop by more than a factor of two

4.2 APT Calculations by M. Fikani

The Accelerator Production of Tritium (APT) project has similar goals and requirements for minimizing beam loss along the linac, and much attention has been paid to minimizing activation. Calculations by Fikani [11] considered beam loss at three energies: 470, 1100, and 1700 MeV for a number of different irradiation and decay times. The geometrical model used was more realistic than that used in the SNS calculations, with a series of RF cavities and quadrupole magnets that correspond closely to a section of the APT lattice. Dose rates were calculated at 1-meter from the beam centerline and at 1-meter increments down the length of the simulated linac section. Fig. 9 shows the dose rate as a function of axial position for one of the conditions.
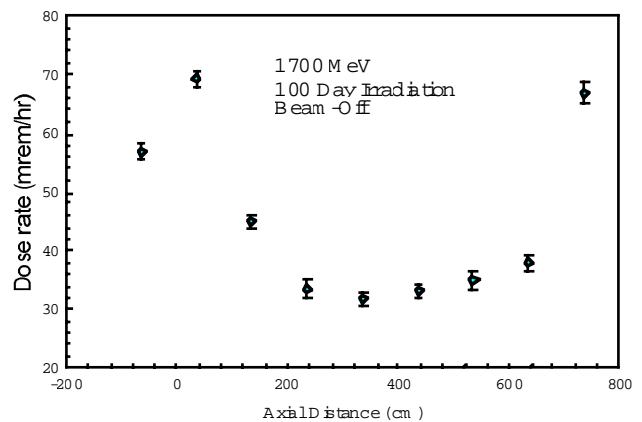

Fig. 9. Dose rate as a function of axial position along the beam line. The points near zero and 750 cm are near quadrupole magnets [11].

The peak dose rate occurs 1 meter downstream from the front face of the first quadrupole magnet. The dose rate decreases after this point by about a factor of two, with the minimum dose rate next to the accelerator module. As one approaches the magnets after this accelerator module the dose rate increases again to near peak levels. The following calculations use the axial position corresponding to the peak in Fig. 9.

65

Figures 10 and 11 show irradiation and decay profiles calculated at 1100 MeV for various wait times and irradiation times, respectively.
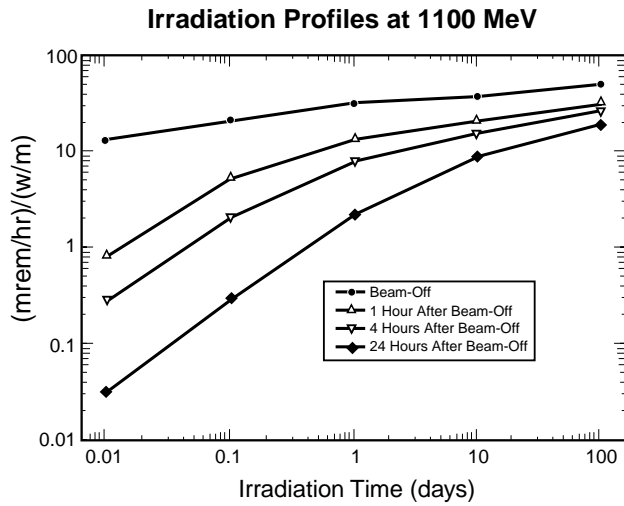
Irradiation Profiles at 1100 MeV

Fig. 10. Irradiation profiles at 1100 MeV at one meter for various wait times [11].
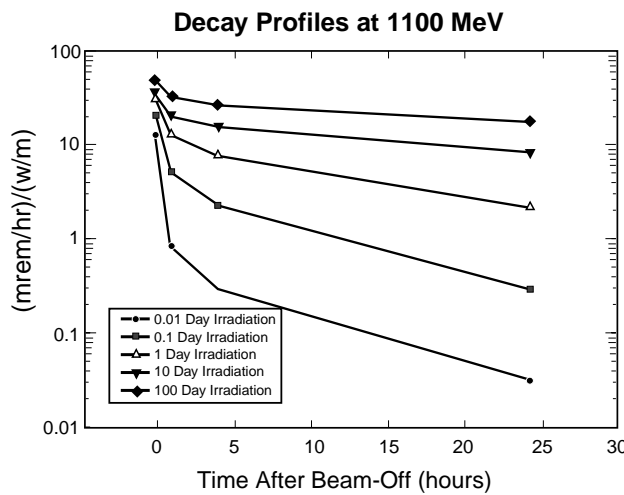
Decay Profiles at 1100 MeV

Fig. 11. Decay profiles at 1100 MeV at one meter for various irradiation times [11].

These graphs are plotted in mrem/hr per watt/m of loss, which minimizes energy dependence as discussed earlier.

5 ACTIVATION OF THE LANSCE LINAC

In an earlier section (see Fig. 3), we showed the relative activation measured in the LANSCE tunnel after a long run period at near 1 MW beam power. For the purpose of comparing with beam dynamic calculations, these data were normalized at one location. Readings taken under similar conditions along the beamline indicate the profile shown in Fig. 12 for a section of beamline just downstream of the 100-MeV transition region,
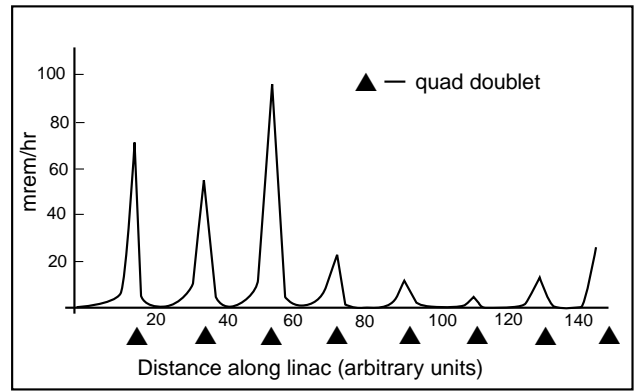
Fig. 12. Activation versus distance from the start of the LANSCE CCL. As expected the lost is greatest at the quadrupole doublets and near to the transition region.

When one is specifying activation along a linac, it must be clear whether the data represent the average along the tunnel or the "average peak" activation. For hands-on maintenance criteria, we use the peak measurements. This is a conservative approach that takes into account the fact that maintenance is often required in the regions between accelerating sections, near the quadrupole magnets.

Lawrence et al. [12] obtained a rough experimental calibration of activation vs. beam loss using the following procedure and assumptions. Following a shutdown of the LANSCE accelerator, a radiation survey was performed in which measurements were taken 30 cm from the beam pipe along the length of the accelerator. The estimate assumes that, to a first approximation, the level of activation is proportional to the number of neutrons produced at a given location

$$A = aN,$$

where A is the activation, N is the number of neutrons, and a is a proportionality constant. The number of protons required to produce the N neutrons can be obtained from measurements of the neutron yield per proton for copper and iron, Y(E), shown in Fig. 13. It follows that the number of protons is given by

$$P = A/aY$$

where P is the number of lost protons at a given location. This calculation was performed for every location along the length of the accelerator where an activation measurement was made. The sum of the results is proportional to the total number of lost protons. Making use of the measured total beam loss in the CCL, typically around 400 nA at the 0.8 MW operating level, they obtain the proportionality constant a and calculated the number of lost protons at the location of every activation measurement.
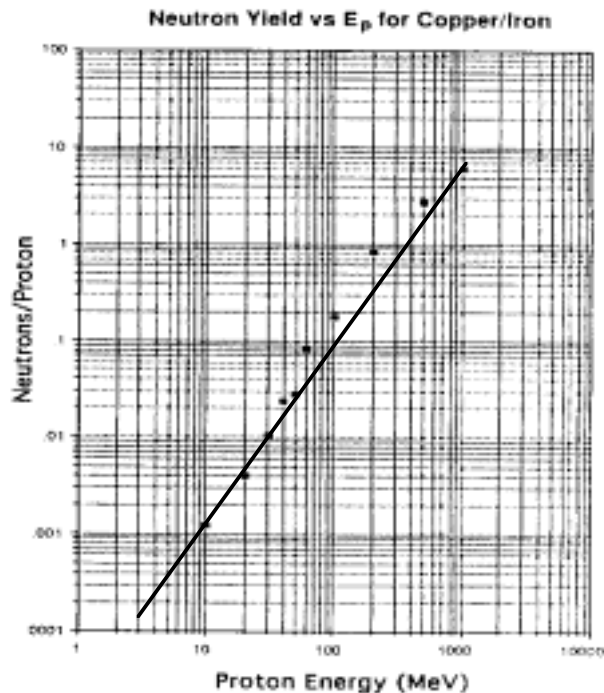
Fig. 13. Neutron yield per incident proton as a function of proton energy. The line through the data is a guide to the eye for this energy range.

Finally, by correcting for varying tank lengths, one obtains the beam loss profile shown earlier in Fig. 3. Two high-loss regions appear (just after 100 MeV and 212 MeV), but most of the CCL operates with very low losses, below 0.2 nA/m, corresponding to a fractional loss of about 2×10^{-7}/m. These values are representative of typical operation. Comparing the losses shown in Fig. 3 with the measured activation levels of Fig. 12, one can deduce that a loss of about 10 nA/m at 100-200 MeV (about 1 to 2 watt/m) leads to a peak activation between 60 and 100 mrem/hr. This is a higher number than that extrapolated from the calibration at 1000 MeV (see Fig. 15 in the Summary), but is in better agreement with the calculation of Ref. [10] for 333 MeV (55 mrem/hr per watt/m at 30 cm). At the high-energy end, Lawrence [12] found that losses of about 0.2 nA/m (see Fig. 3) led to peak activations of about 4 mrem/hr, giving a rough experimental calibration of 20 mrem/hr per nA/m (or 25 mrem/hr per watt/m) at 800 MeV. This number is substantially lower than the calculations. Therefore, these measurements and their interpretations do not lead to an accurate experimental calibration but bracket the Monte-Carlo calculations.

6 PSR LOSSES

The proton accumulator ring at LANSCE has provided data on activation at a higher level than that of the linac. Following a recent operation period with an upgraded injection system [13] a detailed set of activation measurements was taken under controlled conditions. The operating conditions were reported in ref. [13] and correspond to a continuous average loss of about 300 nA with a "stored beam" loss of 110-170 nA. The activation was measured [14] at the positions indicated in Fig. 14, which are at the ends of each of the quadrupole magnets in the ring. As in the linac, these are generally the limiting apertures and thus represent the highest readings. In the PSR, however, there are known losses at injection and extraction, so some judgement must be used in comparing beam loss with activation. The method we used is as follows.
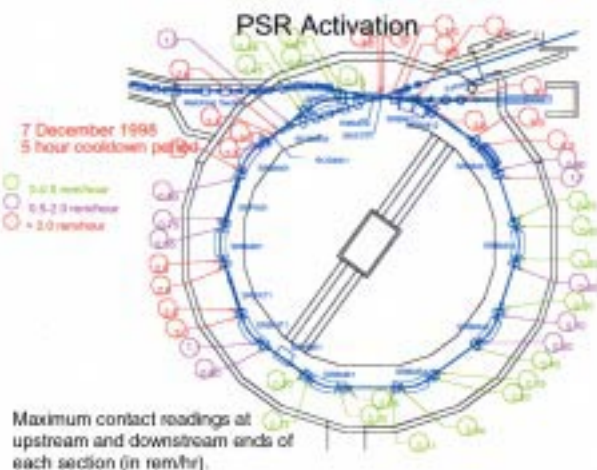
Fig. 14. Schematic of the PSR at LANSCE showing the locations of the activation readings taken following shutdown. Although the readings cannot be seen on this scale, they range from 40 mrem/hr to 10 rem/hr.

Taking the average of 17 "low" readings (below 1 rem/hr) in the ring sections away from the injection and extraction regions, we obtain an average activation of 290 mrem/hr on contact with the 4-inch beam pipe near the quads, five hours after turning the beam off. From experience (and in agreement with Fig. 8), the readings at one foot would be a factor 2 to 3 less, or about 100 mrem/hr. If one assumes that the stored beam losses occur uniformly around the ring, then this loss of ~140 nA corresponds to ~1 watt/m for the 800-MeV beam around the 93-m circumference. This gives an average "peak" calibration of about 100 mrem/hr per wait/m, in good agreement with the calculations for SNS and APT. However, in the PSR it is believed that about one-half of the stored beam loss occurs on the extraction aperture, which is the most limiting aperture in the ring [14]. If one corrects for this, then only half of the stored beam loss is distributed throughout the ring, resulting in a calibration of about 200 mrem/hr per watt/m at 800 MeV. An alternative interpretation of the data uses the average of all 47 activation measurements (1.68 rem/hr) corresponding to the total current loss of 300 nA. This gives an average "peak" calibration of 650 mrem/hr per watt/m on contact, or about 200 mrem/hr per watt/m at 30 cm, both at 800

MeV, five hours after shutdown. Therefore, these PSR calibrations are at best accurate to within a factor of two.

7 MAINTENANCE DEFINITIONS

As activation levels increase, maintenance activities on the linac become more difficult and time consuming. Table 2, taken from ref. [12] shows approximately how the level of machine activation affects the maintenance environment. Hands-on maintenance can be performed at higher levels than 10 mrem/hr, although with more limited access times and stringent administrative control.

Table 2. Levels of Activation and Type of Maintenance

Level of Activation	Type of Maintenance
< 10 mrem/hr	Unconstrained "hands-on" maintenance
10 mrem/hr–100 mrem/hr	Hands-on maintenance; limited access time
100 mrem/hr–10 rem/hr	Hands-on maintenance, strictly controlled; very limited access time
>10 rem/hr	Remote maintenance required

7.1 Maintenance Restrictions at LANSCE

Anticipated personnel exposure is clearly the best basis for deciding the need for and length of a cool-down period. Total personnel exposure can be estimated from measured activity rates at 30 cm and expected exposure time for each worker. When it is undesirable or impractical to measure exposure rates before entry, historical data may be used to make this estimate. At PSR, for example, the readings in Fig. 14 were taken after five hours cool-down, so one should multiply by approximately a factor of three to estimate levels immediately after ceasing operation [14]. This can be verified from the curves in Fig. 12.

The administrative guidelines at LANSCE are:

- If the estimated total exposure for all personnel would be approximately 100 mrem (or 40 mrem for an individual) if the entry were made immediately, a cool-down period of two hours is suggested.

- If the estimated total exposure for all personnel would be greater than 100 mrem (or greater than 40 mrem for an individual) if the entry were made immediately, a cool-down period of four hours is suggested.

- No cool-down period is recommended for short entries for equipment adjustment, observations or sweeps, etc., unless several consecutive entries are anticipated that would result in more than 100-mrem total exposure. In that case, one should plan the entries to afford as much cool-down time as practical.

7.2 Availability Implications

The availability characteristics of a system are determined by its reliability (failure rate) and maintainability (ease of maintenance). RAM analyses use the following relations between A (availability), MTBF (mean time between failure) and MTTR (mean time to repair) for components in series.

$$A = \Pi_{i=1,N} A_i$$

where

$$A_i = MTBF/(MTBF+MTTR).$$

Since availability is inversely related MTTR, activation of components that result in longer wait times before maintenance can be performed could be an important consideration. As a simple example, consider a system that has a MTBF=10,000 hours, takes one hour to repair, and there are 100 such systems in the linac. If access can be obtained immediately after failure, the availability of these systems is 99.0%. However, if a wait time of four hours is required for access, the availability drops to 95.1%. Preliminary RAM models, developed for the SNS linac during the CDR [3], included systems in the accelerator tunnel contributing to the overall availability, and therefore the linac availability is somewhat sensitive to the activation levels. Only very preliminary quantification of these concepts has been attempted [16].

8 SUMMARY

Monte-Carlo calculations for both SNS and APT indicate that the peak dose rate is about 80 mrem/hr per watt/m of beam loss at 1000 MeV, measured at a distance of 30 cm from the beam pipe several hours after shutdown. Experimental data are difficult to interpret and have large errors, but numbers from 25 to 200 mrem/hr per watt/m can be deduced from LANSCE linac and PSR measurements near 800 MeV. It is stressed that these are peak readings that occur near limiting apertures (quadrupole magnets). Readings averaged over the entire length of the accelerating structure will be less, but maintenance is often performed in the inter-segment region where the quadrupoles are located. Table 3 summarizes the results of this review.

Table 3. Calibration of "Peak" Activation vs. Beam Loss Near 1000 MeV at 30 cm, Several Hours After Shutdown.

Source	Ref.	Energy (MeV)	mrem/hr per watt/m
Calculations			
Santoro et al. (SNS)	10	1000	80
Fikani (APT)	11	1100	90
Experimental			
Lawrence (LANSCE)	12	800	~25
Fitzgerald (PSR)	13,14	800	100-200

Even at a loss level of 1 watt/m (the SNS linac specification) hands-on maintenance is still possible, although with limited access time and strict administrative controls. Table 2 gives guidelines that are applied at LANSCE. Clearly, it is advantageous to keep the losses as low as possible, and the goal should be on the order of 0.1 watt/m, where unrestricted hands-on maintenance and quick access will lead to higher machine availability. The following graph [15] shows projected activation corresponding to 1 watt/m beam loss when normalized by the SNS calculation of ref. [10] at 1000 MeV. The ref. [11] calculation and calibraion points using LANSCE and PSR data at 800 MeV are shown for comparison.
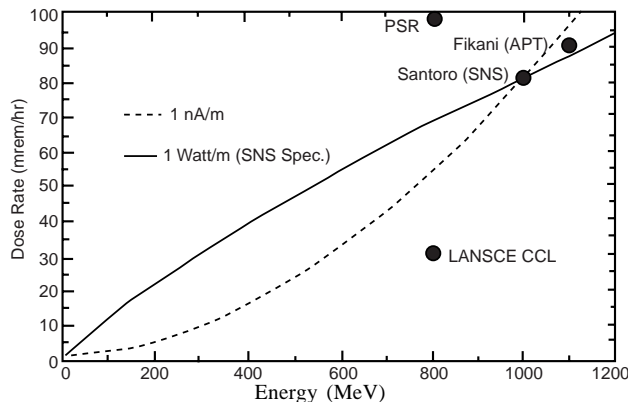
Fig. 15. Predicted peak dose rate from activation at 30 cm about four hours after shutdown for the SNS specification of 1 watt/m [15] and the calibration of Ref [10].

We point out that Monte-Carlo calculations at 333 MeV and 667 MeV from Ref. [10] are higher than the curves shown, indicating that the assumption that activation is proportional to number of neutrons produced (used for the curves in Fig. 15) may underestimate the dose rate below 1000 MeV.

9   ACKNOWLEDGEMENTS

REFERENCES

[1] A. Jason et al., *A Linac for the SNS*, Proc. of the XIX Intl. Linac Conf., Chicago, IL, August 1998. 415.

[2] R. Hardekopf et al., *Linac Design for the SNS*, Second Intl. Topical Meeting on Nuclear Applications of Accelerator Technology, Gatlinburg, TN, Sept. 1998. 208.

[3] SNS Conceptual Design Review (CDR), June 1997, http://www.ornl.gov/~nsns/, Chap. 3.

[4] T. Wangler, *RF Linear Accelerators*, John Wiley & Sons, Inc., New York, 1998; and private communication.

[5] H. Takeda, J. Billen, T. Bhatia, *Beam Dynamics Simulation of the SNS Linear Accelerator,* Proc. of the XIX Intl. Linac Conf., Chicago, IL, August 1998, 499; and B. Blind, R. Garnett, *Performance of Several SNS MEBT Designs,* LA-UR-99-5529 (unpublished).

[6] R. Garnett, R. Mills, and T. Wangler, *Beam Dynamics Simulation of the LAMPF Linear Accelerator,* Proc. of the 1990 Linac Conf., Albuquerque, NM, 1990; and E. Gray, T. Wangler, LANL Technical Note AOT-1:84-123, June 1994 (unpublished).

[7] F. Merrill and L. Rybarcyk, *Beam Dynamics Simulations of the LANSCE Linac*, Proc. of the XIX Intl. Linac Conf., Chicago, IL, August 1998. 839.

[8] R. Shafer, *Beam Loss from H- Stripping in the Residual Gas* SNS Technical Note LA-UR-99-2497, May, 1999 (unpublished); and private communication.

[9] A. Jason, private communication.

[10] R. Santoro, J. Johnson, and J. Drishler, *Dose Rate Inside the SNS Linac Tunnel from Activation of the Magnet Copper Conductor and the Concrete Wall*, SNS Technical Note SNS/TSR-0130,(unpublished).

[11] M. Fikani, *Activation Dose Rates in the Accelerator Tunnel - 2*, APT memo PPO-TPO-mem-01551, November, 1998 (unpublished).

[12] G. Lawrence, *Accelerator Production of Tritium,* External Review to ERAB, Oct 1989, and Los Alamos Reports LA-UR-90-4432 *(ATW)*, LA-UR-92-3430 *(APT)*, LA-UR-95-4300 *(LANSCE Upgrade),* and private communication. See also T. Wangler et al., *Basis for Low Beam Loss in the High-Current APT Linac,* Proc. of the XIX Intl. Linac Conf., Chicago, IL, August 1998. 657.

[13] D. Fitzgerald et al., *Commissioning of the Los Alamos PSR Injection Upgrade*, Proc. of the 1999 Particle Accelerator Conference, New York, 1999, 518; and private communication.

[14] D. Fitzgerald, *Guidelines for PSR Work During Operations Periods*, LANL memo LANSCE-2:DHF:98-003, April 1999 (unpublished).

[15] J. Stovall, private communication.

[16] C. Piaszczyk, *Accelerator Reliability Database*, Proc. of the 1999 Particle Accelerator Conference, New York, 1999, 1465; and private communication.

APT LINAC DESIGN FOR LOW BEAM LOSS

Thomas P. Wangler,

Los Alamos National Laboratory, Los Alamos, NM 87545 USA

Abstract

The APT beam-dynamics design goal was to limit the beam losses, especially above 100 MeV where the radioactivation concerns are greatest, to less than 0.1 nA/m. In this paper we discuss the reasons why the APT design is expected to meet these low beam-loss goals.

1 INTRODUCTION

The Secretary of Energy announced in October 1995 the decision to pursue a dual-track strategy for future tritium production, funding both reactor- and accelerator-based systems for a three-year period, after which the DOE would select the most promising method. Since then, the DOE has supported a program to develop a high-intensity proton linear-accelerator design, called Accelerator Production of Tritium (APT). On December 22, 1998, Secretary of Energy Bill Richardson announced that commercial light water reactors will be the primary tritium supply technology. The Secretary designated the APT as the backup technology for tritium supply. APT preliminary design will continue during the next three years (1999-2001) to support the backup role.

In APT, tritium is made by capturing neutrons in He[3]. To supply the neutrons, protons are accelerated to about 1 GeV in a linear accelerator and used to bombard a heavy-metal target made of tungsten and lead, creating neutrons in a spallation process. The resulting neutrons are moderated by collisions with lead and water, increasing the efficiency of their capture in the helium gas flowing through the target to make tritium. The tritium is extracted from the gas continuously. An attraction of APT is that it is considered a very safe and environmentally benign system. The fundamental reason for this is that neutrons are produced by the spallation process rather than by nuclear fission. APT will produce the required neutrons without a nuclear chain reaction, avoiding the production of long-lived radioactive products such as plutonium or neptunium.

Fig.1 shows a block diagram of the APT linac[1], showing a low-energy normal-conducting proton linac that accelerates the beam to 211 MeV, followed by two sections of a superconducting linac. The APT final energy of 1030 MeV is comparable to the final energy of the 800-MeV LANSCE proton linac at Los Alamos. However, APT delivers a continuous (CW) beam current of 100 mA, which is 100 times the average beam current of LANSCE; the beam power is also about 100 times greater than LANSCE, which is at present the world's most powerful linac. Because of the large increase in beam current, one of the most important features of the APT design is the emphasis on designing for low beam loss to limit the potential radioactivation of the accelerator. This requirement is driven by the desire for high availability, to enable the operations personnel to be able to carry out routine maintenance without being hindered by the activation levels along the machine.
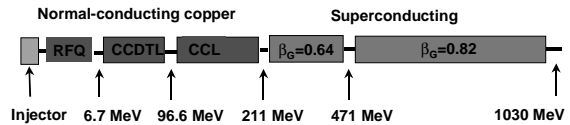

Figure 1. Block diagram of the APT linac

The APT beam-dynamics goal was to limit the beam loss, especially above 100 MeV where the radioactivation concerns are greatest, to less than 0.1 nA/m, which is comparable to levels throughout most of the LANSCE linac, where essentially unconstrained hands-on maintenance is possible. We believe that this goal has been achieved in the APT design for four reasons[2]. First, the APT design avoids the most important beam-loss mechanisms of the LANSCE linac. Second, the basic physics of beam-halo formation is understood, and the APT design choices have been made to minimize the beam halo. Third, the multiparticle simulations for APT predict loss levels smaller than LANSCE. Finally, additional physics effects not included in the simulation code have been investigated, and have been shown to be unimportant. In this paper we will discuss each of these points.

2 APT DESIGN AND BEAM LOSS MECHANISMS IN LANSCE

The APT design avoids the most important beam-loss mechanisms of the LANSCE linac. The APT design eliminates the longitudinal tails that were a main cause of beam loss in LANSCE by using a Radiofrequency Quadrupole linac (RFQ) for bunching. LANSCE does not have an RFQ, because the LANSCE linac construction thirty years ago predated the use of RFQs. The frequency jump between the low and high energy linacs was reduced from a factor of 4 to a factor of 2 to provide a larger rf acceptance at the transition. This transition was moved to lower energy, where any beam losses associated with the transition would produce less radioactivation. Unlike LANSCE, beam-matching capability is provided at all APT transitions. Unlike LANSCE, where both H^{+}

and H$^-$ beams must be accelerated, only H$^+$ beams are accelerated in APT, so beam steering can be much more effective. Beam losses from turn-on transients are essentially eliminated, since APT is not pulsed like LANSCE. Finally, APT has stronger focusing and larger apertures than LANSCE. For example, in the high-energy linac where radioactivation is of greatest concern, the APT superconducting linac apertures are 16 cm in diameter, compared with a 3.8-cm diameter for LANSCE.

3 UNDERSTANDING BEAM HALO IN APT

Understanding beam-halo physics in proton linacs has involved the work of many experts worldwide, including some at this workshop. The dominant beam-halo mechanism is that produced by space-charge forces in a mismatched beam. Beam mismatch excites an envelope mode of the beam. The most important mode for APT is the breathing mode with frequency f_{mode}. For the breathing mode the envelope oscillations in all three planes are in phase. For those particles whose oscillation frequency $f = f_{mode}/2$, a parametric resonance can drive them to large amplitudes, producing halo[3].

The particle-core model[4] has been used to study the motion of test particles in a smooth-focusing channel as they pass through the core and interact with the nonlinear space-charge fields produced by the core. Particle-core models, using different geometries for the bunch, provide a valuable framework for understanding the physics. For a spherical bunch geometry, the equation describing the core oscillation is the usual envelope equation, given by

$$\frac{d^2R}{dz^2} + k_0^2 R - \frac{(4\varepsilon_{rms})^2}{R^3} - \frac{\kappa}{R^2} = 0, \qquad 1)$$

where the space charge parameter κ is

$$\kappa = \frac{q^2 N}{4\pi\varepsilon_0 mc^2\gamma^3\beta^2}. \qquad 2)$$

In Eqs. 1 and 2, R is the radius of the equivalent uniform beam, k_0 is the betatron wavenumber, ε_{rms} is the rms unnormalized emittance, q and m are the charge and mass of the beam particles, ε_0 is the permeability of free space, c is the speed of light, and γ and β are the usual relativistic parameters. The equation of motion for a test particle moving through the core while experiencing a continuous linear external focusing force, and the space-charge force of the core represented by uniform distribution, is given by

$$\frac{d^2x}{dz^2} + k_0^2 x - \frac{\kappa x}{R^3} = 0, \; x < R,$$

$$\frac{d^2x}{dz^2} + k_0^2 x - \frac{\kappa|x|}{x^3} = 0, \; x \geq R. \qquad 3)$$

The quantity x is the displacement of the particle in the x direction, and the motion is symmetric in all three planes. These equations can be solved numerically, assuming a given initial mismatch of the core and initial coordinates for each test particle. Figure 2 shows a large amplitude resonant trajectory together with the mismatched core radius undergoing a breathing-mode core oscillation. The space-charge tune-depression ratio is 0.5, and the initial mismatch parameter is 1.5, where the mismatch parameter equals the ratio of the initial to the matched rms core size. The trajectory solutions are conveniently represented by the stroboscopic phase-space plot (Fig.3), which shows snapshots of an array of particles, initially distributed along the abcissa and ordinate; the phase space is strobed once per core-oscillation cycle, when the core radius is minimum. The core trajectories lie within the inner separatrix in Fig.3. The trajectories for particles under the influence of the parametric resonance lie in the regions between the inner and outer separatrix, in the regions that contains the two stable fixed points that lie on the horizontal axis. Particles that lie within these regions cycle in and out and can be driven to large amplitudes.
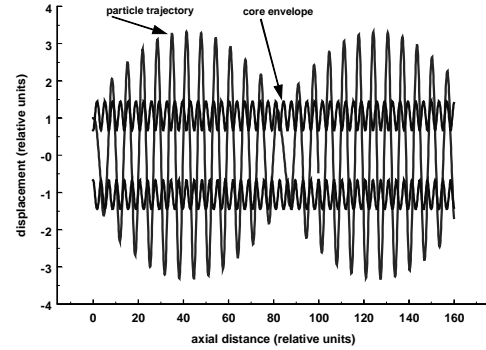

Figure 2. Parametric resonance from the sphere particle-core model. The figure shows a resonant particle trajectory together with the breathing-mode core oscillation.

Conclusions from the numerical solution of Eqs. 1, 2, and 3 for the spherical particle-core model, and a more general spheroidal model[5] of the bunch geometry include the following. The model predicts a maximum resonant particle amplitude for a given mismatch parameter. This amplitude lies at the intersection of the outer separatrix and the horizontal axis in Fig.3. The halo extent is limited for a given mismatch, because the large amplitude particles eventually fall out of resonance, since the particle-oscillation frequencies increase with amplitude. The prediction that the halo amplitude is limited for a given mismatch is confirmed by multiparticle simulations for a smooth focusing system. For more realistic 6-D multiparticle simulations of a linac, this result does not
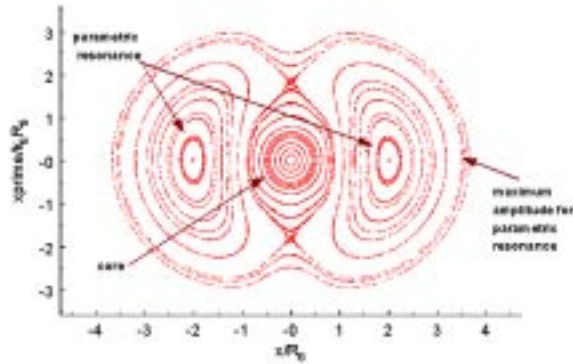
Figure 3. Stroboscopic phase-space plot from the particle-core model of a spherical bunch with the core excited in a breathing mode.

appear to be exact, but is still a good approximation.

The halo amplitudes depend only weakly on the space-charge tune depression ratio, but the halo grows more rapidly at low tune-depression ratios as the beam becomes more space-charge dominated. (The space-charge tune depression is defined as the ratio k/k_0, where k is the betatron wavenumber including the space-charge force of the equivalent uniform beam.) Chaos is observed in the model for tune depression ratios $k/k_0 < 0.3$; the main consequence of the chaos is probably to increase the halo population. When the nonlinear rf longitudinal focusing term is included, it defocuses the beam and reduces the longitudinal particle frequencies, disrupts the resonant condition, and reduces the longitudinal halo[6].

Some APT beam-dynamics design principles to minimize the halo amplitude and intensity have been deduced from the model. One should provide strong longitudinal and transverse focusing, and minimize the effects of beam mismatch by providing matching capability at the transitions, and controlling the machine errors that lead to distributed mismatch. The longitudinal and transverse space-charge tune depression ratios should be limited to $k/k_0 < 0.3$, to avoid chaos that increases the halo population. One should provide aperture radii that are significantly larger than the maximum halo amplitude. The use of large aperture superconducting cavities for APT helps in this regard. The rf or longitudinal separatrix provides the longitudinal limit, but the nonlinear rf focusing surpresses the parametric resonance and helps to keep the beam from approaching that separatrix. In realistic multiparticle simulations of the APT linac, it takes a very large mismatch to produce loss of particles from the bucket.

4 MULTIPARTICLE SIMULATIONS OF THE APT LINAC

The particle-core models are not used for a detailed description of the dynamics in a real linac, which requires a multiparticle simulation code with a detailed model of the linac, including a periodic instead of smooth focusing channel.The halo is expected to be caused primarily by

distributed linac errors in quadrupole gradients, accelerating gradients, and rf phases that produce many small mismatches. The simulation code uses the Monte Carlo approach to choose these machine errors within specified tolerances. Computer simulations can then be used to make resulting probabilistic predictions of the beam distribution including the halo.

The simulation code uses the particle-in-cell (PIC) method at each step to solve the Vlasov-Poisson equations numerically. The program computes the space-charge field at each time step, and applies it together with the focusing fields to advance the simulation particles from the output of the RFQ through the linac to the target. The input beam distribution is derived from beam simulations carried out earlier between the ion source output and output of the RFQ.

Multiparticle simulations of the APT linac predict that the beam loss will be low. For example, twenty simulation runs were made with 100,000 simulation particles each, and different sets of random errors for each run. Each simulation particle carries enough charge to provide the correct total beam current. (The actual number of particles in the bunch is about 10^9 particles.) Results are shown in Fig. 4. Shown are 20 runs with different random errors and 100,000 particles per run. The particles are run through the linac all the way to the target. The input distribution was obtained by previous
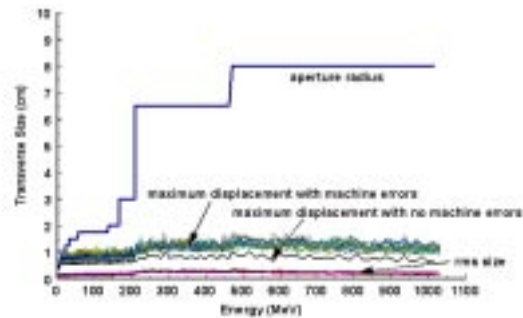

Figure 4. Rms size and maximum particle displacement with and without machine errors are shown together with the aperture radius, as a function of energy.

multiparticle simulation through the LEBT and the RFQ.

No particle loss occured above 20 MeV. Loss of a single particle above 100 MeV would correspond to a loss rate of 0.05 nA/m, lower than the APT design goal. A total of five particles were lost after the RFQ, all with energies below 20 MeV. This loss rate corresponds to a very small activation level, estimated to be < 1 mRem/hr. In another simulation, several 10^7 particle runs were made using parallel computers, and with a full set of errors after the RFQ. These runs produced no particle loss after the RFQ.

5 ADDITIONAL EFFECTS NOT INCLUDED IN THE SIMUATION CODE

Additional physics effects not included in the simulation code have been investigated and all have turned out to be unimportant for APT. These effects include Coulomb scattering, beam/cavity interactions, and background electron influences. Although it may be thought that Coulomb scattering of the particles in the beam is already accounted for by the space-charge subroutine of the simulation code, the PIC space-charge method describes only the average Coulomb force between the particles. Discrete particle-collisions (intrabeam scattering) are not included by the PIC calculation. Nevertheless, discrete particle collisions are generally found to be negligible in linac beams, although they can be important in a simulation code that calculates the interaction of fewer particles, each with greater charge than the real particles.

An analytic calculation of the discrete particle collisions for the APT beam confirms that these effects will be insignificant[7]. The Coulomb collisions add an outer shell to the beam, which is a small increase compared with the margin between the beam and the aperture radius for APT. The total population of this outer shell for APT was found to be negligibly small. In addition, calculation of the Coulomb scattering of the beam from residual gas atoms at a 10^{-7} torr vacuum pressure, also gave a negligible contribution to the halo[8]. The overall conclusion is that the beam spends too little time in the linac for these effects to be important.

The APT proton-beam-induced wake effects are estimated[9] to produce an electric field at the beam that is a factor of 10^4 smaller than the applied accelerating field. The wake fields have a negligible effect on the dynamics of the APT proton beam. The beam-breakup instability (BBU) caused by beam-induced deflecting modes was examined[10] for the superconducting cavities in APT. It was found that BBU is unimportant in APT for three reasons. First, because of fabrication errors, there is a spread of the deflecting mode frequencies of the different cavities, which means that the cavities do not cooperate effectively, as required for a strong instability. Second, because of substantial transverse focusing in APT, the effects of the deflecting modes, even if excited, are a small perturbation relative to the total focusing force. Finally, higher-order mode (HOM) couplers, planned for the APT superconducting cavities, load the deflecting modes to give an added safety margin.

Some background electron effects in APT were also investigated. Simulation studies showed that beam mismatch caused by possible charge neutralization in the drift spaces is small compared with the contributions from the other linac errors[11]. In addition, simulation of the proton beam interacting with electrons, trapped in the fields of the focusing quadrupole magnets, showed a negligible disturbance of the beam[12].

6 CONCLUSIONS

We have discussed reasons why the APT design is expected to meet the goals for very low beam losses. The APT design avoids the known beam-loss mechanisms in the LANSCE linac. The basic physics of beam halo, caused by beam mismatches, is now understood, and the APT design choices were made to minimize the beam halo. At high energies, the APT design has a much larger aperture to rms beam-size ratio (13 to 50) than the LANSCE linac (5 to 7). Realistic multiparticle simulations including linac errors, predict no losses above 20 MeV. Finally, additional physics effects, not included in the simulation code, have been shown to be unimportant.

7 ACKNOWLEDGEMENTS

REFERENCES

[1] G.P.Lawrence, Proc. of the XIX International Linac Conference, August 23-28, 1998, Chicago, IL, 26.

[2] T.P.Wangler, E.R.Gray, F.L.Krawczyk, S.S.Kurennoy, G.P.Lawrence, and R.D.Ryne, Proc. of the XIX International Linac Conference, August 23-28, 1998, Chicago, IL, 657.

[3] R.L.Gluckstern, Phys.Rev.Lett. 73 (1994)1247.

[4] For example, see T.P.Wangler, K.R.Crandall, R.Ryne, and T.S.Wang, Phys.Rev. ST Accel. Beams 1 (084201)1998.

[5] R.L.Gluckstern, A.V.Fedotov, S.S.Kurennoy, and R.D.Ryne, Phys.Rev., E58, 4977(1998).

[6] J.Barnard and S.Lund, 1997 Part. Accel. Conf., Vancouver, British Columbia,, Canada, 1929, and 1932.

[7] R.L.Gluckstern, and A.V.Fedotov, Phys.Rev. ST Accel.Beams 3,(054201)1999.

[8] R.L.Gluckstern, private communication.

[9] F.Krawczyk, private communication.

[10] R.L.Gluckstern, private communication.

[11] B.Blind, private communication.

[12] P.Channell, Los Alamos Report LA-CP-98-238, Oct.14,1998.

Low-Loss Design Optimization for the SNS Accumulator Ring[1]

J.Wei[2], D. Abell, J. Beebe-Wang,
M. Blaskiewicz, P. Cameron,
N. Catalan-Lasheras, G. Danby, A. Fedotov,
C. Gardner, J. Jackson, Y. Y. Lee, H. Ludewig,
N. Malitsky, W. Meng, D. Raparia, N. Tsoupas,
W. T. Weng, S. Y. Zhang

Brookhaven National Laboratory, Upton, New York 11973

Abstract

This paper summarizes the low-loss design for the Spallation Neutron Source accumulator ring [1]. A hybrid lattice consisting of FODO arcs and doublet straights provides optimum matching and flexibility for injection and collimation. For this lattice, optimization focuses on five design goals: a space-charge tune shift low enough (below 0.15) to avoid strong resonances; adequate transverse and momentum acceptance for efficient beam collimation; injection optimized for desired target beam shape and minimal halo development; compensation of magnet field errors; and control of impedance and instability (vacuum chamber coating and step tapering). With an expected collimation efficiency of more than 90%, the uncontrolled fractional beam loss is expected to be at 10^{-4} level.

1 INTRODUCTION

In recent years, high intensity ion beams have been proposed for a wide variety of applications; these include spallation neutron sources, neutrino factories, transmutation of nuclear waste, heavy ion fusion, muon collider drivers [2]. Beam power in these machines, usually 1 Mega-Watt (MW) or more, is an order of magnitude above that in existing accelerator facilities. In designing these next-generation facilities, the primary concern is that radio-activation caused by excessive uncontrolled beam loss can limit a machine's availability and maintainability . Based on operational experience at the LAMPF Linac [4] at Los Alamos and the AGS and Booster [5] at Brookhaven National Laboratory, hands-on maintenance [3] demands an average uncontrolled beam loss not exceeding a couple of Watts of beam power per tunnel meter. At Mega-Watt power levels, this corresponds to a fractional beam loss of 10^{-6} per meter. Equivalently, for a storage ring of several hundred meter circumference, the tolerable fractional beam loss is about 10^{-4}.

Existing proton synchrotrons and accumulator rings have beam losses as high as several tens of percent, mostly at injection, capture and initial ramping. Uncontrolled beam losses are usually attributed to (1) a high space change tune shift (0.25 or larger) at injection; (2) limited physical and momentum acceptance; (3) premature H^- and H^0 stripping and injection foil scattering; (4) large magnet field errors, dipole-quadrupole matching errors (for rapid cycling synchrotrons), and misalignments; (5) instabilities (e.g. PSR instability). Compared with rapid cycling synchrotrons, an accumulator ring simplifies the capture process and avoids ramping complications. The lowest achieved beam loss is about 3×10^{-3} at the Proton Storage Ring (PSR) at the Los Alamos National Laboratory. This loss value, however, is still more than an order of magnitude higher than desired for next-generation machines. A low-loss design must carefully address the above five issues.

The Spallation Neutron Source (SNS) is based on an accelerator producing an average proton beam power of 2 MW at a repetition rate of 60 Hz [1, 6]. Table 1 lists the main parameters of the SNS and some other existing and proposed neutron facilities. During 1999, the first year

Table 1: Main parameters of some existing and proposed accelerator-based neutron facilities.

Machine	Energy [GeV]	Intensity [ppp]	Rep-rate [Hz]	Power [MW]
Existing:				
LANSCE	0.8	2.3×10^{13}	20	0.07
ISIS	0.8	2.5×10^{13}	50	0.2
Proposed:				
NSP (Japan)	3.0	8.0×10^{13}	25	1.0
SNS (US)	1.0	2.1×10^{14}	60	2.0
ESS (Europe)	1.334	2.3×10^{14}	50	2.5

of construction, a study was performed comparing a full-energy linac with accumulator ring to a rapid cycling synchrotron. The study concluded that the stringent beam loss limit of a 2-MW source requires a RCS design that is technically challenging and less cost effective [7]. The SNS accelerator complex now comprises a source and front end, a 1 GeV full-energy linac, an accumulator ring, and its transfer lines. With a circumference of 220 meters, the accumulator ring compresses the proton beam into 0.6 μs pulses of 2×10^{14} particles, and delivers them at a rate of 60 Hz to a liquid mercury target for neutron spallation production.

This paper summarizes the low-loss design optimization for the SNS accumulator ring [8, 9]. Many of the design concepts and conclusions can be applied to future high-intensity facilities. Section 2 discusses our low-loss design philosophy. Section 3 presents the FODO-doublet hybrid lattice. Considerations of physical and momentum acceptance are given in Section 4. In Section 5, we compare injection painting scenarios and discuss injection halo control. Section 6 discusses the extraction layout. In Section 7, we address loss mechanisms, halo development, collimation, and beam gap cleaning. Magnet field error analysis, and chromatic and resonance corrections are discussed in Sections 8 and 9. Impedance and instability issues are discussed in Section 10. A summary is given in Section 11.

[2]e–mail: wei1@bnl.gov

2 LOW-LOSS DESIGN PHILOSOPHY

Reliability and maintainability are of primary importance to the SNS facility. Hands-on maintenance [3] for the accumulator ring demands an average radio-activation at or below $1 - 2$ mSv/hour 30 cm from the machine device [3]. The corresponding uncontrolled beam loss is 10^{-4} for a 1 GeV beam.

To achieve this goal, the SNS ring design avoids the five common practices discussed above that lead to heavy beam loss: The beam is painted to a quasi-uniform distribution to keep space-charge tune shift below 0.15. A transverse acceptance/emittance ratio of about 3 allows the beam tail and beam halo to be cleaned by the collimation system before hitting the rest of the ring. A stationary RF bucket confines the beam to within 70% of its momentum acceptance ($\Delta p/p = \pm 1\%$), while the machine vacuum chamber provides a full momentum aperture of $\pm 2\%$ in $\Delta p/p$. The layout and magnetic field at injection are designed to prevent premature H^- and H^0 stripping and excessive foil hitting. A moderate main magnet field avoids saturation effects, and shimmed pole tip ends in both dipole and quadrupole magnets help compensate fringe field effects. Finally, vacuum chambers are coated, chamber steps are tapered, and injection beam momentum is broadened to avoid instabilities [10, 11, 12].

Efficient beam halo collection is essential for maintaining a low uncontrolled beam loss [13, 14]. To facilitate multi-stage collimation and momentum cleaning using a multi-turn beam gap kicker system [15], a wide transverse and momentum acceptance is essential. With the collimation system designed to be more than 90% efficient, the total allowed beam loss on the collimators [16] is about 10^{-3}.

Flexibility is another important design goal. A matched FODO/doublet lattice is chosen because FODO arcs allow easy chromatic and resonance correction, while long uninterrupted doublet straights make the arrangement of injection modules independent of lattice tuning, and allow for optimal placement of collimators for phase-space collimation [13].

To address the issue of engineering reliability [2], collimators and machine hardware are designed to withstand an average 10^{-2} beam power. In addition, the machine is designed to withstand a couple of full beam pulses for commissioning and emergency handling.

3 FODO-DOUBLET HYBRID LATTICE

3.1 Layout and functions

Lattices used in typical high-intensity proton accelerators have either a FODO structure (AGS Booster [17], IPNS Upgrade [18], Japanese Neutron Science Project (NSP) ring [19], previous SNS ring [1], etc.) or a doublet/triplet structure (ISIS, ESS [20], etc.). A FODO lattice structure has the advantage of relatively low quadrupole gradient, relatively smooth lattice function variation, and easy implementation of chromatic and resonance corrections. How-

ever, the uninterrupted drift space is often short and not flexible for injection and collimation arrangements. Possible lattice mismatch caused by unequal FODO cell lengths can reduce machine acceptance. On the other hand, a doublet/triplet lattice structure has the advantage of long uninterrupted drift spaces for injection and collimation optimization.

The newly optimized SNS ring lattice has a hybrid structure with FODO bending arcs and doublet straight sections [6]. The lattice combines the simplicity and ease of correction of the FODO structure with the flexibility of the doublet structure. As shown in Fig. 1, the accumulator ring has a four-fold symmetry comprising four FODO arcs and four dispersion-free straights. The four straight sections house injection, collimation, RF, and extraction systems, respectively. Each straight section consists of one 9-m and two 5.5-m long dispersion-free drifts.
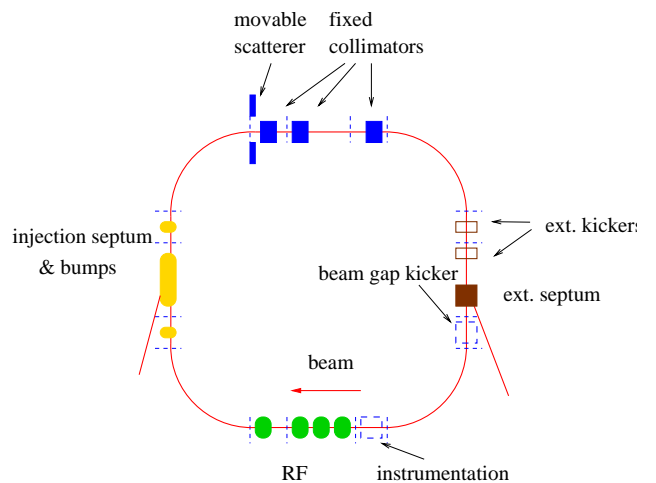

Figure 1: Schematic layout of the SNS accumulator ring. The four straight sections are designed for beam injection, collimation, extraction and RF systems, respectively.

Fig. 2 shows the layout and content of one of the four super periods. Each arc consists of four 8-m long FODO cells. Within each arc, five of the quadrupoles, at sites of large dispersion, are sandwiched by a chromatic sextupole and an orbit correction dipole. The other quadrupoles are sandwiched by two corrector packages containing both linear elements for orbit correction and decoupling, and nonlinear elements for resonance corrections.

3.2 Lattice functions and matching

The FODO arcs and doublet straights are optically matched to ensure maximum betatron acceptance. A horizontal betatron phase advance of 2π radians across each arc makes each arc an achromat. The dispersion is zero in the straight sections. Each dipole is centered between two quadrupoles so as to maximize the vertical acceptance of the dipoles.
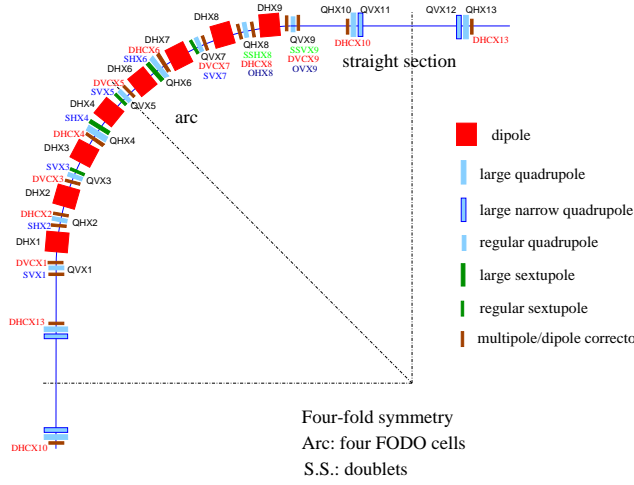
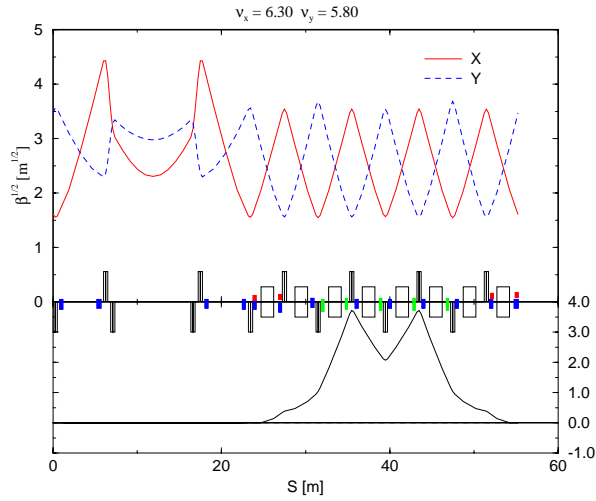Figure 2: Schematic layout and content of the ring arc.

Four-fold symmetry
Arc: four FODO cells
S.S.: doublets

Table 2: Comparison of SNS ring working points in the tune space.

(Q_x, Q_y)	Advantage	Disadvantage
(6.30, 5.80)	perfect matching split tune high tunes	near $2Q_x + 2Q_y = 24$ (space charge) near $2Q_x = 12$
(6.30, 5.27)	perfect matching split tune	near $3Q_y = 16$ near $2Q_y - Q_x = 4$ near $2Q_x = 12$
(5.82, 5.80)	coupled painting away from integer	large β_{max}/β_{min} coupling & growth loss-heavy for CERN $2Q_x - 2Q_y = 0$
(5.82, 4.80)	split tune away from integer	large β_{max}/β_{min} near $2Q_y - Q_x = 4$ loss-heavy for CERN

Figure 3: Lattice functions of one lattice super period consisting of a FODO arc and a doublet straight section.

3.3 Working points

Both the horizontal and vertical tunes can be adjusted by more than one unit without producing significant optical mismatch. The vertical tune is adjusted using the arc quadrupoles powered in two families. The horizontal tune is adjusted using the straight-section quadrupoles powered in three families.

Working points in tune space are chosen mainly to avoid major low-order structure resonances. Table 2 compares four candidates in (Q_x, Q_y) tune space. Working points with tunes split by more than a half-integer avoid possible strong coupling caused by space-charge forces and systematic magnet errors, thus preserving the painted beam distribution for the target.

4 PHYSICAL AND MOMENTUM ACCEPTANCE

In the transverse direction, the beam is painted to a large emittance during injection to reduce the space-charge force.

In the longitudinal direction, the beam momentum is broadened in the linac-to-ring transfer line using a "wobbling" RF cavity to improve particle painting in longitudinal phase space.

An adequate acceptance/emittance ratio is key to minimizing beam loss and to facilitating beam collimation and beam-in-gap cleaning. The transverse acceptance of the ring vacuum chamber (480 πmm·mr) is chosen to be about triple the full beam emittance. Fig. 4 schematically illustrates the transverse beam emittance, collimation admittance, and vacuum chamber acceptance. The green hexagon represents the vacuum chamber cross section (23 cm width, 15.2 cm height). The red squares and circles correspond to off-momentum ($\Delta p/p = \pm 1\%$) beam profiles achieved by correlated and anti-correlated painting.
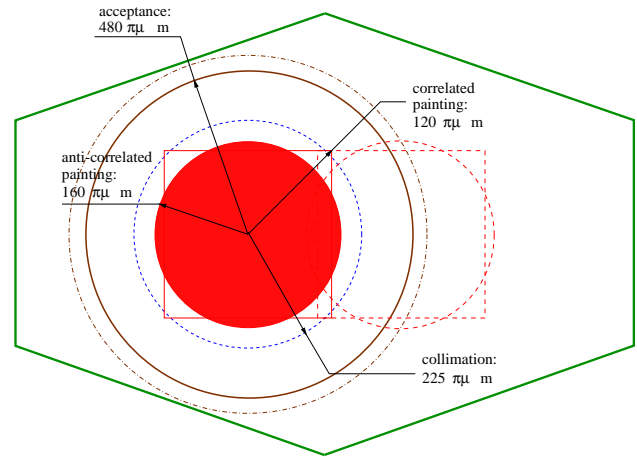

Figure 4: Schematic illustration of the beam emittance, collimation admittance, and vacuum chamber acceptance of the SNS ring. The vacuum chamber acceptance is 480 πmm·mr; the total transverse emittance of the beam is either 160 πmm·mr for anti-correlated painting or 240 πmm·mr for correlated painting. Ring collimation (blue) is designed with 225 to 260 πmm·mr admittance.

76

The beam momentum ($\Delta p/p$) is broadened to a full spread of $\pm 0.7\%$ in the linac-to-ring transfer line. The beam is then injected into a static dual-harmonic RF bucket with a momentum acceptance of $\pm 1\%$ (Table 3). With chromatic sextupoles for off-momentum optical compensation, the ring vacuum chamber can provide a momentum acceptance of $\pm 2\%$ for the full beam. The longitudinal beam tail escaping the RF bucket is excited by the beam-in-gap kicker and collected by the collimation system.

Table 3: Beam momentum spread, RF bucket acceptance and machine vacuum chamber acceptance.

Item	Value
Beam momentum full spread	± 0.007
RF acceptance at 40 kV (h=1)	± 0.010
Ring acceptance (480 πmm·mr)	± 0.010
Ring acceptance (160 πmm·mr)	± 0.020

5 INJECTION

5.1 Injection layout

As shown in Fig. 5, a 9-m drift between quadrupole doublets houses the fixed injection chicane. The field of the injection magnet is 3 kG to keep premature H^- stripping below 10^{-6} per meter. To prevent stripping of H^0 in $n = 4$ and lower excited states, the injection stripping foil is located at the downstream end of the injection dipole, and the field of the subsequent dipole magnet is 2.4 kG. The fringe field of the injection dipole is shaped so that stripped electrons spiral down to where they can be easily collected.

The two 5.5-m drifts accommodate symmetrically located horizontal and vertical dynamic kickers used for injection painting. The β-function perturbation caused by the injection chicane and the orbit bumps is about 2%. The maximum residual dispersion is about 0.2 m. The tune shift produced by the chicane (0.004) is small comparing with that produced by space-charge forces.

The fixed chicane does not cross ring lattice magnets. During lattice tuning, the strengths of the dynamic kickers are adjusted so that orbits in the fixed chicane stays constant. The injection system is thus decoupled from the lattice tuning.

5.2 Painting scheme comparison

Injection painting creates the transverse density and beam profile desired by the mercury target. Various painting schemes are explored: correlated, anti-correlated [21], and transverse coupled painting, as shown in Fig. 7.

Ideally, anti-correlated painting using opposite horizontal and vertical orbit bumps produces a K-V like distribution with an elliptical transverse profile and uniform density distribution in both transverse directions. Such a distribution can also be realized by painting in one direction and steering in the other direction. However, in the presence of space charge this scheme produces an excessive beam halo during
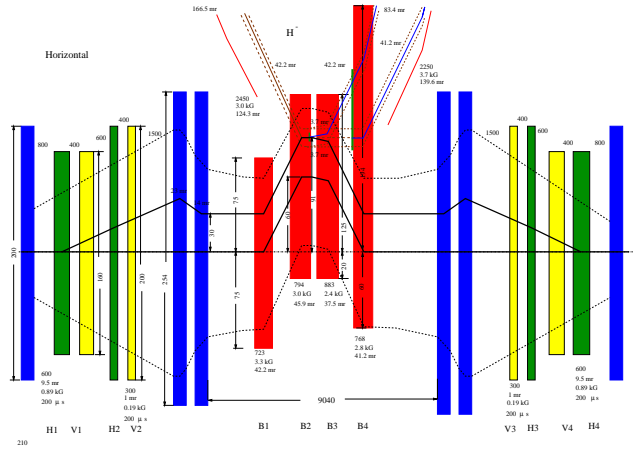

Figure 5: Schematic layout of the injection straight section. The red elements are the fixed injection chicane, the blue elements are ring lattice quadrupoles, and the yellow and green elements are the vertical and horizontal dynamic kickers, respectively.
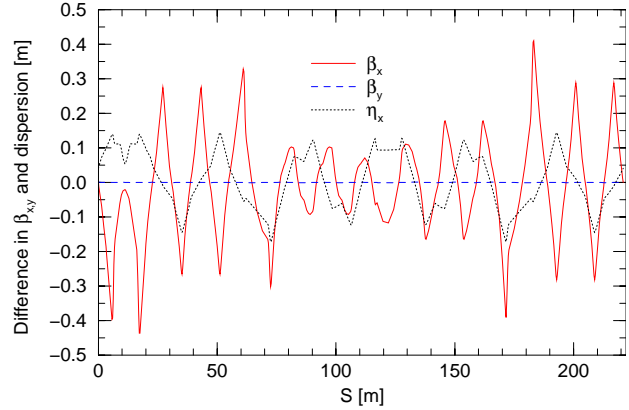

Figure 6: Lattice perturbation caused by injection chicane and the painting bumps.

the early stage of painting when the beam is narrow in one direction, as shown in Fig. 8.

Correlated painting using parallel horizontal and vertical orbit bumps produces a rectangular transverse profile. This scheme has the advantage that the beam halo is constantly painted over by freshly injected beams. The main concern is whether the rectangular beam profile can be preserved in the presence of coupling produced by space charge and magnet errors. Fig. 9 shows that splitting the transverse tunes can greatly reduce the impact of a systematic skew quadrupole component. At a space charge tune shift of 0.15, the effective increase in maximum emittance caused by the space-charge force is about 40% when the tunes are split by a half-integer.

6 EXTRACTION

The accumulated beam in the SNS ring forms a single 590 ns long bunch with a gap of 250 ns. Extraction is a two-step process: kick the beam vertically with fast kickers into a Lambertson-type septum magnet; then use the septum magnet to deflect the beam horizontally. The extraction system
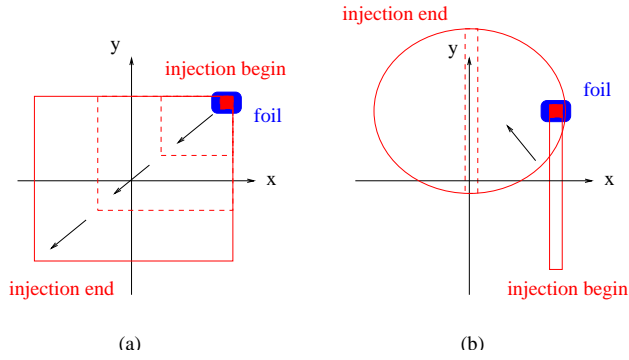
Figure 7: Two possible painting schemes: correlated (left) bumps resulting in rectangular shaped transverse profile, and anti-correlated bumps resulting in elliptical shaped profile.
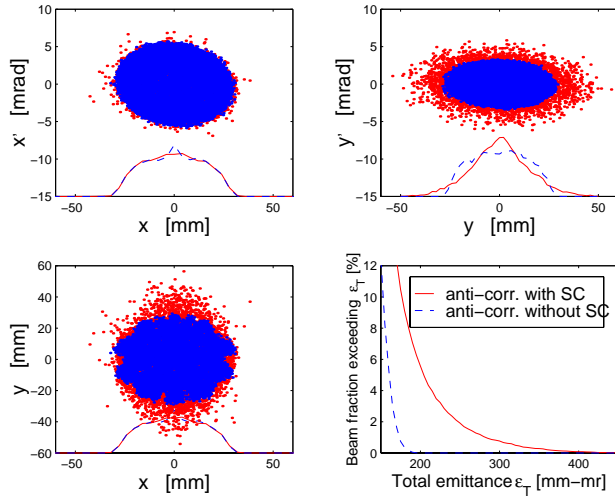

Figure 8: Vertical emittance growth in anti-correlated painting.

consists of 14 fast kickers and a single Lambertson septum, as shown in Fig. 10.

7 LOSS, HALO AND COLLIMATION

7.1 Beam loss mechanisms

Mechanisms leading to beam loss in the ring and transfer lines include incoming linac beam halo, incoming beam gap residual, H^- stripping, injection foil scattering, accidental extraction kicker malfunction, space-charge forces, magnet imperfections, and magnet misalignments. The incoming linac halo is cleaned by the linac-to-ring transfer line collimation system. A beam-in-gap kicker is used to clean the residual in the gap between subsequent beam pulses. Injection painting is designed to maintain an average of less than 6 foil hits per particle during the full 1200-turn accumulation. The extraction channel acceptance is designed to tolerate a failure of two out of fourteen extraction kicker magnets.

Table 4 lists the tune spread produced by space charge, natural chromaticity, magnet imperfection, fringe field, etc., as an indicator of their impact on the beam. Tune spread produced by kinematic nonlinearity is independently ob-
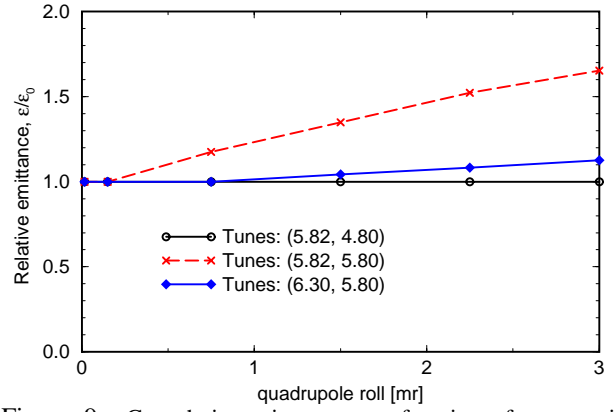
Figure 9: Growth in emittance as a function of systematic quadrupole roll for unsplit tune, half-integer split tune, and integer split tune working point. Only one quadrupole per lattice super period is rolled.
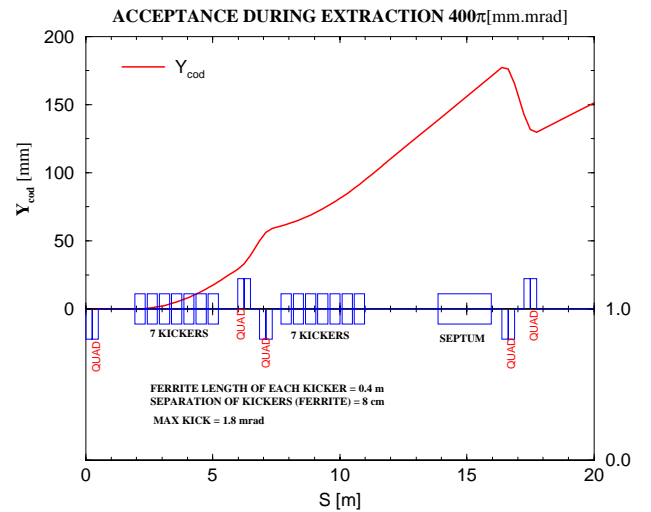

Figure 10: Ring extraction layout and closed orbit.

tained with TEAPOT [22] and MARYLIE [23] codes. Tune spread produced by the hard-edge fringe field model is obtained with MARYLIE.

7.2 Beam tail and halo development

Space-charge forces and magnet field errors can drive particles into resonance resulting in emittance increase and particle loss. Fig. 11 shows SIMPSONS [24] simulation result indicating the beam tail developed in the presence of space charge and magnetic errors when operating at the same-tune working point (5.82, 5.80). The tail development can be significantly reduced when a split-tune working point is chosen instead. These results have been independently confirmed using ORBIT codes [25] and UAL packages [26].

7.3 Collimation efficiency

Fig. 12 shows a comparison of collimation efficiency between the previous all-FODO lattice and the present hybrid lattice. With the long drift space provided by the hybrid lattice, the collimators can now be arranged at locations of
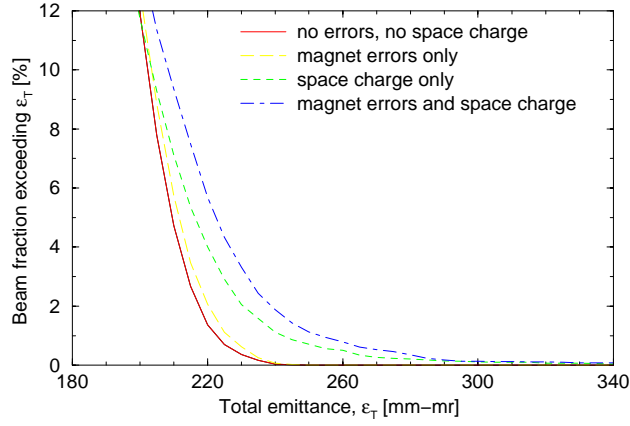
Figure 11: Beam tail driven by space charge and magnet errors. The same-tune working point (5.82, 5.80) is chosen to illustrate the impact.

optimum betatron phase to enhance the efficiency. A detailed discussion on the SNS ring collimation is given in Ref. [13].
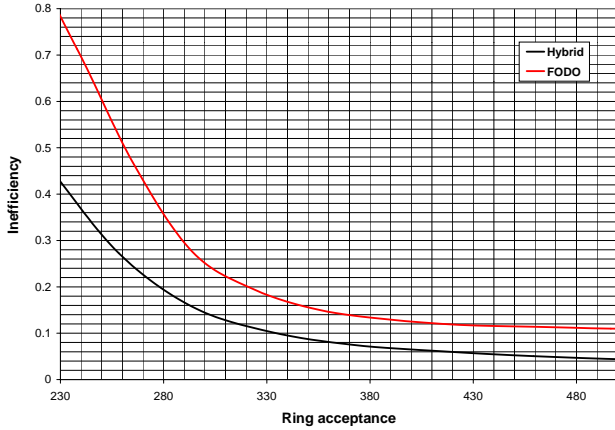

Figure 12: Comparison of collimation inefficiency between the previous all-FODO lattice (top curve) and the present hybrid lattice (bottom curve). The inefficiency is defined as the number of halo particles escaping the collimation system after one turn above a given amplitude.

8   MAGNET FIELD ERROR ANALYSIS

8.1   Expected field errors and compensation

The bore size of the SNS ring magnets is necessarily large to provide the required acceptance. The aspect ratio of the quadrupole bore ID to its magnetic length is about 0.5. With such a high aspect ratio, contribution from the magnet ends is significant. Table 5 indicates that in the absence of pole tip shimming, the error of the first allowed multipole (dodecapole, b_5) in the quadrupole magnet is exceedingly large. Multipole contribution from the un-shimmed dipole pole end contains a similarly large sextupole component.

With detailed pole-tip compensation, the integral field error can be greatly reduced. Table 6 shows the expected

magnetic error of the ring quadrupoles based on the measurement data of the AGS Booster magnets. Table 7 shows the expected misalignment of the magnets.

8.2   Dynamic aperture

As an example of dynamic aperture study, Figure 13 shows the impact of magnet field errors and the improvement from field compensation and orbit correction. The 6-dimensional (6-D) element-by-element computer tracking is performed with TEAPOT codes [22] and UAL [26] packages over the entire 1200 turns of accumulation. Initially, particles are launched at three momenta ($\Delta p/p = 0, \pm 0.7\%$) in five transverse directions with increasing betatron amplitude. The average dynamic aperture and the statistical errors are obtained from the results of 10 random seeds.
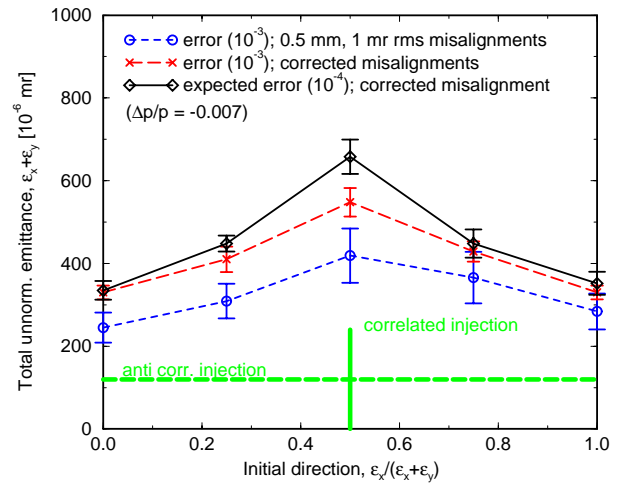

Figure 13: Dynamic aperture of the previous FODO lattice obtained from 6-D TEAPOT computer tracking.

9   CHROMATIC AND RESONANCE CORRECTION

Four families of chromatic sextupoles are needed to adjust the chromaticity to desired values across the beam momentum of $\pm 0.7\%$. Fig. 14 shows that with a two-family scheme, the optical distortion in β-function is as much as 30% for the off-momentum orbit. With a four-family scheme, the off-momentum optics can be greatly improved. Potential structure resonances are corrected by corrector magnet packages containing skew quadrupole, normal and skew sextupole, and octupole elements.

10   IMPEDANCE AND INSTABILITIES

The broadband impedance (Z/n) contributed by the chamber steps, BPM tanks, bellows, and vacuum ports and valves is in the range of j5 to j10 Ohms, smaller or comparable to the broadband impedance measured in the AGS, CERN PS, SPS, and ISR. To minimize resonance effects and complications, we taper the vacuum chamber steps and

Table 4: Tune spread produced by various mechanisms on a 2 MW beam with transverse emittance of 480 πmm·mr and momentum spread of $\pm 1\%$.

Mechanism	Full tune spread
Space charge	0.15
Chromaticity	± 0.08
Kinematic nonlinearity	0.001
Fringe field (hard edge)	0.025
Uncompensated ring magnet error	± 0.02
Compensated ring magnet error	± 0.002
Injection fixed chicane	0.004
Injection painting bump	0.001

Table 5: Integrated quadrupole end field from one magnet end before pole tip end shimming, extracted from 3D TOSCA calculation. Normalized to 10^{-4} of the main field at the reference radius R_{ref}. For regular ring quadrupoles, $R_{ref} = 10$ cm; for large ring quadrupoles, $R_{ref} = 12$ cm (approximately 92% of the quadrupole iron pole tip radius).

n	Normal		Skew	
	$\langle b_n \rangle$	$\sigma(b_n)$	$\langle a_n \rangle$	$\sigma(a_n)$
2	0.4	–	0.0	–
3	0.1	–	0.0	–
4	0.7	–	0.0	–
5	121	–	0.0	–

Table 6: Expected magnetic errors of ring quadrupoles. The multipoles are normalized to 10^{-4} of the main field at the reference radius R_{ref}.

n	Normal		Skew	
	$\langle b_n \rangle$	$\sigma(b_n)$	$\langle a_n \rangle$	$\sigma(a_n)$
Body	[unit]			
2	0.0	-2.46	0.0	-2.5
3	0.0	-0.76	0.0	-2.0
4	0.0	-0.63	0.0	1.29
5	0.20	0.0	0.0	1.45
6	0.0	0.02	0.0	0.25
7	0.0	-0.63	0.0	0.31
8	0.0	0.17	0.0	-0.11
9	0.70	0.0	0.0	1.04

Table 7: Expected alignment errors of ring magnets based on the survey measurement of the AGS Booster magnets and the AGS-to-RHIC transfer line magnets.

Item	Value
Integral field variation (rms)	10^{-4}
Integral field, transverse variation (rms)	10^{-4}
Ring dipole sagitta deviation	3 cm
Magnetic center position (rms)	$0.1 - 0.5$ mm
Magnet longitudinal position (rms)	0.5 mm
Mean field roll angle (rms)	$0.2 - 1$ mr
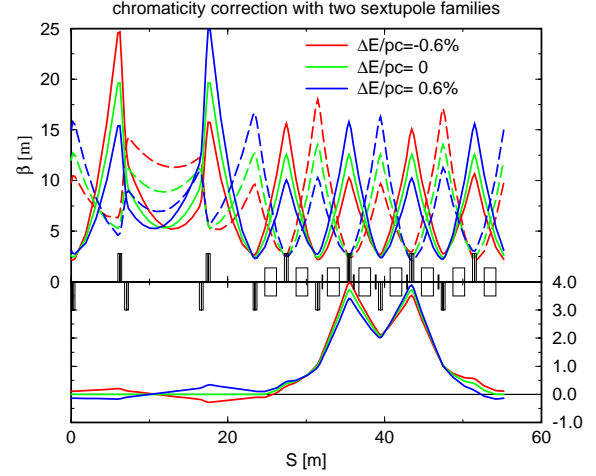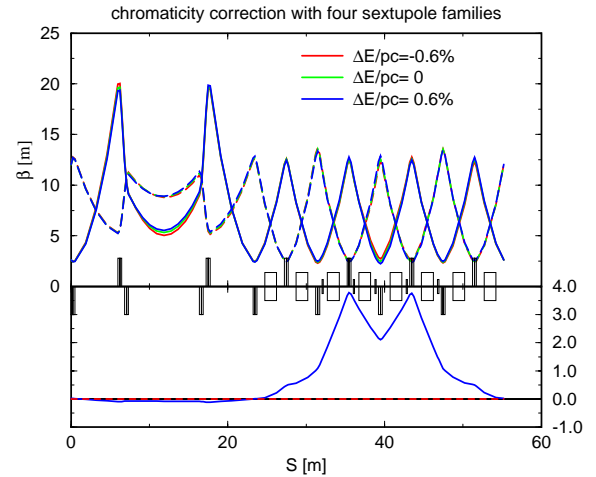
Figure 14: Off-momentum lattice function perturbation caused by a two-family chromaticity sextupole correction (top) and the improvement with a four-family sextupole scheme (bottom).

shield bellows and ports. The transverse impedance of the window frame extraction kickers is sensitive to winding terminations and stray parameters. We are considering optimization of the terminations to reduce kicker impedance.

Operational experience at the AGS and Booster has shown that the conventional formulation used for the resistive wall instability over-estimates the growth rate, presumably due to the fact that various Landau damping mechanisms are neglected. This conventional formulation predicts the SNS growth rate of a modest 1 ms at the end of stacking. Hence, the choice of stainless steel chamber is adequate. The inner surface of the vacuum chambers will be coated with TiN to reduce secondary electron emission [27].

11   SUMMARY

A FODO-doublet hybrid lattice provides optimum matching and flexibility for the Spallation Neutron Source accumulator ring. For this lattice, design optimization has

five goals: allow a low space charge tune shift (below 0.15) to avoid resonances; provide adequate transverse and momentum acceptance for beam collimation (acceptance/emittance ratio about 3); optimize injection to obtain desired target beam shape and minimize halo development; analyze and compensate magnet field errors; and control impedance and instability (e.g., via vacuum chamber coating and step tapering). With an expected collimation efficiency of more than 90%, the uncontrolled fractional beam loss is expected to be about 10^{-4}, thus achieving the design goal for machine availability and maintainability.

12 ACKNOWLEDGMENTS

13 REFERENCES

[1] *Spallation Neutron Source Design Manual*, June 1998.

[2] W.T. Weng, *SNS Accumulator Ring Design and Space Charge Considerations*, Workshop on Space Charge Physics in High Intensity Hadron Rings, AIP Conference Proceedings 448 (1998), p. 152.

[3] The so-called hands-on maintenance condition corresponds to an average radiation activation level of 1 to 2 mSv/hour measured at a distance of 30 cm from the machine device, 4 hours after machine shut-down of an extended run of 30 days or longer. See Summary of Workshop on Beam Scraping and Collimation, 1999 (to be published).

[4] T. Wangler, *RF Linear Accelerators*, Wiley & Sons, p. 285.

[5] T. Roser, private communications, 1999.

[6] *Preliminary Change Request for the SNS Ring Hybrid Lattice*, BNL/SNS technical Note 66, edited by J. Wei (1999).

[7] *Preliminary Design Report of a Rapid Cycling Synchrotron for the Spallation Neutron Source*, edited by J. Wei (to be published).

[8] J. Wei, J. Beebe-Wang, M. Blaskiewicz, P. Cameron, G. Danby, C.J. Gardner, J. Jackson, Y.Y. Lee, H. Ludewig, N. Malitsky, D. Raparia, N. Tsoupas, W.T. Weng, S.Y. Zhang, "Beam-Loss Based Design Optimization for the Spallation Neutron Source Ring" Proceedings of Particle Accelerator Conference, New York (1999) p. 3185.

[9] C. Gardner, Y. Y. Lee, N. Tsoupas, J. Wei, "An Alternative Lattice for the Spallation Neutron Source Accumulator Ring", Proceedings of Particle Accelerator Conference, New York (1999) p. 3182.

[10] M. Blaskiewicz, *Instabilities in the SNS*, PAC99 (1999) p. 1611.

[11] S.Y. Zhang, SNS Ring Technical Notes 33 (1997), 43 (1998), 61 (1999).

[12] S.Y. Zhang, *Secondary Electron Production at the SNS Storage Ring Collimator*, PAC99 (1999) p. 3297.

[13] N. Catalan-Lasheras, et al, Workshop on beam scraping and collimation, 1999 (to be published).

[14] N. Catalan-Lasheras, *Transverse and Longitudinal Beam Collimation in a High-Energy Proton Collider (LHC)*, Ph. D Thesis, Universidad de Zaragoza (1999).

[15] R. Witkover, et al, *Beam Instrumentation for the Spallation Neutron Source Ring*, PAC99 (1999) p. 2250.

[16] H. Ludewig, et al *Collimator Systems for the SNS Ring*, PAC99 (1999) p. 548.

[17] *Booster Design Manual*, Brookhaven National Laboratory (1986).

[18] Y. Cho, et al, *A 2-GeV, 1-MW Pulsed Proton Source for a Spallation Source*, EPAC96 (1996) p. 521.

[19] Y. Mori and S. Machida, private communications.

[20] G. Rees, private communications.

[21] J. Beebe-Wang, et al, *Transverse Phase Space Painting For SNS Accumulator Ring Injection*, PAC99 (1999) p. 1743.

[22] L. Schachinger, R. Talman, Part. Accel. **22**, 35 (1987).

[23] A. J. Dragt, et al, *MARYLIE 3.0 User's Manual*, University of Maryland, Physics Department Report (1999).

[24] S. Machida, *Space-Charge Effects in Low-Energy Proton Synchrotrons*, Nucl. Instrum. Methods, **A309** (1991) 43.

[25] ORBIT: written by J. Galambos et al.

[26] N. Malitsky, et al, *UAL-Based Simulation Environment for Spallation Neutron Source Ring*, PAC99 (1999) p. 2713.

[27] Recent experiments at the PSR indicate measured electrons is significantly less in TiN coated chambers than in stainless steel chambers. R. Macek, private communications.

Radiation Protection in 3GeV Synchrotron of JAERI-KEK Joint Project

H. Yokomizo and 3GeV Ring Group, JAERI, Tokai-mura, Naka-gun, Ibaraki, 319-1195, Japan

Abstract

The joint project of JAERI and KEK widely promotes advanced sciences in early next century based on high intensity proton accelerators. This includes three accelerators; a 600MeV linac, a 3GeV rapid cycling synchrotron (RCS) and a 50GeV synchrotron. The RCS is required to provide 1MW pulsed protons onto a spallation target for neutron production with a pulse length of less than 1μsec, as well as to provide a high quality protons to the 50GeV synchrotron. The design criteria of the radiation strength and the beam loss are discussed to handle a high intensity proton in the RCS to keep the machine radio-actively clean. The value of 1w/m beam loss is used in the design of the accelerator tunnel at the place with uncontrollable beam loss. The emittance of scrapers and beam ducts is reasonably chosen to minimize the beam loss as well as the construction cost.

1 INTRODUCTION

Japan Atomic Energy Research Institute (JAERI).and High Energy Accelerator Research Organization (KEK) agreed to combine their projects; neutron science project and Japan Hadron Facility to one joint project of a high intensity proton accelerators[1], which will be constructed in Tokai site of JAERI. This will cover a wide variety of science and engineering requiring high-power proton beam such as pulsed spallation neutron source, an accelerator-driven nuclear waste transmutation system, the fundamental particle physics, nuclear physics and a long-baseline tau-neutrino experiment.

The accelerator complex is composed of a 600MeV 50Hz linac including a super-conducting linac from 400MeV to 600MeV, a 3GeV, 25Hz rapid-cycling synchrotron(RCS) and a 50GeV 0.3Hz synchrotron. The linac beam is provided to the RCS with beam qualities of 50mA peak current, 0.5msec pulse length and 25Hz repetition rate, and to the transmutation experiment with same beam qualities as RCS, alternately.

The RCS accelerates the proton energy from 400MeV to 3GeV with the rate of 25Hz at initial phase. The injection energy into RCS will be upgraded to 600MeV in future when the super-conducting linac will be proven to produce a stable beam with a high quality. An average beam current is 0.333mA in RCS. The proton beam from RCS is provided to the 50GeV synchrotron by sequential four pulses (5%) among 25Hz pulses during 3.3sec and the rest of pulses (95%) are provided to three experimental areas: a pulsed spallation-neutron area, a muon experimental area and an exotic nulei experimental area, which are located in series.

2 3GeV RAPID-CYCLING SYNCHROTRON

The main parameters of 3GeV synchrotron are shown in Table 1. The lattice is designed to have three fold symmetry as shown in Fig. 1. A long straight section is composed of three cells, which provide 6m long free space per each cell. One straight section is dedicated to the injection magnet system by one cell and to a transverse beam collimation-collector system by two cells. Another straight section is dedicated to the
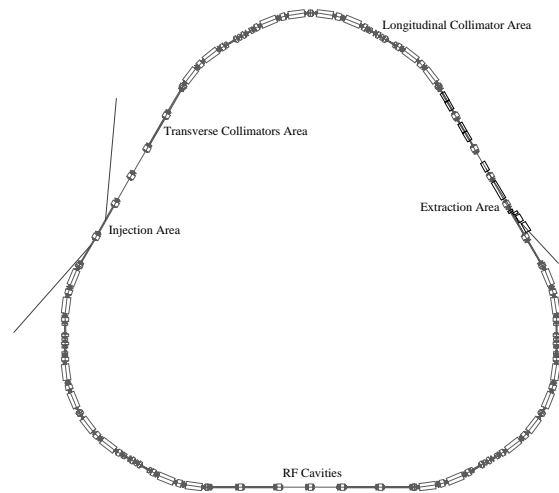
extraction system by one and half-cells and to a longitudinal collimation-collector system by one cell. The last one straight section is used for the space of ten RF cavities with 1.5m length per each.

Fig.1 3GeV synchrotron

Table 1. Major parameters of 3GeV synchrotron

Output energy		3 GeV
Input energy		400 MeV (600 MeV)
Operation frequency		25 Hz (Rapid cycle)
Particles		8.3×10^{13} ppp
Output power		1 MW
Lattice		FODO
Circumference		314 m
Superperiod		3
Cell number		27
Tune	X	7.35
	Y	5.8
Chromaticity	X	-9.0
	Y	-8.7
Momentum compaction factor		0.013

γ_t	9.0
Harmonics	2
Radio-frequency	1.36-1.86 MHz
RF voltage	420 kV
BM Number	24
Angle	15°
Type	Rectangular
Length	3.05 m
Radius	11.6 m
Field	1.1 T
QM Number	54
Families	6
Length	0.5, 0.75, 1m
Max-gradient	5 T/m
SM Number	18
Families	2
Length	0.4 m
Max-gradient'	$25 T/m^2$

The arc section consists of two modules of three FODO cells with two missing bends in the middle cell. This arrangement of the bending magnets makes momentum compaction factor tunable and also provides dispersion-free straight sections.

The maximum field strength of the bending magnets is at most 1.1T because of fast ramping. For the same reason, the maximum gradient of quadrupole and sextupole magnets is 5T/m and $25T/m^2$, respectively. The nominal tunes of x and y direction are 7.35 and 5.8, respectively and the tunability is kept adjustable within ±0.5. The momentum compaction factor is adjusted to be 0.013 in order to have the transition energy far from the extraction energy of 3GeV. Betatron oscillation amplitude and dispersion functions are shown in Fig. 2. The dispersion function becomes so large at the arc section that the longitudinal collimator will be installed in this location.
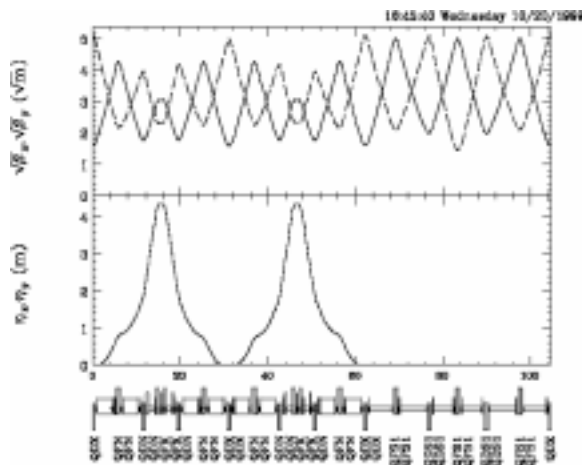

Fig.2 Betatron oscillation amplitude and dispersion functions

Proton beam is injected at the energy of 400MeV. The peak beam current is 50mA and average current is 0.333mA. Macro-pulse length is 0.5msec, which corresponds to the duration of injection. The chopping factor of the proton beam is 54% with 396nsec pulse length every 734nsec. Injected beam parameters are summarized in Table 2.

Table 2. Injected beam for 3GeV synchrotron

Beam energy	400 MeV
Repetition rate	25 Hz
Beam current (peak)	50 mA at 400 MeV injection
Average current	0.333 mA
Macro-pulse width	0.5 msec
Chopping factor	396 nsec / 734 nsec(54%)
Injection	681 pulses
Momentum spread	$\Delta p/p < 0.1$-$0.3\%(100\%)$
Emittance	4πmm∗mrad(100%)

The injected beam is painted in the area of 144 πmm∗mrad emittance for both horizontal and vertical planes in the 3GeV synchrotron. The emittance of the collimator and the beam duct are shown in Table 3. The collimator size is larger than the painted beam size by factor 1.5 to allow the beam brow-up. The duct size is larger than the collimator size by a factor of 1.5. For the magnet design, the thickness of the beam duct is reserved to be 16.5mm including the 1.5mm clearance between the duct surface and the magnet surface.

Table 3. Emittance

Injection painting	144 πmm∗mrad
Collimator	216 πmm∗mrad
Duct size	320 πmm∗mrad
Output beam	54 πmm∗mrad
Output aperture	216 πmm∗mrad

3 RADIATION PROTECTION

3.1 Beam Loss Estimation

Therqe are several points expecting the beam loss, such as an injection point, extraction point, beam dumps and scrapers. In order to determine the tunnel thickness, The beam losses at several points are evaluated as shown in Table 4. A large loss is expected at the injection section because of the charge exchange failure and a large angle scattering. About 2% of injected 600MeV beam is allowed to be lost at the injection area in our design. The loss should be very low at the extraction section by 0.1% of an output power. The power into the 3GeV beam dump is also kept very low by 1/25 times 1/10 of the full power 1MW to construct without a cooling water system. The beam loss at the other locations in RCS are kept lower than 1W/m to permit a human access for maintenance.

Table 4. Beam Loss expected in 3GeV Synchrotron

Injection point	4 kW
(Including transverse scraper)	
H0 beam dump	4 kW
Extraction point	1 kW
(Including longitudinal scraper)	
3GeV beam dump	4 kW
(Future upgrade, 40kW)	
Rest of 3GeV ring	1W/m
Beam transport line	1 W/m

3.2 Allowed Radiation

For human safety, the radiation should be less than some values during the beam operation. Table 5 shows design criteria of the allowed radiation in this joint project. Ground surface above the beam tunnel corresponds to the case of unrestricted public access. The soil radiation includes the ground water activation effect. Radiation of the soil produces 3.7Bq/g radio-activities in the case of the point loss, and one order smaller in the case of the line loss. Human access of radiation workers is unrestrictedly allowed at the place with the radiation of less than 6μSv. The access time will be controlled at the place with the radiation of larger than this values.

Table 5. Design Values of Allowed Radiation

Ground surface	0. 2 μSv/h
Soil radiation(point loss)	11.4 μSv/h
Soil radiation(line loss)	1.14 μSv/h
Skyshine at site boundary	30 μSv/y
Human access area	6 μSv/h

3.3 Accelerator Tunnel design

The typical cross sectional size is 6m in width and 3.5m in height in the RCS accelerator tunnel. The beam is located at 1.2m from the floor, and 3.5m away from the wall of the maintenance corridor side. The tunnel width is wider to be 8m at the injection and extraction sections for reserving extra-shield and space of a hands-on-maintenance. The nominal thickness of the tunnel concrete is required to be about 1.5m for side walls and about 2m for the floor and the ceiling, which should be covered by the soil of 5m below the ground surface. Thicker wall is required at the injection, extraction sections and the beam dump locations. The thickest ceiling is about 5m at the injection and extraction sections.

4 CONCLUSION

Design study of the high intensity proton accelerator complex has been started by JAERI and KEK for the joint project to explore the advanced science covering the wide range of the basic physics, applied science and the nuclear technologies.

The RCS(rapid cycle synchrotron) is second accelerator among threes, and has two roles as a booster to a 50GeV synchrotron and to a pulsed spallation neutron source. The beam loss and the radiation protection are important issues in the RCS for human access around the accelerator, as well as from point of view of the construction cost. In our design, the value of 1W/m is used for uncontrollable beam loss at any places, except the intended loss points.

REFERENCE

[1] 'The joint project for high-intensity proton accelerators', by The joint project team of JAERI and KEK, JAERI-Tech 99-056, KEK Report99-4, 1999.

Tolerable Beam Loss at High-Intensity Proton Machines

O. E. Krivosheev and N. V. Mokhov

Fermi National Accelerator Laboratory
Batavia, Illinois 60510

Abstract

Tolerable beam losses are estimated for high-intensity ring accelerators with proton energy of 3 to 16 GeV. Dependence on beam energy, lattice and magnet geometry is studied via full Monte Carlo MARS14 simulations in lattice elements, shielding, tunnel and surrounding dirt with realistic geometry, materials and magnetic fields.

1 INTRODUCTION

Several high-intensity proton accelerators are under operation, construction or design all around the world. Their beam energy ranges from several hundred MeV to 50 GeV with the beam power of up to 4 MW. One of them is the Proton Driver (PD), a 16 GeV high-intensity rapid cycling proton synchrotron planned at Fermilab. There are many common problems at the machines of such a class. A very high beam power implies serious constrains on beam losses in the machine. The hands-on maintenance, component lifetime, ground-water activation and radiation shielding are the most important issues driven by beam loss rates under normal operation and accidental conditions. This paper estimates tolerable beam loss levels in a several GeV energy range.

2 REGULATORY REQUIREMENTS

1. *Prompt radiation:* the criterion for dose rate at non-controlled areas on accessible outside surfaces of the shield is 0.05 mrem/hr at normal operation and 1 mrem/hr for the worse case due to accidents [1]. Currently, the document [1] uses the phrase "credible accident". The one hour continuous maximum intensity loss was required in the past but is not required under all conditions anymore. In many cases, it is not even possible for a machine to do this. It is unfair to designers of future accelerators to force this requirement. The document [1] requires that the machine designers describe and justify what a possible credible worse case accident is, and design the shielding—or modify operation of the machine—according to that [2].

2. *Hands-on maintenance:* residual dose rate of 100 mrem/hr at 30 cm from the component surface, after 100 day irradiation at 4 hrs after shutdown. Averaged over the components dose rate should be less than 10-20 mrem/hr. It is worth to note that the (100 days / 4 hrs / 30 cm) condition is practically equivalent to the (30 days / 1 day / 0 cm) one.

3. *Ground-water activation:* do not exceed radionuclide concentration limits $C_{i,reg}$ of 20 pCi/ml for ^{3}H and 0.4 pCi/ml for ^{22}Na in any nearby drinking water supplies. These limits have the meaning that if water containing only one of the radionuclides at the limit were used by someone as their primary source of drinking water, that individual would receive an annual dose equivalent of 4 mrem.

4. *Component radiation damage:* machine component lifetime of 20 years. Assume 10 Mrad/yr in the hot spots.

3 GROUND-WATER ACTIVATION

Ref. [1] defines the concentration limits for the two long-lived isotopes that most easily leach and migrate to the ground water: ^{3}H (half time $\tau_{1/2}$=12.32 yr, β^- decay mode) and ^{22}Na ($\tau_{1/2}$=2.604 yr, β^+ and γ decay modes). One should calculate creation and build-up of those nuclides. After irradiation over the time t, the concentration of a radionuclide i in the ground water in soil immediately outside the beam loss region is

$$C_i\left(\frac{pCi}{ml}\right) = \frac{1}{0.037}N_p S_{av}\frac{K_i L_i(1-e^{-t/\tau_i})}{n}, \qquad (3.1)$$

where N_p is the number of protons per second at the source, S_{av} is the star density above 50 MeV (stars/cm^3/proton) averaged over a volume surrounding the source out to an appropriate boundary (e. g., to 0.1% of the maximum star density at the entrance to the soil, that is a "99.9% star volume"), K_i is the radionuclide production yield (atoms/star), L_i is the leachability factor, n is the soil porosity, that is the ratio of the volume of void in the soil (generally filled with water), to the volume of rock (unitless), and τ_i is the mean lifetime of the radionuclide i, $\tau=\tau_{1/2}/\ln 2$. The $K_i L_i$ and w_i are the site specific parameters. Taking the Fermilab NuMI project [3] as an example, one gets for the glacial till: $K_{^3H} L_{^3H}$ = 0.075 atoms/star, $K_{^{22}Na} L_{^{22}Na}$ = 0.0035 atoms/star, and n=0.30. The sum of the fractions of radionuclide contamination (relative to regulatory limits $C_{i,reg}$) must be less than one for all radionuclides [3, 4]:

$$C_{tot} = \sum_{i=1}^{N}\frac{R_i C_i}{C_{i,reg}} \leq 1, \qquad (3.2)$$

where R_i is the reduction factor for the nuclide i due to vertical transport through the material surrounding the tunnel and horizontal transport in the aquifer. Usually, R_i is taken to be unity in such materials as dolomite, but $R_i < 1$ in glacial till and similar materials [4]. Using R_i=1 would therefore overestimate the result [2].

4 CALCULATION MODEL

The MARS code system [5] is used to perform all the calculations in this study. A new interface library has been

developed—using ideas and code of Ref. [6]—which allows one to read and build complex machine geometry directly from the MAD lattice description. The call-back mechanism is used to achieve such a goal. Namely, the user describes the geometry components at $\vec{r} = \vec{0}$ and unrotated, their field, materials and volumes as callable function with well-defined signature and registers them with the MAD interface code. Using information on lattice description, MAD generates rotation matrices and translation vectors for each particular elements together with glue elements. The call-back mechanism also allows one to register and call specific geometry, field and initialization function for any non-standard element in the lattice. The dipole, quadrupole and sextupole field components from the MAD lattice description are transfered to the respective field functions in order to correlate the field with lattice bending angle. An example of the PD pre-booster lattice geometry generated is shown in Fig. 1.

Figure 2: MARS model of a Fermilab Booster arc cell.

Figure 1: MARS model of a PD 3 GeV pre-booster arc cell.
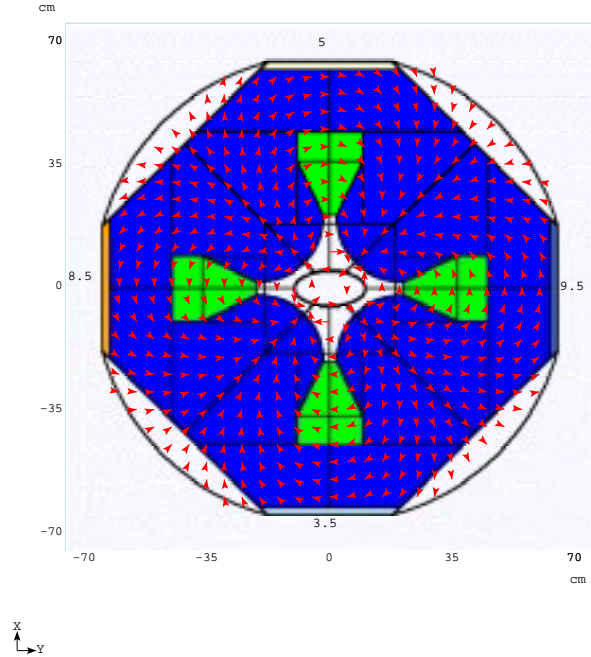
Figure 3: MARS model of 16 GeV PD quadrupole.

Using this MAD/MARS interface, the arc cells were built as per [7] and [8] for the Fermilab 8 GeV Booster(Fig. 2) and for the Proton Driver 3 GeV pre-booster (Fig. 1) and a 16 GeV ring. The lengths of the arc sections considered were about 20, 50 and 80 meters for 3, 8 and 16 GeV machines, respectively. The beam-lines include magnets, quadrupoles, bare beam-pipes (drifts) and tunnel geometry. The magnetic fields for the particular components were also implemented into the model. Typical cross-sectional views of the lattice elements in the calculation model are shown in Fig. 3 and Fig. 4.

As data and calculations show, beam loss distributions are quite different in different machines under given conditions. To deduct the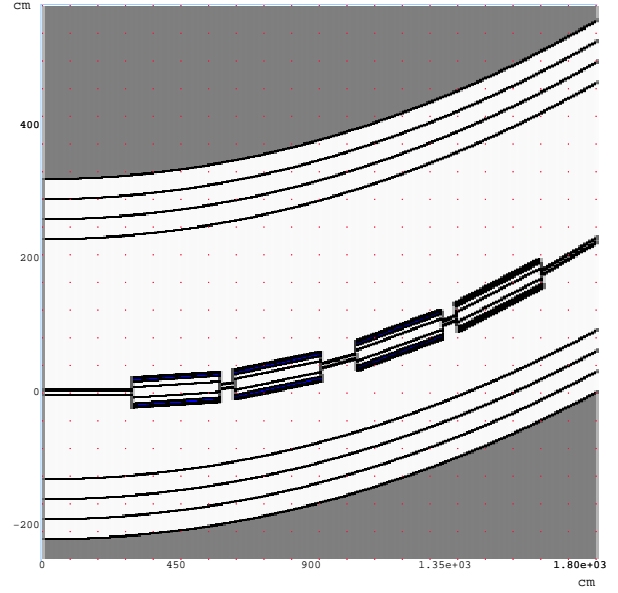 tolerable beam loss, it is assumed in this study for all three machines that the beam loss rate is quasi-uniform along the considered arc region and that protons hit the beam-pipe under a grazing angle of 1 mrad horizontally inwards for the 3 and 16 GeV machines and vertically up for the 8 GeV Booster. More realistic source can certainly be generated with such a tracking code as STRUCT [9].

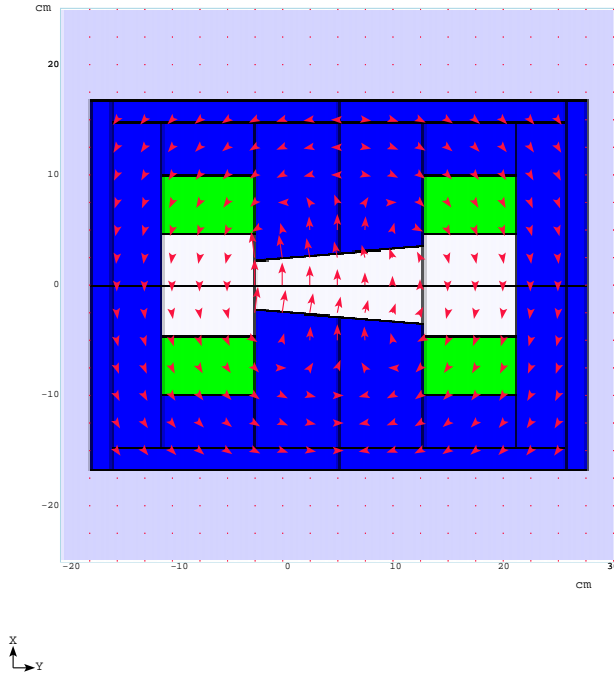Results of calculations are normalized per the beam loss

Figure 4: MARS model of Fermilab Booster defoc magnet.

of 1 W/m which is equivalent to

- $2.1 \cdot 10^9$ protons/(m·sec) for 3 GeV machine,
- $7.8 \cdot 10^8$ protons/(m·sec) for 8 GeV machine,
- $3.9 \cdot 10^8$ protons/(m·sec) for 16 GeV machine.

Calculated are energy deposition in dipole and quadrupole coils, star density near the magnet surface in order to deduce residual dose on contact using ω-factors for 30 days of irradiation and 1 day of cooling, averaged over the "99.9% volume" star density in soil to calculate the groundwater activation assuming a 20 yr irradiation time and the glacial till parameters with R_i=1, and dose equivalent distribution soil to estimate radiation shielding parameters.

5   RESULTS

5.1   16 GeV Proton Driver

Calculated peak residual dose rates on contact are shown in Fig. 5. The dose near the bare beam pipes exceeds the design goal for hot regions of 100 mrem/hr, being noticeably lower near the magnets due to significant absorption of soft photons in the dipole and quadrupole materials. One sees that hands-on maintenance is a serious issue with about 3 W/m as a tolerable maximum beam loss rate in the lattice elements, except for the long bare beam pipes where one should decrease the loss rate to 0.25 W/m to reduce the dose to 100 mrem/hr. One needs further reduction to bring the dose down to a good practice value of about 10-20 mrem/hr. Alternatively, one can think of providing simple shielding around the bare beam pipes. For ground-water activation

C_{tot}=0.975 immediately outside the 40-cm tunnel wall (see Eq. (2)), that allows 1.03 W/m beam loss rate. The peak accumulated dose in the coils is about 2 Mrad/yr at 1 W/m beam loss rate which is acceptable with use of appropriate materials for insulation.
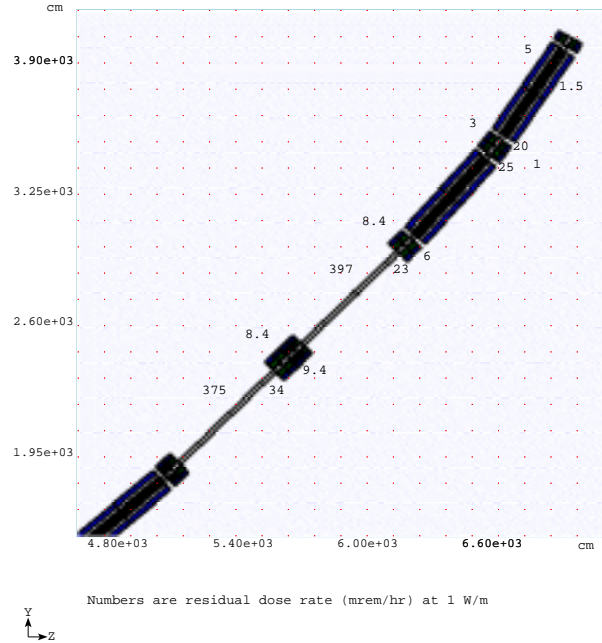

Numbers are residual dose rate (mrem/hr) at 1 W/m

Figure 5: Peak residual dose rates (mrem/hr) on the outer surface of the arc elements at 1 W/m uniform beam loss rate in the 16 GeV Proton Driver.

5.2   Fermilab Booster

At 1 W/m uniform beam loss in the arcs, the peak residual dose rates on contact are up to 350 mrem/hr on bare beam-pipes and 6 to 12 mrem/hr on magnet surfaces. The peak accumulated dose in the coils is about 0.6 Mrad/yr. For ground water C_{tot}=0.44, that allows 2.27 W/m. Therefore, hands-on maintenance is the limiting factor for the Fermilab Booster and the tolerable beam loss rate is ≤0.3 W/m.

5.3   3 GeV Pre-booster

At 1 W/m uniform beam loss in the arcs, the peak residual dose rates on contact are up to 150 mrem/hr on bare beam-pipes and 7 to 14 mrem/hr on magnet surfaces. Compared to the 16-GeV case, dose on the pipes is lower because the drifts are shorter, only 12.5 cm. The peak accumulated dose in the coils is about 1.6 Mrad/yr. For ground water C_{tot}=0.29, that allows 3.45 W/m. The tolerable beam loss rate is ≤0.67 W/m.

6   TUNNEL SHIELDING

Another distinctive value is the amount of dirt required for tunnel shielding. Dose on the outer shielding surface depends on the beam energy in a complex way. Assuming a

quasi-local beam loss in the dipole magnet positioned in the center of a 2-m radius tunnel with a 0.3 m concrete wall, dose equivalent was calculated with MARS14 as a function of a dirt thickness (ρ =2.24 g/cm^3). Fig. 6 shows this dependence for a 400 MeV beam (injection) and for three top beam energies considered in this paper under the same geometry, tunnel and beam conditions. As expected [10], dose at high energies scales as E$^\alpha$, where α is about 0.8, while $\alpha \geq 1$ at proton energies below about 1 GeV.
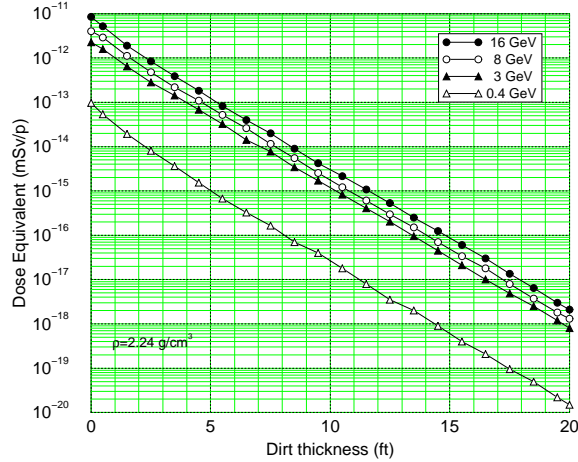
Figure 6: Prompt dose equivalent *vs* dirt thickness around the tunnel at a point-like loss of proton beams of different energies.

At the 16 GeV 15 Hz Proton Driver with 3×10^{13} circulating protons, the dose which corresponds to the 1 mrem limit for the worse case point-like loss of 1.62×10^{18} protons for an hour is D_0=6.18×10^{-24} Sv per proton (1 Sv = 100 Rem), requiring about 28 feet of the dirt shielding around the tunnel. With the accidental beam loss of 0.1% of the above—that can be defined as a *credible* accident for this machine—the shield thickness at 16 GeV is reduced to 18 feet.

7   CONCLUSIONS

- Each machine has different lattices, magnet geometry and materials, as well as properties of the soils around the tunnel. Beam loss distributions, driven by the collimation system performance (if such a system is implemented into the machine), are also quite different. Therefore, the tolerable beam loss should be determined for each machine individually together with the appropriate worse case beam loss scenario.

- In the cases studied in this paper, dose accumulated in the magnet coils is not a limiting factor.

- To meet the concentration limits immediately outside the 40-cm tunnel wall with the reduction factor R_i=1, the beam loss rates should be below than 1.03, 2.27

and 3.45 W/m in the arcs of the considered 16, 8 and 3-GeV machines, respectively.

- Hands-on maintenance is the limiting factor in all the considered cases, requiring beam loss rates in the arcs be as low as 0.1–0.25 W/m, if the beam-pipes are long and not shielded, and ∼1–3 W/m in the shielded case and in the magnets.

- Radiation shielding thickness scales non-linearly with the beam energy below about 1 GeV.

8   REFERENCES

[1] "Fermilab Radiological Control Manual", Article 236, http://www-esh.fnal.gov/FRCM/.

[2] J. D. Cossairt, Private communication.

[3] N. Grossman et al., "Refinement of Groundwater Protection for the NuMI Project", Fermilab-TM-2103 (2000).

[4] J. D. Cossairt, A. J. Elwyn, P. Kesich, A. Malensek, N. V. Mokhov, and A. Wehmann, "The Concentration Model Revisited", Fermilab-EP-Note-17 (1999).

[5] N. V. Mokhov, "The MARS Code System User's Guide", Fermilab-FN-628 (1995); O. E. Krivosheev and N. V. Mokhov, "A New MARS and its Applications", Fermilab-Conf-98/43 (1998); N. V. Mokhov, S. I. Striganov, A. Van Ginneken, S. G. Mashnik, A. J. Sierk, and J. Ranft, "MARS Code Developments", Fermilab-Conf-98/379 (1998); http://www-ap.fnal.gov/MARS/.

[6] D. N. Mokhov, O. E. Krivosheev, E. McCrory et al, "MAD parsing and conversion code", Fermilab-TM-2115 (2000).

[7] "FNAL Booster manual" Fermilab-TM-693 (1976).

[8] S. Holmes, editor, "A Development Plan for the Fermilab Proton Source", Fermilab-TM-2021 (1997).

[9] I. S. Baishev, A. I. Drozhdin and N. V. Mokhov, "STRUCT Program User's Reference Manual", SSCL–MAN–0034 (1994); http://www-ap.fnal.gov/~drozhdin/STRUCT/STR2.html.

[10] T. A. Gabriel, D. E. Groom, P. K. Job, N. V. Mokhov and G. R. Stevenson, Nucl. Instrum. Meth., **A338**, pp. 336-347 (1994).

OPERATIONAL EXPERIENCE WITH BEAM LOSS, SHIELDING AND RESIDUAL RADIATION IN THE FERMILAB PROTON SOURCE

R. C. Webber, Fermilab[*], P.O. Box 500, Batavia, IL 60510

Abstract

A report on beam loss, radiation shielding, and residual radiation experiences and status in the Fermilab Linac and Booster is presented. Historically, the Linac/Booster system has served only as an injector for the relatively low repetition rate Main Ring synchrotron. With the construction of an 8 GeV target station for the 5 Hz MiniBooNE neutrino beam and rapid multi-batch injection into the Main Injector for the NUMI experiment, the demand for Booster protons will increase dramatically over the next few years. Booster beam loss reduction and control are key to the entire future Fermilab high energy physics program.

1 THE LINAC

The original Fermilab Linac was designed and built as a 200 MeV proton accelerator in about 1969. It consisted of nine 200 MHz Alvarez style drift tube accelerating tanks. In 1977-78 the Booster was modified for multi-turn charge exchange injection and Linac was converted to accelerate H⁻ beam. Except for the ion source and preaccelerator, this was a minor change for Linac. It meant longer beam pulse lengths and lower pulse currents, typically 30 microseconds at 35 mA. In 1992-93, motivated by a desire to reduce space charge effects in the Booster, the four high energy drift tube tanks were replaced by 800 MHz side-coupled structures to increase the final Linac beam energy to 400 MeV. In addition to serving as an injector for the Booster, the Linac supplies 66 MeV H⁻ beam to the Fermilab Neutron Therapy Facility (NTF) for clinical cancer treatment. A ramped bending magnet between Tanks 4 and 5 steers beam to that facility between high energy physics (HEP) pulses.

The Linac RF power systems pulse continuously at 15 Hz; however, except for NTF operation, beam is not accelerated every 15 Hz cycle. Both the beam rate and pulse length are programmable for HEP needs. Typical operation is now 45 mA for 10-30 usec at an average rate of 0.5 Hz. This corresponds to an average beam current of 0.5 uA and 200 watts of beam power. The present capability of the 400 MeV Linac system is easily 20 uA or 8 kW (45 mA @15 Hz @30 microseconds). Acceleration efficiency from 10 to 400 MeV is >95% (see Figure 1). In early 1999, the Linac was outfitted with a proton source as a test to assess the ultimate beam current capability of the new high energy system. 400 MeV beam currents >90mA

were accelerated before beam loading in the RF systems and beam losses became significant. It was determined that the existing cavities and RF power systems should not limit operations up to 80 mA for pulse lengths approaching 100 usec.
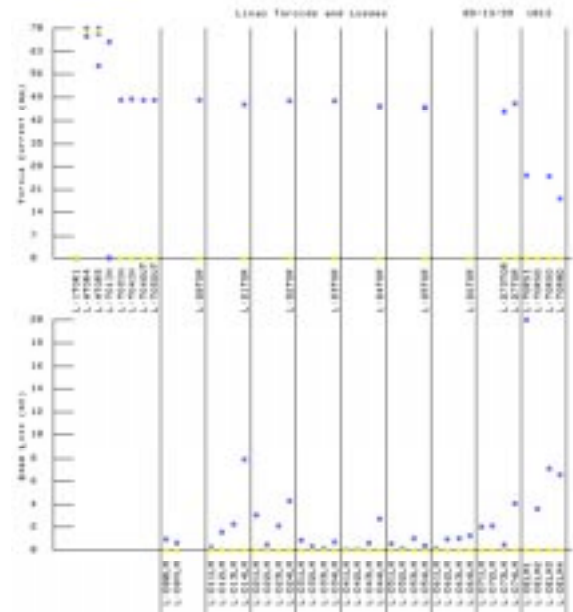

Fig. 1. Typical Fermilab Linac Beam Current (top) and Beam Loss Monitor (bottom) Display

Linac radiation shielding considerations [1] currently constrain operation to within a safety envelope of 3.5E17 400 MeV particles per hour. There are several interlocked radiation detectors monitoring sensitive locations to limit radiation under possible accident conditions. Given present operating conditions, detector trips are rare. Linac shielding limitations and detector trips may become an operational concern as the average HEP beam pulse rate increases, although Booster will be the tighter bottleneck.

Residual radiation levels of Linac beamline components have not been a significant problem for equipment maintenance. The highest radiation area in the Linac enclosure is the 400 MeV switchyard where a fast beam chopper sweeps beam across a Lambertson magnet to control the length of the beam pulse transported to the Booster. Figure 2 shows residual radiation readings taken along the Linac (excluding the 400 MeV switchyard
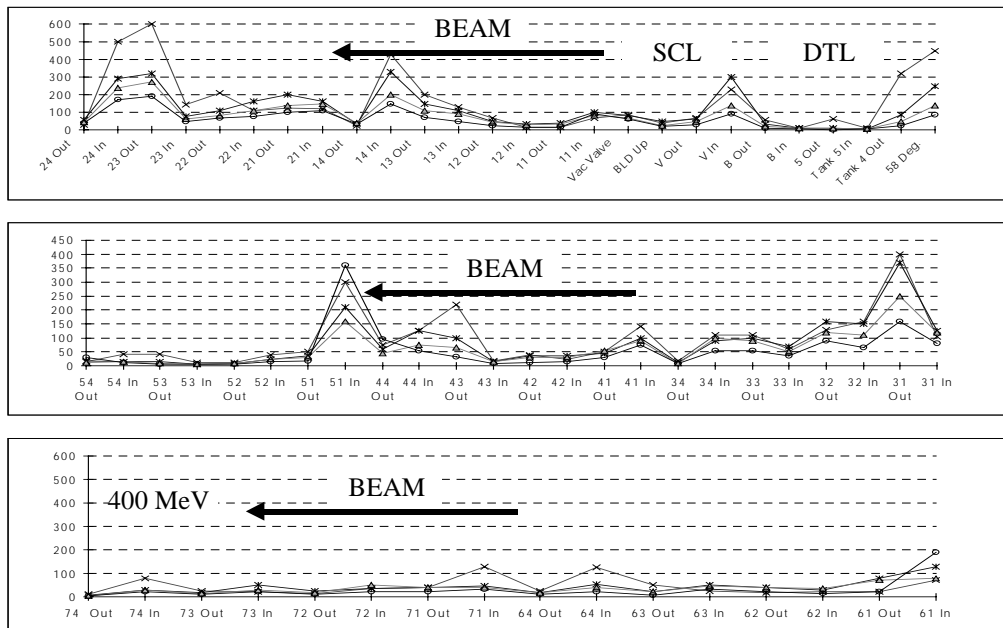
Fig. 2. Linac Residual Radiation Levels
Readings in mRem/hr "On Contact" after Several Hours Cooldown

region) on four different dates during the November 1994 to March 1996 period. Linac was regularly running around 1.3E16 particles per hour for Fermilab Collider Run I antiproton production during this time. Readings were taken "on contact" several hours after beam was turned off. In general, the high peak readings represent only very small regions of the beamline.

2   THE BOOSTER

The Fermilab Booster is a rapid cycling 8 GeV proton synchrotron built in 1970 [2]. Fundamental characteristics of the machine include a 15Hz sinusoidal magnetic cycle, a mean radius of 75 meters, adiabatic rf capture of the injected beam into harmonic 84 buckets, and a gamma transition of 5.4.   Booster was originally built for 200 MeV single turn proton injection with various possibilities for multi-turn proton injection schemes. It was modified for multi-turn H⁻ charge exchange injection in 1977 and then upgraded for the 400 MeV injection energy in 1992.

2.1 Performance and Demands for 8 GeV Protons

Beam intensities exceeding 5.5E12 protons per pulse (ppp) to 8 GeV have been achieved in the Booster. Typical operation is at >4E12 ppp with 8-10 injected turns (2.2 usec per turn at injection). Figure 3 shows the typical Booster beam charge signal through the cycle for operation at two different intensities. The efficiency of beam extracted to beam injected is >80% at 1E12 and falls to around 60% for >4E12. As seen in Figure 3 most of the loss occurs in the first 5 msec. Beam loss occurs at various uncontrolled locations around the ring.
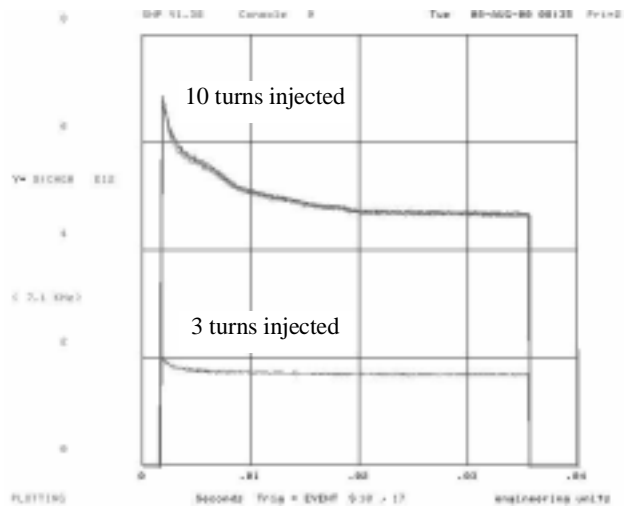

Fig. 3. Typical Booster Beam Intensity Through Cycle

Historically, Booster has run as high as 3E12 ppp at 2.5 Hz (2.7E16 protons per hour (pph)) for extended periods during Main Ring fixed target operations in the 1970's. Since that time construction of office buildings over the Booster tunnel, more restrictive radiation exposure regulations, and relocation of the Booster primary extraction point as Main Injector replaced the Main Ring have conspired to shrink the envelope for safe operations. Fermilab Collider Run II starting in March 2001 calls for Booster to provide 5E12 ppp at 0.7 Hz (1.26E16 pph). By 2003, with both MiniBooNE and NUMI experiments operational the demand rises to 5E12 ppp at 8 Hz, i.e. 1.44E17 pph. (Note for scaling purposes that 1E16/hr = 0.44 uA = 3.5 kW at 8 GeV.)

Within the coming year, the entire Fermilab program will be proton limited by allowed radiation around the Booster. Physical realities and the desire to maintain present building utilization severely limit options for additional shielding. Meeting these demands for 8 GeV protons within the radiation safety guidelines and controlling residual radiation levels to allow efficient maintenance of beamline components are key to the future of the entire Fermilab HEP program.

2.2 Booster 1998 Radiation Shielding Assessment

A complete reassessment of the Booster radiation shielding situation was undertaken in 1998 [3]. This effort was necessitated by several factors:

- the existing assessment was inadequate for anticipated proton requirements
- the primary extraction point was relocated for the Main Injector
- the existing assessment relied on a particular loss signature at a few locations to protect the entire ring which limited machine development flexibility, e.g. magnet moves and high energy orbit changes
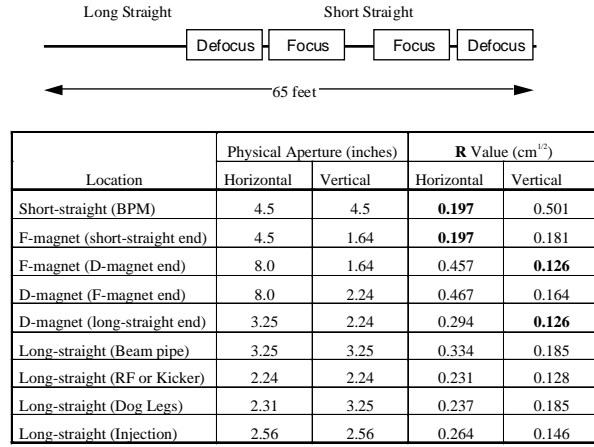
The new assessment was extensive:

- the complete shielding geometry for the entire ring was reviewed
- the utilization of all buildings and grounds in the Booster vicinity was reviewed
- many measurements and simulations were done to understand radiation patterns and levels for "normal" and for "accident" conditions
- numerous soil borings were taken for soil activation measurements

It was immediately obvious that the passive shielding around most of the Booster is woefully inadequate for the desired operating beam intensity. Efforts concentrated on establishing an array of interlocked radiation detectors to ensure a safety envelope for personnel in buildings and grounds around the Booster.

The Booster lattice is a regular DOFOFODO pattern comprised of gradient magnets. It was expected that radiation patterns due to beam loss should reflect the lattice periodicity. Figure 4 depicts the typical Booster lattice period with a chart of physical apertures and apertures normalized to beam size. Quite naturally, limiting apertures are associated with specific locations in the lattice. Measurements and simulations were performed for all conceivable beam loss scenarios to verify radiation patterns and to establish suitable locations for interlocked detectors with assurance of complete coverage.

Figure 5 shows measured surface radiation through thirteen feet of earth shielding directly above Period 9 in the Booster while using corrector dipoles to dump all the injected 400MeV beam in that period on the first turn. The family of curves corresponds to different corrector settings in attempts to lose beam at all possible locations in that lattice period. Clearly the radiation patterns bear a strong relationship to the lattice elements. For all possible

Location	Physical Aperture (inches)		R Value ($cm^{1/2}$)	
	Horizontal	Vertical	Horizontal	Vertical
Short-straight (BPM)	4.5	4.5	**0.197**	0.501
F-magnet (short-straight end)	4.5	1.64	**0.197**	0.181
F-magnet (D-magnet end)	8.0	1.64	0.457	**0.126**
D-magnet (F-magnet end)	8.0	2.24	0.467	0.164
D-magnet (long-straight end)	3.25	2.24	0.294	**0.126**
Long-straight (Beam pipe)	3.25	3.25	0.334	0.185
Long-straight (RF or Kicker)	2.24	2.24	0.231	0.128
Long-straight (Dog Legs)	2.31	3.25	0.237	0.185
Long-straight (Injection)	2.56	2.56	0.264	0.146

$$R = physical\_aperture / \sqrt{\beta}$$

Fig. 4. Booster Lattice Period and Apertures
Limiting Apertures in Bold Numbers

beam losses within the period, the radiation is strongly peaked at one of two locations associated with either the long or short straight section apertures. The Booster lattice consists of 24 periods, so there are 48 regular potential radiation peaks around the ring.

In an effort to assess the energy sensitivity of this characteristic pattern, beam was lost at different energies by gating off the accelerating RF at various times during the acceleration cycle. Correction dipoles were adjusted so as to cause the losses to preferentially occur as much as possible at one place in the ring, in this case Periods 6 and 7. The resulting surface radiation measurements (scaled to 1.35E17 pph) are shown in Figure 6. The location of the radiation peaks is seen to be energy independent and in agreement with the pattern for radiation due to mis-steered 400 MeV beam. At the higher energies (>6 GeV), the measured radiation is actually less than at lower energy. This simply illustrates the fact that it is physically not possible to lose the entire beam at one point in the ring at high energy. The largest dose occurs at the point of intended loss, but many particles are actually lost elsewhere around the ring. Peak dose rates through the thirteen feet of shielding scale to >2R/hour at 1.3E17 pph, highlighting the inadequacy of Booster's passive shielding.

Drawings like Figure 7 were produced for each different tunnel/surface building cross section to identify the thinnest shielding at each location and to establish the critical areas to be protected by interlocked detectors. Given this geometry information, the radiation measurement data, and supporting MARS calculations, the locations for >50 interlocked radiation detectors were established to protect the areas around the Booster. Note that single pulse accidents are not an issue and the interlocked detectors are fast enough to provide the required level of protection. Figure 8 shows the resulting final detector array deployment overlaid on a building utilization map.
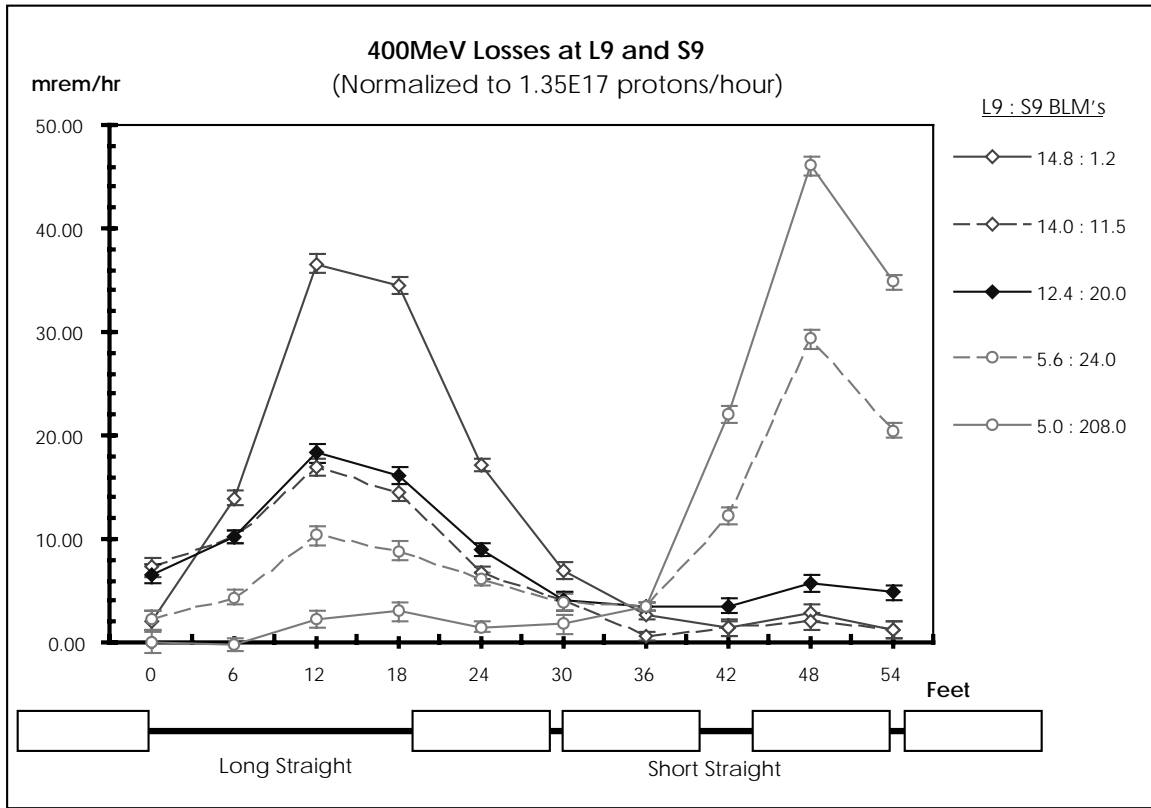
Fig. 5. Measured Surface Radiation Levels Through Thirteen Feet of Earth Shielding
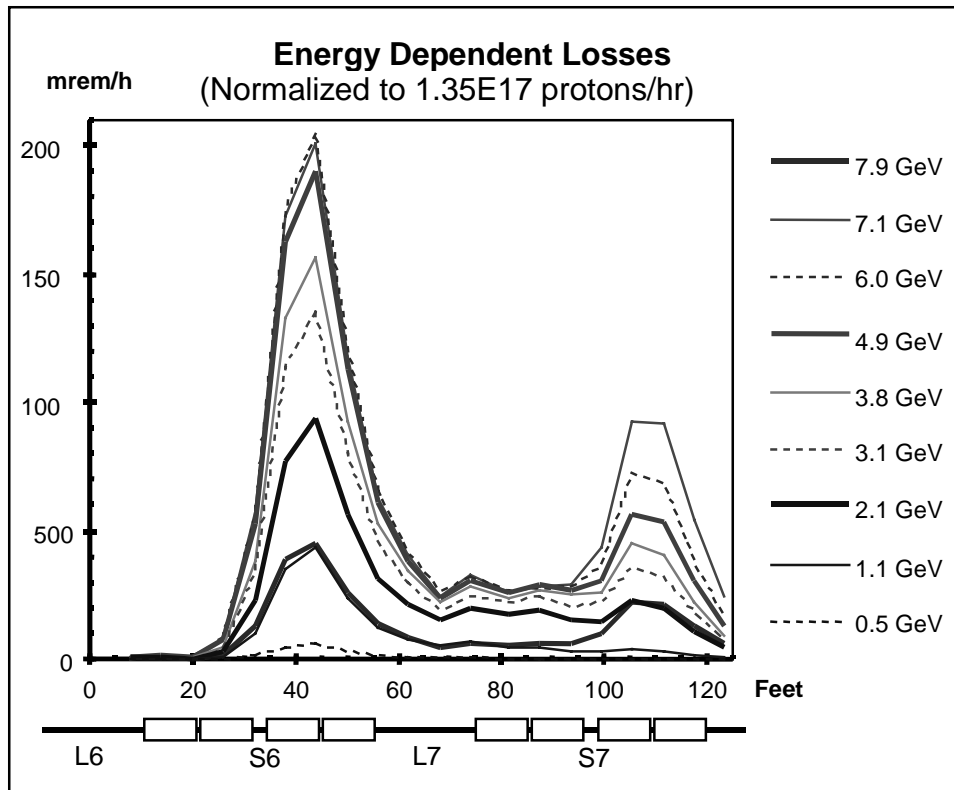Attempting to Dump All Injected 400 MeV Beam in One Period (scaled to 1.35E17 pph)

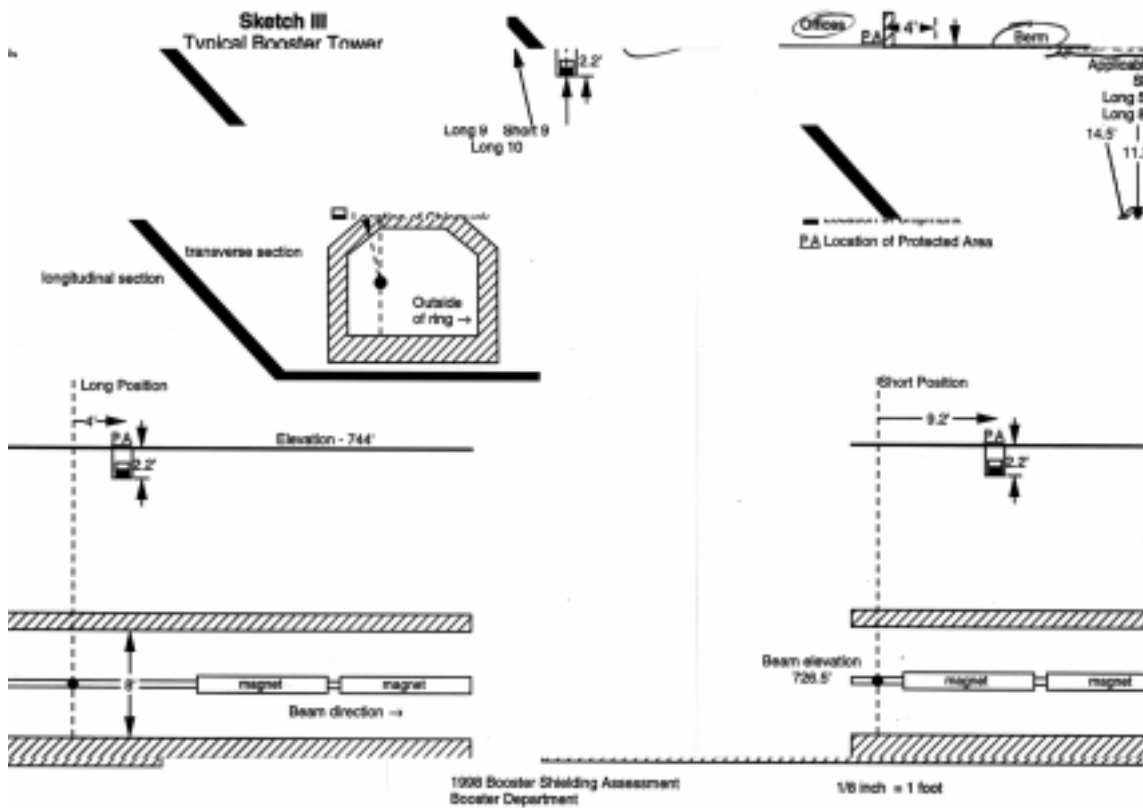Fig. 6. Energy Dependence Measurements of Surface Radiation

92

Fig. 7.   Typical Shielding Drawing Produced as Part of Booster Assessment

2.3   Booster Residual Radiation

Hands-on maintenance of beamline equipment has not been greatly impacted to date by component irradiation issues. The best reference period for quantizing residual rates is during Collider Run I when Booster operated for extended periods at 8E15 pph. Figure 9 is a typical radiation survey data sheet from that time period showing rates >2 R/hr at one foot on the extraction septum, the hottest spot in the Booster. Rates at the injection girder during Run I would have been around 500 mR/hr at one foot. Short straight section hot spots correspondingly ranged from 10-100 mR/hr and long straight apertures like rf cavities and kicker magnets were from 50-200 mR/hr.

Monitoring and controlling residual radiation will be crucial to maintaining Booster's historically high reliability and low downtime for Run II and beyond.

2.4   Towards Loss Reduction and Control

Booster beam loss is the result of numerous causes, some well understood and some not.

Beam from Linac is injected with 200 Mhz bunch structure. The revolution frequency in Booster during the multi-turn injection is not controlled to be a subharmonic of that frequency. The 200 Mhz bunch structures of successive turns interlace randomly and the remaining structure is allowed to de-bunch within a few turns. This beam is then semi-adiabatically captured by the Booster rf in 38 Mhz buckets. Some beam is lost as a result of this process. Efforts continue to understand and improve the efficiency of this process.

Space charge effects have long been associated with Booster beam loss; this was the motivation for increasing the injection energy from 200 to 400 MeV. Machine performance has improved, but debate continues as to whether the predicted improvement has been in fact quantitatively realized and to what extent space charge remains a significant problem.

Alignment and apertures have long been an issue in the Booster and continue to be addressed. There is an ongoing program of magnet moves to correct misalignments, open apertures, and adjust the high field closed orbit. DC corrector magnets are used to set the injection orbit, but as acceleration proceeds the effect of these elements diminishes and poor orbit control results. This, coupled with the small dynamic aperture of the Booster gradient magnets, makes for a touch-and-go situation to control transverse tunes and chromaticity even with existing ramped trim quads and sextupoles. The rf cavities, occupying eight of the twenty-four long straight sections, present themselves as limiting apertures.
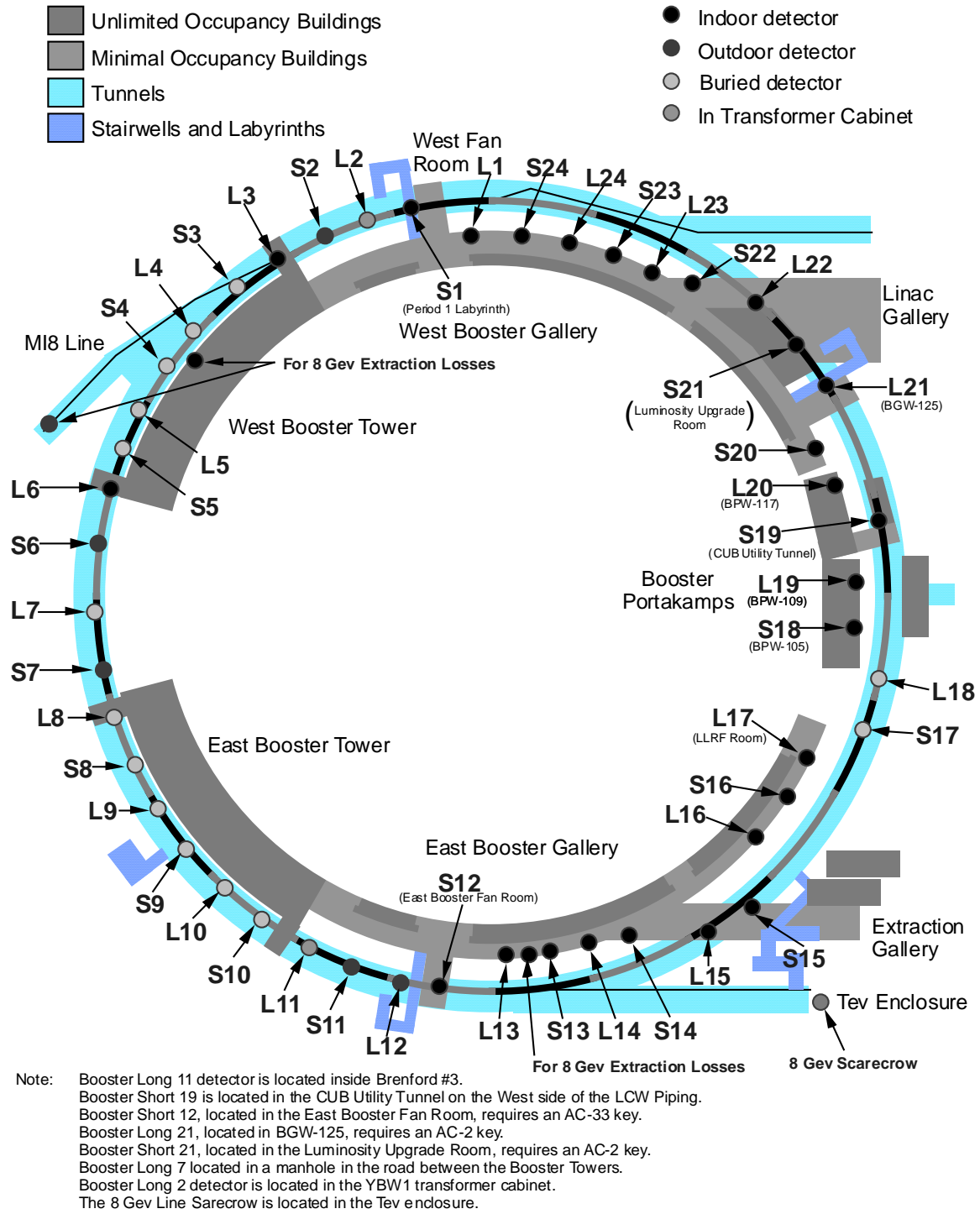
93

Booster Interlock Detector Locations

Legend:
- Unlimited Occupancy Buildings
- Minimal Occupancy Buildings
- Tunnels
- Stairwells and Labyrinths

- ● Indoor detector
- ● Outdoor detector
- ○ Buried detector
- ● In Transformer Cabinet

West Fan Room

S2 L2 L1 S24 L24 S23 L23

S3 L3

S4 L4 S22 L22

MI8 Line

S1 (Period 1 Labyrinth)

West Booster Gallery

Linac Gallery

For 8 Gev Extraction Losses

West Booster Tower

S21 (Luminosity Upgrade Room)

L21 (BGW-125)

L5 S5

S20

L6 S6

L20 (BPW-117)

S19 (CUB Utility Tunnel)

L7

Booster Portakamps

L19 (BPW-109)

S7

L18 (BPW-105)

L8

East Booster Tower

S17 L17 (LLRF Room)

S8

L18

L9

S16 L16

S9 L10

East Booster Gallery

S12 (East Booster Fan Room)

L15 S15

S10 L11 S11 L12 L13 S13 L14 S14

For 8 Gev Extraction Losses

Extraction Gallery

Tev Enclosure

8 Gev Scarecrow

Note: Booster Long 11 detector is located inside Brenford #3.
        Booster Short 19 is located in the CUB Utility Tunnel on the West side of the LCW Piping.
        Booster Short 12, located in the East Booster Fan Room, requires an AC-33 key.
        Booster Long 21, located in BGW-125, requires an AC-2 key.
        Booster Short 21, located in the Luminosity Upgrade Room, requires an AC-2 key.
        Booster Long 7 located in a manhole in the road between the Booster Towers.
        Booster Long 2 detector is located in the YBW1 transformer cabinet.
        The 8 Gev Line Sarecrow is located in the Tev enclosure.

Fig. 8. Booster Area Utilization Map and Interlocked Radiation Detector Deployment Map
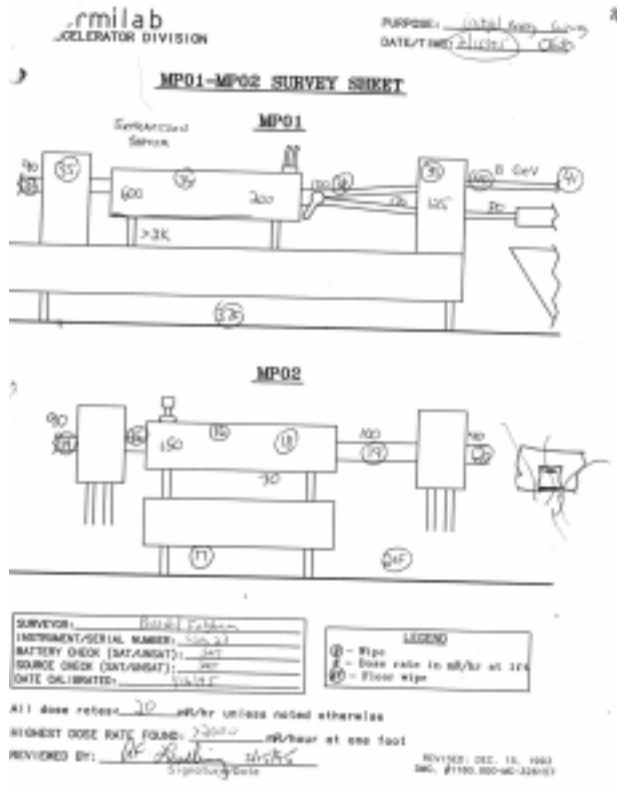
Fig. 9. Radiation Survey at Extraction Septum During Collider Run II (mR/hr at 1 ft. 24 hrs. after beam off)

R&D activity is underway to produce a modified cavity with increased drift tube aperture and satisfactory rf performance as a proof-of-principle.

At intensities above 3.5E12 ppp, coupled bunch longitudinal instabilities will cause beam loss after transition time in the cycle. Four single mode longitudinal dampers are used to control these instabilities.

Historically, Booster has operated with beam in all buckets. This results in extraction losses when the finite risetime of the extraction kicker wipes out two of the eighty-four bunches on the extraction septum magnet. This systematic 2% loss at 8 GeV is significant, especially since the extraction point happens to be located below offices at a region with the most stringent radiation controls. An additional four feet of steel shielding was installed under the offices in 1998. Recently a fast short-pulse kicker has been implemented to create a short gap in the Booster beam shortly after injection. Synchronizing this gap with the extraction kicker provides an important reduction in 8 GeV losses at the sensitive extraction location for the price of dumping some 400 MeV beam into a Booster magnet at a less sensitive location. This method of gap creation is far from ideal, but currently provides significant relief from the most pressing problem.

Further plans include

- improved longitudinal dampers to control coupled bunch instabilities at higher intensities
- design and installation of a scraper/collimator system to force unavoidable losses to occur at a controlled location which may be well shielded
- a cleaner method of creating a beam gap for the extraction kicker
- an improved beam loss monitor data acquisition system to better track machine performance trends

3 CONCLUSIONS

Beam loss and radiation issues will remain a chronic and increasingly important problem for the Fermilab Booster. A large array of interlocked radiation detectors has been deployed to ensure adherence to Fermilab Radiological Control Manual standards despite insufficient passive shielding. Learning to operate the Booster within this tightly constrained envelope at the required proton throughput rates is key to planned Fermilab high energy physics programs.

4 ACKNOWLEDGEMENTS

REFERENCES

[1] Fermilab Linac Shielding Assessment, Fermilab.
[2] 'Booster Synchrotron', edited by E.L. Hubbard, Fermilab, TM-0405, 1973.
[3] 1998 Booster Shielding Assessment, Fermilab, 1998.

IV. BEAM COLLIMATION

Beam Collimation Working Group Summary

D. Kaltchev, Y. Mori

The topics discussed were:

1. Comparison of different collimation methods (efficiency, design and engineering);

2. Momentum collimation and how to catch particles lost during rf capture and those due to large dp/p;

3. Location of collimators: requirements, dedicated sections, adaptation to an existing lattice.

The machines discussed were the proposed high intensity proton synchrotrons: ESS in Europe and SNS in Oakridge - neutron sources, the JHF booster, the 16 GeV Proton Driver as first stage of a $\mu\mu$-collider and the LHC. Among the operating machines: the Tevatron and the ISIS synchrotron.

For the needs of this working group, *collimation efficiency* was defined to be the fraction of beam halo particles collected within the collimation section during multiturn operation, relative to the total number of particles lost around the ring (relative controlled particle loss). One needs exact counts for absorption and outscatter, hence Monte Carlo simulations are required with high demands on precision – several such codes were reported: STRUCT–MARS, K2, the code of C. Warsop. Efficiency near or above 99% over $10^2 - 10^3$ turns is usually aimed for, as well as low halo hit rates (particles/sec) at crucial locations around the ring such as secondary collimators, cold elements and particle detectors.

The advantage of the *two-stage scheme* compared to the single collimator was acknowledged – particles backscattered from the latter continue to circulate. Comparative simulation studies (Tevatron Run II) give a factor of 4-10 in beam loss.

As far as lattice permits, the betatron phases of collectors with respect to scatterer are chosen according to the "$\mu, \pi/2, \pi - \mu$" scheme, with the $\pi/2$ collimator sometimes missing (see below). Derivation of the above phases is based upon the "black absorber" model: 1) single passage; 2) artificially wide distribution of initial angles at primary; 3) "black-absorber" secondaries. The advantage is that efficiency can be redefined in terms of the maximum surviving halo amplitude (a number) and numerical minimization applied. This model has been explored beyond single-plane collimation (mostly for the needs of LHC; works of J.B. Jeanneret et al). Some recent results were reported (D. Kaltchev) – the code DJ (Distribution of Jaws) provides optimization of jaw locations and angles for an arbitrary lattice (phase-advance and dispersion functions). The underlying assumption is that a high one-passage "black absorber" efficiency means also a high multi-turn Monte Carlo efficiency. The latter is the final criterion in any case. Some deviations from the "black absorber" optimum solution, presumably due to the multiturn definition of efficiency, are

– using a single instead of double-jaw collimator. This seems to be more a rule than exception. For a single jaw, the average impact depth over many turns is higher. Also, it allows to collimate particles with selected sign of the momentum deviation (negative, i.e. low energy side for the Tevatron). In the double-jaw case, having independent position control of the opposing jaw would help finding the closed orbit in realistic operation.

– most systems are designed separately in the horizontal and vertical planes. In some cases small tilt angles are applied (9 degrees in the ESS study). An optimization aiming to capture in a single passage the halo particles with large betatron amplitudes in both planes (jaw tilt angles varied too), is carried out in the LHC design.

– orthogonal scattering is sometimes neglected. Neglecting the $\pi/2$ jaw is justified if scattering orthogonal to the plane of collimation is not taken into account. The third collimator helps in the SNS hybrid lattice (N. Catalan), with computations done for both black and realistic secondaries.

– deviations of around 10% from the phases "$\mu, \pi/2, \pi - \mu$" do not affect significantly the tracking results (ESS accumulator and most other designs).

Full optimization studies were presented (A. Drozhdin, N. Mokhov) of the Tevatron Run II and of the preliminary lattice for the 16 GeV Proton Driver. This included graphs of particle losses around the rings (W/m) computed with MARS. More than 99% of losses are collected at top energy.

Direct experimental confirmation of the two-stage scheme was reported by Nuria Catalan – the 120 GeV SPS beam is made to coast towards a system of scatterer and two collectors, arranged so that all halo fractions are accounted for. The measured rates agree with simulations (K2 code).

One could further notice, that the efficiency is related to parameters such as average impact depth and number of revolutions between hits. Such results were discussed on this workshop – Tevatron Run II, ESS accumulator (C. Warsop) and had been reported previously – HERA (M. Seidel), LHC (T. Risselada) and others. The impact parameter depends on proximity to resonances (for a linear machine) and on the collimator arrangement – for instance larger number of primary collimators means that fewer turns are needed to achieve the same efficiency, but also smaller impact depth.

The shape of collimators used is: (in transverse direction) flat, "L"-shaped with independent hor./vert. degrees of freedom (Tevatron); slightly angled (ESS accumulator study); fully angled (LHC) and (in longitudinal direction) set back with respect to the beam envelope, with a slope to match the beam envelope (Tevatron Run II).

The *bent crystal* shows promising results with respect to lifetime and cost and the expressed concerns were mostly about the introduced by the crystal angle spread in a multiturn operation. Halo extraction with an *electrostatic deflector* was successfully tried in the $\mu\mu$-collider design. Magnetized collimators were not discussed.

For *momentum collimation* a ring lattice location with high dispersion is needed for the primary collimator. Ex-

ceptions (ways to avoid this) are the beam-gap kicker foreseen at SNS and placing the scatterer in a curved transport channel (ESS accumulator). In a dedicated lattice with dispersless straight sections, the ideal primary location seems to be the highest point of the last dispersion peak before the straight section (as in the JHF 3GeV Booster, Y. Mori). In the last work, a flat-top dispersion peak is achieved by splitting the focusing quadrupole in the last "missing magnet" cell. In general, space limitations in the arc and difficulties in increasing the dispersion in the straight section, force us to search for compromises.

D. Kaltchev presented a mix of theory, on which the code DJ is based, and observations made during distributing jaws for the LHC – the advantages of placing the primary jaw at the highest point of the normalized dispersion peak (zero derivative) are: 1) more amplitude space is left for halo circulation at high momenta; 2) secondary collimators act the same way for all momenta (known result). The code DJ provides mixed betatron-momentum optimization of the jaw locations for an arbitrary lattice.

An important remark (A. Drozhdin) was about the benefit of placing the secondary jaw in a location with high dispersion as well, if such location is available.

Two-stage betatron and momentum collimation studies with applications to LHC

D. Kaltchev[1]

TRIUMF, 4004 Wesbrook Mall, Vancouver, B.C., Canada V6T 2A3

We consider a single passage of the circulating beam through some set of collimators, primary and secondary ones, all located in a bend free lattice section. We assume that the primary collimators are "pure scatters" – circulating particles scatter at their edges (and only there) in forward direction thus creating secondary halo. The function of the secondary collimators positioned at a little higher aperture n_2 is to intercept the halo. The secondaries are "black absorbers" – any particle touching them is considered lost.

In this report we investigate the following problems [1], [2]:

Let's fix the lattice of the collimation section and the collimators. How to compute the maximum betatron invariants (amplitudes) of a secondary halo particle surviving all secondary collimators: in-plane horizontal $A_{x,max} \equiv max\sqrt{x_0^2 + x_0'^2}$, vertical $A_{y,max} \equiv max\sqrt{y_0^2 + y_0'^2}$ and combined $A_{max} \equiv max\sqrt{x_0^2 + x_0'^2 + y_0^2 + y_0'^2}$. In these definitions x_0, y_0 are initial normalized coordinates of halo particles (points along the primary collimator borders) and x_0', y_0' are initial normalized angles ranging from $-\infty$ to $+\infty$ to describe all possible forward directions.

For arbitrary optics and set of halo sources x_0, y_0 and for the case of flat collimators (pairs of opposing jaws), $A_{x,max}$, $A_{y,max}$, A_{max} are computed by the code DJ (Distribution of Jaws) [3]. Circular collimators can be approximated by many-side polygons and treated the same way. The mapping procedure implemented in DJ is equivalent to linear tracking but is much faster.

To describe momentum collimation in an arbitrary lattice (matched dispersion non-zero) we consider [4] monochromatic δ-fraction of the circulating beam and assume that the relative off-momentum offset $\delta \equiv \Delta p/p$ of the particles is the same before and after scattering. The same mapping technique is then used to compute the momentum dependence of the maximum *betatronic* parts of the amplitudes of escaping particles: $A_{x,max}(\delta)$, $A_{y,max}(\delta)$, $A_{max}(\delta)$. These functions are decreasing in most cases and continuous if the set of source points is continuous. Some restrictions apply on the value of the normalized dispersion at the primary collimator and its derivative, if one wants to protect over one turn locations with highest dispersion around the ring (the LHC arc).

For betatron collimation, the combined invariant A_{max} (important for the LHC) can be computed without a code, by plotting contours of constant 4D-emittance on the plane of initial betatron phases. In a simple example (lattice) we

show that small A_{max} can only be obtained if the difference between horizontal and vertical betatron phase advances (the split) varies along the collimation section. The role of the varying phase advance split was first pointed out by Risselada [5].

Next comes the optimization problem: where and what secondary collimators one should locate to get minimum $A_{x,max}$, $A_{y,max}$, A_{max} for a given δ (or a combination of these taken with some weights)? The code provides automatic minimization procedure (simulated annealing method) which has the advantage that it produces many equivalent solutions (secondary jaw distributions).

1 2-STAGE BETATRON COLLIMATION SYSTEMS

1.1 1D case

In case of collimation in a plane, Fig 1, the primary collimator is located at $s = 0$ at amplitude n_1 (in units of σ) and the secondary ones are at amplitude $n_2 > n_1$. The phase advance along the beamline is $\mu(s)$, with $\mu(0) = 0$. The halo sources are two points $x_0 = \pm n_1$ with initial non-normalized angles within $(-\frac{\pi}{2}, \frac{\pi}{2})$. The task is to find secondary jaw configuration that minimizes $A_{max} \equiv max\sqrt{x_0^2 + x_0'^2}$ (maximum is taken over all normalized angles x_0' corresponding to surviving trajectories). The optimum configuration is: two secondary collimators located at phases μ_{opt} and $\pi - \mu_{opt}$, where $\mu_{opt} \equiv arccos(n_1/n_2)$. The minimum value is $A_{max} = n_2$ and at optimum the maximum initial angle corresponding to surviving trajectory is $|x_{0,max}'| = \sqrt{n_2^2 - n_1^2}$. We notice that $A_{max} = n_2$ is the smallest achievable amplitude, i.e. the system acts as a *"1 D pipe"*.
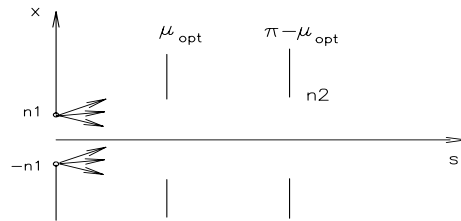
1.2 2D case, circular symmetry

All primary and secondary collimators are circular and the horizontal and vertical phase advances are equal $\mu_x(s) = \mu_y(s)$ for all s. The halo is defined by: $x_0^2 + y_0^2 = n_1^2$ with non-normalized angles in both planes within $(-\frac{\pi}{2}, \frac{\pi}{2})$. The aim is to minimize $A_{max} \equiv max\sqrt{x_0^2 + x_0'^2 + y_0^2 + y_0'^2}$. The optimum phases are $\mu_{x,opt}$, $\pi - \mu_{y,opt}$ and $\pi/2$. Using the two optimum collimators described above 1D pipe is created in each x and y plane, but also a third collimator at phase $\pi/2$ has to be added in order to minimize A_{max}. For instance with $n_1 = 6, n_2 = 7$, one gets $A_{max} \sim 9.2$.

[1]e–mail: Dobrin.Kaltchev@cern.ch

1.3 2D case, arbitrary lattice

Now let the lattice is described by two arbitrary phase advance functions $\mu_x(s), \mu_y(s)$ with $\mu_x(0) = \mu_y(0) = 0$ and the halo sources and minimized object A_{max} are the same as in the previous section. Equivalently, we can describe the optics by the "split function" $\mu^-(\mu^+)$ where $\mu^\pm(s) \equiv \mu_x(s) \pm \mu_y(s)$. What is the optimum arrangement of secondary collimators?

– it can be found numerically for the case of jaws. The algorithm is given in the next chapter for the more general case of momentum collimation (arbitrary δ).

– a "2D pipe" can be built for every source point (x_0, y_0) in the following way. One should place a collimator for every solution (pair μ_x, μ_y) of the equation:

$$\frac{(x_0)^2}{\cos^2\mu_x} + \frac{(y_0)^2}{\cos^2\mu_y} = n_2^2 \qquad (1.1)$$

If so, then the absolute minimum $A_{max} = n_2$ is achieved.

This definition may look too abstract because 1) even for one source point it requires an infinite number of collimators and 2) if x_0, y_0 are unequal and both non-zero then realistic lattices satisfying it do not exist. We expect however that for solutions providing $A_{max} \sim n_2$, i.e for a large number of optimized collimators in a "good" lattice, the optimum set of phases is not far from the ideal one. It can also be demonstrated that in order to minimize A_{max} lattice locations s with both large and small split $\mu^-(s)$ must be present. The proof is based on the "method of contours" – an alternative method to compute A_{max} without any code. We postpone with this until Chapter 3.

2 OPTIMIZATION OF A JAW COLLIMATION SYSTEMS (BETATRON AND MOMENTUM) BY CODE DJ (DISTRIBUTION OF JAWS).

2.1 Halo definition for $\delta \neq 0$

To define the halo we follow the motion of some circulating particle with $\delta \neq 0$, which becomes particle of the halo trough scattering at point $P = (x_0, y_0)$ (angle and amplitude jump).

The horizontal invariant before the scatter (Fig 1) is $A_{x,circ\ beam} = |x_0 - \delta\,\eta_0|$ and after the scatter the invariants are: horizontal

$$A_x(x_0, x_0') = \sqrt{(x_0 - \delta\eta_0)^2 + (x_0' - \delta\eta_0')^2} \qquad (2.2)$$

and combined

$$A(x_0, x_0') = \sqrt{(x_0 - \delta\eta_0)^2 + (x_0' - \delta\eta_0')^2 + y_0^2 + y_0'^2} \quad (2.3)$$

Within the collimation section (there are no bends; the radius vectors of **3** and **4** perform rigid rotation around the origin) the halo trajectory **3** is:

$$x(s) = x_0\,\cos\mu_x(s) + x_0'\,\sin\mu_x(s) \qquad (2.4)$$

(+ similar for y). Here $\eta \equiv \frac{D_x}{\sqrt{\beta_x\varepsilon}}$ is the normalized dispersion $D_x \neq 0$ is the matched dispersion, ε is the emittance.

Everywhere index 0 denotes values at the primary collimator (point P) and η' denotes derivative of η with respect to the horizontal phase advance μ_x.

In the LHC case, with one pair of opposing primary jaws, Fig 1, the halo exists ($A_{x,circ\ beam} \neq 0$) if 1) $|x_0| \geq |\delta\eta_0|$ and 2) x_0 has the same sign as $\delta\eta_0$ (the circle should not intersect the opposing jaw). Only those sources x_0, y_0 contribute to the δ-fraction of the halo for which 1) and 2) are simultaneously fulfilled. If η_0 is positive, then the halo momenta satisfy: $|\delta| < \delta_{max} \equiv \max_P |x_0|/\eta_0$, where $\max_P$ means maximum over the sources P.
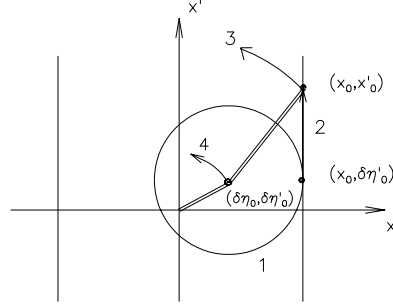

Figure 1: **1** Circulating beam particle invariant circle. **2** Scattering. **3** Secondary halo trajectory. **4** δ-centre motion.

2.2 Halo Computation for $\delta \neq 0$ (code DJ)

Each pair of opposing parallel jaws is defined by its longitudinal coordinate s and tilt angle α around the longitudinal axis. For fixed jaws, lattice functions $\mu_x(s)$, $\mu_y(s)$, $\eta(s)$ and δ, the maximum amplitudes $A_{x,max}$, $A_{y,max}$, A_{max} surviving all secondary jaws are computed as follows:

1. Generate N_P points $P = (x_0, y_0)$ along primary jaw borders;

2. For each point P:

– map (Fig 2) the line boundaries of all secondary jaws on the plane of initial-angles (x_0', y_0') by using the reverse of (2.4) (δ-independent linear transform)

– find all intersecting points of line-images; among these points find the vertices $(x_0', y_0')_i$ ($i = 1...N_{vert}^{(P)}$) of the "escape window (a polygon)".

– compute at each vertex $A_{x,i} = A_x(x_0, x_{0,i}')$

– find the largest $A_{x,i}$: $A_{x,max,P} = \max_i A_{x,i}$

3. Repeat the same for all points P and compute the maximum of the maxima:

$A_{x,max} = \max_P A_{x,max,P}$; $P \in all\ primary\ POJ$

DJ also stores the maximum initial angle corresponding to surviving trajectory and the vertex index corresponding to $A_{x,max}$ (maximum vertex). The same is done for A_{max} and $A_{y,max}$.

The escape polygon $(x_{0,i}', y_{0,i}')$ is independent of δ. It depends only on the lattice and the jaw setup, and represents an escape window in angle space, whose corners move, or may be screened out, as the source P is varied.

Figure 3: δ dependent halo limits

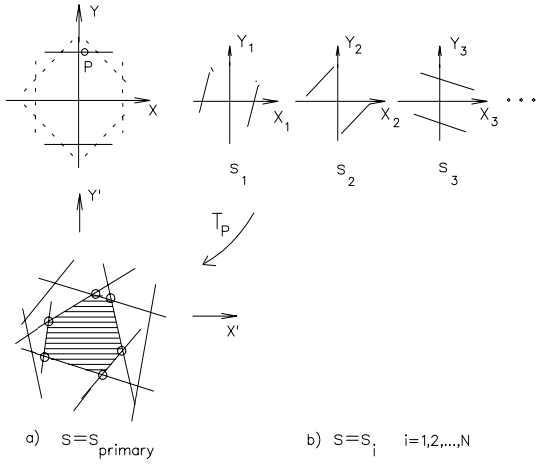Figure 4: Escape polygon and maximum vertex

Figure 2: (a) - Normalized coordinate space (above) and angle space (below) at the longitudinal position $s_{primary}$ of the primary pair of jaws; (b) N secondary pairs of jaws. For each point P: 1) each pair of parallel lines (stripe) in coordinate space is mapped into a stripe in angle space; 2) the overlap region of all stripes forms the escape polygon (shaded).

2.3 δ-dependence of the halo limits. The requirement for zero derivative of the normalized dispersion at the primary collimator.

In the LHC only horizontal primary jaws are present ($|x_0| = n_1$), therefore after minimization the source $P = (x_0, y_0)$ producing A_{max} is for all δ the outermost point of the jaw (the one with maximum y_0). One can therefore assume for a while that P is fixed.

We represent the surviving halo on the plane amplitude-δ, for simplicity taking only the fraction with δ > 0. The invariants of surviving particles are below the curve $A_{max}(\delta)$. This curve is continuous if the sources are, although its derivative may not be.

If the maximum vertex (x'_{0,i_A}, y'_{0,i_A}) is fixed the (explicit) dependence on δ is given by:

$$A_{max} = \sqrt{(x_0 - \delta\eta_0)^2 + (x'_{0,i_A} - \delta\eta'_0)^2 + y_0^2 + y'^2_{0,i_A}} \quad (2.5)$$

If the normalized dispersion derivative at the primary collimator $|\eta'_0|$ is zero, then the maximum vertex index does not change and A_{max} is given by (2.5) for all δ – monotonously decreasing function, Fig 3 (left). If η'_0 is nonzero, then $A_{max}(\delta)$ is composed of mini-curves of the kind (2.5), each corresponding to a new maximum vertex, Fig 3 (right). In this case $A_{max}(\delta)$ is still decreasing, but not as fast. From this point of view *having small $|\eta'_0|$ is preferred, but not an absolute condition for momentum collimation.*

Fig 3 shows the vertices of the escape polygon $(x'_{0,i}, y'_{0,i})$ and $A \equiv A_{max}$, which is defined as the maximum distance from the point T to a vertex. As δ increases, T advances to T′, the maximum-vertex changes, but A_{max} is continuous (A=A′). In the case $\eta'_0 = 0$, T remains on the ordinate axis
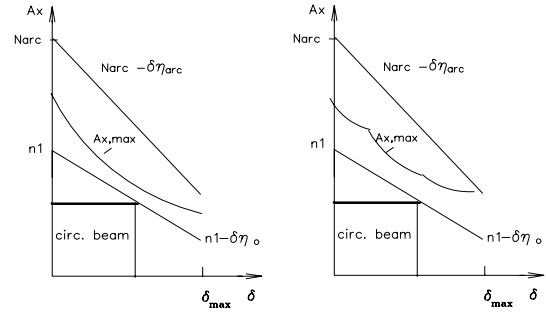
and the maximum vertex is independent of δ.
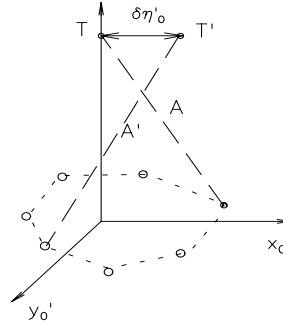
Another advantage of placing the primary collimator at a location with $\eta'_0 = 0$ is that *minimization of A_{max} can be done with equal results for any δ.* This is because both the escaping polygon and the index i_A are δ-independent. An optimum jaw arrangement found for $\delta = 0$ (betatron collimation) remains the optimum one for any δ.

If the set of sources P is arbitrary (skew primary also present) the maximum source P may also change with δ. In general $A_{max}(\delta)$ is built of mini-curves (2.5) each corresponding to a different value of x_0, y_0 and/or of the maximum vertex i_A.

2.4 Protecting ring locations with maximum dispersion. The requirement for high normalized dispersion at the primary collimator.

We denote by N_{arc} (σ_x units) the available horizontal aperture at a ring location where the dispersion D_x is maximum. At this location $\eta_x = \eta_{arc}$ and the halo particle coordinate (2.4) is:

$$x_{arc} = A_x \cos(\mu_{x,arc} + \mu_0) + \delta\,\eta_{arc} \leq A_x + \delta\eta_{arc} \quad (2.6)$$

On Fig 3, left and right, the secondary halo occupies an area restricted from above by the line representing the primary collimator (with slope η_0) and from below by the curve $A_{x,max}(\delta)$. For the arc to be protected ($x_{arc} < N_{arc}$) the latter curve should be below the line representing the arc (slope η_{arc}):

$$A_{x,max} < N_{arc} - \delta\eta_{arc} \quad (2.7)$$

A large normalized dispersion at the primary $\eta_0 \sim \eta_{arc}$ (nearly parallel lines) is needed because it provides wider

103

amplitude interval for the halo at δ near δ_{max}.

For example we take as before $x_0 = n_1$, $\eta'_0 = 0$ and assume that a 1D pipe is created in the horizontal plane. The value of the maximum vertex is known: $x'_{0,i_{Ax}} = \sqrt{n_2^2 - n_1^2}$ and we can use it to compute (2.7) for $\delta = \delta_{max} = x_0/\eta_0$. In the expression for $A_{x,max}$ ((5) without the y terms) the first term under the square root disappears and we get $A_{x,max} = x'_{0,i_{Ax}} = \sqrt{n_2^2 - n_1^2}$. The condition for protected arc is:

$$\sqrt{n_2^2 - n_1^2} + (\eta_{arc}/\eta_0)\, n_1 < N_{arc}. \qquad (2.8)$$

To improve things one can decrease either the ratio η_{arc}/η_0, or both n_1 and n_2. The latter choice may cause the primary collimator to cut into the circulating beam rectangle near the bucket edge, Fig 3. The vertical size of this rectangle is defined by the betatron primaries.

With LHC parameters: $n_1 = 8$, $n_2 = 9$, $\eta_{arc} = 0.16/\sqrt{\varepsilon_x}$, $\eta_0 = 0.2/\sqrt{\varepsilon_x}$ the condition (8) becomes $N_{arc} > 10.5$.

3 SIMPLE BETATRON COLLIMATION THEORY WITH PHASE ADVANCE SPLIT

3.1 The halo emittance function A and the collimator function C

Halo is defined by initials: x_0, y_0 on the circle $x_0^2 + y_0^2 = n_1^2$ and normalized angles $-\infty < x'_0 < \infty, -\infty < y'_0 < \infty$. We introduce initial phases μ_{x0}, μ_{y0} as shown on Fig 5.
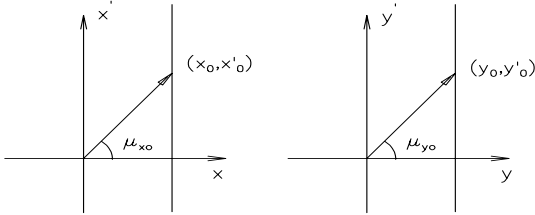
Figure 5: Definition of μ_{x0}, μ_{y0}.

The halo trajectories are

$$x = A_{x0} \cos(\mu_{x0} - \mu_x), \qquad (3.9)$$

where $A_{x0} = \sqrt{x_0^2 + x_0'^2} = x_0/\cos\mu_{x0}$ (similar for y). The four dimensional emittance of particles in the halo produced by the source x_0, y_0 is $A = \sqrt{A_{x0}^2 + A_{y0}^2}$ so we denote $A \equiv (A/n_2)^2$:

$$A(\mu_{x0}, \mu_{y0}) = \frac{(x_0/n_2)^2}{\cos^2\mu_{x0}} + \frac{(y_0/n_2)^2}{\cos^2\mu_{y0}} \qquad (3.10)$$

A as always positive and reaches a minimum for $\mu_{x0} = 0, \mu_{y0} = 0$, with value $n_1^2/n_2^2 < 1$. A has periodicities π in both coordinates. The surface A looks like a bowl that is asymptotic to a square chimney, Fig 6 (top).
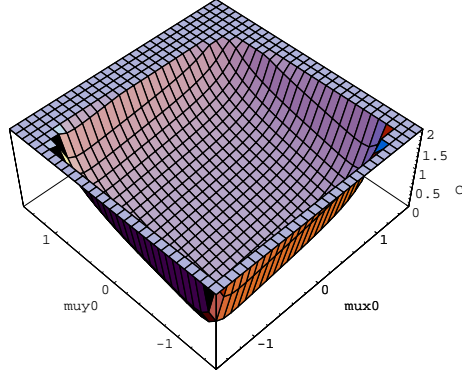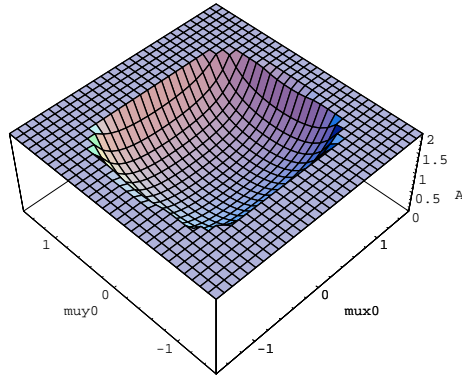

Figure 6: Functions $A(\mu_{x0}, \mu_{y0})$ (top) and $C(\mu_{x0}, \mu_{y0}, 0.535, 0.535)$ (bottom) on the square $-\frac{\pi}{2} < \mu_{x0}, \mu_{y0} < \frac{\pi}{2}$. C is below A except at the collimator point where they are tangent

Consider a secondary collimator located at phase advances μ_x, μ_y. At such collimator:

$$x = A_{x0} \cos(\mu_{x0} - \mu_x); \quad y = A_{y0} \cos(\mu_{y0} - \mu_y) \qquad (3.11)$$

All particles for which $(x^2 + y^2)/n_2^2 > 1$ are stopped, so we define the secondary collimator function C

$$C(\mu_{x0}, \mu_{y0}, \mu_x, \mu_y) = \qquad (3.12)$$
$$\frac{(x_0/n_2)^2}{\cos^2\mu_{x0}} \cos^2(\mu_{x0} - \mu_x) + \frac{(y_0/n_2)^2}{\cos^2\mu_{y0}} \cos^2(\mu_{y0} - \mu_y)$$

Particles with $C > 1$ are stopped. C has the same periodicity and same asymptotes as A so we may compare them directly. The collimator function C, Fig 6 (bottom), is everywhere below A except at the point $\mu_{x0} = \mu_x$, $\mu_{y0} = \mu_y$, *where they are tangent.*

3.2 Betatron collimation analysis

For example, we take some source point $x_0/n_2 = 0.5, y_0/n_2 = 0.7$ ($n_1/n_2 = 0.86$) and locate in the lattice a single circular collimator at phases $\mu_x = \mu_y = \mu_o$, where $\mu_0 = 0.535$ is the solution of $A(\mu_o, \mu_o)=1$), hence

the collimator pair phases is on the contour A=1 (the reason will become clear soon)

Fig 7 shows several contours of A and the contour $C(\mu_{x0}, \mu_{y0}, 0.535, 0.535) = 1$. The normalized squared A_{max} is simply the maximum A-contour value that can be found within the "escape window" which is the inside portion of the contour C=1, Fig 8.

Now we take four collimators (Fig 9) at phases:

1: (μ_o, μ_o) , split = 0
2: $(-\mu_o, -\mu_o)$, split = 0
3: $(\mu_o, -\mu_o)$, split = $2\mu_o$
4: $(-\mu_o, +\mu_o)$, split = $-2\mu_o$

The intersection of the inside portion of all four contours gives the set of particles escaping the system. The maximum "escaping" A is 1.3, so $A_{max} = \sqrt{1.3}\, n_2 = 1.14\, n_2$

The surfaces A and C are tangent at the collimator point. Therefore large A_{max} cannot escape if the collimator phases are chosen near the contour A=1 and this contour is surrounded by collimator contours from all sides. The last condition is only possible if *some of the collimators are at locations with large enough split between the horizontal and vertical phase advances*. If there is collimator for each solution of $A(\mu_x, \mu_y) = 1$, then all particles with $A_{max} > 1$ will be stopped (2D pipe).

I would like to thank R. Servrankcx, J.B. Jeanneret, T. Risselada and S. Koscielniak for sharing their ideas and helpfull discussions and the SL-AP Group team for their interest and support.

4   REFERENCES

[1] T. Trenkler, J.B. Jeanneret,Particle Accelerators, 50, 287(1995) and the bibliography therein.

[2] D. Kaltchev, M.K. Crdddock, R.V. Servranckx, J.B. Jeanneret, Optimization of Collimator Jaw Locations for the LHC, Proc. EPAC96 (Barcelona, June 1996), ed. S. Myers et al., 1432-4.

[3] Design of betatron and momentum collimation systems with DJ (Distribution of jaws). DJ user's manual. TRIUMF Note, TRI-DX-99-16, April 99 (download source from *http://decu10.triumf.ca:8080/dk/pub.html*)

[4] D.I. Kaltchev et al., PAC97, Vancouver,June 1997 and CERN LHC Proj.Rep 134,1997.

[5] T. Risselada, Optical Requirements for an LHC Cleaning insertion with Elliptical Collimators, SL Note 95-67, 1995.

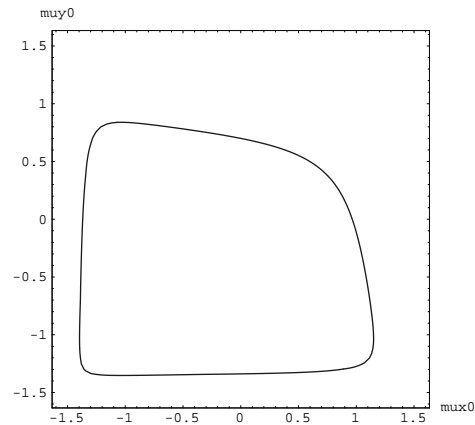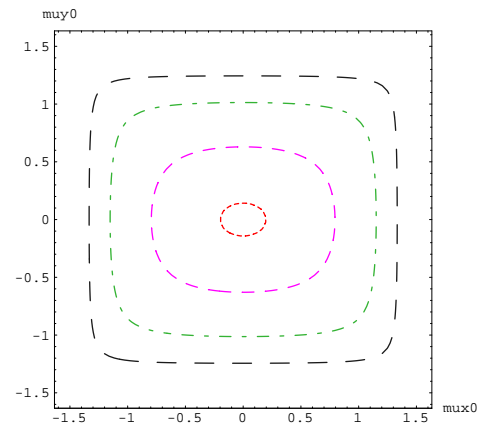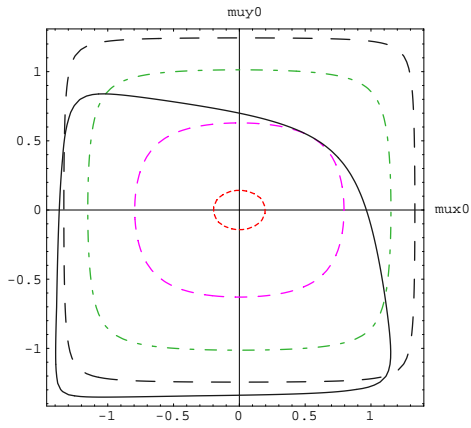Figure 7: Contours A=0.75, 1, 2, 5 (top) and contour C=1 (bottom).

Figure 8: One collimator with betatron phases chosen on the contour A=1.

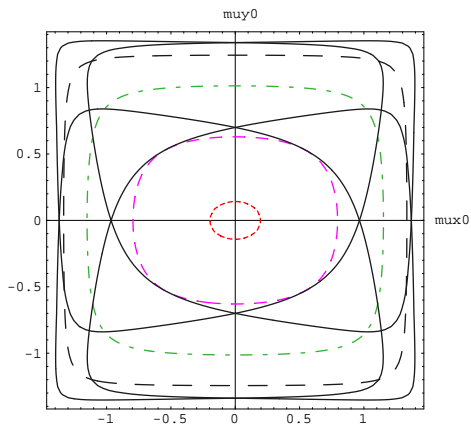Figure 9: Four collimators with phases on the contour A=1.

Beam Loss and Collimation at SNS Ring[1]

N. Catalan-Lasheras[2], Y. Y. Lee, H. Ludewig,
D. Raparia, J. Wei

Brookhaven National Laboratory, USA

Abstract

The future Spallation Neutron Source (SNS) requires a very low fraction of uncontrolled beam losses (10^{-4}) in order to achieve hands on maintenance. Collimator systems are being designed for the High Energy Beam Transport (HEBT) line, Accumulator Ring (AR) and Ring To Target Beam transport (RTBT) line. Special care has been taken when defining the overall acceptance. Scattering simulations performed with the actual model of the ring indicate a highly efficient collimation system. Preliminary studies to determine the residual radiation dose have been carried out.

1 INTRODUCTION

The future Spallation Neutron Source is designed to deliver a proton beam of 2MW of power. The accelerator consists of a full energy (1 GeV) linear accelerator providing a H^- beam to an accumulator ring. The proton accumulator ring (AR), as well as the two transfer lines, High Energy Beam Transport (HEBT) and Ring to Target Beam Transport (RTBT) are the responsibility of Brookhaven National Laboratory

One of the principal requirements is to achieve hands-on maintenance and high machine availability. Collimators are placed at strategic positions around the ring to remove particles outside the beam core and to localize losses in special zones. These locations will then become the only hot spots of the machine in which remote handling is required. In this paper, we describe the collimation systems designed for both transport lines and the ring. In section 2 we summarize the requirements for the collimation system, based on the expected level of beam losses. The description of the collimation systems is given in section 3. In section 4 we present initial results on the residual dose expected in the accumulator ring.

2 CLEANING REQUIREMENTS

The condition of hands-on maintenance requires that the average residual radiation in the tunnel does not exceed 1mSv/hr (measured at 30 cm away from the device surface, 4 hours after machine shut-down of an extensive operation). This condition is based on operational experience at mayor facilities like the Alternating Gradient Synchrotron (AGS) and booster at Brookhaven, or the Linac and Proton Storage Ring (PSR) at Los Alamos.

Experimental and numerical studies indicate 1-2 Watt of beam power per tunnel meter as an upper limit for uncon-

trolled beam loss [1]. For the SNS operating at 1GeV beam energy, that implies a fractional uncontrolled beam loss of 10^{-4}.

Special collimators have been foreseen for the SNS ring and are described in reference [2]. They have been carefully designed and shielded to minimize the production of secondary radiation and its subsequent leakage. The whole structure consists of a heterogeneous assembly of different materials including borated light water and stainless steel. They are also intended to dissipate heat efficiently and resist up to two whole pulses in the event of an accidental malfunction.

Another concern is the production of secondary electrons in the collimator surface which lead to collective instabilities. Special care was taken in the choice of collimator material to minimize electron desorption. Experimental studies are now in progress to help determine the final profile [3].

To achieve a high collimation efficiency, we have to provide enough ring aperture to contain both primary beam as well as the secondary halo created after out-scattering in the collimator [4]. With a sufficient aperture, these protons circulate freely around the ring until they are intercepted by secondary collimators. The maximum extension of this secondary halo is minimized by properly choosing the location of secondary collimators [5].

In order to provide flexibility for beam injection and collimation, we have recently redesigned the ring lattice [6]. A long straight section allows improved efficiency with a minimum set of collimators.

2.1 Expected losses

The fraction of uncontrolled loss is determined by two factors. The first of them is the fraction of total beam susceptible of being lost in the ring. A certain number of protons leave the stable core of the beam and form a primary halo. On the other hand, deviations of the closed orbit drive the beam to the vacuum pipe producing also losses. In general, the fraction of the beam lost in the machine n_{loss} can be estimated or measured. The second factor is the efficiency of the collimator system defined as the fraction of particles absorbed by the collimator system n_{abs} from the total initially interacting with it n_{col}, $e_{col} = n_{abs}/n_{col}$. Our first concern is to intercept any particle susceptible of being lost making $n_{col} = n_{loss}$. Then, a very high collimation efficiency has to be achieved.

In the case of the SNS accumulator ring, the final fraction for uncontrolled beam loss has to be smaller than 10^{-4} to allow hands on maintenance.

$$n_{loss}e_{col} = 10^{-4}$$

In general there are two different types of losses that have to be considered separately. On one hand, we have the so called continuous losses produced randomly around the machine and during the cycle. The inelastic scattering of the beam protons with the residual gas in the vacuum pipe is an example of this kind of losses.

---

[2]e–mail: catalan@bnl.gov

Loss mechanism	Fract.	Type	Cure
HEBT			
H- stripping	$< 10^{-4}$	Cont	Inc
RING			
Inj. foil energy stragg	10^{-5}	Cont	BIG
Inj. foil nuclear scatt	$6 \cdot 10^{-5}$	Loc(s)	Inc
Space-charge	10^{-3}	Cont	Ring-c
Coulomb scattering	10^{-8}	Cont	Ring-c
RTBT			
Kicker failure	10^{-3}	Loc(t)	RTBT-c

Table 1: Expected fractional losses in the transfer lines and accumulator ring of the SNS accelerator. They have been classified as continuous (cont) and Local, in time (Loc(t)) or space (Loc(s)). In the last column we indicate the appropriate system dealing with them as Ring Hebt or RTBT collimators, Beam in Gap (BIG) cleaner or uncontrolled losses.

On the other hand, we have local loses. They are localized either in time or in space. Examples of this type are accidental losses are produced by missfiring an extraction kicker or injection losses. They are more difficult to prevent and they have to be treated separately in a case by case basis.

For the SNS accumulator ring we expect the space-charge halo growth to be the principal cause of continuous losses. The beam scattering in the residual gas has been estimated for a pressure of 10^{-8} torrs and has been found to be negligible [7].

Injection losses are expected to be a non negligible source of local loss. Energy straggling in the stripper foil at injection draws a fraction of the beam outside the momentum acceptance. These protons are lost at the time of extraction or at dispersive locations in the ring [8]. Besides, partial stripping and elastic scattering in the foil also produces local losses The estimate losses produced by these phenomena are shown in table 2.1.

In table 2.1 we give expected values for losses in the ring and transfer lines. Losses are classified as continuous or local losses. The different systems dealing with them are also indicated. They are described later in this paper.

2.2 Acceptance

In the HEBT line the acceptance is larger than 30π mm mrad enough to accommodate a 1π mm mrad beam coming from the linac. The limiting aperture in the line is the debuncher cavities where the aperture is reduced. Scrapers are installed in the line at even tighter aperture to protect the cavities from eventual losses.

The final beam accumulated in the ring has a total emittance of $120\text{-}160\pi$ mm mrad depending on the painting scheme and the space charge forces [6]. The nominal aperture for primary collimator has initially been set between $180\text{-}225\pi$ mm mrad. This aperture can be adjusted if necessary during operation. Secondary collimators are to be located around 300π mm mrad. Based on geometric projections of secondary absorber [9], the secondary halo extent is about 450πmm mrad.

In view of these considerations, we require an acceptance of 480π mm mrad and 1% momentum deviation $\delta p/p_0$ in both the ring and RTBT line. The arc aperture and beam envelope using these values is presented in figure 2.2. Arc acceptance depends on the choice of working point and the optics matching. the minimum acceptance is about 480πmm mrad for a momentum deviation of 1%. Under nominal conditions, the global acceptance of the ring is limited in the injection and extraction regions where the required values (A=480 at $dp/p_0 = 1\%$) are satisfied.
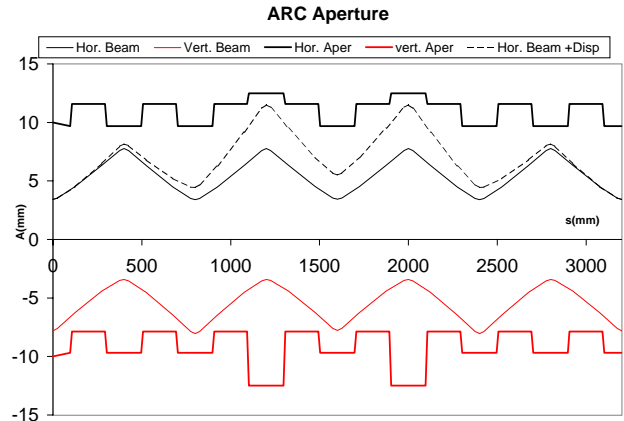

Figure 1: Longitudinal view of the arc aperture and beam envelope. Solid line represents a beam with an emittance of 480π mm mrad. On top of it, the same emittance with a momentum deviation of 1% has been plotted.

The RTBT line has an overall aperture of 480π mm mrad. This aperture is enough to house the beam after a failure of one of the extraction kickers. In this case, the beam is stopped by the RTBT collimators (see section 3.3).

3 COLLIMATION SYSTEMS

3.1 HEBT line

The HEBT line determines the beam quality before injection. The beam coming from the linac is shaped in the six-dimensional phase space. To reduce the probability of uncontrolled losses in the ring three pairs of scrapers are installed in the line [10]. One for momentum and two for transverse collimation. Each one of the scrapers is complemented by an absorber downstream which captures the H^+ ions. The evolution of the beam along the collimation system is shown in figure 3.1.

The scrapers radius is chosen to protect the RF cavity against beam losses. With limited space, collimators location is optimized to provide full collimation of the phase space. The momentum collimator is located at the maximum dispersion point in the achromat. All scrapers in the line are movable to adjust to the actual operating conditions.
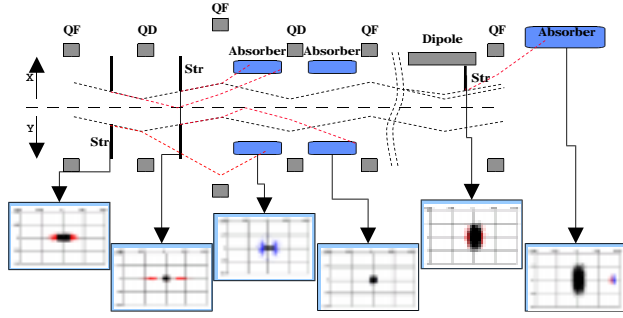
Figure 2: Schematic view of the HEBT cleaning system and the evolution of the beam along the line. H^- ions constitute the core of the beam around which the halo particles are first stripped and then absorbed by the system.

3.2 Ring

As mentioned in section 2, betatron cleaning, momentum cleaning and beam gap cleaning are needed to reduce uncontrolled beam losses. Betatron cleaning is performed with a multistage collimation system while momentum and gap cleaning are both performed with the assistance of a fast kicker in what is called Beam-in-Gap (BIG) cleaner.

Betatron collimation

One of the four straight sections of the accumulator ring is dedicated to beam cleaning. The available length of 20m is divided in three uninterrupted straight sections. The total phase advance in the straight section is about 180 degrees in both the horizontal and vertical planes. Due to budget considerations and operational flexibility only a fraction of it is occupied with collimators.

A system consisting of one primary movable scraper and two secondary fixed aperture collimators has been chosen for the baseline design. Systems with one and three secondary collimators were also tested and found not to be optimal. The secondary collimators were numerically located to minimize the secondary halo extent [9]. Their relative phase advance with respect to the primary absorber are $\Delta\mu_x = 26°, 161°$ and $\Delta\mu_y = 43°, 144°$ respectively. The phase space proyection of the collimation system is shown in figure 3.2.

Figure 3.2 shows the lattice functions in one superperiod and the locations on the lattice of the scraper and secondary collimators. The acceptance is $A_{prim} = 225\,(2.5\sigma_{rms})$ for the primary collimator and and $A_{sec} = 275\,(2.75\sigma_{rms})$ for the secondary.

We run Montecarlo simulations [11] for this system including scattering in the collimators and a linear approximation for the ring. The initial conditions are independent of the mechanism of halo formation. The protons amplitude is increased each turn in small steps to simulate small impact parameters in the primary collimators. The amplitude of each proton A_i is recorded immediately after their first interaction with the collimators. In figure 3.2, we plot the rel-
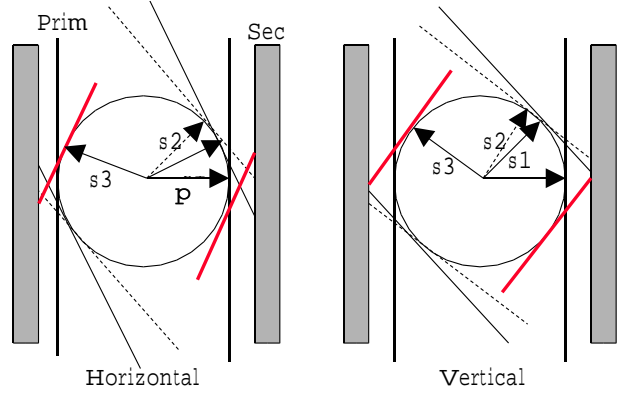

Figure 3: View of the normalized phase-space in the collimation section. The circulating beam lays in a circle while the primary and secondary colimators are vertical lines. The secondary halo created in the primary collimator is a line $x_0 = x_{prim}, x'_0$ that rotates following the phase advance. This secondary halo is chopped by secondary collimators at optimized.
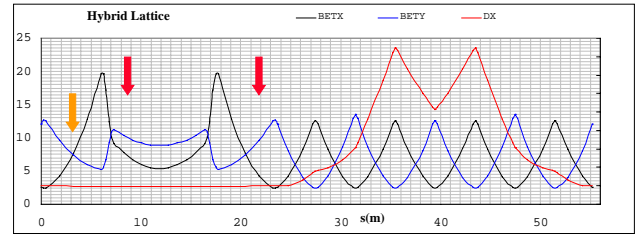

Figure 4: Lattice of the SNS accumulator ring superperiod. The first region is the dispersion free straight section. The first (yellow) arrow represents the scraper position, other two arrows stand for secondary collimators

ative number of protons $n(A)$ escaping the collimation section with amplitude above a certain value $A_i > A$.

The one-pass efficiency for the system depends on the acceptance of the ring itself. The larger the acceptance the bigger the chances for a proton to be absorbed by the secondary collimators in successive turns. From the plot we can estimate what we call the one-turn inefficiency for the nominal aperture as $n(480)/n_0 = 0.05$. Assuming that %5 of the protons reaching the collimators is lost in the next turn somewhere in the ring, 95% is an upper boundary for the final efficiency.

From this simulation also confirmed that the acceptance is sufficient for collimation requirements. Even if the final figures have to be refined, the present value of $480 pi$mm mrad appears to be a good compromise.

Beam gap cleaner

As the space in the arcs is limited and the straight sections are dispersion free, there is no space in the ring to provide a dedicated momentum cleaning section. On the other hand, the protons lying outside of the bucket drift in longitudinal space and occupy the gap between bunches. This "beam in
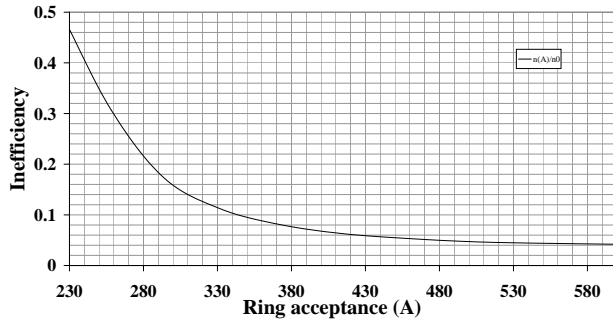
Figure 5: Survival plot for the accumulator ring transverse collimation system.

Figure 7: Schematic view of the RTBT scrapers

gap" is lost during extraction increasing the level of uncontrolled loss. A solution is to install a fast rise kicker in the line that fires between subsequent revolutions. The kicker0 drives the protons to the collimators in several turns (typically 10-20) as illustrated in figure 3.2. This principle has already been experimentally demonstrated in the National Synchrotron Light Source (NSLS) at Brookhaven[12]. The kick has to be optimized to be as fast as possible and keep the kicked beam inside the ring acceptance. The final specifications of this Beam In Gap (BIG) cleaner are currently being studied.
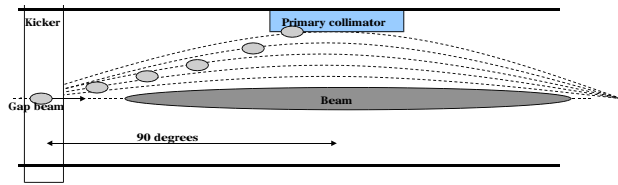

Figure 6: Schematic view of the Beam in Gap (BIG) cleaner.

3.3   RTBT line

Two collimators are installed halfway along the RTBT line. Their position in the line is shown in figure 3.3. They are fix aperture collimators with a relative phase advance of 90 degrees between them. They constitute the main aperture restriction on the line but are not intended to interfere with the beam. Their function is to prevent the beam from reaching the target in the eventuality of a missteered bunch. This situation may be the caused by the failure of one of the extraction kickers.

4   RESIDUAL DOSE

The halo protons, captured in the collimators, produce spallation products the majority of which, are contained by the collimator and surrounding shielding. A fraction leaks out of the collimation and add to the background radiation level.

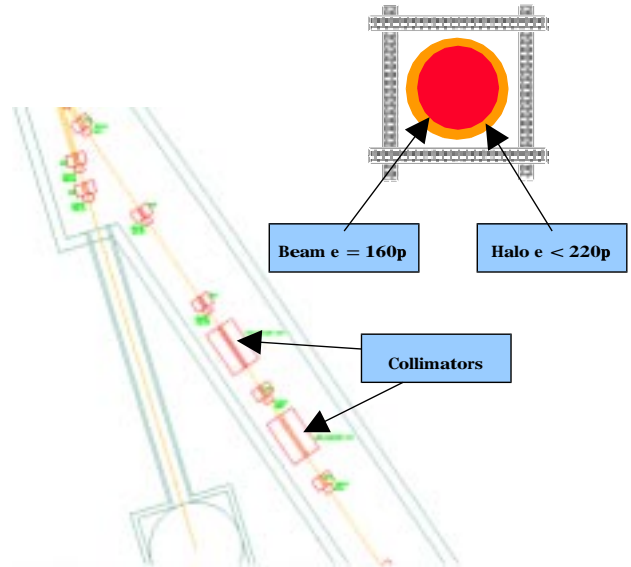A preliminary estimate of doses in the tunnel after the shutdown of the machine was made. The study involved simulations of spallation products, neutron flux, isotopes decay and gamma radiation. The detailed report of the simulation and its results can be found in reference [13]. We summarize here two distinct cases. In the first case we estimated the radiation dose around a generic section of ring containing a quadrupole and in the second the dose produced by the heavy losses in a collimator. In both cases it is assumed that the accelerator operates at 2MW for 180 days. The results were initially obtained for the time step immediately following machine shutdown. They were appropriately escalated to the corresponding values after four hours of cooldown.

4.1   Uncontrolled losses around the machine

The background dose in the tunnel was estimated based on a loss rate of 1 Watt/m. An corresponding flux of protons was impinged on a quadrupole/pipe assembly with an appropriate incident angle. The calculation was carried out using a simplified model of the standard quadrupole designed for the SNS accumulator ring. The residual dose after shutdown is indicated in figure 4.1. The maximum dose at one feet distance from the pipe is about 1mSv/hr. This value is low but not negligible.

4.2   Radiation levels around collimators

Both shielded and unshielded collimator were considered. The estimate of the proton current was based in a controlled loss fraction of 10^{-3} for a machine operating at 2MW.

It was found that there was a strong anisotropy in the distribution of radiation leaving the collimator. Radiation leaking out through shielding is strongly attenuated. However, photons leaving the collimator volume in the direction of the connected vacuum chamber are be essentially unin-
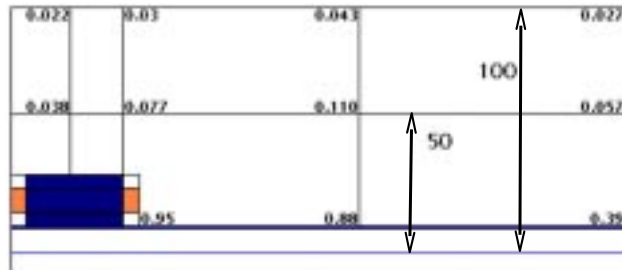
Figure 8: Dose levels after shutdown around a quadrupole/pipe assembly.

hibited. The residual radiation is also higher in the upstream end of the collimator as losses are concentrated around this point. This is corrected by shaping or locating the collimator in such a way that protons get absorbed around the middle of the structure.

The residual radiation doses for the unshielded collimator have a maximum value about 20 rem/hr at one foot from the vacuum pipe surface. Under normal operation conditions the collimator will be shielded with iron in the radial and axial directions. A movable lead shield may be used in the event of maintenance work close to the collimator. In this case, the overall dose is reduced by a factor $\approx$100 compared to the unshielded case.

5   SUMMARY

The accelerator acceptance is sufficient to house the circulating beam as well as the secondary halo generated in the srappers. The aperture restrictions in the ring and transport lines are being identified.

A six dimensional cleaning system has been layed out for the accumulator ring, HEBT and RTBT lines. The actual design offers enough flexibility to adapt to real operating conditions. With the present design of the transverse collimation system in the ring, we can reach an efficiency of 95%. Detailed simulations including the aperture of each element are under way to establish the final efficiency of the system.

Residual dose studies show that uncontrolled losses at the level of 1 Watt/m are just about right to allow hands on maintenance. Around the collimators, shielding has to be provided and remote handling is mandatory. A movable shield reduces the dose levels in the upstream and downstream areas to acceptable levels in the eventuality of repairs close to these areas.

6   ACKNOWLEDGEMENTS

7   REFERENCES

[1] T. Wangler. *RF Linear Accelerators*, chapter Beam Loss and Beam Halo. Wiley & Sons, 1998.

[2] H. Ludewig et al. Collimator systems for the SNS ring. In *1999 Particle Accelerator Conference, New York*, 1999.

[3] P. Thieberger et al. Secondary electron yields and their dependence on the angle of incidence on stainless steel surfaces for three energetic ion beams. Technical Report 64, BNL/SNS, 1999.

[4] J.B. Jeanneret T. Trenkler. The principles of two stage betatron and momentum collimation in circular accelerators. *Part. Accel.*, 50(4):287–311, 1995.

[5] J.B. Jeanneret. Optics of a two-stage collimation system. *Phys. Rev. ST Accel. Beams*, 1:081001, 1998.

[6] J. Wei. Preliminary change request for the SNS ring hybrid lattice. Technical Report 66, BNL/SNS, 1999.

[7] H. C. Hseuh. Design of the NSNS accumulator ring vacuum system. Technical Report 15, BNL/SNS, 1997.

[8] D. Raparia. Estimated beam loss due to energy straggling through the charge exchange injecton foil. Technical Report 58, BNL/SNS, 1999.

[9] D. Kaltchev. Numerical optimization of collimator jaw orientations and locations in the LHC. In *1997 Particle Accelerator Conference, Vancouver*, 1999.

[10] Y.Y. Lee D. Raparia, J. Alessi. Collimation in the HEBT. Technical Report 52, BNL/SNS, 1999.

[11] J.B. Jeanneret T. Trenkler. *K2: A Software Package Evaluating Collimation Systems in Circular Colliders*. CERN SL/AP.

[12] D.P. Siddons R.J. Nawrocky, U. Bergmann. A bunch killer for the NSLS X-Ray electron storage ring. In *1993 Particle Accelerator Conference, Washinghton*, 1993.

[13] H. Ludewig. Preliminary estimate of dose following machine shutdown from collimators, vacuum chamber walls and adjacent magnets. Technical Report 67, BNL/SNS, 1999.

BEAM LOSS COLLECTION IN THE ESS RINGS

C. M. Warsop, Rutherford Appleton Laboratory, Oxfordshire, UK.

Abstract

The two 50 Hz, 1.334 GeV rings of the European Spallation Source accumulate 2.34×10^{14} protons per pulse in each ring over the 700 turn injection process. The requirement for low and controlled loss for the 5 MW beam, to keep activation low enough for hands on maintenance, has dominated much of the machine design. Interactions with the stripping foil are expected to cause <0.02% regular losses in the rings. Ideally, this and all other loss, will be efficiently localised on optimised collector systems located in well-shielded regions of the machine. The design of the loss collection systems is presented along with features thought to be important for optimal performance. In particular the effects of jaw location, transverse and longitudinal geometry are considered. The nature of expected losses is also reviewed, including probable and possible losses under fault conditions, where fast or unusual loss modes may affect the expected collector operation. Some early results from Monte Carlo simulations are also described.

1 THE ESS ACCELERATORS

The ESS Accelerators are designed to provide a mean beam power of 5 MW in ~1 μs pulses of protons at 50 Hz. The requirement for low loss, to allow hands on maintenance over most of the machine, has dominated the accelerator design.

1.1 Design for Low Loss

The accelerators consist of a 1.334 GeV H⁻ linac and two 50 Hz accumulator rings [1]. Much of the linac design has been influenced by the need for low loss in the rings. The requirement to minimise the number of injected turns (to reduce associated losses and foil heating) has fixed peak currents. Chopping at the ring revolution frequency allows for lossless RF capture and extraction. Finally, the 43 m radius achromat, with 3D collimation exploiting efficient H⁻ stripping, protects the ring from many possible linac problems.

1.2 Accumulator Rings

The two 1.334 GeV rings operate in parallel at 50 Hz, each accumulating 2.34×10^{14} protons over the 700 turn charge exchange injection process. Injection utilises 3-D painting to produce optimal distributions in the ring. The design of the injection region allows for the efficient removal of stripped electrons and non or partially stripped H⁻. The dual harmonic RF system captures the chopped injected beam, maintaining a gap for extraction. Once

both of the rings are filled, the beams are extracted in a single turn and transported to the target.

The ring design has recently been revised [2] because of concerns over high foil temperatures. The ring mean radius has been increased from 26 to 35 m, thereby reducing the number of injected turns and thus foil interactions and temperature. This has been achieved by adding an extra triplet cell to the dispersionless straights, and has provided real benefits in making optimal locations for collectors available.

In the rings, simulations suggest that the painting and longitudinal trapping processes should not involve significant loss. All the expected losses are associated with scattering in the stripping foil, and are now reduced along with the number of foil interactions. Beam loss collection systems in the rings are required to localise most of the expected loss, and any losses due to fault or unforeseen conditions. Effective collector systems will be essential for successful machine operation.

2 ANALYSIS OF LOSSES

The aim of the collection system is to maximise localisation of loss and resultant activation, and to protect the machine from physical damage. In addition to localising loss during circulation in the ring, the beam must be suitable for near lossless extraction. In order to produce an optimised collection system it is necessary to consider in some detail the losses expected.

2.1 Controlled and Uncontrolled Loss

Uncontrolled losses, i.e. those distributed in an uncontrolled way around the machine, must be kept to levels of about 1 nA/m/GeV, or 0.01%, to allow hands on maintenance. Controlled loss, i.e. that localised in the collector systems and associated shielding, can be higher but should be minimised. The higher the controlled loss, the higher the collector efficiency required.

2.2 Regular and Irregular/Fault Loss

Regular loss, i.e. that occurring at 50 Hz, 24 hours a day during operational running, is the most important to control. Irregular losses are generally higher losses that either trip the beam off due to a fault condition, or are tolerated at a lower rep rate during set up. Optimising protection against irregular loss is an important secondary aim. It is assumed that a comprehensive set of diagnostics switch the beam off in one pulse if there are intolerable fault losses.

2.3 Loss Mode

Beam is lost when it exceeds one or more of the machine acceptances. Loss in each of the horizontal, vertical and longitudinal planes is dealt with by a dedicated collector system. The manner in which beam comes to exceed acceptances ('loss mode'), affects how efficiently it is collected: this is typically characterised by the growth rate. The beam collection system should be optimised for the regular expected loss mode, with reasonable provision for other likely loss modes.

2.4 Expected Loss Mechanisms

The dominant regular losses are associated with the foil. Elastic interactions lead to an emittance increase for some particles. Ionisation energy loss and the associated straggling produce a negative momentum tail. Inelastic interactions also lead to some losses. These losses are expected to total $\leq 0.02\%$. Other possible regular losses are due to the emittance increase associated with space charge. A non ideal set up could also produce regular transverse or longitudinal losses. Irregular/fault condition losses could be transverse, longitudinal, and over a wide range of growth rates; anything from mis-steerings to RF cavity failure.

2.5 Growth Rates

The efficiency of the collector system is highly dependent on the growth rate of the loss. For typical transverse losses in the ESS accumulator ring, growth rates of ~50 μm/turn are expected [3]. Other loss rates are categorised in Table 1. Note that very slow growth may not be a problem if the beam does not reach the acceptance limits in the ~100-1400 turns the beam circulates in the rings.

Table 1
Typical Transverse Growth Rates

Growth Rate	Category
0 – 10 μm/turn	slow
10 – 100 μm/turn	typical
> 100 μm/turn	fast

Elastic scattering events in the foil produce a distribution of emittance increases, many of which will be covered by slow or typical categories, but some receiving larger scatters will be better described as fast. Similarly, motion of some particles losing larger fractions of momentum in the foil would be better described by a fast growth rate. Losses due to space charge and minor machine tuning errors are likely to lead to slow or typical growth rates. Major causes of fast loss will probably be associated with fault conditions which trip off the beam.

For a well optimised collector system it is important that all three loss categories are allowed for. Conventional designs will generally perform well with the first two categories, but may not for the third, fast loss.

3 LOSS COLLECTION SYSTEMS

There is generous provision for collector systems in the extended ESS Rings. A long dispersionless straight covering >180° in the horizontal and vertical betatron phase is provided for betatron collection, with high dispersion regions available for momentum collection. There are three collector systems, each optimised for the removal of particular types of loss.

Figure 1
ESS Rings and Collectors
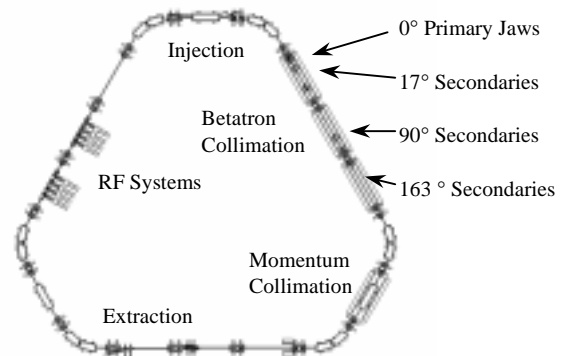
3.1 Betatron System

This is expected to be the most important system, removing most of the regular losses, particularly those associated with the foil.

The system is based on a standard set of primary jaws, which intercept the main beam and define the usable aperture, and secondary jaws, optimised for collecting out-scatter from the primaries. Collimation limits are shown in Table 2; primary collimators are set at $260\,\pi$ mm mr. Consideration of tolerances and alignment leads to the secondary jaws being set back by ~2 mm or at $285\,\pi$ mm mr. Application of the basic 1-D collector optimisation procedure [4,5], places secondary collectors at 17° and 163° in betatron phase. To allow for scatter orthogonal to the plane of a given collector system, jaws are also included at 90°. These sets of jaws, on both sides of the beam at 0°, 17°, 90° and 163°, are duplicated in the horizontal and vertical plane. In the triplet structure of the lattice, the phase advances in the transverse planes are similar, and so each set of horizontal and vertical jaws is combined in a box type assembly. Full 2-D optimisation of jaws and jaw shapes will be considered below.

Collimation Limits

Zero space charge painted beam	150 π mm mr
Primary Collimation (ε_p)	260 π mm mr
Secondary Collimation (ε_s)	285 π mm mr
Aperture (ε_A)	480 π mm mr
Momentum Acceptance dp/p	± 0.6 %

3.2 Momentum Tail System

The ionisation energy loss and associated straggling in the foil introduces a large negative momentum error into a significant fraction of particles. Regular loss levels of <0.01% are expected due to this. The high dispersion at the foil enhances the betatron motion of such particles, which can then be effectively removed at the next peak of their motion. This is reached 180° downstream in betatron phase, conveniently in the main collector straight. The primary betatron jaw on the inner radius of the machine doubles as a momentum tail collector, its phase being optimised with respect to the foil. Low momentum particles out-scattering from the primary jaw then encounter the optimised system of betatron secondary jaws.

3.3 General Momentum System

Careful design of the ESS, in particular chopping and the collimation in the achromat, mean general momentum losses should be very small. However, it is likely that there will be some longitudinal loss, either due to fault conditions, or to leakage from the betatron collectors. Therefore, momentum collimation is included.

The momentum collimation limits are chosen such that beam must exceed both the secondary betatron collimation limit (ε_s=285 π mm mr), and the momentum limits dp/p ± 0.6%, to be intercepted by the momentum system. Placing collimation *behind* the normal betatron limit (ε_p=260 π mm mr), for beam within the momentum acceptance, allows more particles to be removed by the larger, more fully shielded betatron system. The high normalised dispersion region in the ESS lattice (D = 2.0 m$^{1/2}$), downstream from the betatron collector straight, provides good conditions for momentum collimation. A double jawed primary is placed as near as possible to the dispersion maximum, with similar secondaries as near to their optimal phases as possible.

4 OPTIMISATION OF COLLECTOR SYSTEMS

There are many free parameters in optimising collector systems, e.g. the number and position of jaws, materials, transverse and longitudinal geometry. The basic objectives are to minimise out-scatter from primary jaws, control the removal time of the halo, and to maximise out-scatter interception. The choice of optimal configuration will generally depend on the loss mode assumed.

4.1 Effect of Loss Mode and Growth Rate

Conventionally, slow/typical growth rates (Table 1) are assumed, with the result that particles approach the collectors slowly enough to hit near the optimal region of the primary jaw first. This is true unless fast growth rates are present, when the particles additionally see larger/different sections of primary collectors and also secondary collectors.

In the case of fast loss, collector action is changed and so generally, the optimisation is different. A beam with emittance significantly exceeding the secondary collector limit (285 π mm mr), now sees the complete collector system, primary and secondary jaws. There is then no provision for out-scatter of the significant number of particles hitting the 'secondary' collectors, and as a result efficiency is reduced. In this situation all collectors are effectively acting as primaries.

In fact, for this situation to occur on most collector systems, growth rates have to be fairly fast. The probability of hitting the primary collectors is much higher than for the secondaries, even when emittance exceeds secondary limits. However, when very fast loss is present, it turns out that a well optimised conventional system as outlined above (i.e. double jaws at 0°, 17°, 90° and 163°), works very effectively. For very fast loss it is assumed rapid removal (~1 turn) is the priority, to prevent loss elsewhere. A comprehensive set of collectors will indeed remove most fast loss in a single turn (see Section 5.3), in effect treating main beam as out-scatter. A reduced set of secondary collectors, not covering all betatron phases in one pass, will not provide this protection. It is of some interest to study efficiencies as a function of growth rate, and in particular how the cross over from conventional *primary-secondary* operation to *all-primary* operation affects performance.

4.2 Number and Position of Jaws

The number and positions of the jaws have been based on ideal 1D systems, and with the ESS ring optics this is expected to be near the optimum. However, these optimisations will be checked with the numerical 2D optimisation codes [6] before the design is finalised. Similarly, the effectiveness of collector operation overall, including out-scatter effects, will be studied with a Monte Carlo simulation.

4.3 Transverse Geometry

Transverse shaping of collector jaws is determined to a significant extent by the vacuum chamber geometry. Circular or elliptic shaped vacuum chambers require similar jaw geometries. On the ESS rings, the square vacuum chambers allow for some freedom in design. Even though the beam is not painted over much of the square acceptance, it is provided for efficient collection and low loss.

114

The efficiency of collection is determined largely by the percentage of beam out-scattered from the primary collector surface. The probability of out-scatter is a very sensitive function of impact depth and angle (see below). Previous work [7] has shown careful shaping can significantly enhance the mean impact depth, and thus efficiency. Reducing the area occupied by the collectors in phase space at a given emittance, e.g. by using a '¼-jaw' rather than a full 'double jaw', Figure 2 (a) & (b), reduces the probability of interception. This means that removal is delayed and, on average, impact depths are enhanced for particles with slowly growing emittance. Also, the impact depth is enhanced if the 2D probability distribution of linear betatron motion is exploited by angling the jaws. The price paid for enhanced impact depth is increased collection time; this is not usually a problem if beam does not exceed the machine aperture.

Figure 2
Transverse Jaw Shapes, Real Space

(a) Double Flat Jaw   (b) Single Angled ¼ - Jaw   (c) Combined System
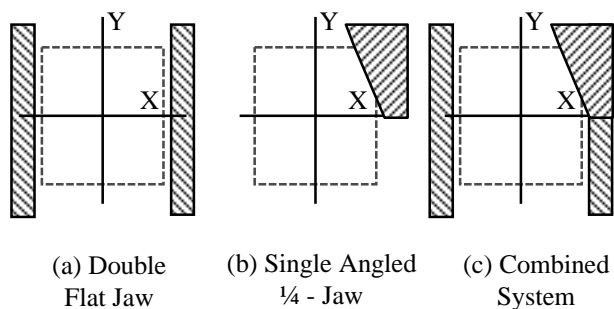
Enhancements to impact depths and thus efficiency, as expected from ¼-jaws, are certainly desirable for the ESS collectors. However, because the beam can spend as little as ~100 turns in one of the rings, it is important to quickly remove any beam that exceeds the acceptance of the extraction system. To fulfil both of these requirements a combined system is planned (Figure 2 c), which incorporates a single angled jaw at smaller emittances (240 π mm mr), and full double flat jaws at the nominal extraction acceptance (260 π mm mr).

Simple Monte Carlo simulations [8], which included only 2D linear betatron motion and jaw geometries, have been used to study the effect of the proposed jaw shapes. These allowed distributions of impact depths and removal times to be studied as a function of growth rate. Allowance was also made for the finite Q spread expected. These simulations clearly showed that although a single ¼-jaw enhanced the impact depth, it could take many hundreds of turns to remove the halo. In contrast, double flat jaws intercepted beam quickly (≤50 turns), but at a reduced mean impact depth. The simulation results for jaw geometries shown in Figures 2(a) and (c) are summarised in Table 3. For fast growth rates impact depths are essentially the same, at slower growth rates enhancements by factors of 2 to 8 are expected with the

angled jaw. Therefore the proposed geometry, Figure 2(c), provides efficient removal for both fast and slow loss. The angle on the inclined jaw (9°) was chosen to enhance the impact depth whilst minimising the reduction in useful acceptance.

Table 3
Mean Impact Depths (ID) at various Growth Rates for Different Jaw Shapes, from simple simulation

Growth Rate (μm/turn)	10^4	10^3	100	10	1
Double Jaws both flat as Figure 2(a)					
Mean ID (mm)	11.8	2.2	0.5	0.1	0.02
Double Jaws one with 9° angle Figure 2 (c)					
Mean ID (mm)	11.0	2.5	1.3	0.5	0.16

4.4 Longitudinal Configuration and Geometry

In many designs the primary jaw is effectively a short deflector, which scatters the particles into larger volumes of secondary collector material down stream, which 'absorb' the primary particle and most of its products. Another approach is to increase the volume of the primary so that it 'absorbs' as well as deflects. The former approach removes particles over a greater number of turns, with more particles surviving a single encounter with the primary. Jaws performing the 'absorbing' function must be several interaction lengths long, or ideally a proton range to absorb secondary products. This means that absorbers may have lengths up to ~2 m for graphite; deflectors will be much shorter.

It is not obvious which approach produces the most efficient results overall, and this is to be studied with Monte Carlo particle scattering simulations. Presently, for ESS, a system where the primary deflects and absorbs is favoured, on the basis that beam is removed quickly and therefore locally.

Whichever longitudinal configuration is chosen, there are two important effects when selecting primary jaw length and shape. Particles passing through the collector lose momentum by ionisation energy loss, and there is potential for producing a momentum tail which may not be lost locally. For particles with a faster growth rate, it may also be important to consider the possibility of particles hitting the inner face of the collector if it has significant longitudinal extension. This could reduce the efficiency of the system.

5 MONTE CARLO SIMULATIONS

5.1 Outline and Aims

A Monte Carlo code including the effects of proton elastic

single and multiple scattering, inelastic scattering, ionisation energy loss, straggling, full 3D geometry and beam optics has been developed. It is based on the condensed step random walk method. This has made use of some collimator routines of ACCSIM, various CERN routines and methods outlined in the GEANT manual. The aim is to understand and optimise the loss locations of protons; it is assumed that the activation products are contained within the shielding of the collector region. Analysis of activation products and final dose rates is left to other codes designed for the purpose. The code has been recently developed and requires some further bench marking. However, there are some initial results of interest.

5.2 Out Scatter as a Function of Impact Depth

A 'pencil' beam of ~10^5 particles, parallel to the collector edge, impinging on the centre of the primary collector face was simulated. This was repeated for various impact depths, and the total out-scatter from the betatron system recorded, see Table 4. Note that these are preliminary results, for a non optimised collector system.

Table 4
Out-scatter of Betatron System
as a function of Impact Depth on Primary Jaw

Emittance	270.0	265.0	261.0	260.5
Impact Depth	1 mm	0.5 mm	0.1 mm	50 µm
Percent outscattered	0.6±0.1	1.8±0.2	14.4±0.3	30.8±1

The results give the expected sensitivity of efficiency to impact depth, and emphasise the importance of its enhancement as described above.

5.3 Collection of Large Emittance Beam; Fast Loss

Another test run with the code investigated how well the betatron system would intercept a beam with a very large horizontal emittance, i.e. fast loss. A crude beam model of zero vertical emittance, and large horizontal emittance (distributed uniformly on the 440 π mm mr contour in (x,x') space), was directed into the collector system. The action of the secondary collectors, in addition to the primaries, meant >90% of the beam was stopped in the collector straight in one pass. As described above, this could be very useful for fault/fast loss.

5.4 Plans

After some final bench marking of the code, extensive studies are planned. The code gives full information on the out-scattered distribution of protons, including the geometric location, transverse phase space and energy distributions. This will be very helpful in optimising the overall design.

The action of all the collector systems working together will be studied. Transverse and longitudinal loss, at various growth rates, and over multiple turns will be simulated. Studies of processes in the foil will also be possible. Tests will be run for all likely loss modes, and the results used to tighten up systems and estimate efficiencies. The ultimate aim will be to ensure good protection overall. It is expected that collection efficiencies of over 90% will be possible for important loss modes.

6 PRACTICAL CONSIDERATIONS

6.1 Materials: Activation and Heat

Graphite is the favoured material for collector jaws, principally because of low prompt secondary production and quickly decaying activation products. Also, its low atomic mass increases the volume over which energy is deposited, and reduces heating and stress problems. Stainless steel may also be used for secondary collectors.

At expected levels of loss, ≤0.02%, beam power deposited on collectors per ring is ≤500 W, and this is easily within the capability of water cooled graphite jaws. Graphite collectors on the ISIS Synchrotron operate regularly at ~1 kW. It is assumed that repetitive losses of large amounts of beam (>>0.02%), will be prevented by suitable diagnostics and beam trips. It is not expected that the occasional loss of up to a whole pulse, distributed along the considerable total mass of the collector system, will cause any problems.

6.2 Construction

A modular box type construction is planned [1], with collector jaws enclosed inside. The main jaws would be graphite, mounted in a steel construction. The primary collectors would be water-cooled. The mechanical design would be optimised for quick active handling, allowing for rapid removal and replacement. All the main collector regions would be enclosed in a sealed concrete housing, probably lined with a low activation material. Additional collimation around the beam pipe may be included to absorb out-scattered products and protect components. The same *active handling* concepts as employed on ISIS are planned. These allow hands on maintenance with minimal doses. Key factors are mobile, adaptable and re-configurable shielding, with provision for quick movement and handling of active components.

It is highly desirable operationally to have remotely controllable jaws, to allow flexibility in machine set up. However, movement of ~1 m long collectors is not trivial, and plans so far have assumed movable front face sections of ~10 cm, but fixed otherwise. The correct alignment of the beam to the collector then depends on precise and flexible orbit control, which is not unreasonable in a storage ring. Experience on other machines, with ~1 m long adjustable collectors, suggests that these may be

practical. This needs to be studied in the context of the ESS apertures.

7 SUMMARY AND PLANS

Recent increases to the ESS ring size have allowed for a highly optimised system of collectors. The outline design of the systems is now well established. A comprehensive set of three collector systems should provide protection for the machine under regular operational and fault/experimental conditions. The studies planned, including extensive use of suitable Monte Carlo codes, are aimed at advancing the understanding of factors affecting overall optimisation, e.g. jaw geometry and emittance growth rate.

8 ACKNOWLEDGEMENTS

The author had many enlightening discussions with other participants at the workshop, the fruit of which is included. Thanks are also due to G H Rees for many helpful comments.

REFERENCES

[1] ESS Feasibility Study, Vol. 3, ESS 96-53M, *(available from KFA Julich or RAL).*
[2] I S K Gardner, 'The ESS Accelerator R&D Programme Status', ESS Report ESS 99-95-A.
[3] H Schonauer, 'On the Use of Predeflectors for Improved Beam Loss Compensation', Proc. of EPAC 92, Berlin, Germany.
[4] P J Bryant, E Klein, 'Design of Betatron and Momentum Collimation Systems', CERN Report CERN SL/92-40 (AP)
[5] T Trenkler, J B Jeanneret, "Principles of Two Stage Betatron and Momentum Collimation in Circular Accelerators", CERN SL/95-03 (AP).
[6] D I Kaltchev et al, 'Optimisation of Collimator Jaws Locations For LHC', Proc. of EPAC 96, Sitges, Spain.
[7] P J Bryant, 'Some Advantages of Inclined Collimators', CERN Report CERN SL/92-24 (AP)
[8] C M Warsop, 'Beam Loss Collection in the ESS Accumulator Rings', Proc. of EPAC 98, Stockholm, Sweden.

Beam Collimation System for a 16 GeV Proton Driver [1]

A. I. Drozhdin[2], C. J. Johnstone and
N. V. Mokhov

Fermi National Accelerator Laboratory
P.O. Box 500, Batavia, Illinois 60510

Abstract

It is shown that with the appropriate lattice and collimation design, one can control beam loss in the 16 GeV Fermilab Proton Driver. Based on detailed Monte-Carlo simulations, a *3-stage collimation system* is proposed which consists of primary, secondary and supplementary collimators located in a special 60 m long injection section along with a painting system. It allows localization of more than 99% of beam loss to this section with only a 0.3 W/m (on average) beam loss rate in the rest of the machine. As a result, beam loss and induced radiation effects in lattice elements can be reduced to levels which are defined as acceptable.

1 INTRODUCTION

The proton driver under design at Fermilab is a 16 GeV high intensity rapid cycling proton synchrotron [1, 2]. A very high beam power—1.2 MW in phase-I and 4 MW in phase-II—implies serious constraints on beam losses in the machine. The main concern are the hands-on maintenance and ground-water activation [3]. Only with a very efficient beam collimation system can one reduce uncontrolled beam losses to such an extent that the machine can meet the criteria established for allowable radiation levels.

Table 1: Proton Driver phase-I parameters.

Injection kinetic energy (GeV)	0.4
Top kinetic energy (GeV)	16
Circumference (m)	632.114
Painting injection duration (μs)	90
Dipole field (T)	1.354
Injected 95% emittance ε_N (mm.mrad)	2.6
After painting emittance ε_N (mm.mrad)	50
Protons per bunch at extraction	7.5×10^{12}
Number of bunches	4
Total intensity at extraction	3×10^{13}
Repetition rate (Hz)	15
Longitudinal emittance (eV$\times$s)	0.1
RF frequency (MHz)	53

The parameters of the preliminary 16 GeV Proton Driver racetrack lattice used in this study are presented in Table 1. There are two long straight sections in the ring. The first one, 90 m long with zero dispersion, is used for RF system

[2]e–mail: drozhdin@fnal.gov

and extraction. The second one (60 m long) is used for injection and beam halo collimation. The β-functions and dispersion in the entire ring are shown in Fig. 1.
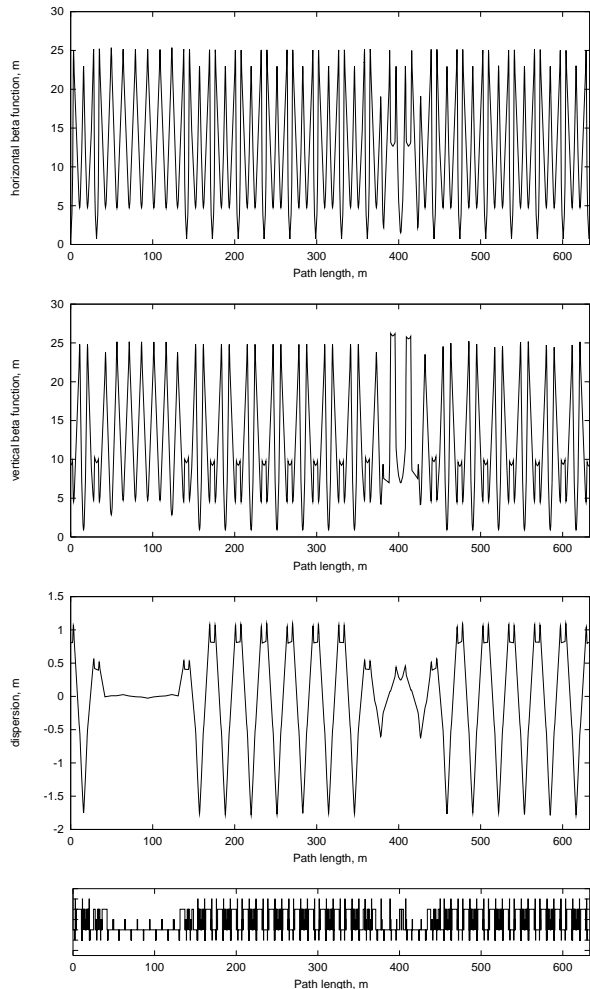

Figure 1: Lattice β-functions and dispersion.

A multi-turn particle tracking is performed through the accelerator which includes beam halo interactions in the collimators using the STRUCT [4] code. Realistic strengths along with aperture restrictions are taken into account for individual lattice components during these calculations. Particles lost in the accelerator are stored into input files for the next step in the study. With these input files, full-scale Monte-Carlo hadronic and electromagnetic shower simulations are done for the lattice and tunnel components, including shielding with realistic geometry, materials and magnetic field, using the MARS [5] code. For such calculations, it is assumed that 10% of the beam is lost at injection and 1% is lost at the ramp and flat top.

The injection section β-functions, beam size after painting, and dispersion are shown in Fig. 2. The separation needed between the circulating proton beam and the injected H^- beam is provided by two 2 m long accelerator magnets located on both sides of the foil (Fig. 3). At the quadrupole doublet the separation is 389 mm, allow-
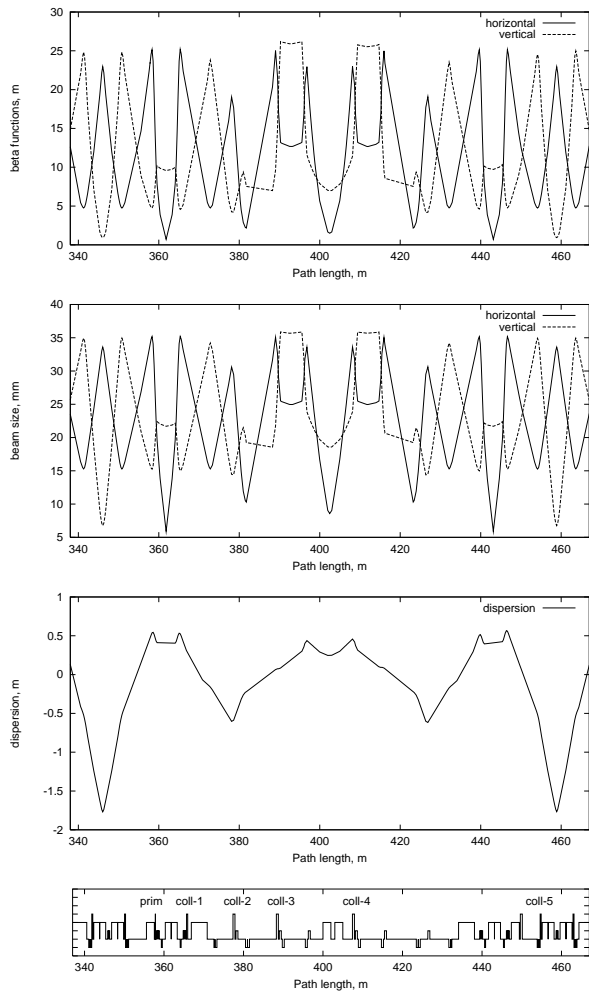
Figure 2: Injection section β-functions, beam size after painting and dispersion.
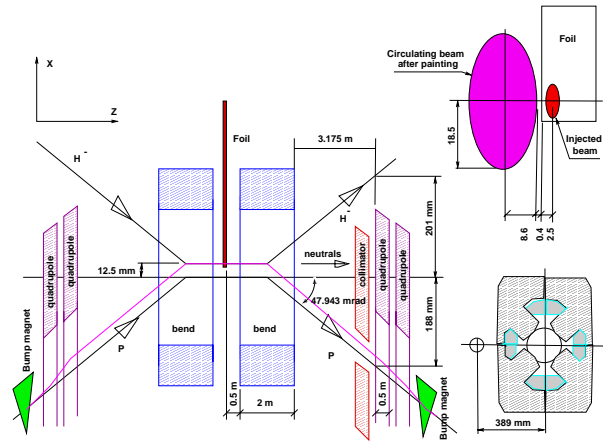

Figure 3: Beam painting scheme.

growth in beam size, show that beam loss rates in the ring without collimation reach 2 kW/m (Fig. 4) which is significantly higher than the above limits.
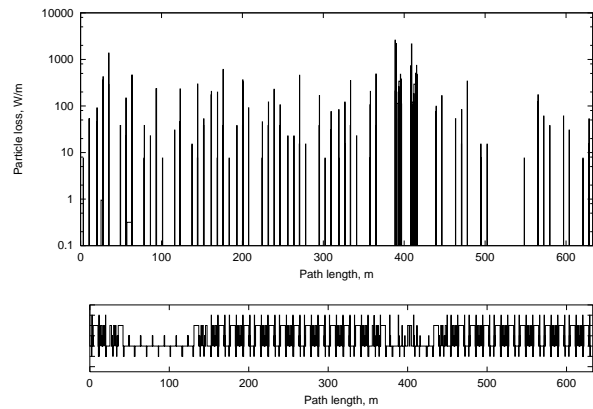

Figure 4: Beam loss in the lattice without collimation.

ing the H^- beam to bypass the quadrupole. Injection painting is used to provide a uniform density distribution of the beam in the transverse plane and is accomplished using two 0.5 m long fast-ramping orbit bump magnets. These magnets move the circulating proton orbit at the beginning of injection by 10.25 mm onto a thin graphite stripping foil located in the middle of the straight section. The overlay of the proton orbit relative to the H^- trajectory and, hence, the density distribution, is controlled using the detailed ramp of these orbit bump magnets whose maximum field reaches 3 kG. A collimator between the doublet and the stripping foil is used to absorb residual neutral components.

2 COLLIMATION AT TOP ENERGY

The beam power at the top energy in phase-I is 1.2 MW. At 16 GeV in the arc of the considered lattice, the limits for hands-on maintenance are 0.25 W/m in the bare beam pipes and 3 W/m in magnets, while the ground-water limit is 0.6 W/m [3]. Calculations performed for a slow rate of

With that in mind, the purpose of the beam halo cleaning system is to localize proton losses in a specially shielded short section, in this way reducing irradiation of the rest of the machine to the prescribed levels. A beam collimation system has been designed using the available space in the injection straight section and consists of horizontal and vertical primary collimators (scatterers) and five secondary collimators (Fig. 2).

For stable operating conditions, the beam size grows slowly, resulting in a small step size in the impact parameter of halo protons on the collimators of the order of a few μm. A thin primary collimator, when introduced into the lattice as a limiting aperture, increases this proton amplitude due to multiple Coulomb scattering and thus drastically increases the proton impact parameter on subsequent downstream secondary collimators. The net result is a significant reduction of the out-scattered proton yield and total beam loss in the machine components. In addition, it decreases localized overheating of collimator jaws and miti-

gates stringent requirements on the collimator alignment.

Table 2: β-functions at the collimators and phase advance between the primary and secondary collimators.

Collimator	β-function (m)		Phase advance (deg)	
	horizontal	vertical	horizontal	vertical
Primary	23.46	5.11	0	0
COLL-1	24.16	4.76	157	57
COLL-2	15.94	5.82	231	120
COLL-3	20.35	6.99	353	279
COLL-4	17.69	10.46	175	18
COLL-5	13.82	9.48	212	349

Secondary collimators need to be placed at phase advances which are optimal to intercept most of particles out-scattered from the primary collimators during the first turn after the beam halo interacts with the primary collimator. The phase space of the protons at the collimators is shown in Fig. 5. The optimal phase advance is around $k \cdot \pi \pm 30^o$. Phase advances between the primary and secondary collimators are presented in Table 2. All horizontal secondary collimators and vertical COLL-4 and COLL-5 have good phase advances with respect to the primary collimator.
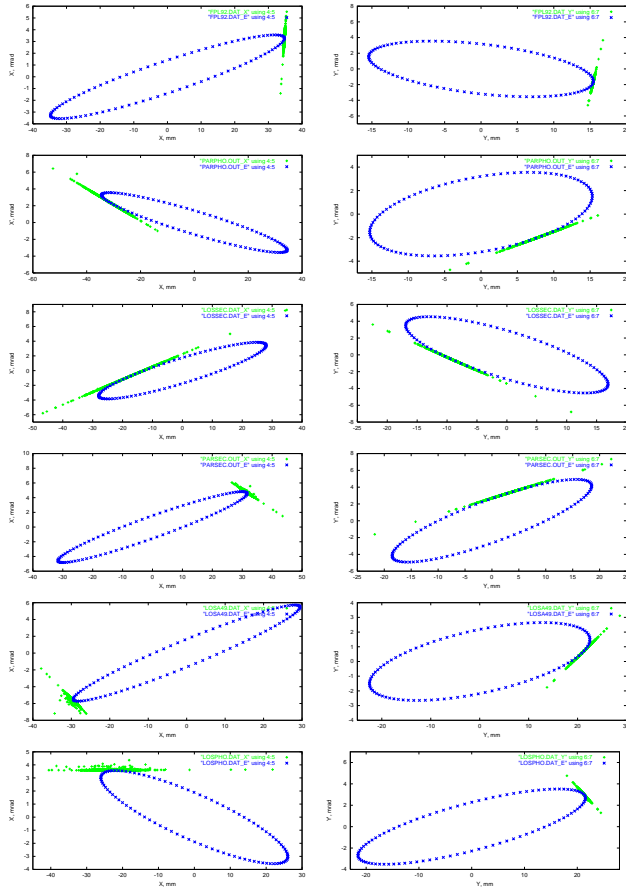

Figure 5: Horizontal (left) and vertical (right) phase space at the primary collimator (top), and at the five secondary collimators.

Calculated beam loss distributions are shown in Fig. 6.

Here a primary collimator (1-mm thick tungsten) is positioned at the edge of the beam after painting, while the secondary collimators (0.5-m long steel) are positioned farther from the beam at various distances. Secondary collimators still generate out-scattered particles lost later in the lattice. One can reduce this component with a *3-stage collimation system* positioning several *main* secondary collimators close to the beam to deal with protons scattered in the primary collimator and several *supplementary* collimators farther from the beam to catch particles out-scattered from the main secondary collimators. With a supplementary collimator COLL-4 at 5 mm from the beam, peak losses at S=460 m are down from 20 to 2 W/m. Additional collimator COLL-5 further reduces losses in the ring. Particle loss in the accelerator using different sets of collimators are presented in Table 3.
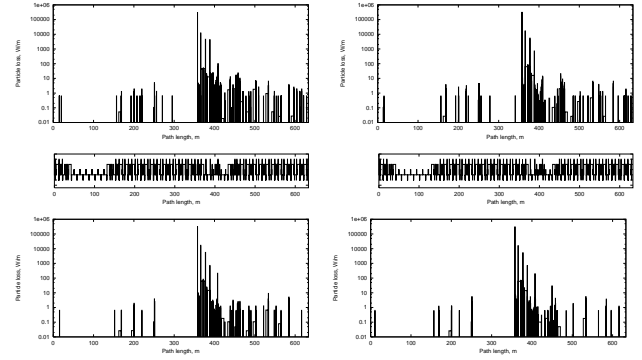

Figure 6: 16-GeV beam loss distributions in the lattice. *Top, left*: COLL-1,2,3 at 0.5 mm. *Top, right*: COLL-1,2 at 0.5 mm, COLL-3 at 3 mm. *Bottom, left*: COLL-1,2 at 0.5 mm, COLL-3 at 3 mm, COLL-4 at 5 mm. *Bottom, right*: The same, with additional COLL-5 at 5 mm.

The thickness and material of primary collimators affect the out-scattered proton angular distribution and nuclear interaction rate. Such a thin scatterer should give a considerable angular kick to the halo particles, but their amplitude should remain smaller than the machine aperture on their way to the secondary collimators. Calculated beam losses are presented in Fig. 7 and in Table 4 for tungsten collimators of several thicknesses with 0.5-m long steel collimators COLL-1 and COLL-2 at 0.5 mm, COLL-3 at 3 mm and COLL-4,5 at 5 mm from the beam edge. A 1 mm collimator provides minimal peak loss rate in the ring.

The β-function varies along the length of a secondary collimator, therefore the collimator apertures are assumed to be tapered follow the beam envelope after the painting. Longer secondary collimators reduce the punchthrough probability and we found that at 16 GeV the minimal length is 0.5 m of steel. As Table 2 and Fig. 8 show, the optimal length is close to 1 m.

According to our calculations 99.82% of beam halo can be intercepted in the collimation section (path length from 358 m to 450 m). The rest is lost outside the collimation section along the machine length of 541 m with average loss

Table 3: Beam loss at 16 GeV: *a)* upstream of the collimation region, *b)* downstream of that, *c)* total in the ring, *d)* peak loss rate in the ring.

Collimator		Beam loss			
Name	Offset	*a*	*b*	*c*	*d*
	mm	%	%	%	W/m
COLL-1	0.5				
COLL-2	0.5	0.072	4.511	4.583	99.9
COLL-3	0.5				
COLL-1	0.5				
COLL-2	0.5	0.099	0.534	0.633	20.2
COLL-3	3.0				
COLL-1	0.5				
COLL-2	0.5				
COLL-3	3.0	0.045	0.233	0.278	5.6
COLL-4	5.0				
COLL-1	0.5				
COLL-2	0.5				
COLL-3	3.0	0.047	0.131	0.177	5.6
COLL-4	5.0				
COLL-5	5.0				

Table 4: Beam loss at 16 GeV *vs* primary collimator thickness *t*: *a)* upstream of the collimation region, *b)* downstream of that, *c)* total in the ring, *d)* peak loss rate in the ring.

	Beam loss			
t	*a*	*b*	*c*	*d*
mm	%	%	%	W/m
0.5	0.038	0.183	0.221	8.7
1.0	0.047	0.131	0.177	5.6
1.5	0.052	0.128	0.180	5.6
2.0	0.054	0.138	0.192	6.2
3.0	0.062	0.114	0.176	9.4

Table 5: Peak loss rate (W/m) in the ring at 16 GeV *vs* secondary collimator length *L*: *a)* upstream of the collimation region, *b)* downstream of that.

L (m)	*a*	*b*
0.25	3.8	18.1
0.50	5.6	5.6
1.00	1.9	1.9
2.00	3.0	1.6

of 0.3 W/m. At several locations, the peak loss rate is up to 5.6 W/m exceeding the tolerable limits. These locations can be locally shielded. Beam loss rates in the collimation system section itself are very high implying a special shielding design. Collimators, magnets and other equipment in the utility section require special cooling as well as fast disconnects and remote control.

3   INJECTION

A practicality in a rapid cycling proton synchrotron dictates a stationary collimator approach with collimator jaws in a fixed position with respect to the beam orbit during the entire cycle. With 10% of intensity lost at injection, 1% at the top energy, and the collimator positions described in the previous section, the calculated beam loss distributions at injection and top energy are shown in Fig. 9. At injection, the peak loss rate in the lattice outside the collimation system is only 0.1 W/m compared to 5.6 W/m at 16 GeV.

4   PERFORMANCE IMPROVEMENT

The same 1 mm thick primary collimator is used as a compromise between the energy loss in the collimator at injection and collimation efficiency at top energy. At injection, halo protons loose a significant fraction of their momentum in such a collimator, resulting in increased beam loss downstream as compared to halo protons at the top energy. To decrease these losses, three additional collimators can be installed in the system in horizontal and vertical planes at 3 mm from the beam edge. Corresponding beam loss dis-
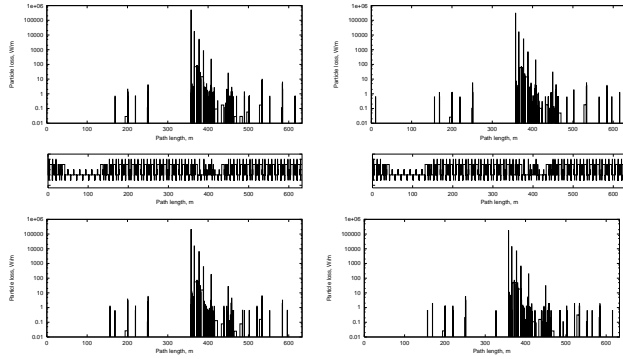

Figure 7: Beam loss with 0.5 mm (top, left), 1 mm (top, right), 2 mm (bottom, left), and 3 mm (bottom, right) thick primary tungsten collimators.
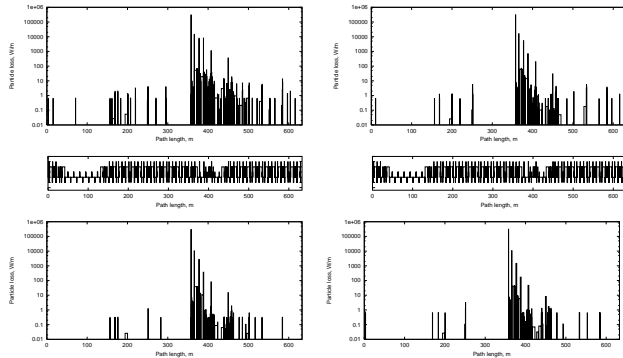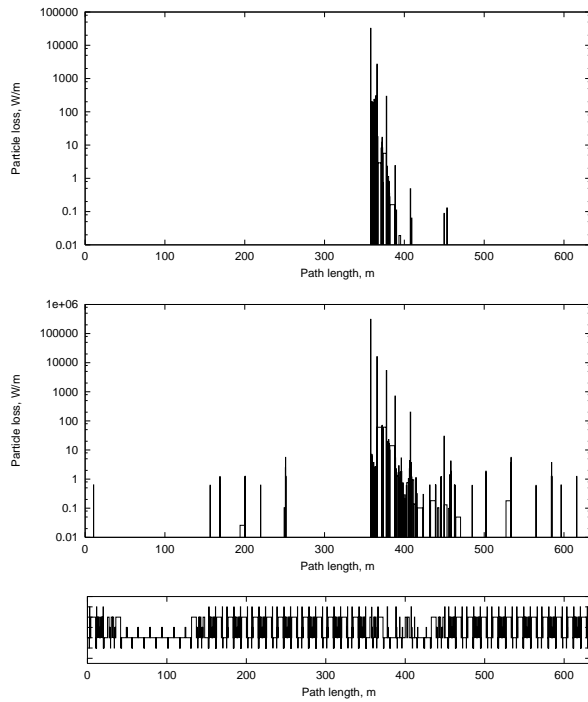

Figure 8: Beam loss distributions for 0.25 and 0.5-m (top) and for 1 and 2 m (bottom) long secondary collimators.

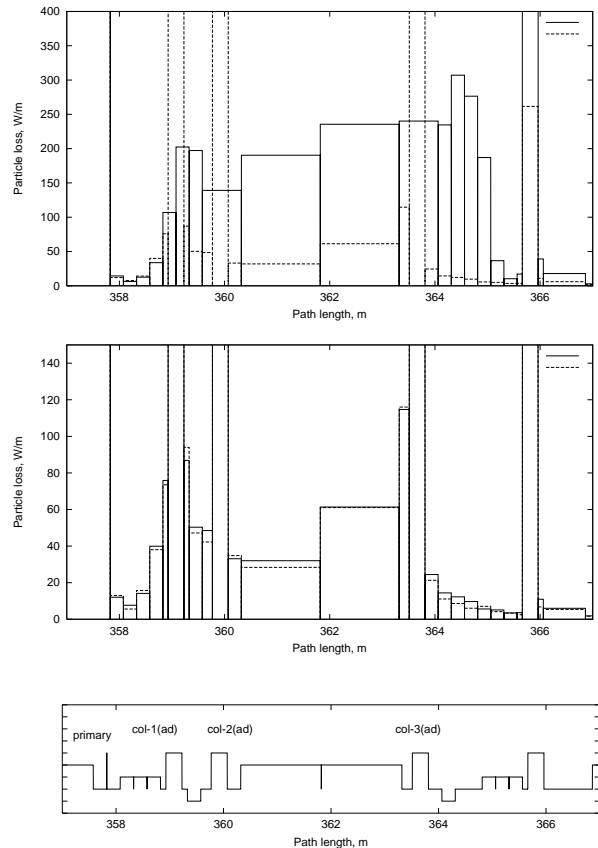Figure 9: Beam loss at injection (top), and at the top energy (bottom).

Figure 10: Beam loss at injection immediately downstream of the primary collimator. *Top*: baseline (solid) and with additional collimators (dashed). *Bottom*: with additional collimators non-magnetized (solid) and magnetized (dashed).

tributions in the collimation section are shown in Figs. 10 and 11. These additional collimators increase slightly particle loss in the first 10 m of the collimation system at the top energy (from 5 W/m to 8 W/m), but reduce losses at injection in that region by a factor of four (from 240 W/m to 60 W/m). As shown in Fig. 12, beam loss in the rest of the machine doesn't change with the additional collimators.

Magnetization of these additional collimators to 0.4 T reduces losses by 10% as shown at the bottom of Figs. 10 and 11. The r.m.s multiple Coulomb scattering angle in the steel collimator of one radiation length (17.6 mm) is equal to 16 mrad at injection. Deflection by the 0.4 T magnetic field at the same length is 2.2 mrad only; therefore magnetization does not improve collimator performance noticeably.

5 CONCLUSIONS

A proposed beam collimation system allows more than 99% of the beam loss to be localized in a specially designed region of the injection section. The system consists of a 1-mm thick tungsten primary collimator sitting at the edge of the beam after painting, and two main secondary collimators which are positioned with 0.5-mm offset with respect to the primary collimators. Supplementary secondary collimators placed with 3 mm and 5 mm offset are used to catch the protons emitted from the main secondary collimators. All secondary collimators are 0.5-m long copper with the aperture tapered according to the beam envelope after painting. At 16 GeV beam loss rates outside the collimation section are on average 0.3 W/m which is below the tolerable limits. The peak loss rates at several locations reach 5.6 W/m, and

will require local shielding. At injection maximum beam loss rates in the arcs are below 0.1-0.3 W/m.

6 REFERENCES

[1] S. Holmes, editor, "A Development Plan for the Fermilab Proton Source", Fermilab-TM-2021 (1997).

[2] W. Chou, "Proton Driver", these proceedings.

[3] O. E. Krivosheev and N. V. Mokhov, "Tolerable Beam Losses and Shielding", these proceedings.

[4] I. S. Baishev, A. I. Drozhdin and N. V. Mokhov, "STRUCT Program User's Reference Manual", SSCL–MAN–0034 (1994); http://www-ap.fnal.gov/~drozhdin/STRUCT/STR2.html.

[5] N. V. Mokhov, "The MARS Code System User Guide, Version 13(95)", Fermilab-FN-628 (1995); N. V. Mokhov et al., Fermilab-Conf-98/379 (1998); LANL Report LA-UR-98-5716 (1998); *nucl-th/9812038 v2 16 Dec 1998*; http://www-ap.fnal.gov/MARS/.
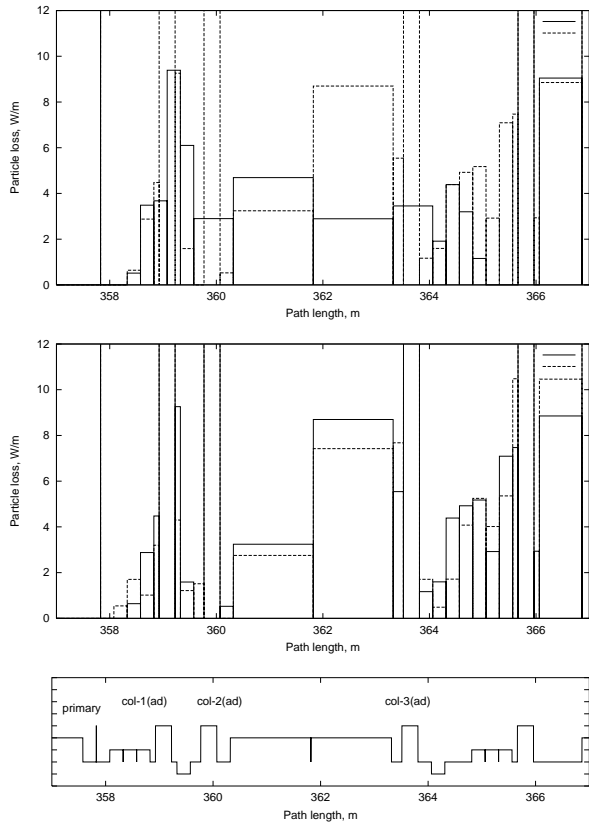
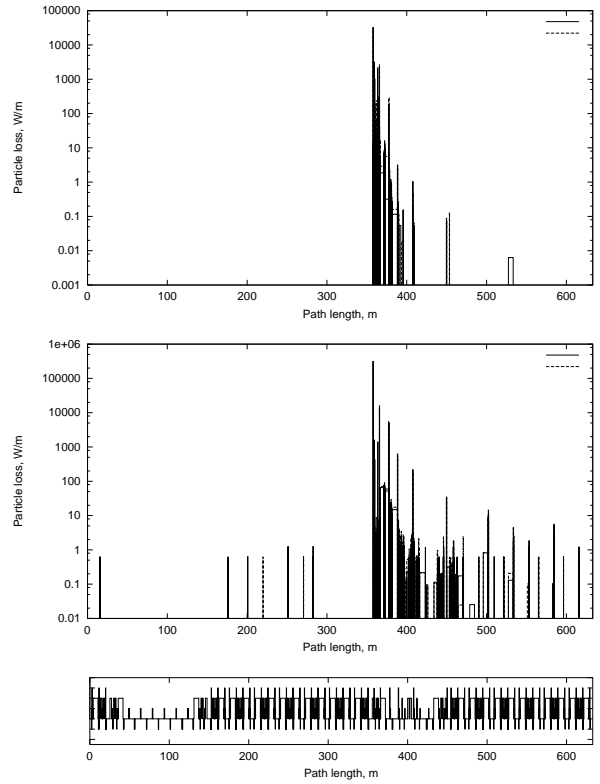Figure 11: Same as in Fig. 10, at the top energy.

Figure 12: Beam loss in the entire machine at injection (top) and at the top energy (bottom) for the system with (solid line) and without (dashed line) additional collimators.

An Update on the Tevatron Collimator System for Collider Run II

M. Church, Fermilab[†], PO Box 500 Batavia, IL, 60510

Abstract

This paper updates the reader on progress since the last report on this subject[1]. The new beam halo collimation system to be installed in the Tevatron for Collider Run II is nearing completion. All collimators have been completed, and 6 out of 13 collimators have been installed in the Tevatron and are currently being tested. All controls have been installed and software algorithms are being developed for both beam halo scraping and proton removal. The remainder of the collimators will be installed by April 2000 and will be fully commissioned with colliding beams during the engineering run between May 2000 and November 2000.

1 INTRODUCTION

The Tevatron is a proton-antiproton storage ring which will be operated at 1 TeV beam energy during Collider Run II. There are two interaction regions, located 1/3 of the ring apart, which will service colliding beam detectors. The primary purpose of the new collimation system is to reduce the detector backgrounds due to beam halo. This is expected to be a serious issue, since the luminosity will be 10 times higher than in Collider Run I. In addition, some of the collimators will be used to remove the proton beam at the end of a store, so that the antiprotons can be decelerated and extracted back to the Recycler Ring for recooling and reuse.

2 DESIGN AND LAYOUT

The collimation system is a two-stage system. Primary scattering targets are followed by secondary absorbing collimators at an appropriate phase advance downstream. The principle behind this system has been described elsewhere[2]. The locations of the targets and collimators in the Tevatron are based on tracking and beam loss simulations by Drozhdin, et. al.[3] and on other constraints imposed by an already existing machine. The layout finally arrived at is shown in Fig. 1. There are a total of 12 targets/collimators to be used for beam halo removal -- a primary target and two associated secondary collimators each for low momentum protons, for high momentum protons, for low momentum antiprotons, and for high momentum antiprotons. There is one additional collimator to be used for proton removal only.

The only locations in the Tevatron with non-zero horizontal dispersion are at the IR's, and therefore momentum collimation and transverse collimation are necessarily mixed in the horizontal plane. There is limited available warm space in the Tevatron, and this puts severe constraints on where the collimators and targets can be located in the ring. Depending on beam conditions and location, the beam sigmas range from .25 mm to 1 mm. During beam halo removal, we anticipate moving the primary targets to within 5 beam sigmas from beam center and the secondary collimators to within 6 beam sigmas from beam center.

It is difficult to make significant changes in the Tevatron lattice (and, indeed, in any already existing machine) in order to modify phase advances, beam separations, dispersion functions, and beta functions. However, a small (~20°) local phase bump will be implemented in part of the ring in order to obtain better vertical beam separation between the protons and antiprotons at the F17 collimators. This will be done by reconfiguring the existing six tune quadrupole circuits and powering some additional quadrupoles independently in order to match to the IR inserts. Table 1 shows the beta functions, dispersion functions, beam separations, and phase advances from primary target to secondary collimators.

3 MECHANICAL DESCRIPTION

The collimator consists of 2 pieces of stainless steel, 1.5m long, bolted together in an L-shape configuration. These pieces are machined and ground to ±25μm tolerance and then electropolished. This assembly is welded inside a stainless steel box with bellows on each end. The bellows are connected to stationary beampipe on either end. The entire assembly is supported by two cradles which can be moved independently in both the vertical and horizontal directions by stepping motors. The limit on the motion is ±25.4mm, and currently the smallest step size is 25.4μm, although this could be reduced to 3.2μm if necessary. The support system and bellows are such that each end of the collimator can be moved independently to opposite ends of its range of motion with no mechanical binding. Position readback is provided by LVDTs (linear differential voltage transformers), and mechanical damage is prevented by limit switches on all degrees of motion. The stepping motors each develop 1125 in-oz (.81 m-kg) of torque and are geared such that one motor turn corresponds to 1.27mm in collimator translation. The maximum speed is

---
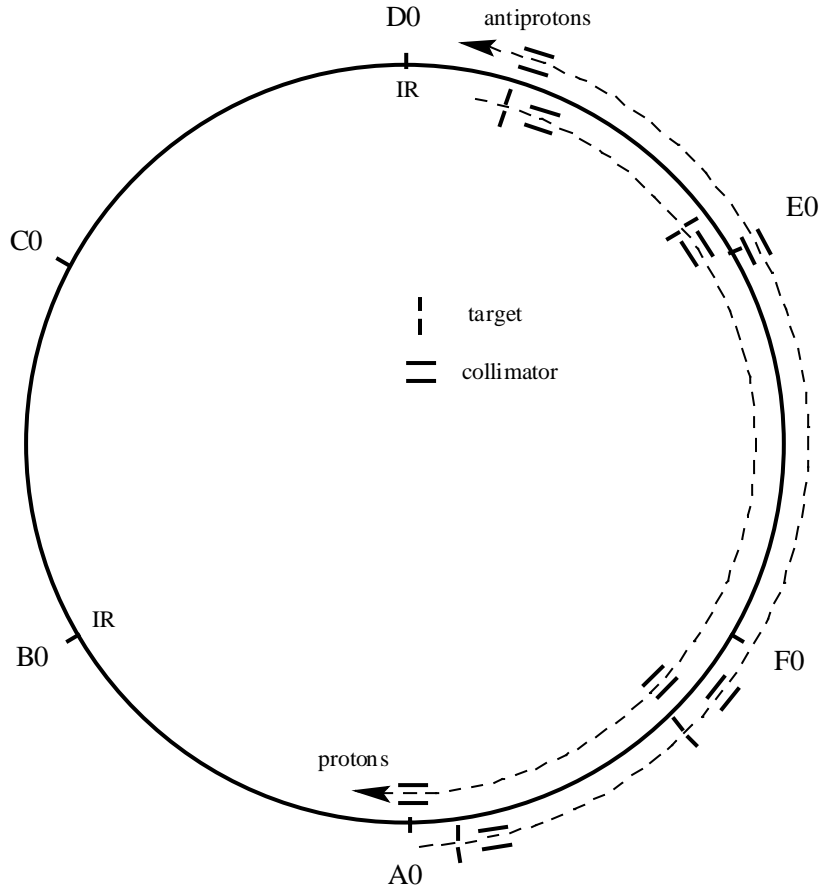
Figure 1: Layout of Tevatron beam halo targets and collimators for Run II.

collimator	protons		antiprotons		β_x (m)	β_y (m)	D_x (m)	beam separation	
	ϕ_x (deg) (mod 360)	ϕ_y (deg) (mod 360)	ϕ_x (deg) (mod 360)	ϕ_y (deg) (mod 360)				x (mm)	y (mm)
D17 target	0	0	326	349	87	34	5.7	4.4	1,9
D17(2)	6	12	320	337	63	47	4.9	3.5	2.7
D17(3)	8	14	318	335	58	52	4.7	3.2	2.9
D49 target	171	187	156	153	88	75	1.8	5.0	3.1
E0(1)	183	195	143	142	59	94	1.7	3.6	4.1
E0(2)	213	225	112	123	96	59	2.3	2.2	4.4
E0(3)	214	227	111	121	99	59	2.4	2.1	4.4
F17(1)	148	167	177	182	91	32	5.9	5.6	1.0
F17(2)	149	169	176	179	85	35	5.7	5.4	1.2
F17 target	156	180	170	168	61	50	4.9	4.6	2.1
F48	312	302	14	46	99	29	1.8	5.7	1.4
F49 target	326	349	0	0	179	40	2.5	7.9	1.3
A0	331	14			160	61	2.6	7.4	3.2

Table 1: Beta functions, dispersions, phase advances from target, and beam separations at collimators.

currently set at about 1.2 turns/second which translates to 1.5mm/sec of transverse collimator speed. The maximum speed is actually limited by the inductance of the motor coils, which broadens the stepping pulse width and causes them to overlap in time at too high a stepping rate.

The primary targets are similar to the collimators, except the stainless steel L-assembly is only .06m in length, and the entire assembly is supported on only one movable cradle. The scattering targets are tungsten wings, 5mm thick, which are bolted to the L-assembly and protrude .6mm further into the aperture than the stainless steel.

4 BEAM STUDIES

During the current fixed target program, there has been some limited opportunity for dedicated beam studies with the collimators. This time has been used to understand collimator alignment issues, understand collimator mechanical tolerances, understand beam loss limits, develop automated scraping algorithms, and generally "get the bugs out" of a new system. To date, all of these studies have been done at 150 GeV.

For beam halo scraping, when the collimators are moved from the full out position to within 5-6 beam sigmas from the beam, their motion will be controlled via fast feedback from local loss monitors and a global beam current monitor. This feedback loop is in the locally controlling cpu and can occur at up to 720 Hz. It has been successfully tested at low intensity. The algorithms for

sequencing the motion of the 12 targets/collimators are also being developed and tested. Future studies will also be done at 800 GeV.

5 PROTON REMOVAL

In the future, it will be required to remove the protons from the machine at the end of a collider store in order to efficiently decelerate the antiprotons for reuse. In order to do this quickly and without quenching the Tevatron, four normal conducting dipoles (old MR B2's) have been installed in the E0 long straight section of the Tevatron and powered in a dogleg configuration. During proton removal, this dogleg will be turned on, and a special collimator with tungsten wings bolted to each end will be gradually inserted into the proton beam between the first and second dipoles (see Fig. 2). The scattered particles will be mostly pointing toward the tunnel wall away from the superconducting magnets. In addition, two more collimators just downstream of the dogleg will help shield the superconducting magnets from particle spray. This will allow for rapid extinction of the proton beam, without danger of quenching. This procedure has been tested successfully at low energy and at low intensity, and it will be tested at higher intensity and higher energy in the near future. It appears likely that the entire proton beam (10^{13} particles) can be cleanly removed from the machine in about 120 seconds.
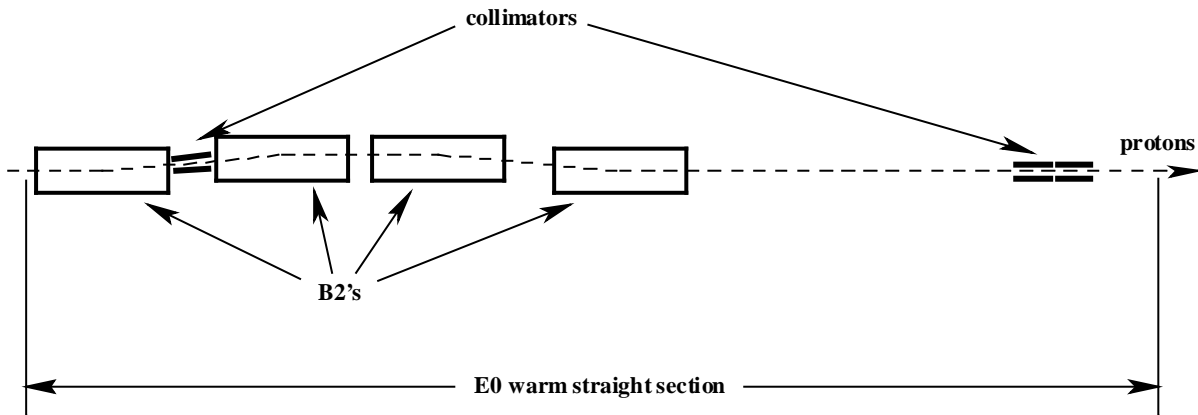

Figure 2: Proton removal dogleg at E0 straight section.

REFERENCES

[1] M Church, "Proposed Tevatron Collimation System for Collider Run II", International Symposium on Near Beam Physics, ed. R Carrigan and N Mokhov, Fermilab, Batavia, IL, p. 134 (1997)

[2] M Seidel, "The Proton Collimation System of HERA", DESY 94-103, (1994)

[3] A Drozhdin, et. al., "Tevatron Run-II Beam Collimation System", Proceedings of the 1999 Particle Accelerator Conference, NYC (to be published); and Fermilab-Conf-99/059

Crystal Collimation Experiment on 70-GeV Proton Accelerator

A. G. Afonin, V. M. Biryukov[1], V. N. Chepegin,
Y. A. Chesnokov, V. I. Kotov, V. I. Terekhov,
E. F. Troyanov, Yu. S. Fedotov

Institute for High Energy Physics, Protvino, Russia

Yu. M. Ivanov,

Nuclear Physics Institute, St.Petersburg, Russia

W.Scandale,

CERN, Geneva

M. B. H. Breese

University of Surrey, UK

Abstract

The first proof-of-principle experiment on "crystal collimation" was performed with 70-GeV protons on IHEP accelerator. A bent crystal installed in the ring as a primary element upstream of a collimator has reduced the radiation levels downstream in the accelerator by a factor of two. The measurements agree with Monte Carlo predictions.

1 INTRODUCTION

Bent-crystal technique is well established for extracting high energy beams from accelerators. It was successfully applied at the energies up to 900 GeV[1], and simulations were able to predict the results correctly. Recent experiments at IHEP Protvino[2] have demonstrated that this technique can be quite efficient: 50-70% of the beam have been extracted using a thin (3-5 mm) *Si* channeling crystal with bending of 0.5-1.5 mrad, with intensity of the extracted 70-GeV beam up to 6×10^{11} protons per spill. At this intensity, no cooling measures were taken and no reduction in the efficiency observed. At IHEP Protvino this technique has been routinely used since 1987 to deliver a 70 GeV beam to particle physics experiments. One of the IHEP crystals did extract 70 GeV protons over 10 years since 1989 without replacement and without any degradation seen! It was shown in the experiments at BNL AGS and at CERN SPS that radiation damage in channeling crystals is sizable only at over $(2\text{-}4) \times 10^{20}$ proton/cm^2.

The theory of crystal extraction is based mainly on detailed Monte Carlo simulations tracking the particles through a curved crystal lattice and the accelerator environment in a multipass mode. Our code CATCH was successfully tested in the extraction experiments at CERN, FNAL, and IHEP in 1992-99[3]. Monte Carlo predictions, suggesting a "multipass" mode of crystal extraction where efficiency is dominated by the multiplicity of particle encounters with a short crystal, have lead to the breakthrough in the extraction efficiency demonstrated at IHEP Protvino[2].

Crystal can channel a charged particle if it comes within so-called critical angle θ_c, about ± 150 µrad$/\sqrt{pv(GeV)}$ in

---

[1]e–mail: biryukov@mx.ihep.su

silicon. This restricts crystal efficiency in divergent beams. However, if a crystal is installed in a circulating beam, particle may scatter in inefficient encounters and have new chances on later turns. To benefit from the "multi-pass" channeling, the crystal must be short enough to reduce beam losses in multiple encounters with it.

It should be promising to apply this bent-crystal technique for a beam halo scraping in accelerators and storage rings[4, 5]. A bent crystal, serving as a primary element, should bend halo particles onto a secondary collimator. A demonstration experiment of this kind was performed at IHEP where for the first time a significant reduction in the accelerator background was obtained with a bent crystal incorporated into beam cleaning system[2].

A crystal collimation system for a gold ion beam is now being installed at RHIC in collaboration with IHEP[6], and –upon success– it will serve there on permanent basis.

2 CRYSTAL DEFLECTOR

Bending a short crystal to be installed in the accelerator vacuum chamber is not easy. The first crystal used in the course of our experiment of 1997-1999 was of Si(111) type and performed as a short plate of a big height, $0.5 \times 40 \times 7$ mm^3 (thickness, height, and length along the beam direction, respectively). It was bent transversally with a metal holder which had a hole of 20 mm size for beam passage, and gave the channeled protons a deflection of 1.7 mrad. Despite an angular distortion (a "twist") in that design, encouraging results on beam extraction were obtained in our first run in December 1997, Figure 1. The peak extraction efficiency reached about 20% and the extracted beam intensity was up to 1.9×10^{11} [7]. Here and later on in the paper, the extraction efficiency is defined as the ratio of the extracted beam intensity as measured in the external beamline to all the beam loss in the accelerator.

To further increase the extraction efficiency, further crystals (without twist) were made from a monolithic Si piece in a shape of "O" at the Petersburg Nuclear Physics Institute, as described in Ref. [8]. The crystals Si(110) used in our recent runs had the length along the beam direction of only 5 mm. The bent part of the crystal was just 3 mm long, and the straight ends were 1 mm each.

Such a crystal, with bending angle of 1.5 mrad, was successfully tested in March 1998 and has shown extraction efficiencies over 40% [8]. In the mean time we have changed the crystal location in order to use another septum magnet (with partition thickness of 2.5 mm instead of 8 mm as in the old scheme) where a smaller bending angle is required from a crystal. This change was also motivated by the intention to test even shorter crystals (two of them, 2.5 and 3.0 mm long, are already undergoing tests). The crystal used in this location was new, but of the same design and dimensions as earlier described[8]. The bending angle used in this run was 0.65 mrad.
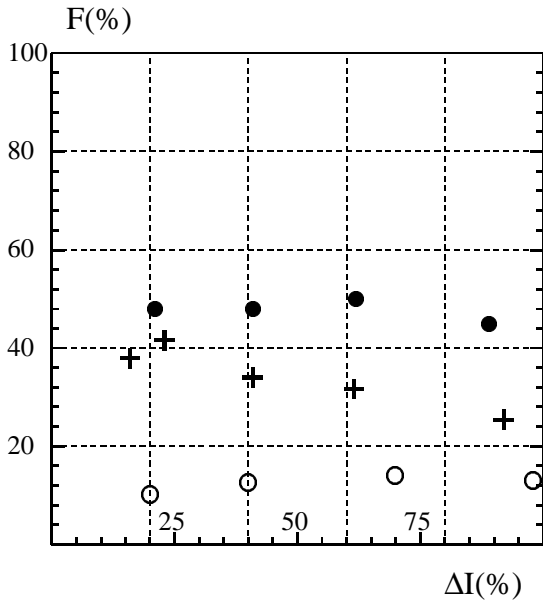
Figure 1: Spill-averaged efficiency of extraction as measured with 5-mm crystal 0.65 mrad bent (●), December 1998; 5-mm crystal 1.5 mrad bent (+), March 1998; 7-mm twisted crystal 1.7 mrad bent (o), December 1997; plotted against the beam fraction taken from the accelerator.

3 STUDY OF CRYSTAL WORK IN SLOW-EXTRACTION MODE

Experiments on crystal-assisted slow extraction and scraping are very similar on the part of crystal component, the only difference being the target of the channeled deflected beam — is it an external beamline or beam absorber. This is why we were able to study the crystal work first in the conditions of slow extraction where we could measure the amount and characteristics of the channeled beam more easiely.

The general schematics of beam extraction by a crystal is shown in Ref.[8]. As the small angles of deflection are insufficient for a direct extraction of the beam from the accelerator, a crystal served as a primary element in the existing scheme of slow extraction. Crystal was placed in straight section 106 of the accelerator upstream of a septum-magnet of slow-extraction system. The accuracy of the crystal horizontal and angular translations was 0.1 mm and 13.5 μrad, respectively. The horizontal emittance of the circulating proton beam was about 2π mm×mrad, and the beam divergence at the crystal location was 0.6 mrad. A local distortion of the orbit by means of bump windings in magnets moved the beam slowly toward the crystal. To obtain a uniform rate of the beam at crystal, a monitor for close loop operation based on a photomultiplier with scintillator was used to automatically adjust the orbit distortion. We used also function generator to control current in bump windings.

The beam deflection to the septum and its transmission through the beam line of extraction were supervised with a

complex system of beam diagnostics, including TV system, loss monitors, profilometers, intensity monitors[8]. All the diagnostics devices were firstly tested in fast-extraction mode and calibrated with beam transformers. The background conditions were periodically measured with and without crystal. According to the measurements, the fraction of background particles (e.g. elastically scattered protons) together with the apparatus noise did not exceed 4% of the useful signal level. This background was subtracted from the efficiency figures shown in the paper. The fraction of the beam directed to the crystal was defined as the difference between the measurements of the circulating beam intensity done with beam transformers before and after the beam extraction, with the systematic error of 1%. The extraction efficiency was evaluated in every cycle of acceleration.

4 CRYSTAL EFFICIENCY

The accelerator beam intensity during the experiment was about $1.3{\times}10^{12}$ protons per cycle. The fraction of the circulating beam incident on the crystal ΔI was varied from 20 to 90%. The spill duration of the channeled beam in the feedback regime was on the order of 0.5 s. The plateau of the IHEP U-70 accelerator magnet cycle is 2 s long while the overall cycle of the machine is 9.6 s. Figure 1 shows the efficiency of extraction averaged over the spill, as measured in our three experiments of 1997-98. In the last one, the efficiency was about 50% even when all the accelerator beam was directed onto the crystal. The spill-averaged efficiency figures were reproducible with 1% accuracy from run to run. The dependence of the extracted beam intensity on orientation of the crystal was about the same as in Ref.[8] and not shown here. The highest intensity of the extracted beam, for $1.15{\times}10^{12}$ protons incident at the crystal in a cycle, was equal to $5.2{\times}10^{11}$.

As the beam moves radially toward the crystal, the proton incidence angle drifts at the crystal. For this reason the extraction efficiency varies in time during the spill, especially for a large beam fraction used. The peak extraction efficiency in a spill was always greater than 60%. The absolute extraction efficiency as obtained in our Monte Carlo simulations agree with the measurements to accuracy of about 5% for spill-averaged figures.

5 CRYSTAL COLLIMATION EXPERIMENT

Bent crystal, situated in the halo of a circulating beam, can be the primary element in a scraping system, thus serving as an 'active' collimator. In this case, the only difference from extraction is that channeled particles are bent onto a secondary collimator instead of the extraction beamline. The bent particles are then intercepted (with sufficiently big impact parameter) at the secondary element and absorbed there.

We have performed the first demonstration experiment on crystal-assisted collimation. A bent crystal, with the same dimensions as the extraction crystals described above
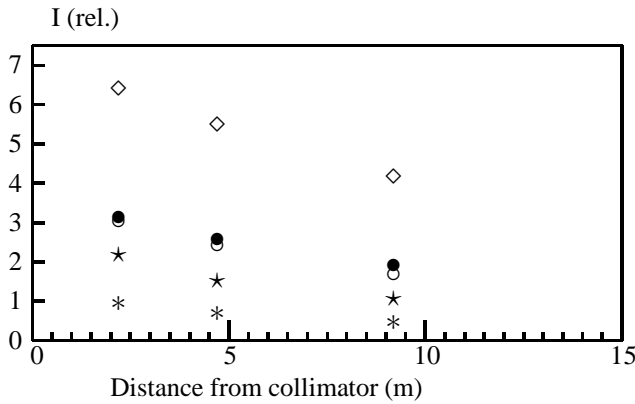
I (rel.)

Figure 2: Radiation levels as monitored at three places along the ring in the vicinity of FEP, for different cases (bottom up): ∗ - beam kicked onto absorber by a kicker magnet; ⋆ - aligned crystal as primary; ○ - FEP works as primary; ● - misaligned crystal as primary; ⋄ - Si target downstream of FEP is primary.

and with bending angle of 1 mrad, was positioned upstream of a secondary collimator (stainless steel absorber 4 cm wide, 18 cm high, 250 cm long) "FEP" and closer to the beam in the horizontal plane. As the horizontal betatron tune is 9.73 in our accelerator, it was most convenient to intercept the bent beam at FEP not immediately on the first turn, but after 3 turns in the accelerator. In this case the deflection angle of 1 mrad transforms into more than 20 mm horizontal offset, and so the bent beam enters the FEP collimator at some ∼15 mm from the FEP edge. The optimal horizontal position of the crystal w.r.t. the FEP edge was found to be ∼10 mm.

Radiation levels were monitored at three places along the ring in the vicinity of FEP, from ∼2 to ∼10 meters downstream of the backward edge of the collimator. Several different cases have been studied.

- The whole accelerator beam was kicked into the middle of the FEP face by a kicker magnet. That's an ideal case for a beam interception and absorption, so the resulting radiation levels (nonzero due to escape of some primary and secondary particles from the FEP body) can be considered as a kind of pedestal for the results obtained then with several actual scraping methods. These lowest levels are shown in Figure 2 by (∗) marks.

- When FEP was a primary element scraping the beam halo continously, the halo particles were entering FEP very close to its edge (at sub-micron depths) so the escape of particles from FEP body because of outscattering was very important. This resulted in higher radiation levels (○) as shown in Figure 2.

- A bent silicon crystal was introduced then about 60 cm upstream of the forward edge of FEP. Crystal served as a primary element of the scraping system, being closer

to the circulating beam than FEP, with the offset of about 5-15 mm in the radial plane. When the crystal was misaligned, it was acting as an amorphous target scattering particles. The collimator downstream could intercept some of the scattered particles. The radiation levels measured (●) in this setting were not so different from the preceding case of direct (by FEP) scraping of the beam halo.

- When the crystal was aligned to the best angle w.r.t. the incident beam, a substantial number of halo particles was channeled and deflected into the depth of FEP for best absorption. The monitored radiation levels with aligned crystal serving as primary element are shown (⋆) in Figure 2. One can conclude that about one half of the halo was extracted and forwarded to a safe place (i.e. the middle of FEP face) for absorption, reducing the radiation background in the ring correspondingly.

- Finally, another case studied was a silicon target (amorphous) positioned downstream of FEP as a primary element. In this case the machine was not protected from the scattered particles originating in the target, so the radiation levels achieved (⋄) were the highest.
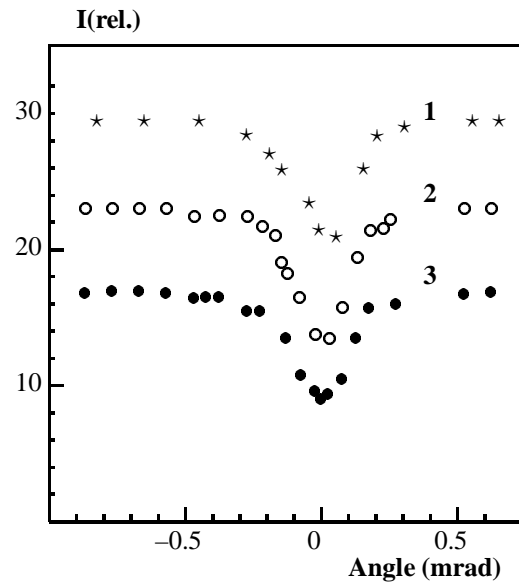
I(rel.)

Figure 3: Measured irradiation in detectors 1, 2, 3 as function of crystal angle.

Figure 3 shows how the radiation level depends on the angular alignment of the crystal. At the best crystal angle, preferable for channeling, the radiation levels decrease by up to factor of ∼two in the places of monitoring. This is explained by the fact that ∼50% of the incident beam is channeled by the crystal and deflected to the depth of FEP where absorbed. In the case when crystal was out and the beam was scraped directly by FEP, the radiation at the monitors

was at about the same level as in the case of disaligned crystal.
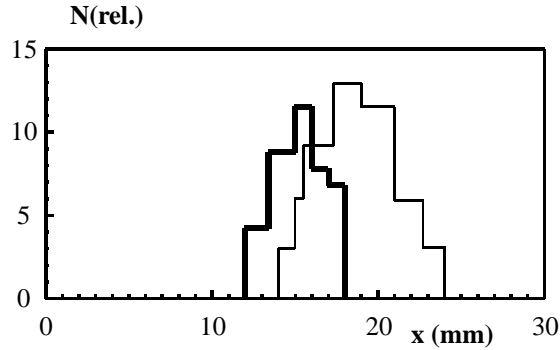
N(rel.)

Figure 4: Profiles measured at FEP entry face: the channeled beam (thick line) and the beam (thin line) deflected by kicker magnet.

We were able to check the crystal efficiency figure by alternative means, measuring the profile and intensity of the particles incident at the FEP entry face. The channeled beam had a narrow profile and was well distanced from the FEP edge, as shows Figure 4 where this profile is shown in comparison with the profile of the accelerator beam deflected onto FEP by a kicker magnet. From comparison of the two profiles, from crystal and from kicker, we again derived the crystal efficiency, which was found to be about 50%, in agreement with the radiation monitoring figures and with the earlier shown figures of extraction efficiency with crystal in straight section 106.

6   CONCLUSIONS

The crystal-assisted method of beam steering (for scraping or slow extraction) demonstrates peak efficiencies in the order of 60-70% and shows reliable, reproducible and predictable work. Crystal can channel at least $5\text{-}6\times10^{11}$ ppp with no cooling measures taken and no degradation seen.

In our experiment this technique was for the first time demonstrated for scraping of the beam halo. Such application has been studied by computer simulation for several machines, notably RHIC [6] and Tevatron [9]. We have shown that radiation levels in accelerator can be significantly decreased by means of channeling crystal incorporated into beam cleaning system as a primary element.

We continue tests with crystals as short as down to 1 mm, where Monte Carlo predicts 80-90% efficiency of steering. We study different techniques to prepare bent crystal lattices with required size, one of the most interesting approaches is described in Ref.[10].

7   ACKNOWLEDGEMENTS

8   REFERENCES

[1] C.T.Murphy, et al.(E853 Collab.) "First results from bent crystal extraction at the Fermilab Tevatron". Nucl. Instr. and Meth. B 119 (1996), 231

[2] A.G.Afonin, V.M.Biryukov, V.N.Chepegin et al., "New projects of crystal extraction at IHEP 70-GeV accelerator". Particle Accelerator Conference Proceedings (New York, 1999); CERN LHC 99-2 (MMS), Geneva 1999.

[3] V.M. Biryukov, Yu.A. Chesnokov and V.I.Kotov, "Crystal Channeling and its Application at High Energy Accelerators". Berlin: Springer (1997)

[4] M.Maslov, N.Mokhov, I.Yazynin, "The SSC Beam Scraper System", SSCL-484 (1991)

[5] V.M.Biryukov, p. 179 in Proceedings of "Near Beam Physics" Symp., Fermilab (1997)

[6] D. Trbojevic, V. Biryukov, M. Harrison, B. Parker, P. Thompson, A. Stevens, N. Mokhov, A. Drozhdin. "A Study of RHIC Crystal Collimation" EPAC Proceedings (Stockholm, 1998)

[7] A.G.Afonin et al., *JETP Lett.* **67** (1998) 741.

[8] A.G.Afonin et al., Phys. Lett. **B 435** (1998), 240.

[9] V.M.Biryukov, A.I.Drozhdin, N.V.Mokhov. "On Possible Use of Bent Crystal to Improve Tevatron Beam Scraping". PAC Proceedings (New York, 1999). Fermilab-Conf-99/072 (1999).

[10] M.B.H.Breese, NIM **B 132** (1997) 540

Observations on Betatron Collimation and the Effect of Tune Splitting

S. Koscielniak, TRIUMF, 4004 Wesbrook Mall, Vancouver, B.C., Canada V6T 2A3

Abstract

We find the conditions for optimal collimator location by the method of "Lagrange undetermined multipliers". We give a 'global' explanation for the advantage of tune splitting on betatron collimation in terms of the envelope of all possible optimal collimator positions. We make analytic calculations of the maximum amplitude of surviving particles for elliptic and jaw-type collimators at a variety of optimal locations. All statements and results reported in this brief resume are substantiated and derived in a lengthy 1997 TRIUMF internal report[6] along with further elaboration of the properties of the $\mathcal{A}$, $\mathcal{C}$ and $\mathcal{J}$ functions.

Part I

Conclusions

1 INTRODUCTION

The optics of the machine in the collimation sector will be referred to as the *lattice*. We take a longitudinal coordinate s along the optic axis. Let X, Y be horizontal and vertical coordinates relative to the optic axis, and introduce reduced coordinates $x = X/\sqrt{\beta_x}$, $y = Y/\sqrt{\beta_y}$ where β_x, β_y are the betatron functions. In terms of x, y the beam envelope is perfectly cylindrical. Consider a primary cylindrical aperture (in x, y) of radius r_0 and a source point x_0, y_0 on its circumference such that $x_0^2 + y_0^2 = r_0^2$. Particles impinging on the aperture-surface are nuclear-scattered into 2π solid angle. Thus particles emanating from the source point can have a variety of amplitudes A_x, A_y and phases ϕ_{0x}, ϕ_{0y} that give the same x_0, y_0, namely:

$$A_x = x_0/\cos\phi_{0x} \quad \text{and} \quad A_y = y_0/\cos\phi_{0y}. \quad (1)$$

Suppose there is a collimator downstream of the source-aperture which may either be circular of radius r, or a pair of parallel faced jaws diametrically opposite one another. The radius perpendicular to a jaw has length r, also. The ratio $r_0/r \leq 1$ is denoted $\cos\psi$. The phase advance to the collimator is ϕ_{1x}, ϕ_{1y}; and so the possible values of displacements of the source particles after they have transited downstream to the collimator are:

$$x = A_x \cos(\phi_{1x} - \phi_{0x}) \quad \text{and} \quad y = A_y \cos(\phi_{1y} - \phi_{0y}). \quad (2)$$

Note, ϕ_0 depends on the particle whereas ϕ_1 depends on the lattice.

1.1 Function definitions

Let us define the amplitude function A to be

$$A(\phi_{0x}, \phi_{0y}) = \frac{(A_x^2 + A_y^2)}{r^2} = \left[\frac{x_0}{r\cos\phi_{0x}}\right]^2 + \left[\frac{y_0}{r\cos\phi_{0y}}\right]^2. \quad (3)$$

Actually, there are a family of such functions as the source point x_0, y_0 varies.

We define the circular collimator function C to be

$$C(\phi_{0x}, \phi_{0y}; \phi_{1x}, \phi_{1y}) = (x^2 + y^2)/r^2 \quad (4)$$

$$= (A_x/r)^2 \cos^2(\phi_{1x} - \phi_{0x}) + (A_y/r)^2 \cos^2(\phi_{1y} - \phi_{0y}).$$

Clearly $A \geq C$. Particles which satisfy $C \geq 1$ are stopped whereas particles which satisfy $C < 1$ pass through the collimator unimpeded.

Let us define the jaw collimator function J. Suppose the jaws form an angle α with the horizontal or x-axis.

$$J(\phi_{0x}, \phi_{0y}; \phi_{1x}, \phi_{1y}) = (x\sin\alpha + y\cos\alpha)/r \quad (5)$$

$$= (A_x/r)\sin\alpha\cos(\phi_{1x} - \phi_{0x}) + (A_y/r)\cos\alpha\cos(\phi_{1y} - \phi_{0y}).$$

For this jaw, particles which satisfy $J \geq 1$ are stopped whereas those which satisfy $J < 1$ survive.

It may be stating the obvious but one must always take the A and C functions (or A and J) in mutually corresponding pairs keyed by identical values of x_0, y_0. Suppose we consider A, C, J as functions of ϕ_{0x}, ϕ_{0y} for given, fixed ϕ_{1x}, ϕ_{1y}. The intersection of a level plane with these functions will give rise to a contour in the ϕ_{0x}, ϕ_{0y} plane. We shall call the corresponding contours $\mathcal{A}_l, \mathcal{C}_l, \mathcal{J}_l$ where the suffix denotes the level, l. For given x_0, y_0 and l, there are families of $\mathcal{C}_l$ contours depending on the location ϕ_{1x}, ϕ_{1y}.

2 SUMMARY OF CONCLUSIONS

The "below the tree-tops" objective of an efficient collimation scheme is to best approximate some particular $\mathcal{A}_1$ by a superposition of $\mathcal{C}$ (or of $\mathcal{J}$) contours subject to the constraints imposed by the beam optics on the phase advances ϕ_{1x}, ϕ_{1y} of the various collimators used. The "above the tree-tops" objective is to find collimator phase advances that fill the space occupied (in the plane of intial phases) by the continuous family of all possible curves $\{\mathcal{A}_1(x_0, y_0)\}$.

The perfect solution to the "high-level" objective is to make a circular (or octagonal, for jaws) pipe that extends from $\phi_1 = \psi$ to $\pi - \psi$. Of course, this is not practicable. Moreover, the continuous pipe corresponds to an infinite number of collimators. *Consequently, the task becomes to place a small, finite number of collimators so as to generate some surface that is as close as possible to $\{\mathcal{A}_1\}$.* Now, although an optimum collimator or jaw cuts at $A \equiv 1$ for only one value of $\phi_{0x}, \phi_{0y}, x_0, y_0$, nevertheless it cuts neighbouring points close to $A = 1$ because extrema are locally quadratic. Hence, a small number of collimators or jaws will cut a crenellated surface (rather like a castle with cusp-shaped battlements and towers) close to $\mathcal{A}_1$. Though it takes an infinite number of thin collimators to cut at $A = 1$ for all ϕ_{0x}, ϕ_{0y}, it requires only a small finite number (e.g. 3 circular collimators or 24 jaws) to cut the amplitude down to $A \leq 2$ for all initial phases.

131

2.1 Circular collimators

For the case of circular collimators, one can cut the amplitudes down to $A \leq 1 + 2(r_0/r)^2$ using two $\mathcal{C}$ contours at $\phi_{1x} = \phi_{1y} = \pm \psi$ independent of source x_0, y_0. The amplitudes can be further reduced to $A \leq 1 + (r_0/r)^2$ by adding a single $\mathcal{C}$ contour due to a collimator at $\phi_{1x} = \phi_{1y} = \pm \pi/2$. Adding further collimators becomes progressively less efficient. Lattices with un-split or split phase-advances both allow to find suitable locations for the three collimators.

If the optics of the collimation sector of the machine determines that $\phi_x(s) \neq \phi_y(s)$, then immediately there are *more* intersections of the phase-advance trace with the $\{\mathcal{A}_1\}$-region; and automatically there is the possibility to make more cuts at level $l = 1$ than in the case of a lattice with no splitting of the phase advances. The lattice with tune splitting has a further advantage. Suppose we are forced to look for phase advance solutions at a level higher than $l = 1$. The envelopes of the $\mathcal{A}_l$ curves have l rise most rapidly as one moves along the diagonal of the ϕ_{1x}, ϕ_{1y}-plane. If the $\phi_{1x,y}$ trace moves off the diagonal (preferably approximately perpendicular to it), then one can find solutions at a lower level than if one had been forced to stay on the diagonal. Consequently, we should expect a large split in the phase advances to be advantageous and that good collimator solutions appear distant from the diagonal.

The *disadvantage* of a phase-advance splitting, is that the collimation efficiency (i.e. maximum amplitude of surviving particles) depends on the source location x_0, y_0. However, provided the axes of the ϕ_{1x}, ϕ_{1y} plane are avoided, then this is not much of a detraction.

2.2 Jaw-type collimators

The obvious strategy of synthesizing three octagonal apertures from 24 jaws to imitate three circular collimators (placed at $\phi_1, \pi - \phi_1, \pi/2$) is a profitable one. However, horizontal and vertical jaws at the $\pi/2$ phase advance are not very effective, and may be omitted leading to a total of $8 + 12 = 20$ jaws. Because a single jaw obstructs a single side of the beam path (e.g. either upper or lower, but not both) object and image jaws must be placed on opposite sides of the particle beam. The maximum amplitude remaining after the superposition of these jaws is difficult to calculate, but a probably pessimistic upper bound is $A \leq 1 + 1/\sin^2 \psi$.

Lessons learnt from the placement of circular collimators are applicable to jaws. Phase advances on the ϕ_{1x}, ϕ_{1y} axes should be avoided. Phase advances on the diagonal collimate symmetrically in the x and y directions. A greater number of optimal phase advances for jaw locations becomes available if the tunes are split in the collimation sector of the machine.

In the following parts of this document, we shall first explore the properties of $A, \mathcal{A}$; then study the behaviour of $C, \mathcal{C}$ so as to elucidate the good locations for circular collimators; then finally consider the properties of $J, \mathcal{J}$ so

as to suggest a strategy for placing jaws.

3 THE AMPLITUDE FUNCTION

3.1 General behaviour

Because of the squaring ($A = A_x^2 + A_y^2$) the function A is reflection symmetric in the two half-planes. Further, if $x_0 = y_0$, then the function repeats itself in the four quadrants of the (ϕ_{0x}, ϕ_{0y}) plane. A may be written:

$$A = (r_0/r)^2 + (x_0/r)^2 \tan^2 \phi_{0x} + (y_0/r)^2 \tan^2 \phi_{0y} . \quad (6)$$

The minimum value of $A = (r_0/r)^2 < 1$ occurs at $(0,0)$. In the neighbourhood of this point, the amplitude function is parabolic. However, for large values $|\phi_{0x}| \to \pi/2$ and $|\phi_{0y}| \to \pi/2$ the amplitude function rises like a rectangular-sided chimney.

3.2 Contours $A = l$

The family of contours $\mathcal{A}_l$ which are generated by varying the source point x_0, y_0, and each of which is a set of (ϕ_{0x}, ϕ_{0y}) coordinate pairs that satisfy $A(x_0, y_0) = 1$, has two surprising properties:

- all pass through $\phi_{0x} = \pm \phi_{0y} = \pm \psi(l)$

- all are bounded (from above and below) by the lines $\phi_{0x} = \pm \psi(l)$ and $\phi_{0y} = \pm \psi(l)$,

where the rather special angle ψ is given by

$$\psi(l) = \arccos[r_0/(r\sqrt{l})] \quad \text{and} \quad r_0 \leq r \times \sqrt{l} . \quad (7)$$

The source points may be parametrized by the azimuthal angle θ: $x_0 = r_0 \cos \theta$ and $y_0 = r_0 \sin \theta$. The case $y_0 = 0$ leads to a 'contour' which is composed of two straight lines parallel to the ϕ_{0y}-axis given by $\phi_{0x} = \pm \psi$. The case $x_0 = 0$ leads to a 'contour' which is composed of two straight lines parallel to the ϕ_{0x}-axis given by $\phi_{0y} = \pm \psi$.

3.2.1 Inner square

The intersection of these four lines gives rise to a square with vertices at $|\phi_{0x}| = |\phi_{0y}| = \psi$. If we vary x_0 and y_0 we find various squashed-ellipse shaped contours; but all of them pass through the vertices of a single square! and none of the ellipses pass inside it. Consequently, the square is the inner envelope of all possible $\mathcal{A}_l$ contours.

3.2.2 Outer cross

If we vary x_0, y_0 we find various contours; but none of them pass outside an outer 12-sided boundary in the shape of a cross with four-fold symmetry. The extremities of the cross touch the lines $\phi_{0x} = \pm \pi/2$ and $\phi_{0y} = \pm \pi/2$. The vertices of the cross nearest the origin 'cut-back' to the inner-square. The envelope is composed of the intersection of the two straight lines $\phi_{0x} = \pm \psi(l)$ and $\phi_{0y} = \pm \psi(l)$. It should be evident that as l increases, so $\psi(l)$ increases and so the bounding cross dilates as one moves to higher level curves; and in the limit $l \to \infty$ and $\psi \to \pi/2$ the cross degenerates to a square.

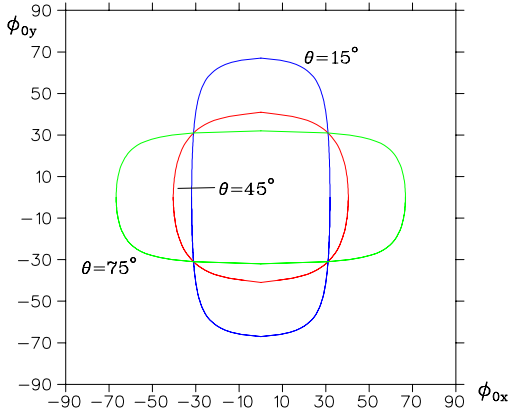Figure 1: Example $\mathcal{A}_1$ curves for various source points θ.
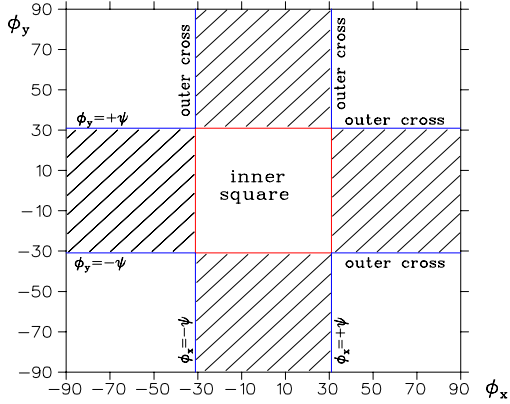

Figure 2: Region occupied by all $\mathcal{A}_1$ (i.e. the "outer ross") is shown with cross-hatching.

4   REGION OCCUPIED BY ALL $\mathcal{A}_L$

The totality of initial phases that satisfy $A = l$ as we move over all points (x_0, y_0) on the source aperture, shall be called $\{\mathcal{A}_l\}$. We have already found the boundaries of this area; the 'inner square' and the 'outer cross' with 'cutbacks' to the inner-square. So the area $\{\mathcal{A}_l\}$ is composed of four rectangular segments. For given r_0/r, as the level l increases so ψ increases, which implies that the unoccupied inner-square dilates and that the unoccupied area about the outer-cross contracts. It should be clear that one moves most quickly from one $\{\mathcal{A}_l\}$-region to another higher $\{\mathcal{A}_m\}$-region $(m > l)$ when one moves (outward from the origin) along the diagonals of the ϕ_{0x}, ϕ_{0y}-plane.

4.1   Region occupied by all $\mathcal{A}_1$

The region $\{\mathcal{A}_1\}$, but in the ϕ_{1x}, ϕ_{1y}-plane, is the object that we must try and construct from a superposition of segments taken from $\mathcal{C}$ (or $\mathcal{J}$) curves; because if we do this all cuts to the family of A functions will be at level $l = 1$.

Part II

Circular collimator

Let us consider the functions $C(\phi_{0x}, \phi_{0y})$ for a variety of fixed values of the collimator phase advance (ϕ_{1x}, ϕ_{1y}). C

only has solutions ϕ_{0x}, ϕ_{0y} for ϕ_{1x}, ϕ_{1y} within the domain between the "inner-square" and the "outer cross". The C trajectories in the ϕ_{0x}, ϕ_{0y} plane are bounded from below by the inner square. C is *not* symmetric under the substitutions $\phi_{0x} \to -\phi_{0x}$ and/or $\phi_{0y} \to -\phi_{0y}$. Consequently, the general $\mathcal{C}_1$ contour has rather an odd shape (a sort of distorted/asymmetric ovoid). However, there are useful special cases where a higher symmetry is manifest; as in section 6. It is stating the obvious, but a collimator with phase-advance outside a region $\{\mathcal{A}_l\}$ will contribute nothing to the collimation of $A(x_0, y_0)$ at level l; but it will contribute toward the collimation of A at a level greater than l.

5   OPTIMUM PHASE ADVANCES ϕ_{1X}, ϕ_{1Y}

Let us take a low-level approach. If we consider some general $\mathcal{C}$ and project the contour up on to the corresponding A-function, then we find A at the intersection points is typically much greater than unity. The altitude of the intersections could be reduced if we can bring $\mathcal{C}$ closer to $\mathcal{A}_1$. But this is not sufficient; because $\mathcal{C}$ is lop-sided there are some intersections (of $\mathcal{C}$ projected on to A) at very low and some at very high altitudes. Hence we are led to the "low level" objective: to make from segments of various $\mathcal{C}$ contours (with differing ϕ_{1x}, ϕ_{1y}, but the same x_0, y_0) the best approximation to the desired $\mathcal{A}_1$ contour. Usually one segment of a particular $\mathcal{C}$ contour is closer to $\mathcal{A}_1$ than any other. Thus we need to do two things:

- find the neighbourhoods of the closest segments
- move these segments close to the origin of the ϕ_{0x}, ϕ_{0y} plane.

We can hope that a careful choice of the phase advances ϕ_{1x}, ϕ_{1y} will bring the segments of various $\mathcal{C}$ closer to $\mathcal{A}_1$. Actually, because the solution is $\phi_{0x,y} = \phi_{1x,y}$ this procedure turns into a "boot-strapping process" that is skillfully short cut using the technique of "Lagrange multipliers" introduced in Appendix A. Each of the segments $\mathcal{C}$ is closest to the corresponding $\mathcal{A}_1$ when $\phi_{0x} = \phi_{1x}$ and $\phi_{0y} = \phi_{1y}$ *and* where the phase advances must satisfy the condition:

$$\left(\frac{r_0}{r}\right)^2 \left[\frac{\cos^2 \theta}{\cos^2 \phi_{1x}} + \frac{\sin^2 \theta}{\cos^2 \phi_{1y}}\right]^2 = 1 . \qquad (8)$$

Because equation (8) is formally identical with the amplitude function, $A = 1$, so its properties are those given in section 3.1. It follows that (for some particular source point x_0, y_0) we can construct $\mathcal{A}_1$ from an infinite set of $\mathcal{C}(\phi_{x1}, \phi_{y1})$. Unfortunately, to account for all possible combinations x_0, y_0 requires an infinity of ϕ_{1x}, ϕ_{1y} pairs that fill the area of the $\{\mathcal{A}_1\}$-region. And this is how we came to discover the "high-level" or "above the tree tops" objective stated in section 2. But this is equivalent to making a section of continuous pipe and must must be considered too ambitious. Fortuitously, quite a good approximation to $\mathcal{A}_1(\theta)$ curves can be made with only a few intersecting $\mathcal{C}(\theta)$ segments, provided that the collimator phase advances are judiciously chosen.

5.1 Single collimator

A single collimator, alone, with optimum phase advances, will reduce the amplitude to $A = 1$ at the point $\phi_{0x} = \phi_{1x}$, $\phi_{0y} = \phi_{1y}$; but elsewhere the amplitude will be larger. See figure 3. Indeed, in the vicinity of $\tan \phi_{0x,y} = \tan \phi_{1x,y} - 1/\sin 2\phi_{1x,y}$ the amplitude A will be very large. For some particular source point θ, the circular collimator is little better than a jaw placed perpendicular to the radius through angle θ — because for practical purposes there is no distinction between very large (due to circular) and infinite amplitude (due to jaw).

5.2 Two collimators

We need another collimator to cut down the very large amplitudes that were missed by the first. The contour $\mathcal{C}'$ is a mirror image of the contour $\mathcal{C}$ due to the first collimator if the phase advances to the second collimator are $-\phi_{1x}, -\phi_{1y}$. But this is upstream of the first collimator! However, $\cos^2(\pi - \alpha) = \cos^2(-\alpha)$ and $\sin^2(\pi - \alpha) = \sin^2(-\alpha)$. So consider, now, the use of an 'object' collimator at phase advance ϕ_{1x}, ϕ_{1y} and an 'image' collimator at $\pi - \phi_{1x}, \pi - \phi_{1y}$. See figure 4. If the phase advance is optimum, then at the two points $\phi_{0x} = \pm\phi_{1x}$, $\phi_{0y} = \pm\phi_{1y}$ the amplitude $A = 1$. The maximum amplitude occurs at the intersection of the two contours $\mathcal{C}$ and $\mathcal{C}'$ and is very large if either collimator is paced along the ϕ_{1x} or ϕ_{1y} axes.
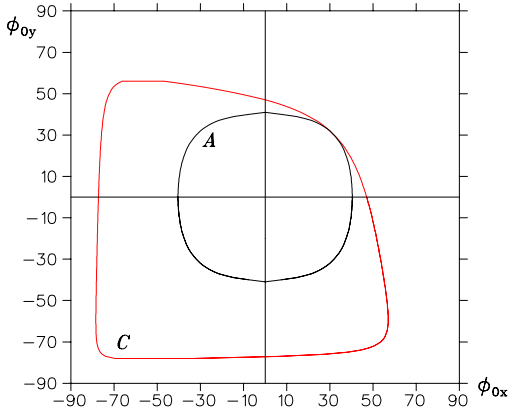

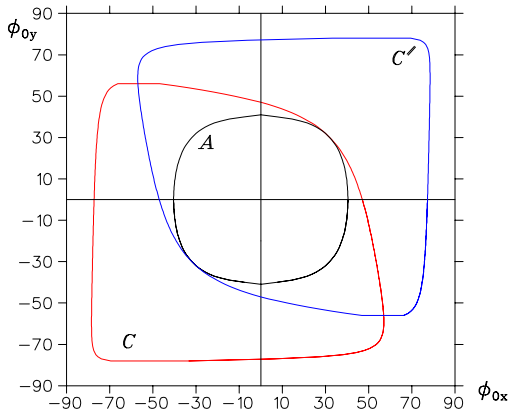Figure 3: Single collimator at $\phi_1 = \psi$; $\theta = 45°$.

Figure 4: Two collimators, at $\phi_1 = \psi$ and $\phi_1 = \pi - \psi$.

6 COLLIMATORS ON THE ϕ_1-DIAGONALS

Suppose the phase advances to the collimator satisfy $|\phi_{1x}| = |\phi_{1y}|$ (that is the collimator position lies on one of the diagonals of the ϕ_{1x}, ϕ_{1y} plane). In this case, the maximum value of the amplitude function (for surviving particles) is *independent* of the source position:

$$A \le \left(\frac{r_0}{r}\right)^2 \left[2 + \frac{(r/r_0)^2 - 1}{\sin^2 \phi_1}\right] . \qquad (9)$$

If the optimum phase advance is used, $\phi_1 = \psi$, then $A \le 1 + 2(r_0/r)^2$ and the particle amplitudes are $r\sqrt{A}$.

6.1 Special symmetry location

Let us consider how to introduce a third collimator, figure 5, so as to cut down the amplitude A in the neighbourhood of the intersection of the contours $\mathcal{C}$ and $\mathcal{C}'$. With a single additional collimator we need to simultaneously and symmetrically cut down the amplitudes. We find the requisite condition to be $|\phi_{x1}| = |\phi_{y1}| = \pi/2$. In this case, the identity $\sec^2 z = (1 + \tan^2 z)$ implies that $A = C + (r_0/r)^2$ *independent* of the source point; and so the collimator function shares the same symmetry as A.

At this moment, it is simple to find what amplitudes are collimated. Particles with initial phases (ϕ_{0x}, ϕ_{0y}) outside the contour $\mathcal{C}_1$ are stopped. If we project up this contour on to the amplitude function we shall obtain some new contour. Almost always this "intersection contour" is *not* a level curve of A because the height of the intersection will vary with the initial phases. But in this special case, the intersection curve is equal to $\mathcal{A}_{1+r_0^2/r^2}$. Hence this specially chosen collimator will stop all particles with initial amplitudes $\sqrt{A_x^2 + A_y^2} \ge \sqrt{r^2 + r_0^2}$.

7 CONSTRAINED BY THE LATTICE

In reality, the optical lattice constrains the phase advances to be:

$$\phi_{1x}[\phi_{1y}(s)] \quad \text{or} \quad \phi_{1y}[\phi_{1x}(s)] , \qquad (10)$$

depending on which we prefer. We shall call the locus of (10) as s varies the phase-advance *trace*. The lattice constraint can be introduced by an extra Lagrange multiplier, Appendix A.1. For each source angle θ, there is an optimal ϕ_{1x}, ϕ_{1y} pair that simultaneously satisfies both equations (8) and (10). These phase advance combinations are the intersection of the *trace* with the domain $\{\mathcal{A}_1\}$. Typically, a small discrete subset from the continuum band of ϕ_{1x}, ϕ_{1y} pairs give satisfactory collimation.

7.1 No tune splitting

In the case that there is no tune splitting along the collimator section, $\phi_{1x} = \phi_{1y}$ we find the *only solution* for the phase advance is $\phi_{1x,y} = \pm\psi(1)$. The negative value is of course upstream, but is equivalent to the location $\phi_{1x} = \phi_{1y} = (\pi - \psi)$ downstream of the source aperture. Figure 6 shows the introduction of three strategically
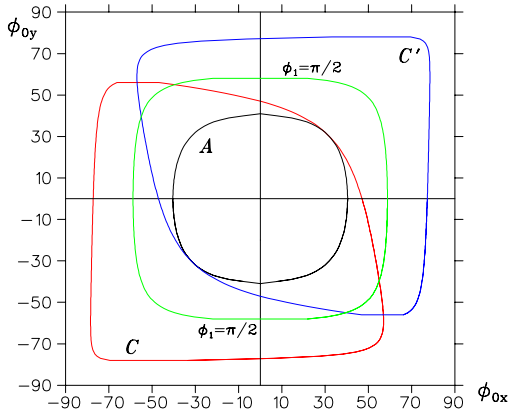
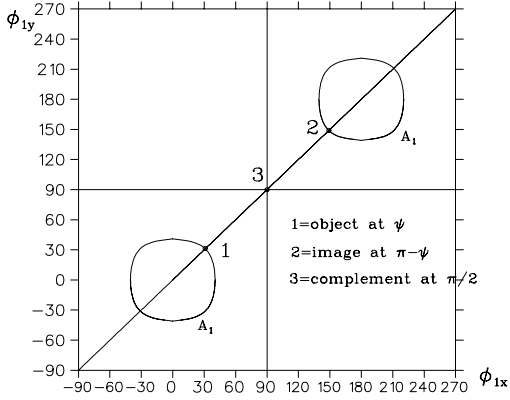Figure 5: Cuts due to 3 collimators in the plane of initial phases; source point $\theta = 45°$.

Figure 6: Placement of 3 collimators in the plane of phase advances.

placed collimators in the ϕ_{1x}, ϕ_{1y} plane. Figures 3,4,5 show the progressive cuts made as these collimators are added for the case $\theta = 45°$.

7.1.1 More collimators

We have found only two points in the $\{\mathcal{A}_1\}$-region, and so this is somewhat of a disaster! Ideally we should like many more collimators placed at optimum phase advances. If, however, we broaden our view to encompass the possibility of finding phase advances that lie in higher level regions $\{\mathcal{A}_{l>1}\}$, then additional solutions may be found. However, these will be less efficient collimators because:

- cutting at level $l > 1$
- area of ϕ_{0x}, ϕ_{0y} clipped away is smaller.

7.2 *Lattice with tune splitting*

The $\{\mathcal{A}_1\}$-region contains all possible solutions of the optimum phase advance condition (8). If the optics of the collimation sector of the machine determines that $\phi_x(s) \neq \phi_y(s)$, then immediately there are *more* intersections (see figure 7) of the phase-advance trace with the $\{\mathcal{A}_1\}$-region; and automatically there is the possibility to make more cuts at level $l = 1$ than in the case of a lattice with no splitting of the phase advances.

The lattice with tune splitting has a further advantage. Suppose we are forced to look for phase advance solutions at a level higher than $l = 1$. The envelopes of the $\mathcal{A}_l$ curves have l rise most rapidly as one moves along the diagonal of the plane of phase advances. If the phase advance trace moves off the diagonal (preferably approximately perpendicular to it), then one can find solutions at a lower level than if one had been forced to stay on the diagonal. Consequently, we should expect a large split in the phase advances to be advantageous and that good collimator solutions appear distant from the diagonal.

The *disadvantage* of a split in the phase advances to the collimators, is that the optimal phase advance (or equivalently the efficiency of collimation) depends on the source location θ. But this deficiency is more than made up for by the greater choice of collimator locations that result in cuts at $\mathcal{A}_1$.

7.2.1 Sinusoidal tune split

As an example, suppose the phase advances to the collimator are split with a sinusoidal modulation:

$$\phi_{1x} = \nu s + \Delta \sin(k\nu s) \quad \text{and} \quad \phi_{1y} = \nu s - \Delta \sin(k\nu s) . \quad (11)$$

The wavenumber k must be an even integer divided by an odd integer (in order to have phase advances $\phi_{1x,y}$, $\pi - \phi_{1x,y}$ and $\pi/2$). The collimator locations are given by

$$\cos(2\nu s) \approx J_0(2\Delta) \cos 2\psi + \quad (12)$$

$$[1 - J_0^2(2\Delta) + 2J_1(2\Delta) \cos 2\theta \sin 2\psi \sin k\psi]/J_0(2\Delta) ,$$

which shows clearly, that there are a range of optimum phase-advances as the source angle θ varies. The approximation is quite good if $|\Delta| < 1/4$.

For the LHC lattice, the phase split is rather larger than $1/4$, and so we solved numerically for the optimum phase advance ϕ^+ as a function of the source point as parametrized by angle θ. We have done this for a lattice with $\Delta = \pi/8$ and $k = 2$ and $r_0/r = 6/7$, and the result is given in figure 7 below. A perhaps better value would be $k = 1$ or $k = 3$ which leads to greater symmetry between the x and y planes.
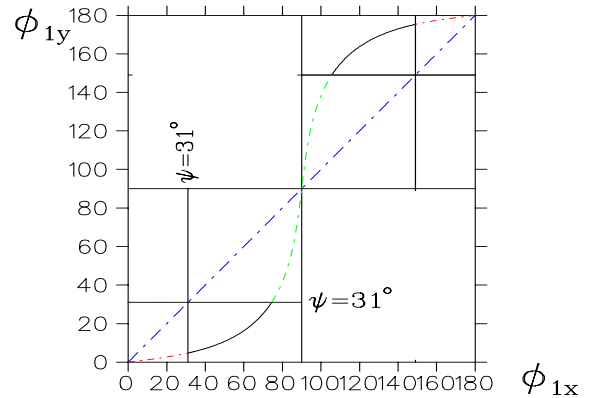

Figure 7: Trace of optimum collimator phase advance (solid lines) for lattice with sinusoidally split tune.

Part III

Jaw-type Collimator

8 INTRODUCTION

Consider the collimation of an elliptic source by a system of jaws. The $\mathcal{A}_l$ curves do not change, rather it is the collimator curves become jaw contours $\mathcal{J}(\phi_{0x}, \phi_{0y})$. The $\mathcal{J}$ contours are open. Figure 8 shows the placement of a single jaw with respect to the coordinate system of the source aperture. The jaw has the property that all particles with initial amplitudes satisfying $J = (x \sin\alpha + y \cos\alpha)/r \geq 1$ are stopped. If $0 \leq \alpha \leq \pi/4$ then we have an 'upper jaw', and the corresponding lower jaw is given by $\alpha = (\pi - \alpha)$. Roughly speaking, an upper jaw close to the source aperture collimates $y_0 > 0$ whereas a lower jaw collimates $y_0 < 0$.

At the "low-level", our goal is to make an $\mathcal{A}_1$ contour (for some particular x_0, y_0) from segments of various jaw contours $\mathcal{J}$ by using the freedom to select the phase advances ϕ_{1x}, ϕ_{1y}. Before attempting this, let us study some properties of the jaw function J and its contour $\mathcal{J}$ created by intersection with the level plane $l = 1$.

In sections 9,11 we study jaws placed parallel to the x and y axes; and in sections 12,13 we study jaws parallel to the diagonals $x = \pm y$. A combination of eight such jaws can give an octagonal aperture which is a fair approximation to a circular collimator.
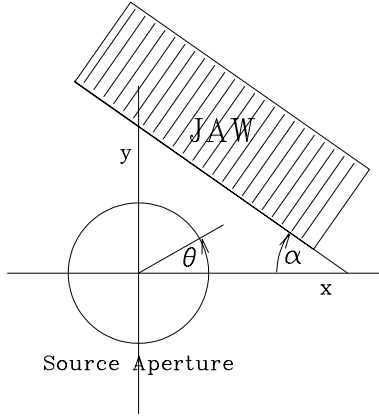

Figure 8: View along the optic axis of source aperture and jaw inclined at angle α.

9 SINGLE JAW, CASES $\alpha = 0, \pi$

Let us consider the phase advance ϕ_{1y} to be given and fixed and investigate how the jaw contour moves in the ϕ_{0x}, ϕ_{0y}-plane as a function of the source point x_0, y_0. Each one of these $\mathcal{J}$ curves, has of course a corresponding $\mathcal{A}(x_0, y_0)$.

9.1 The curves $\mathcal{J}(y_0)$

When the jaw inclination $\alpha = 0$, then the jaw-face is parallel to the x-axis (horizontal) and the collimation is mostly of the vertical motion. In this case, the $\mathcal{J}$ contour is the single line parallel to the ϕ_{0x}-axis and with ϕ_{0y}-axis intercept

given by:

$$y_0 \cos(\phi_{1y} - \phi_{0y}) = r \cos\phi_{0y} . \qquad (13)$$

This 'contour' clearly sweeps over the ϕ_{0x}, ϕ_{0y}-plane as y_0 moves. In order to avoid confusion with the general ordinate ϕ_{0y}, let us call the intercept value $\phi_{Jy}(y_0, \phi_{1y})$. $\phi_{Jy} \to \pi/2$ as $y_0 \to 0$ independent of ϕ_{1y}; and that the 'contour' moves nearest to the origin when $y_0 \to r_0$.

To find which particles are collimated (and what are the maximum amplitudes) we must project up from the jaw-contour on to the corresponding A function. The A-function on the section $\phi_{0y} = \phi_{Jy}$ is given by:

$$A(y_0) = \frac{A_x^2}{r^2} + \frac{1}{\cos^2(\phi_{1y} - \phi_{Jy})} , \qquad (14)$$

where $A_x^2 = (r_0^2 - y_0^2)/\cos^2\phi_{0x}$. For $0 \leq \phi_{0y} < \phi_{Jy}$ the amplitude function is everywhere smaller than this.

9.2 Optimal phase advance

Suppose we wish to find the jaw phase advance ϕ_{1y} which gives the lowest possible section of the amplitude function for some particular y_0. Essentially, this means to move the $\mathcal{J}$ line as close as possible to the origin. This occurs when $\phi_{Jy} = \phi_{1y}$, as can be established by reference to equation (14). Substitution in (13) then immediately gives the phase advance $\cos\phi_{1y} = y_0/r$.

9.2.1 Section with minimum value of A

Further, inspection of equation (14) reveals that the absolute minimum of A occurs when $y_0 = r_0$, leading to the jaw phase:

$$\phi_{1y} = \phi_{Jy} = \psi = \arccos(r_0/r) . \qquad (15)$$

In this case, $\mathcal{J}$ is coincident with the upper side of the 'inner-square'. Projecting up on to the amplitude function, we find the section $A(\phi_{0x}) = (A_y/r)^2 = 1$ and $A_x = 0$.

9.2.2 Effectiveness of single jaw

Note, though condition (15) is the optimal collimator location for particles leaving from the source point $x_0 = 0$, $y_0 = r_0$, it may not be the optimum location, though, for other source points. So now, for the jaw location $\phi_{1y} = \psi$, let us find the section of the amplitude function for some x_0, y_0 not equal to $0, r_0$. we find:

$$A(\phi_{0x}, y_0) = \frac{(r_0^2 - y_0^2)}{\cos^2\phi_{0x}} + \frac{y_0^2}{(r^2 - r_0^2)}\left[1 + \frac{r^2}{y_0^2} - 2\frac{r_0}{y_0}\right] \geq 1 . \qquad (16)$$

For example, this formula predicts that as the source point $x_0 \to r_0$ and $y_0 \to 0$, so the amplitude tends to:

$$A = \frac{r_0^2}{r^2 \cos^2\phi_{0x}} + \frac{r^2}{(r^2 - r_0^2)} . \qquad (17)$$

Obviously, jaws at $\alpha = 0, \pi$ are very poor collimators of the horizontal betatron motions.
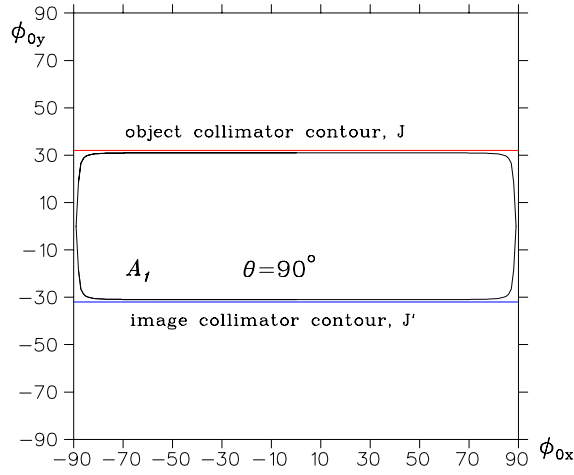
Figure 9: Object plus image jaw collimates all particles with $\theta = 90°$ to $A = 1$.

10   2 & 4 JAWS AT $\alpha = 0, \pi$

10.1   Image jaw

Unfortunately, the jaw placement we have described (section 9.2) does nothing to collimate particles whose intial ϕ_{0y} phases are negative. By inspection of equation (5), a lower jaw (i.e. at negative y) should be placed with a phase advance $\phi_{1y} = \pi - \psi$. See figure 9.

10.2   Lower half of source aperture

The two jaws we have installed so far collimate source points with y_0 positive, but they do nothing to collimate particles coming from the lower half of the source aperture (i.e. y_0 negative). From this observation it follows that a lower jaw placed with a phase advance $\phi_{1y} = \phi_{Jy}$ will collimate particles emanating from the lower half of the source aperture. Such a jaw stops all particles (with negative y_0) whose intial phases are greater than $\phi_{0y} = \phi_{Jy} > 0$. In order to collimate particles with initial phases less than $\phi_{0y} = -\phi_{Jy} < 0$ we need a further upper jaw placed at $\phi_{1y} = (\pi - \phi_{Jy})$ and $\alpha = 0$. The combination of object and image jaws is sketched in figure 10.
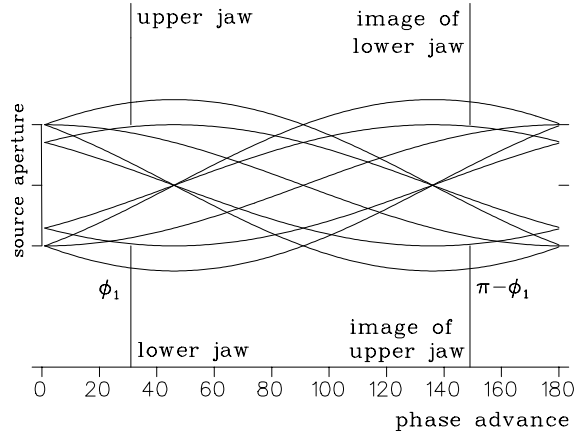

Figure 10: Placements of object and image jaws.

11   SYSTEM OF EIGHT H & V JAWS

A symmetrical system of four jaws (2 upper and 2 lower) will to some degree reduce all y-amplitudes (i.e. A_y is bounded from above). Given that source points satisfy $x_0^2 + y_0^2 = r_0^2$, there will be some collimation of the x-motion, *but* the maximum x-amplitudes (A_x) are unbounded. This problem can eliminated by placing pairs of left and right jaws (i.e. $\alpha = \pi/2$ and $\alpha = 3\pi/2$) at the optimum phase advance $\phi_{1x} = \phi_{Jx}$. The right jaw at phase advance ϕ_{1x} and the left jaw at $(\pi - \phi_{1x})$ will collimate particles with $x_0 > 0$; and visa versa for particles emanating from the left half of the source aperture ($x_0 < 0$).

Table 1 summarizes the jaw placements, while figure 11 shows the corresponding jaw contours $\mathcal{J}$ (for x, y extrema) in the plane of initial phases. We adopt the convention that objects are placed at $\phi_1 = \phi_J$ and images at $\phi_1 = \pi - \phi_J$. The angles α are chosen to best cut particles emanating from azimuthal source position θ, and are given as follows: for objects $\alpha = -(\theta - 90)$ and for images $\alpha = -(\theta + 90)$.

Figure 11 is drawn for the special case of jaws chosen to collimate particles emanating from the horizontal and vertical extrema $x_0 = r_0$ and $y_0 = r_0$, respectively.

Table 1: Jaw inclination versus source azimuth.

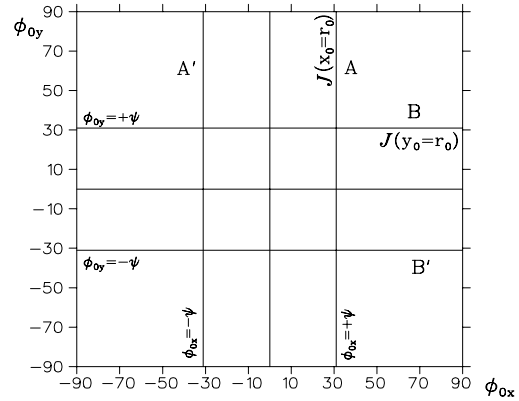| $\theta°$	name	$\alpha°$	curve
0	Right object	90	A
90	Upper object	0	B
180	Left object	-90	A
-90	Lower object	180	B
0	Right image	-90	A'
90	Upper image	180	B'
180	Left image	90	A'
-90	Lower image	0	B'

Figure 11: Jaw contours, $\mathcal{J}$, in the plane of initial phases for various jaw orientations ($\alpha = 0, \pm\pi/2, \pi$) and phase advances. A,B,A',B' refer to Table 1.

11.1   Effectiveness of 8 jaws

The value of the amplitude function for particles that just survive eight jaws is:

$$A(x_0, y_0) = \left(\frac{r_0}{r}\right)^2 + \frac{(r - x_0 \cos \phi_{1x})^2}{r^2 \sin^2 \phi_{1x}} + \frac{(r - y_0 \cos \phi_{1y})^2}{r^2 \sin^2 \phi_{1y}} .$$
(18)

If the phase advances are equal, the expression becomes:

$$A \le \left(\frac{r_0}{r}\right)^2 + \frac{[2r^2 - 2r(x_0 + y_0)\cos\phi_1 + r_0^2 \cos^2\phi_{1x}]}{r^2 \sin^2\phi_{1x}} \; . \tag{19}$$

The function (19) is quite flat: though the intersection of the $\mathcal{J}$ contours is furthest away from the $\mathcal{A}$-curve when $\theta = 45°$, the value of A is not large because the tangent function (see Eqn. 6) has not yet risen steeply. Contrast this with the cases $\theta \approx 0$ or $\theta \approx 90°$: the jaw contours lie very close to the $\mathcal{A}$-curves, but the discrepancy occurs where the tangent function is very large. Note, placing a further four jaws (parallel to x and y axes) at $\phi_1 = \pi/2$ produces only marginal improvement in the degree of collimation.

Though it would be quite difficult to improve the collimation of particles emanating from horizontal and vertical extrema of the source aperture, it is fairly easy to improve the collimation of particles emanating from the diagonals $x = \pm y$ by adding additional jaw contours that pass closer to $\mathcal{A}_1$. To do this one must install jaws parallel to the diagonals of the x, y-plane.

12 DIAGONAL JAWS AT $\alpha = \pi/4$

Starting from a single jaw, we now consider 1,2,4 jaws for various ϕ_1 choices for the special case $\alpha = \pi/4$. Let us consider the "low-level" goal of choosing the jaw phase advances so that some segment of the contour $\mathcal{J}$ is as close as possible to some given amplitude contour $\mathcal{A}_1$. The Lagrange analysis of Appendix B shows that the jaw contour makes its 'closest' approach to the $\mathcal{A}_1$-curve at the location $\phi_{0x} = \phi_{1x}$ and $\phi_{0y} = \phi_{1y}$ provided that the phase advances fulfill the special condition:

$$\frac{\tan\alpha}{\tan\theta} = \frac{\cos\phi_{1x}}{\cos\phi_{1y}} \; . \tag{20}$$

Hence a jaw on the diagonal will provide optimum collimation for source particles emanating from the anti-diagonal of the x, y-plane; see figure 8.

12.1 Symmetric case, $\phi_{1x} = \phi_{1y}$

Consider the properties of the jaw contour $\mathcal{J}$ for $\alpha = \pi/4$ and equal phase advances $\phi_{1x} = \phi_{1y}$. Further restrict to the case $\theta = \pi/4$ and insist that the jaw phase advance is $\phi_1 = \psi$. Let us parametrize $\tan\phi_{0x} = \lambda \tan\phi_{0y}$ and solve for the contour in the form $\phi_{0y}(\lambda)$:

$$(1 + \lambda)\tan\phi_{0y} = 2\tan\psi \quad -1 \le \lambda \le +1 \tag{21}$$

The locus of ϕ_{0y} is the curve A in figure 12.

12.1.1 Intercepts of $\mathcal{J}$ on the diagonal and ϕ_{0y}, ϕ_{0x} axes

Let us set $\lambda = +1$. For optimal collimation, the phase advance $\phi_{0x} = \phi_{0y} = \phi_1$ leads to the the intercept on the diagonal being $\phi_{Jy} = \phi_{Jx} = \psi = \arccos(r_0/r)$.

See figure 12. We set $\lambda = 0$ and use the optimal jaw phase advance $\phi_1 = \psi$. The intercepts of $\mathcal{J}$ with the ϕ_{0y} and ϕ_{0x} axes are given by $\tan\phi_{Jy} = \tan\phi_{Jx} = 2\tan\psi$.

12.1.2 Behaviour near the anti-diagonal

So far we have established the behaviour of $\mathcal{J}$ in the first quadrant. In the second quadrant ($\phi_{0x} < 0, \; \phi_{0y} > 0$) the contour never intercepts the anti-diagonal, but rather approaches asymptotically as $\phi_{0y} \to \pi/2$. In the fourth quadrant ($\phi_{0x} > 0, \; \phi_{0y} < 0$), $\phi_{0y} \to -\pi/2$ from above.
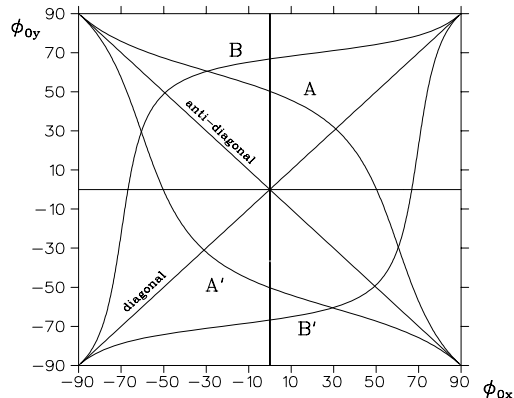

Figure 12: Jaw contours, $\mathcal{J}$, in the plane of initial phases for jaws on the diagonals.

12.1.3 Summary

Particles from the source point $\theta = \pi/4$ and with initial phases greater than given by (21) will be stopped by the jaw at phase advance $\phi_{1x} = \phi_{1y} = \psi$.

12.2 Image jaw

The image jaw with phase advance $(\pi - \psi)$ and inclination $\alpha = -3\pi/4$, leads to a $\mathcal{J}$ contour that is mirror symmetric (about the anti-diagonal) to the $\mathcal{J}(\phi_1 = \psi)$ contour. These two contours make a good approximation to the $\mathcal{A}_1(x_0 = y_0)$ contour in quadrants number one and three; but provides little collimation in quadrants number two and four.

12.3 Jaws at $\phi_1 = \pi/2$

Previously, for the circular collimator we tackled the problem quadrants (2 and 4) by placing an additional collimator at $\phi_{1x} = \phi_{1y} = \pi/2$. Let us find the $\mathcal{J}$ contour for a jaw placed at the same phase advance. Actually, because the jaw has a lower symmetry than the circular collimator, we have to be quite careful as to how we pick the jaw inclination α. When $\phi_{1x} = \phi_{1y} = \pi/2$, the jaw function $J = 1$ can be rearranged to give:

$$\tan\phi_{0y} = \frac{r}{y_0 \cos\alpha} - (x_0/y_0)\tan\alpha\tan\phi_{0x} \; . \tag{22}$$

The ϕ_{0y}-intercept is $\tan\phi_{Jy} = r/(y_0\cos\alpha)$.

For object and image jaws at $\alpha = \pi/4$ and $(\alpha - \pi)$ we obtain contours similar to curves A and A', respectively, in figure 12. However, these are made redundant by the more efficient jaw/image at $\phi_1 = \psi, \pi - \psi$. If we make the substitution $+\alpha \Rightarrow -\alpha$ in (22), then we should find the jaw contour to lie entirely above the diagonal, curve B figure 12; and the contour of the image jaw to lie completely below the diagonal, curve B' figure 12.

Consider, now, that to improve the collimation by an optimal jaw at $\phi_{1x} = \phi_{1y} = \psi$ (curve A, figure 12) and its image jaw at phase advance $\pi - \psi$ and inclination $\alpha - \pi$ (curve A', figure 12), for the case $\alpha = \pi/4$ we need to make additional cuts in the second and fourth quadrants. Clearly, the first two collimators should be supplemented by a jaw at inclination $-\alpha$ (curve B, figure 12) and complemented by a further jaw at inclination $\pi - \alpha$ (curve B', figure 12). Both additional jaws are placed at phase advance $\phi_{1x} = \phi_{1y} = \pi/2$.

12.4 Effectiveness of four jaws

Let us consider how effective are these four jaws in collimating particles emanating from $\theta = \pi/4$. If we project up the object and image $\mathcal{J}$ contours (A and A', Fig. 12) on to the amplitude function A, we find the lowest cut is $A = 1$ at $\phi_{0x} = \phi_{0y} = \psi$. However, their cut at the ends of the anti-diagonal is $A \to \infty$. But fortunately, these particles are cut by the jaws at $\phi_1 = \pi/2$. If we project up the supplement and complement $\mathcal{J}$ contours (B and B') on to the amplitude function A, we find the lowest cut is $A = 1 + (r_0/r)^2 \approx 2$ on the anti-diagonal at $|\tan \phi_{0x}| = |\tan \phi_{0y}| = (r/r_0) > 1$. However, their cut at the ends of the diagonal is $A \to \infty$.

But when all four jaws are used in combination, the highest cut on A is given by the points of intersection of the curves A,B,A',B'. The A,B intersection point is given by:

$$\tan \phi_0 = \frac{r}{r_0} \frac{(1 \pm \sin \phi_1)}{\sin \phi_1} - \frac{\cos \phi_1}{\sin \phi_1} , \qquad (23)$$

where the abscissa ϕ_{0x} is given by the negative sign and the ordinate ϕ_{0y} is given by the positive sign. Substituting these values into the A-function, we find the upper bound on betatron amplitudes emanating from $x_0 = y_0$ is

$$A = 1 + \frac{1}{\sin^2 \psi} = 1 + \frac{r^2}{(r^2 - r_0^2)} . \qquad (24)$$

Here we have used $\phi_1 = \psi$ and $\cos \psi = r_0/r$ (the optimum object jaw location, curve A).

To find the effectiveness in collimating particles emanating from other source points, one should substitute x_0, y_0 into the jaw equation, find the new $\mathcal{J}$ contour, project this up on to the amplitude function and find at what levels A is cut. However, it is clear the jaw on the diagonal will be ineffective in collimating particles emanating from $\theta = 0, \pi/2$, etc..

13 JAWS ALIGNED WITH DIAGONALS

We have seen how to implement a system of four jaws so at to collimate particles emanating from the upper-right diagonal ($\theta = \pi/4$) of the source aperture (i.e. the first x, y-quadrant). Let us establish analogous results for the other quadrants. The naming of the jaws in the tables below follows from the source point they are intended to best collimate, and does not relate to their inclination angle. The "curve" entries in the tables refers to figure 12.

The following table 2 gives the jaw orientations for 'object' jaws at $\phi_1 = \psi$, and 'image' jaws at $\pi - \psi$. For 'object' jaws $\alpha = -(\theta - 90)$, while for 'images' $\alpha = -(\theta + 90)$.

Table 2: Jaw inclination versus source azimuth.

x, y-quad.	$\theta°$	jaw name	$\alpha°$	curve
first	45	Upper-Right object	45	A
second	135	Upper-Left object	-45	A
third	-135	Lower-Left object	-135	A
fourth	-45	Lower-right object	135	A
first	45	Upper-Right image	-135	A'
second	135	Upper-Left image	135	A'
third	-135	Lower-Left image	45	A'
fourth	-45	Lower-right image	-45	A'

The following table 3 gives the jaw orientations for additional collimators placed at the symmetry point $\phi_1 = \pi/2$. The complementary $\mathcal{J}$ contours are mirror images about the diagonals of the ϕ_{0x}, ϕ_{0y}-plane of the $\mathcal{J}$ contours of the supplementary jaws. For 'supplement' jaws $\alpha = +(\theta - 90)$, while for 'complements' $\alpha = +(\theta + 90)$.

Table 3: Summary of jaws placed at phase $\phi_1 = \pi/2$.

θ (deg)	jaw name	α (deg)	curve
45	Upper-Right supplement	-45	B
135	Upper-Left supplement	45	B
-135	Lower-Left supplement	135	B
-45	Lower-Right supplement	-135	B
45	Upper-Right complement	135	B'
135	Upper-Left complement	-135	B'
-135	Lower-Left complement	-45	B'
-45	Lower-Right complement	45	B'

Despite appearances, this table enumerates only four jaws; each one acts as both supplement and complement, but to different azimuthal locations θ.

13.1 System of twelve jaws

A system of twelve jaws chosen according to locations and inclinations given in the tables 2,3 above will collimate all particles emanating from the neighbourhood of the source diagonals to amplitudes less than expression (24).

14 CONCLUSION ON JAW SELECTION

The system of eight jaws described in section 11 will collimate particles emanating from $\theta = 0, \pm\pi/2, \pi$, while the system of twelve jaws enumerated in section 13 will collimate particles emanating from $\theta = \pm\pi/4, \pm 3\pi/4$. However, a problem arises in that one must place many jaws at the same phase advance; and this may not be possible due to space limitations. In this case, some of the jaws must be placed at locations where the lowest cut on the amplitude function is above level one. If this is so, then it is advantageous to utilize a lattice with tune splitting, so that the trace of the phase advance avoids the diagonal $\phi_{1x} = \phi_{1y}$.

15 ACKNOWLEDGEMENTS

16 REFERENCES

[1] L.C. Teng: *Design concepts for the beam scraper system of the main ring*, Fermilab Int. Report FN-196/0400 (1969).

[2] T. Trenkler and J. Jeanneret: *The principles of two stage betatron and momentum collimation in circular accelerators*, LHC Note 312; also Particle Accelerators, Vol.50, pg.287.

[3] T. Risselada: *Optical requirements for an LHC cleaning insertion with elliptical collimators*, SL/Note 95-67 (AP).

[4] D. Kaltchev et al: *Optimization of collimator jaw locations for the LHC*, Proc. 5th European PAC, Sitges, 1996, pg.1432.

[5] D. Kaltchev: private communication; or *Search for the best lattice for betatronic collimation*, SL Seminar 28/04/97.

[6] S. Koscielniak: *Observations on betatron collimation and the effect of tune splitting...*, TRI-DN-97-23.

A CIRCULAR COLLIMATOR

Here, by using the technique of "Lagrange multipliers" we shall find the condition that brings the $\mathcal{C}_1$ contour closest to the $\mathcal{A}_1$ contour, assuming both curves share the same x_0, y_0. The task is equivalent to minimizing A subject to the constraint $C = 1$. The constraint influences the directions in which we can move while searching for the minimum, and this is taken care of by the Lagrange multiplier λ which is to be determined. At the minimum we find:

$$\frac{\partial}{\partial \phi_{0x}}[A + \lambda C] = 0 \quad \text{and} \quad \frac{\partial}{\partial \phi_{0y}}[A + \lambda C] = 0 . \quad (25)$$

leading to the simultaneous equations:

$$-\lambda = \frac{\sin \phi_{0x}}{\sin \phi_{1x}} \frac{1}{\cos(\phi_{1x} - \phi_{0x})} = \frac{\sin \phi_{0y}}{\sin \phi_{1y}} \frac{1}{\cos(\phi_{1y} - \phi_{0y})} . \quad (26)$$

Further we should optimize these conditions with respect to (w.r.t.) variations of ϕ_{1x}, ϕ_{1y}. This minimization gives

equations analogous to (25) but with ϕ_1 replacing ϕ_0 and leads to the conditions:

$$\lambda \sin 2(\phi_{1x} - \phi_{0x}) = \lambda \sin 2(\phi_{1y} - \phi_{0y}) = 0 . \quad (27)$$

Solving the four simultaneous equations (25) and (27) leads immediately to

$$\phi_{0x} = \phi_{1x} \quad \text{and} \quad \phi_{0y} = \phi_{1y} \quad (28)$$

and $\lambda = -1$ which implies the surfaces A and C contact tangentially at the location of closest approach and that $A = C = 1$ at the minimum. Finally, substitution of (26) into A or C gives the optimal phase advance condition

$$\frac{x_0^2}{r^2 \cos^2 \phi_{1x}} + \frac{y_0^2}{r^2 \cos^2 \phi_{1y}} = 1 . \quad (29)$$

A.1 Lattice constraints

The method may be extended to include lattice constraints. Formally, we minimize $A + \lambda_1 C + \lambda_2 L$ where λ_1, λ_2 are undetermined multipliers, $A = A(\phi_0)$, $C = C(\phi_1 - \phi_0)$ and $L = L(\phi_1)$ is the lattice constraint. Let primes ($'$) denote derivative. Minimization w.r.t. ϕ_0 implies $A' + \lambda_1 C' = 0$ which is essentially equations (25,26); whereas minimization w.r.t. ϕ_1 implies $\lambda_1 C' + \lambda_2 L' = 0$. For example, take the lattice with sinusoidal tune splitting:

$$L(\phi_{1x}, \phi_{1y}) = (\phi_{1y} - \phi_{1x})/2 + \Delta \sin[(\phi_{1x} + \phi_{1y})k/2] = 0 .$$

The four differential equations and two constraints may be solved for the six unknowns $(\phi_{0x,y}, \phi_{1x,y}, \lambda_{1,2})$ leading to the solution $\lambda_1 \to -1$, $\lambda_2 \to = 0$, $\phi_{0x,y} = \phi_{1x,y}$ and $\phi_{1x,y}$ given by the intersection of the lattice phase-advance trace with $\{\mathcal{A}_1\}$ (section 3.2.2) as sketched in figure 7.

B JAW COLLIMATOR

Because A contains squares but J does not, the working is a little harder, and the result less definitive. As before, we introduce an undetermined multiplier λ into the minimization of A with the constraint $J = 1$. Minimizations with respect to the particle initial phases (ϕ_{0x}, ϕ_{0y}) require:

$$\frac{\partial}{\partial \phi_{0x}}[A + \lambda J] = 0 \quad \text{and} \quad \frac{\partial}{\partial \phi_{0y}}[A + \lambda J] = 0 . \quad (30)$$

These lead to the simultaneous equations:

$$-\frac{\lambda}{2} = \frac{x_0}{r} \frac{\sin \alpha \tan \phi_{0x}}{\sin \phi_{1x}} = \frac{y_0}{r} \frac{\cos \alpha \tan \phi_{0y}}{\sin \phi_{1y}} . \quad (31)$$

Further, optimization of the minimum w.r.t. variations of ϕ_{1x}, ϕ_{1y} (analogues of Eq. 32) leads to the additional conditions:

$$\lambda \sin(\phi_{1x} - \phi_{0x}) = \lambda \sin(\phi_{1y} - \phi_{0y}) = 0 . \quad (32)$$

Hence the minimum occurs when the initial phases satisfy equations (28), and so

$$\frac{x_0 \sin \alpha}{\cos \phi_{1x}} = \frac{y_0 \cos \alpha}{\cos \phi_{1y}} \quad \text{or} \quad \frac{\tan \alpha}{\tan \theta} = \frac{\cos \phi_{1x}}{\cos \phi_{1y}} . \quad (33)$$

Note, this analysis does not apply to the cases of a purely horizontal or vertical jaw, because in these cases the x and y directions are decoupled.

LIST OF PARTICIPANTS

Jose Alonso (ORNL/LBNL)
Charles Ankenbrandt (FNAL)
Valery Biryukov (IHEP)
Nuria Catalan-Lasheras (BNL)
Weiren Chou - co-chair (FNAL)
Mike Church (FNAL)
K. Angelika Drees (BNL)
Alexandr Drozhdin (FNAL)
Alexei Fedotov (BNL)
Dan Fitzgerald (LANL)
Roland Garoby (CERN)
Robert Gluckstern (UMD)
Robert Hardekopf (LANL)
Jeffrey Holmes (ORNL)
Carol Johnstone (FNAL)
Dobrin Kaltchev (TRIUMF)
Oleg Krivosheev (FNAL)

Sergey Kurennoy (LANL)
Robert Kustom (ANL)
Shinji Machida (KEK)
Nikolai Mokhov - co-chair (FNAL)
Craig Moore (FNAL)
Yoshharu Mori (KEK)
King Ng (FNAL)
Ji Qiang (LANL)
Patti Poole - secretariat (FNAL)
Robert Ryne (LANL)
Cynthia Sazama - secretariat (FNAL)
Thomas Wangler (LANL)
Chris Warsop (RAL)
Robert Webber (FNAL)
Jie Wei (BNL)
Takeichiro Yokoi (KEK)
Hideaki Yokomizo (JAERI)